Digests of TMRC 2017

The 28th Magnetic Recording Conference

Magnetic Recording and Memory

HAMR, MAMR, TDMR, MRAM, AOS

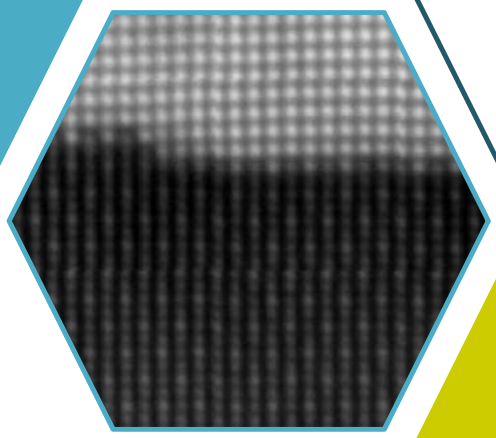

August 2-4

2017

Tsukuba JAPAN

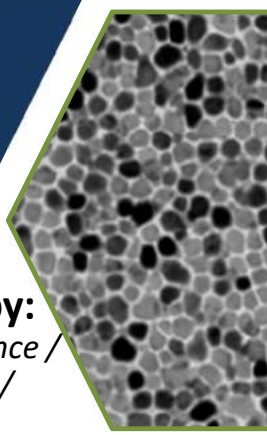

Sponsored by the IEEE Magnetic Society and Co-sponsored by:

National Institute for Materials Science / Japan Society for the Promotion of Science / Cabinet Office, Government of Japan / Japan Science and Technology Agency / Data Storage Systems Center, Carnegie Mellon University / Center for Memory and Recording Research, University of California, San Diego / Center for Micromagnetics and Information Technologies, University of Minnesota / Center for Materials for Information Technology, University of Alabama / Center for Research on Information Storage Materials, Stanford University / Computer Mechanics Laboratory, University of California, Berkeley /

Financial Support from:

Western Digital / Seagate Technology / TDK / Showa Denko K.K. / Broadcom Ltd. / Marvell Technology Group Ltd. / Guzik Technical Enterprises / Tanaka Precious Metals / Institute Tsukuba Convention & Tourism Bureau

Empty

IEEE MAGNETICS

presents

TMRC 2017

August 2nd – 4th, 2017 | Tsukuba, Japan.

The 28th Magnetic Recording Conference will focus on future magnetic storage technologies for hard disk drives and solid state memories. 38 invited papers of the highest quality will be presented orally at the conference and will later be published in the IEEE Transactions on Magnetics. Poster sessions will also be held consecutive to the oral sessions and will feature posters from the invited speakers and accepted contributed posters. Both invited and contributed papers are encouraged for publication.

Topics of interest include:

- Advanced Magnetic Recording for > 2 Tbits/in^2 including Readers, Writers, Servo, Tribology, HDI, Signal Processing.
- Two-Dimensional Magnetic Recording (TDMR)
- Heat Assisted Magnetic Recording (HAMR)
- Heated Dot Magnetic Recording (HDMR)
- Magnetic Solid State Memory (MRAM, STT-RAM, Racetrack)
- Alternative Magnetic Recording Technologies (SMR, MAMR, Tape, All Optical Switching)
- Magnetic Solid State Memory (MRAM, STT-MRAM, VC-MRAM, SOT-MRAM)
- Fundamentals (Metrology, Tooling, Materials, Recording Physics)

TMRC 2017 Committee:

Conference Co-chairs
Ikuya Tagawa, *Tohoku Inst. of Tech.*
Mark Kief, *Seagate*

Treasurers Co-chairs
Chris Rea, *Seagate*
Yukiko Takahashi, *NIMS*

Program Co-chairs
Roger Wood, *Western Digital*
Huaqing Yin, *Seagate*
Satoshi Okamoto, *Tohoku Univ.*
Shinji Yuasa, *AIST*

Local Co-Chairs
Kazuhiro Hono, *NIMS*
Masashi Sahashi, *JST*

Publication Co-Chairs
Michael Alex, *Western Digital*
Akihiko Takeo, *Toshiba*

Publicity
Shin Saito, *Tohoku Univ.*
Tetsuya Kanbe, *Showa Denko*
Hiroaki Muraoka, *Tohoku Univ.*
Katsuji Nakagawa, *Nihon Univ.*
Takeo Kagami, *TDK*

Welcome to TMRC 2017

Welcome to the 28th Magnetic Recording Conference (TMRC 2017). TMRC is an annual forum organized under the auspices of the IEEE Magnetics Society, with the invited presentations published in a special issue of the IEEE Transactions on Magnetics. This year's conference is taking place on August 2 - 4th at the Tsukuba International Congress Center in Tsukuba, Japan.

Never have we seen such rapid data growth. The magnetic recording technology and industry continues to evolve. The Cloud continues to rapidly expand and in the process drive major market changes. The Internet of Things promises to push this trend further with tens of billions of new networked devices. The introduction Cognitive systems will both depend upon and drive information creation and value. The latest whitepaper from IDC forecasts data growing at order of magnitude from 16 Zettabytes (ZB) in 2016 to 163 ZB by 2025 ["Data Age 2025", www.idc.com]. Hard Disk Drive (HDD) areal density (AD) continues to grow but a slower than historic rate as perpendicular magnetic recording exceeds 1.0 Terabytes/in^2. Flash is displacing HDD in laptops/ PC's and gained an important position in datacenters. Multiple new Hard Disk Drive (HDD) recording technologies are being pursued to extend AD to many Terabytes/in^2, including Two-Dimensional Magnetic Recording (TDMR), assisted-write technologies such as Heat Assisted Magnetic Recording (HAMR), perhaps Microwave more. Solid State memory is migrating to 3D Flash and new architectures. Magnetic Solid State Memory is maturing from niche applications to perhaps more with concepts that include MRAM (Magnetic Random Access Memory), STT-MRAM (Spin Torque Transfer -MRAM), VC-MRAM (Voltage Controlled-MRAM), SOT-MRAM (Spin Orbit Torque-MRAM) and others. It is hard to remember a time of greater change or challenge.

TMRC sets itself apart by delivering leading magnetic storage topics with uncommon technical depth. We have broadened the scope in 2017 to address both HDD and MRAM technologies. We are pleased to offer 38 invited lectures from some of the world's leading researchers in the field. The program will feature 2 sessions on HAMR, 2 sessions on MRAM, a session on MAMR, and a session on advanced recording technologies. These 6 oral sessions are complemented by 2 sessions with nearly 60 contributed posters, traditional Bierstube and banquet. Last but not least, we are pleased to welcome our keynote speaker Hirofumi Nagai from Fujitsu.

Events such as the TMRC are an important opportunity for the industry to come together and share important technical progress. This would not be possible without the many volunteers that create and coordinate the conference. Please join me in recognizing the committee of many dedicated individuals that make this year's TMRC possible. This is a strong international, inter-disciplinary group that well demonstrates the hard work and strong execution that is the cornerstone of the HDD industry. Lastly we would like to thank the National Institute for Materials Science in Tsukuba, Japan for generously hosting TMRC this year.

On behalf of The Magnetic Recording Conference Committee, Welcome!

Mark Kief
Co-General Chair

Ikuya Tagawa
Co-General Chair

TMRC 2017 | Sponsors

TMRC 2017 could not have happened without the generous support of our sponsors.

Co-sponsored by:

National Institute for Material Science (NIMS)

Japan Society for the Promotion of Science (JSPS)

Cabinet Office, Government of Japan

Japan Science and Technology Agency (JST)

Financial Support from:

Institute Tsukuba Convention & Tourism Bureau

TMRC 2017 | Exhibitors

東陽テクニカ
TOYO Corporation

JX Nippon Mining & Metals Corporation

Ube Material Industries,Ltd.

TMRC 2017 | Advertisers

Eiko EIKO ENGINEERING,LTD. / EIKO Corporation

QuantumDesignJapan
日本カンタム・デザイン株式会社

TMRC 2017 | Venue

EPOCHAL TSUKUBA (Tsukuba International Congress Center)

2-20-3, Takezono, Tsukuba, Ibaraki, 305-0032, Japan

Website: http://www.epochal.or.jp/eng/

Access to Tsukuba

From Narita Airport

The easiest way to get to Tsukuba is to take the Airport Liner NATT'S, a shuttle bus service. It departs from bus stop #8 at terminal 1 and bus stop #10 at terminal 2. Tickets are available at Keisei counter, which is located on the 1st floor of each terminal. It takes approximately 100 minutes to Tsukuba center (depends on traffic).

Time Table: http://kantetsu.co.jp/img/bus/highway/tsuchiura_narita/timetable_.pdf

Tsukuba Express (TX)

The Tsukuba Express is urban express railway which cover between Akihabara and Tsukuba, in 45 minutes.

About TX: http://www.mir.co.jp/en/about_tx/

From Haneda Airport

The best way to get to Tsukuba from Haneda Airport is to take a shuttle bus service. There are 24 bus services/day coming and going to the airport. The buses leave from the bus stop #13 on the 1F (arrival level). It takes approximately 110 minutes to Tsukuba center (depends on traffic).

Time Table: http://kantetsu.co.jp/img/bus/highway/tsukuba_haneda/time_table.pdf

From Tokyo

The busses between Tokyo and Tsukuba leave from Tokyo station "YAESU-south exit" every 10 to 20 minutes. It takes about 90 minutes to Tsukuba depending on the traffic.

TMRC 2017 | Program Outline

Location	August 2 (Wed)	August 3 (Thr)	August 4 (Fri)
Convention Hall Lobby	Registration 8:15AM	Registration 8:30 AM	Registration 8:30 AM
Convention Hall 200	**8:50AM: Welcome** **Session A** **HAMR I (Media)** 9:00 AM - 12:20 PM Coffee Break 10:30 - 10:50 AM	**Session C** **MRAM I** 8:50 AM - 12:10 PM Coffee Break 10:20 - 10:40 AM	**Session E** **MAMR and Related** 8:50 AM - 12:10 PM Coffee Break 10:20 - 10:40 AM
Multi-purpose Hall	**Lunch** 12:20 PM - 1:20PM	**Lunch** 12:10 PM - 1:10 PM	**Lunch** 12:10 PM - 1:10 PM
Convention Hall 200	**Session B** **Advanced Recording Components and Systems** 1:20 PM - 5:10 PM Coffee Break 2:50 PM - 3:10 PM	**Session D** **HAMR II (Systems)** 1:10 PM - 5:00 PM Coffee Break 2:40 PM - 3:00 PM	**Session F** **MRAM II** 1:10 PM - 4:30 PM Coffee Break 2:40 PM - 3:00 PM **4:30 PM: Closing Remarks**
Multi-purpose Hall	**Session BP** **HAMR & Systems Contributed Posters & Invited A, B, D** Bierstube 5:10 PM - 7:00 PM	**Session DP** **MRMR & MRAM Contributed Posters & Invited C, E, F** Bierstube 5:00 PM - 6:40 PM	**Optional NIMS and AIST tour** Center for Magnetic and Spintronic Materials, NIMS, and Spintronics Research Center, AIST 4:45 PM - 6:45 PM
Okura Frontier Hotel Jupiter		**Banquet** 7:00 PM - 9:00 PM **Keynote** 8:00 PM - 8:30 PM	

(EPOCHAL TSUKUBA Floor Guide)

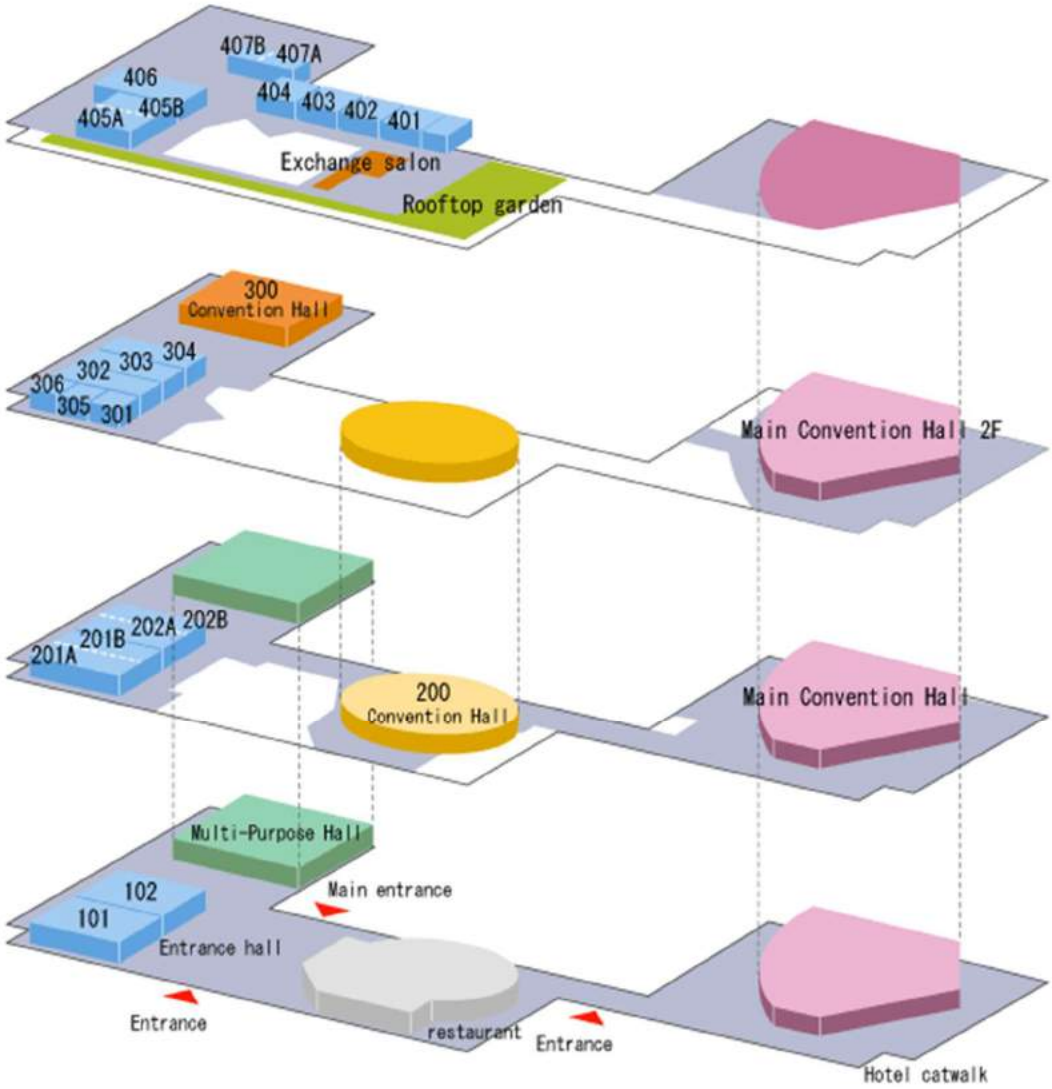

TMRC 2017 | Keynote Speaker

Hirofumi Nagai

AI platform business Unit, Business Strategy office, Fujitsu Ltd.

“AI technology innovation will change to storage and memory !?”

Through introducing Fujitsu's R&D front works on deep learning and on quantum inspired computing, the new roles of storage and memory system will be explored.

Wednesday, August 2, 9:00AM – 12:20PM

Session A: HAMR I (Media)

Session Chairs: Tetsuya Kanbe (Showa Denko) and Eric KC Chang, Pin-Wei Huang (Seagate)

(A1) 9:00AM- **TUNING MAGNETIC ANISOTROPY AND CURIE TEMPERATURE OF $L1_0$-FePt GRANULAR FILMS**
Takehito SHIMATSU*, Takuya ONO, Tomohiro MORIYA, Hitoshi NAKATA, Kazuya KOMIYAMA, Shinji UCHIDA, Hirohisa Oyama, Hiroto KIKUCHI, Hiroyasu KATAOKA, Kiminori SATO, Akira FURUTA, Tsuyoshi YOSHIZAWA, Masatoshi HATAYAMA, Kaoru TSUMURA, Nobuaki KIKUCHI and Osamu KITAKAMI, **Tohoku University, Japan*

(A2) 9:30AM- **ORIGIN OF IN-PLANE COMPONENT FOR $L1_0$-FePt GRANULAR FILMS DEPOSITED ON MgO SINGLE CRYSTAL SUBSTRATE**
J. WANG*, H. SEPEHRI-AMIN, Y.K. TAKAHASHI and K. HONO, **National Institute for Materials Science, Japan*

(A3) 10:00AM- **TEMPERATURE INDUCED CHANGES IN THE OPTICAL AND MATERIAL CHARACTERISTICS OF HAMR MEDIA COC AND ITS EFFECT ON RECORDING PERFORMANCE**
Paul M. JONES*, Zhaohui Z. FAN, Xiaoding MA, Hongbo WANG, Huan H. TANG, **Seagate Technology, USA*

Coffee Break (10:30AM - 10:50AM)

(A4) 10:50AM- **HIGH ENERGY PLASMA BASED CARBON OVERCOAT DEPOSITION ON HEAT-ASSISTED MAGNETIC RECORDING MEDIA**
Sabpreet BHATTI, Rajdeep S. RAWAT and S.N. PIRAMANAYAGAM*, **Nanyang Technological University, Singapore*

(A5) 11:20AM- **CONTROLLING FePt GRAIN SIZE WITH A GRANULAR MgO-C INTERLAYER FOR HAMR**
B. S. D. Ch. S. VARAPRASAD*, B. ZHOU, T. MO, D. E. LAUGHLIN, and J.-G. (Jimmy) ZHU, **Carnegie Mellon University, USA*

(A6) 11:50AM- **COMPOSITE MEDIA FOR HIGH DENSITY HEAT ASSISTED MAGNETIC RECORDING**
Randall H. VICTORA*, and Zengyuan LIU, **University of Minnesota, USA*

Wednesday, August 2, 1:20PM – 5:10PM

Session B: ADVANCED RECORDING COMPONENTS AND SYSTEMS

Session Chairs: Hiroaki Muraoka (Tohoku Univ.) and Fatih Erden (Seagate)

(B1) 1:20PM- **2D VISUALIZATION IN MAGNETIC RECORDING**
Alexander TARATORIN*, Maxim NIKIFOROV, Alexander SHTEYN, Rick SHI and Michael ALEX, **Western Digital Corporation, USA*

(B2) 1:50PM- **ION BEAM BIT PATTERNED MEDIA USING MnGa ALLOY FILMS**
D. OSHIMA*, T. KATO and S. IWATA, **Nagoya University, Japan*

(B3) 2:20PM- **MICROSCOPIC ORIGINS OF ENHANCED OUTPUT OF HEUSLER ALLOY CPP-GMR READERS BY AMORPHOUS UNDERLAYER AND CONDUCTIVE OXIDE SPACER**
T. NAKATANI*, S. Li, Y. SAKURABA, T. T. SASAKI, X. D. XU, H. TAJIRI, T. FURUBAYASHI and K. HONO,
**National Institute for Materials Science, Japan*

Coffee Break (2:50PM - 3:10PM)

(B4) 3:10PM- **2-D EQUALIZATION WITH LOCATION DIVERSITY AND PRE-ADAPTATION TO HANDLE OFFTRACK IN ARRAY READER BASED HARD DISK DRIVES**
George MATHEW*, Scott DZIAK, Kurt WORRELL, Jeff E. SINGLETON, Bruce W. WILSON and Haitao XIA, **Broadcom Limited, USA*

(B5) 3:40PM- **USER AREAL DENSITY OPTIMIZATION FOR CONVENTIONAL AND 2D DETECTORS/DECODERS**
Kheong Sann CHAN*, Ashish JAMES, Sari SHAFIDAH, Susanto RAHARDJA, Jinlu SHEN, Krishnamoorthy SIVAKUMAR, Benjamin J. BELZER,
**Nanjing Institute of Technology, China*

(B6) 4:10PM- **TEMPERATURE OF DATA IN STORAGE DEVICES AND DATA STORAGE SOLUTIONS FOR THE NEXT DECADE**
Kai-Zhong GAO*, Sr. Member IEEE, **Argonne National Laboratory, USA*

(B7) 4:40PM- **ROLE OF MICROSTRUCTURE ON ALL-OPTICAL SWITCHING AND THZ EMMISSION**
E. E. FULLERTON*, **University of California San Diego*

Thursday, August 3, 8:50AM – 12:10PM

Session C: MRAM I

Session Chairs: Justin Shaw (NIST) and Hiroaki Yoda (Toshiba)

(C1) 8:50AM- **4 GBIT DENSITY STT-MRAM USING PERPENDICULAR MAGNETIC TUNNEL JUNCTIONS WITH COMPACT BIT CELL STRUCTURE**
S. M. SEO*, S.-W. CHUNG, T. Y. LEE, J. B. PARK, T. KISHI, M. YOSHIKAWA, H. AIKAWA, T. NAGASE, K. SUNOUCHI, H. KANAYA, A. YAMAMOTO, K. TSUCHIDA, H. OYAMATSU, and S. J. HONG,
**SK Hynix Incorporated, Korea*

(C2) 9:20AM- **SPIN-ORBIT TORQUE SWITCHING DEVICES FOR HIGH-SPEED MEMORIES AND ARTIFICIAL SYNAPSES**
Shunsuke FUKAMI*, Chaoliang ZHANG, Aleksandr KURENKOV, William A. BORDERS, Samik DUTTAGUPTA, and Hideo OHNO,
**Tohoku University, Japan*

(C3) 9:50AM- **MATERIAL DEVELOPMENTS AND NANOSECOND-SCALE SWITCHING PROCESS IN PERPENDICULARLY MAGNETIZED STT-MRAM CELLS**
T. DEVOLDER*, J. SWERTS, S. COUET, W. KIM, G. KAR, V. NIKITIN, J.-V. KIM, P. BOUQUIN, T. LIN, S. MERTENS, and G. KAR,
**CNRS University Paris-Sud, France*

Coffee Break (10:20AM - 10:40AM)

(C4) 10:40AM- **FURTHER TECHNOLOGIES FOR STT-MRAM**
K. YAKUSHIJI*, H. TAKAGI, N. WATANABE, K. Kikuchi, Y. KURASHIMA, A. SUGIHARA, H. KUBOTA and A. FUKUSHIMA, **AIST, Japan*

(C5) 11:10AM- **INVESTIGATION FOR HIGH-DENSITY STT-MRAM**
Hiroyuki TOMITA*, Yoshitsugu TANAKA, Keiichi NAGASAKA, Kanto NAKAMURA, Shinji FURUKAWA, Hitoshi KUBOTA, Akio FUKUSHIMA, Kay YAKUSHIJI, Hiroki MAEHARA and Naoki WATANABE,
**Tokyo Electron Yamanashi Limited, Japan*

(C6) 11:40AM- **RECENT PROGRESS IN VOLTAGE-CONTROLLED MAGNETIC ANISOTROPY: TOWARDS THE REALIZATION OF VOLTAGE-TORQUE MRAM**
T. NOZAKI*, Y. SHIOTA, A. KOZIOŁ-RACHWAŁ, M. TSUJIKAWA, X. XU, T. OHKUBO, T. TSUKAHARA, S. MIWA, M. SUZUKI, S. TAMARU, H. KUBOTA, A. FUKUSHIMA, K. HONO, M. SHIRAI, Y. SUZUKI, **AIST, Japan*

Thursday, August 3, 1:10PM – 5:00PM

Session D: HAMR II (Systems)

Session Chairs: Akira Kikitsu (Toshiba) and Randall Victora (Univ. of Minnesota)

(D1) 1:10PM- **JITTER IN HEAT-ASSISTED MAGNETIC RECORDING**
J. HOHLFELD*, P. SUBEDI, P.J. CZOSCHKE, M. BENAKLI,
**Seagate Technology, USA*

(D2) 1:40PM- **NOISE SOURCES AND MECHANISMS IN HEAT-ASSISTED MAGNETIC RECORDING**
G.J. PARKER and Lei XU*, **Western Digital Coropration, USA*

(D3) 2:10PM- **HEAT ASSISTED INTERLACED MAGNETIC RECORDING**
Steven GRANZ*, Wenzhong ZHU, Chris REA, Ganping JU, Jan-Ulrich THIELE, Tim RAUSCH & Edward GAGE, **Seagate Technology, USA*

Coffee Break (2:40PM - 3:00PM)

(D4) 3:00PM- **DISTRIBUTION-BASED RECORDING MODEL FOR HAMR**
T. MALETZKY*, M. STAFFARONI, and M.M. DOVEK,
**Headway Technologies, USA*

(D5) 3:30PM- **INTERFERENCE FROM ADJACENT TRACKS IN HAMR RECORDING SYSTEMS: SIDE_READING AND ENCROACHMENT**
Peter CZOSCHKE*, Victor SAPOZHNIKOV, Nuttapon CHAIDAUNGSRI and Douglas SAUNDERS, **Seagate Technology, USA*

(D6) 4:00PM- **MAGNETIC HEAD DESIGN FOR TRANSITION CURVATURE CORRECTION IN HAMR**
Jian-Gang (Jimmy) ZHU*, Yuwei QIN, and James BAIN, Cheng-Ming CHOW,
**Carnegie Mellon University, USA*

(D7) 4:30PM- **ENERGY-ASSISTED RECORDING: SYSTEM ARCHITECTURE AND APPLICATIONS**
Bernd LAMBERTS*, Classica JAIN and Remmelt PIT,
**Western Digital Corporation, USA*

Friday, August 4, 8:50AM – 12:10PM

Session E: MAMR and related

Session Chairs: Yukio Nozaki (Keio Univ.) and Kirill Rivkin (Seagate)

(E1) 8:50AM- **THEORETICAL LIMITS OF MICROWAVE ASSISTED MAGNETIC RECORDING (MAMR) EFFECTIVE FIELD GRADIENT**
Kirill RIVKIN* and Mourad BENAKLI, **Seagate Technology, USA*

(E2) 9:20AM- **DESIGN AND DEVELOPMENT OF SPIN-TORQUE-OSCILLATOR FOR MICROWAVE ASSISTED MAGNETIC RECORDING**
H. SEPEHERI-AMIN*, S. BOSU, C. ABERT, Y. SAKURABA, S. KASAI, M. HAYASHI, D. SUESS, and K. HONO,
**National Institute for Materials Science, Japan*

(E3) 9:50AM- **3D MAGNETIC RECORDING BASED ON MAMR TECHNOLOGY**
R. SATO*, H. SUTO, T. KANAO, T. NAGASAWA, and K. MIZUSHIMA,
**Toshiba Corp., Japan*

Coffee Break (10:20AM - 10:40AM)

(E4) 10:40AM- **ANTI-FERROMAGNETICALLY COUPLED MEDIA FOR MICROWAVE ASSISTED MAGNETIC RECORDING**
Simon GREAVES*, Yasushi KANAI and Hiroaki MURAOKA,
**Tohoku University, Japan*

(E5) 11:10AM- **DEVELOPMENT OF MICROWAVE INTERFEROMETER BASED ULTRA-HIGH SENSITIVITY FERROMAGNETIC RESONANCE MEASUREMENT APPARATUS FOR CHARACTERIZING DYNAMICAL PROPERTIES OF MAGNETIC NANODOT**
S. TAMARU*, H. KUBOTA, and A. FUKUSHIMA, **AIST, Japan*

(E6) 11:40AM- **TIME AND SPATIALLY RESOLVED XMCD-FMR MEASUREMENT ON A Co/Pt MULTILAYER DOT EXCITED BY RF MAGNETIC FIELD IN THE GHz REGIME**
Nobuaki KIKUCHI*, Hitoshi OSAWA, Motohiro SUZUKI, Osamu KITAKAMI,
**Tohoku University, Japan*

Friday, August 4, 1:10PM – 5:00PM

Session F: MRAM II

Session Chairs: Thibaut Devolder (Paris-Sud Univ.) and Shinji Yuasa (AIST)

(F1) 1:10PM- **VOLTAGE-CONTROL SPINTRONICS MEMORY HAVING POTENTIALS FOR HIGH-DENSITY AND HIGH-SPEED APPLICATIONS**
H. YODA*, N. SHIMOMURA, Y. OHSAWA, Y. SAITO, Y. KATO, T. INOKUCHI, S. SHIROTORI, K. KOI, M. SHIMIZU, H. SUGIYAMA, S. OIKAWA, B. ALTANSARGAI, M. ISHIKAWA, Y. KAMIGUCHI, K. IKEGAMI, and A. Kurobe, **Toshiba Corporation, Japan*

(F2) 1:40PM- **ADVANCED MAGNETIC TUNNEL JUNCTIONS USING SPINEL OXIDE BARRIERS**
Hiroaki Sukegawa**, National Institute for Materials Science, Japan*

(F3) 2:10PM- **NANO-LAYER OF TETRAGONAL Mn-BASED ALLOYS FOR MRAM APPLICATIONS**
Shigemi MIZUKAMI* and Kazuya SUZUKI, **Tohoku University, Japan*

Coffee Break (2:40PM - 3:00PM)

(F4) 3:00PM- **STORING OR PROCESSING DATA WITH ANTIFERROMAGNETS?**
X. MARTÍ*, I. FINA, **Academy of Sciences of the Czech Republic*

(F5) 3:30PM- **Cr_2O_3 BASED MAGNETOELECTRIC FERRIMAGNET TOWARD MRAM APPLICATIONS**
Tomohiro NOZAKI* and Masashi SAHASHI, **Tohoku University, Japan*

(F6) 4:00PM- **ULTRA-LOW MAGNETIC DAMPING IN METALLIC AND HALF-METALLIC MATERIALS FOR DATA-STORAGE AND MRAM**
Justin M. SHAW*, Martin SCHOEN, Danny THONIG, Eric EDWARDS, Hans NEMBACH, Tom SILVA, Michael SCHEIDER, Matt PUFALL, Charlie KARIS, Olle ERIKSSON,
**National Institute of Standards and Technology, USA*

NOTE

TUNING MAGNETIC ANISOTROPY AND CURIE TEMPERATURE OF $L1_0$-FePt GRANULAR FILMS

Takehito SHIMATSU[1,2], Takuya ONO[3], Tomohiro MORIYA[3], Hitoshi NAKATA[3], Kazuya KOMIYAMA[3], Shinji UCHIDA[3], Hirohisa Oyama[3], Hiroto KIKUCHI[3], Hiroyasu KATAOKA[3], Kiminori SATO[3], Akira FURUTA[3], Tsuyoshi YOSHIZAWA[3], Masatoshi HATAYAMA[1], Kaoru TSUMURA[1], Nobuaki KIKUCHI[4] and Osamu KITAKAMI[4]

1) FRIS, Tohoku University, Sendai, Japan, shimatsu@riec.tohoku.ac.jp

2) RIEC, Tohoku University, Sendai, Japan

3) Fuji Electric Co. Ltd., Tokyo, Japan

4) IMRAM, Tohoku University, Sendai, Japan

I. INTRODUCTION

$L1_0$-FePt granular films with perpendicular magnetization are attractive candidates for use as recording media for heat-assisted magnetic recording (HAMR) [1]. In HAMR, a medium is heated locally using laser irradiation to the Curie temperature (T_c) of FePt. The heating affects a lubricant and carbon overcoat. Some additives to FePt have been examined to reduce T_c while maintaining large K_u [1, 2–4], but T_c reduction degrads K_u considerably. Moreover, carbon and oxide materials are generally used as segregant materials to fabricate a granular structure of FePt. Optimum segregant materials to fabricate a well-segregated granular structure while maintaining large K_u are also important. As described herein, we examined the T_c reduction while maintaining large K_u by substituting some Fe or Pt of FePt with a third material. Moreover, we discuss the magnetic anisotropy of FePt granular media in relation to segregant materials.

II. ADDITION OF THIRD METALS

After fabricating FePt-X (X: third metals) single crystal films, we examined the relation between T_c and K_u. The 10-nm-thick FePt-X films were sputter-deposited on MgO(001) single-crystalline substrates with a 20-nm-thick Pt underlayer at a substrate temperature T_s of 350°C. The film deposition was done using co-sputtering with X targets and Fe-Pt targets with various composition ratios of Fe/Pt. The atomic ratios of Fe, Pt, and X thin films were confirmed using Rutherford backscattering spectrometry (RBS) analysis. Figure 1 presents the relation between values of T_c and K_u of the FePt-X films with X=Cu [5], Mn, and Ru [6]. The relation of T_c and K_u shows a roughly linear trend in all series of films. T_c of the FePtRu films decreased more steadily than that of the other series of films. These results demonstrate that Ru addition can achieve low T_c while maintaining K_u as higher than Mn and Cu addition. Figure 2 depicts relations of anisotropy field H_k (= $2K_u/M_s$, where M_s denotes saturation magnetization) and M_s of these films. Results show that Ru addition decreased H_k moderately, but M_s decreased rapidly. By contrast, Cu and Mn addition drastically decreased H_k. The rapid decrease of T_c by Ru addition occurs because of a sharp decrease of M_s: T_c is related to the magnitude of moments. Ru is a noble metal and is therefore not very reactive to oxygen, which is suitable for fabrication of granular films by adding oxide segregants.

III. SEGREGANT MATERIALS

Stacked films consisting of a FePt-oxide upper layer and a FePt-C template layer are effective to promote columnar growth and $L1_0$-ordering of FePt grains maintaining high K_u [7,8]. Figure 3 shows magnetization loops of FePt-25vol.% oxide (3 nm)/FePt-40vol.%C(2 nm) stacked films comprising various oxide materials. These films were fabricated using co-sputtering on MgO underlayers at a substrate temperature of 450°C in identical deposition conditions. All films are perpendicular films, but marked differences in magnetization curves were observed. These differences are related to segregation structures and K_u. Figure 4 presents values of K_u as a function of the electronegativity of oxide materials for these

Takehito Shimatsu
E-mail: shimatsu@riec.tohoku.ac.jp
tel: +81-22-217-5494

stacked films. The K_u of FePt-GeO_2/FePt-C stacked films is 2.1 × 10^7 erg/cm^3, which corresponds to 3.0 × 10^7 erg/cm^3 of FePt grains [9]. However, K_u decreased as electronegativity decreased, implying that the electronegativity of oxide segregants influences the degree of FePt ordering.

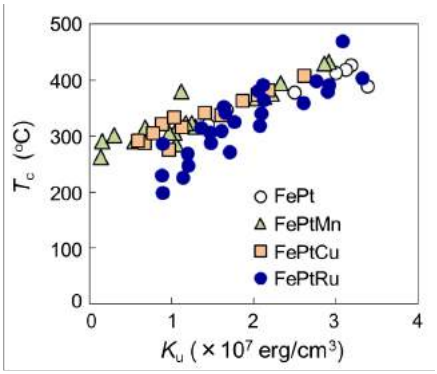

Fig. 1. Relation between values of T_c and K_u for FePtX (X=Mn, Cu, and Ru) films.

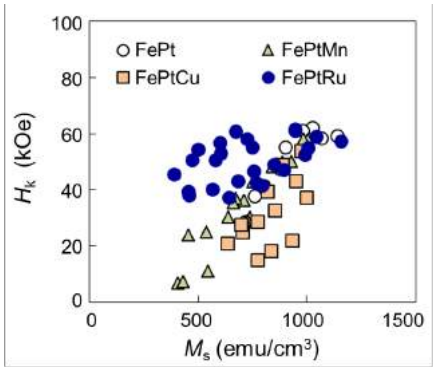

Fig. 2. Relation between values of H_k and M_s for FePtX (X=Mn, Cu, and Ru) films.

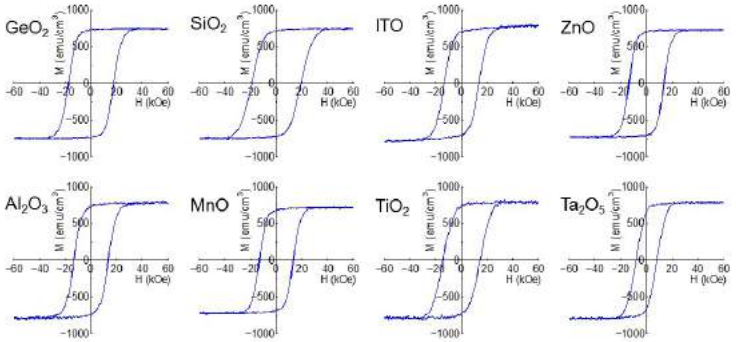

Fig. 3. Magnetization loops for FePt-25 vol.% oxide (3 nm)/FePt -40 vol.% C (2 nm) stacked films with various oxide materials.

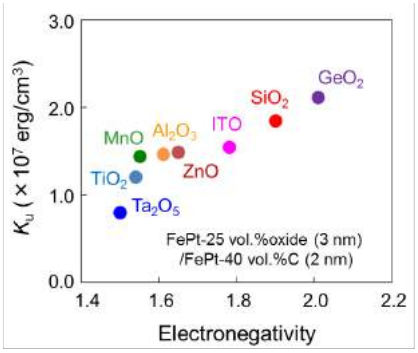

Fig. 4. Values of K_u as a function of electronegativity.

REFERENCES

1) B. M. H. Kryder, E. C. Gage, T. W. McDaniel, W. A. Challener, R. E. Rottmayer, G. Ju, Y. Hsia, and M. F. Erden, *Proc. IEEE*, 96(11) 1810-1835, (2008).
2) B. Wang and K. Barmak, *J. Appl. Phys.* 109 (12) 123916(1-7), (2011).
3) J. Ikemoto, Y. Imai, and S. Nakagawa, *IEEE Trans. Magn.,* 44(11) 3543-3546, (2008).
4) D. A. Gilbert, L.-W. Wang, T. J. Klemmer, J.-U. Thiele, C.-H. Lai, and K. Liu, *Appl. Phys. Lett.,* 102 132406(1-4), (2013).
5) T. Moriya, H. Nakata, K. Komiyama, S. Okamoto, N. Kikuchi, O. Kitakami, and T. Shimatsu, *58th Conference on Magn. Magn. Mater.,* BT-05 (2013).
6) T. Ono, H. Nakata, T. Moriya, N. Kikuchi, S. Okamoto, O. Kitakami, and T. Shimatsu, *Applied Physics Express*, 9, 123002(1-3), (2016).
7) B. S. D. C. S. Varaprasad, M. Chen, Y. K. Takahashi, and K. Hono, *IEEE Trans. Magn*., 49(2) 718-722, (2013).
8) T. Ono, T. Moriya, M. Hatayama, N. Kikuchi, S. Okamoto, O. Kitakami, and T. Shimatsu, *J. Appl. Phys*., 115 17B709(1-3), (2014).
9) T. Ono, T. Moriya, M. Hatayama, K. Tsumura, N. Kikuchi, S. Okamoto, O. Kitakami, and T. Shimatsu, *Applied Physics Letters*, 110 022402(1-4), (2017).

A2

ORIGIN OF IN-PLANE COMPONENT FOR $L1_0$-FePt GRANULAR FILMS DEPOSITED ON MgO SINGLE CRYSTAL SUBSTRATE

J. WANG, H. SEPEHRI-AMIN, Y.K. TAKAHASHI and K. HONO
National Institute for Materials Science, Sengen 1-2-1, Tsukuba 305-0047, Japan
WANG.Jian@nims.go.jp

I. INTRODUCTION

To achieve optimized recording performance, $L1_0$-FePt based HAMR media need to have strong (001)-texture. However, for the FePt grains deposited on (001) textured polycrystalline underlayers usually show serious in-plane components and can significant affect the signal-to-noise ratio (SNR) of the recording medium. The proposed origin of in-plane components in FePt based granular media, such as surface roughness [1] grain boundary [2], misorientation from the seed layer grains [3] and the formation of different variants [4] are still under debate. It is believed that the clarification of the origin of the in-plane components should make a significant impact on the future development of HAMR media. In this work, with detailed microstructure observation, we unexpectedly found that 90 degree misaligned (in-plane magnetic easy axes) FePt grains were detected even FePt epitaxially grow on MgO (001) single crystal substrate. To clarify the origin of such in-plane grains, FePt granular films with different segregant (carbon) composition were deposited on MgO (001) substrates, and their microstructures were studied in detail by aberration corrected scanning transmission electron microscopy (STEM).

II. EXPERIMENTAL

10-nm-thick FePt – x vol.% C (x= 0, 25, 30, 34 and 38) films were DC magnetron co-sputtered on single-crystalline MgO (001) substrates from FePt alloy target and C targets with a base pressure better than 2.5×10^{-7} Pa. The film microstructure was examined by aberration corrected scanning transmission electron microscopy (STEM), Titan G2 80 – 200.

III. RESULTS AND DISCUSSIONS

Without carbon as segregant, $L1_0$-ordered FePt grains form truncated octahedra or island microstructutre with large size distribution on the MgO substrate (not shown here). By the addition of carbon, the morphology of FePt grains is modified into well isolate nanoparticle. Figure 1 shows the in plane bright field TEM images of MgO (001) / FePt- 25.7 vol.% C 10 nm thin films with 5 nm carbon over coating. One can see that the FePt-C layer gives a well-isolated nano-granular structure with average grain size around 9.8 nm. Such media

J.WANG
National Institute for Materials Science
E-mail: WANG.Jian@nims.go.jp
Tel: +81-298-59-6819

gives nice squareness of the out-of-plane magnetization curve with perpendicular coercivity field $\mu H_c \sim 4.4$ T. Also, its narrow and straight in-plane magnetization loop in company with a small remnant magnetization ratio $M_{//} / M_{\perp} \sim 3$ % indicates limited in-plane components of the medium.

However, details microstructure observation indicates that 90 degree misaligned (in-plane magnetic easy axes) FePt grains are formed even on single crystal MgO substrate. Figure 2 shows a typical example, in which two different crystallographic orientations co-exist in one individual FePt grain. Lattice spacing and nano-beam diffraction patterns confirm the red dot marked resign in Fig. 2 has an in-plane c axis. Interestingly, such kind of feature is rarely observed in carbon free FePt granular thin film. It is believed that the diffusion of carbon into the FePt / MgO interface suppress the epitaxial grow of FePt grains which leads to the in-plane c axis. The FePt grains with partially in-plane c axis can hardly affect the magnetization reversal due to the strong directly ferromagnetic coupling with majority of out-of-plane components in one individual grain. But when they are separated with further increased carbon concentration, and then the fully in-plane orientated small FePt grains should response to the in-plane component of the recording media.

REFERENCES

[1] S. Wicht, V. Neu, L. Schultz, B. Rellinghaus, D. Weller, O. Mosendz, G. Parker, S. Pisana, "Atomic resolution structure–property relation in highly anisotropic granular FePt-C films with near-Stoner-Wohlfarth behaviour", *J. Appl. Phys.*, vol. 114, pp. 063906, (2013).

[2] H. Ho, J. Zhu, A. Kulovits, E. D. Laughlin, J.-G. Zhu, "Quantitative transmission electron microscopy analysis of multi-variant grains in present L1 0 -FePt based heat assisted magnetic recording media ", *J. Appl. Phys.*, vol. 116, no. 19, pp. 193510, (2014).

[3] J. Wang, S. Hata, Y.K. Takahashi, H. Sepehri-Amin, B.S.D.Ch.S. Varaprasad, T. Shiroyama, T. Schrefl, and K. Hono, "Effect of MgO underlayer misorientation on the texture and magnetic property of FePt–C granular film", *Acta Mater.*, vol. 91, pp. 41-49, Jun. (2015).

[4] H. Sepehri-Amin a, H. Iwama b, T. Ohkuboa, T. Shima b, K. Hono, "Microstructure and in-plane component of L10-FePt films deposited on MgO and MgAl2O4 substrates", *Scripta Mater.*, vol. 130, pp. 247–251, Dec. (2017).

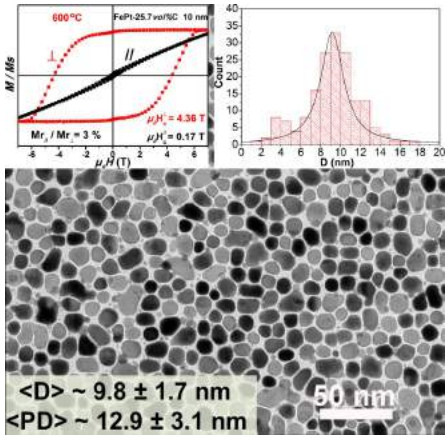

Fig.1 In-plane BF-TEM images of 10 nm FePt-25.7 *vol.%* C on MgO 001 substrate. Inset: OP (red) and IP (black) magnetization curves (left) and grain size distribution (right).

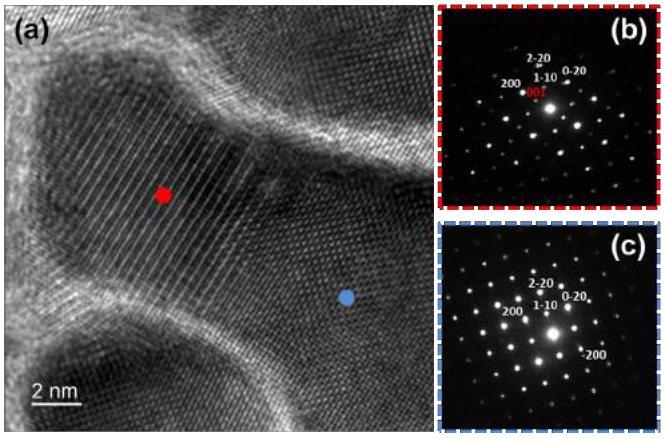

Fig.2 In-plane bright field STEM image (a) and nanobeam diffraction patterns taken from FePt grains with in-plane c axes (b) and out-of-plane c

TEMPERATURE INDUCED CHANGES IN THE OPTICAL AND MATERIAL CHARACTERISTICS OF HAMR MEDIA COC AND ITS EFFECT ON RECORDING PERFORMANCE

Paul M. JONES, Seagate Technology LLC Fremont, USA, Paul.M.Jones@Seagate.Com
Zhaohui Z. FAN, Seagate Technology LLC Fremont, USA, Zhaohui.Z.Zhang@Seagate.com
Xiaoding MA, Seagate Technology LLC Fremont, USA, Xiaoding.Ma@Seagate.com,
Hongbo WANG, Seagate Technology LLC Fremont, USA Hongbo.Wang@Seagate.com,
Huan H. TANG, Seagate Technology LLC Fremont, USA, Huan.H. Tang@Seagate.com

I. INTRODUCTION

Heat Assisted Magnetic Recording (HAMR) makes use of temperature dependent changes in the magnetic storage layer to enhance the writing process [1]. This imminent technology uses light propagating from the AAB to transiently heat the magnetic film within a fixed area, to a target temperature and for a well-defined time. Thus the optimum thermal and optical properties of the entire media film structure are important for the successful implementation of the HAMR interface. Typically, a nano-thin carbon overcoat (COC) film is used to protect the surface of magnetic storage disks from chemical and mechanical degradations. In addition to these attributes, the HAMR COC optical properties are important for a successful HAMR recording film structure. In this presentation we focus our efforts on the influence of the COC on the quality of the HAMR recording. Specifically, the influence of the COC optical properties on the SNR of the written signal as a function of deposition temperature was probed. The change in optical indices with deposition temperature was correlated with Raman spectroscopic measurements that enabled a detailed understanding of the change in the COC structure with temperature. The required laser power to attain HAMR writing and the recording quality were both obtained with HAMR heads. A significant improvement in the written SNR was observed with increasing deposition temperature. A detailed FEM model of this optical/thermal recording system clarified that this SNR increase was due to an increasing media thermal gradient with increasing COC extinction coefficient.

II. RESULTS

The wavelength dependent optical properties of the materials at the head-disk interface are required for a full understanding of how light emanating from the near field transducer (NFT) interacts with HAMR media. The media films closest to the NFT, especially those having high optical extinction coefficient (k), are expected to absorb proportionately more of this incoming light. The optical properties of COC films are sensitive to the exact deposition process and significantly the deposition temperature. [2]. To probe the effects that the optical properties of the COC film has on the HAMR recording, we have deposited films onto media surfaces at increasing temperature. The extinction coefficient of these films (presented in Fig. 1) increase with media surface temperature, which is attributed to material changes in the COC at high temperature, for example: increasing sp^2 content [3]. As a consequence, a larger absorption ($4\pi k/\lambda$) takes place in this layer, incrementally increasing its temperature and allowing the media to attain its target temperature using lower laser power (see Fig. 1). This increased optical efficiency allows the use of approximately 8% lower laser power to attain HAMR writing over the approximately 250 ºC COC deposition temperature range investigated (see Figure 1). It is well known that HAMR writing is dominated by the thermal gradient of the heated spot and is an important consideration when designing the media [1]. A comprehensive FEM head and media model was assembled that incorporated both their optical and thermal characteristics to study the effect that changes in the COC layer have on the media thermal gradient. The thermal gradient calculated with this model increases approximately 10% over the range in k of the studied COC films (see Fig. 2). A measurement of the quality of the written signal on similarly deposited media spanning a smaller range in extinction, shows an incremental improvement of approximately 0.5 dB, thus further supporting the importance of the thermal gradient on HAMR recording physics and its manipulation using the COC optical film properties.

Paul M. Jones
Seagate Technology LLC
Paul.M.Jones@Seagate.com
47488 Kato Road Fremont, California, 94538, USA
510-624-3856

REFERENCES

1) W. Challener, M. F. Erden, E. Gage, Y.-T. Hsia, G. Ju, M. H. Kryder, et al., "Heat assisted magnetic recording", *Proc. IEEE*, 96(11) 1810-1835, (2008)
2) F. W. Smith, "Optical constants of hydrogenated amorphous carbon film", *J. Appl. Phys.,* 55(3) 764-771, (1984)
3) M. Chhowalla, A. C. Ferrari, J. Robertson, and G. A. J. Amaratunga, "Evolution of sp2 bonding with deposition temperature in tetrahedral amorphous carbon studied by Raman spectroscopy", *Appl. Phys. Lett*., 76(11) 1419-1-1419-3, (2000)

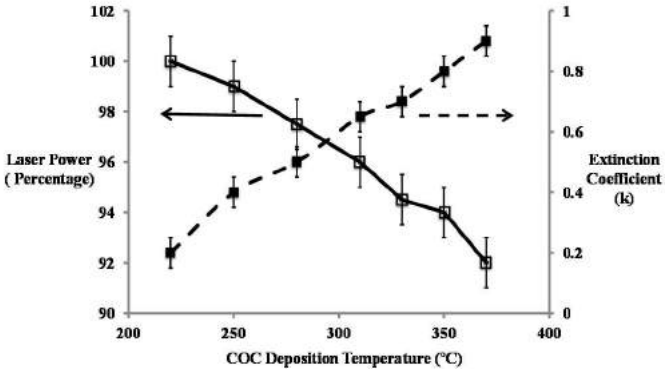

Fig. 1 The measured k (at 800 nm wavelength) of the COC films deposited at incrementally higher temperature and the laser power needed to attain HAMR writing, 100% is set with COC deposited at 220 °C.

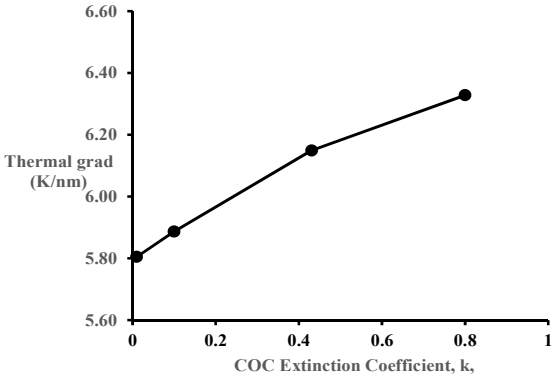

Fig. 2 The change in calculated thermal gradient in HAMR media due to increasing COC extinction coefficient.

HIGH ENERGY PLASMA BASED CARBON OVERCOAT DEPOSITION ON HEAT-ASSISTED MAGNETIC RECORDING MEDIA

Sabpreet BHATTI [1], Rajdeep S. RAWAT[2] and S.N. PIRAMANAYAGAM[1]

1) School of Physical and Mathematical Sciences, Nanyang Technological University, Singapore, prem@ntu.edu.sg

2) National Institute of Education, Nanyang Technological University, Singapore, rajdeep.rawat@nie.edu.sg

I. INTRODUCTION

Carbon overcoat (COC), made of amorphous diamond-like-carbon with good sp^3 fraction is needed to protect the magnetic recording media from the chemical and mechanical damages. Reduction of COC thickness whilst maintaining its functionality of a protective layer is a crucial requirement in increasing areal density. The current deposition techniques are unable to meet the requirements for COC thickness below 1.5 nm, which creates a need for an alternative deposition technique. Heat-Assisted Magnetic Recording, where the media will be heated also require thermally stable COC. High-energy carbon deposition techniques such as filtered cathodic vacuum arc (FCVA) which provide thin overcoats with high corrosion and wear protection generates particles, which hinders its use as COC for hard disk media [1]. Here, we introduce the use of a novel dense plasma focus (DPF) technology to the hard disk community [2]. COC deposition using a pulsed high-energy plasma focus device on FePt perpendicular magnetic media are reported.

II. EXPERIMENTAL DETAILS

Deposition of COC on FePt samples was carried out in a 3.3 kJ Mather type DPF device at different distances from the anode top (varying as 12, 16, 20, 24 and 28 cm). Methane gas was used as the main precursor for carbon deposition, while in some conditions the admixture of methane and argon gas was used to lower the amount of the precursor. The energy flux of the depositing ions is higher at 12 cm distance of deposition and reduces with the increase in the deposition distance. Since the deposition of COC was carried out using high energy density plasma along with higher energy ion flux, the magnetic and structural properties of FePt media might be modified. Hence, the magnetic and structural properties of pre- and post-COC deposited FePt media were compared using Magneto-optic Kerr Effect (MOKE) and the X-Ray Diffractometer (XRD). Simulation studies were also carried out to understand the effect of high energy deposition. Chemical properties of the COC were characterized by XPS and Raman spectroscopy.

III. RESULTS

In phase 1, COC deposited at very high energies were studied. Figure 1(a) shows the reduction in the coercivity of FePt after deposition of COC. This reduction in the coercivity value can be explained because of the exposure to the high energy ions during the deposition process which facilitates the partial transition of ordered FePt $L1_0$ phase to disordered A1 FePt phase [3]. It can also be noticed that the coercivity of deposited FePt reduces as the ion flux of depositing ion increases with decreasing the deposition distance.

The changes in the structural properties of FePt before and after COC deposition are shown in figure 1(b). The bare samples exhibit face-centered tetragonal phase with a stronger intensity of super-lattice (001) reflection peak from the $L1_0$ phase, while the (111) diffraction peak is relatively weak. It is evident from the XRD spectra that the I(001)/I(111) peak intensity ratio decreases for carbon coated FePt samples. The (111) peak position of COC deposited samples has shifted slightly to lower 2θ values as compared to the bare sample of FePt. The shift indicates the partial transition of FePt face-centered tetragonal phase to face-centered cubic phase, which confirms that the carbon deposition in DPF is highly energetic. Figure 1(c) shows the trend of G peak position for the deposited COC in methane and admixture of argon-methane at different deposition distances, measured by visible Raman spectroscopy. As reported by

S.N. Piramanayagam
E-mail: prem@ntu.edu.sg
tel: +65-65923148

A.C. Ferrari et.al. [4], the increase in the G peak's position (observed at lower deposition distance for methane and argon-methane admixture deposited carbon) in figure 1(c) indicates the increase in the fraction of sp^3 carbon. XPS results (Table I) indicated 44 to 47 % ratio of sp^3 to sp^2 carbon, which is promising for the use of DPF deposited carbon as hard disk media COC.

In the next phase, COC deposited at suitable energies, which do not deteriorate the magnetic properties are investigated. The magnetic properties, XPS investigations and the lubrication affinity of such a COC will be discussed in the talk.

IV. CONCLUSION

We have reported here the use of a high energy density pulsed plasma technique for the deposition of COC on the FePt perpendicular magnetic media. MOKE results depicted a change in the coercivity of the FePt media after COC deposition, which can be reduced by depositing COC using lower energies than those in phase 1. XRD results exhibited the partial transition of ordered FePt $L1_0$ phase to disordered FePt A1 phase after the deposition of COC at very high deposition energies. Raman spectroscopy suggested a higher fraction of sp^3 carbon can be achieved at lower deposition distance, which was verified by the XPS results. In conclusion, all these results demonstrate the promising potential of DPF device as an effective device for the COC deposition in future.

REFERENCES

1) Shakerzadeh, M., et al., "The effect of high deposition energy of carbon overcoats on perpendicular magnetic recording media", *Appl. Phys. Let.*, 103(16) 161604, (2013).
2) Soh, L.Y., et al., "Shadowgraphic studies of DLC film deposition process in dense plasma focus device. Plasma Science", *IEEE Trans.*, 32(2) 448-455, (2004).
3) Gaur, N., et al., "Lateral displacement induced disorder in L10-FePt nanostructures by ion-implantation". Sci. Rep. 3, (2013).
4) Ferrari, A. and J. Robertson, "Resonant Raman spectroscopy of disordered, amorphous, and diamondlike carbon", *Phys. Rev. B*, 64(7) 075414, (2001).

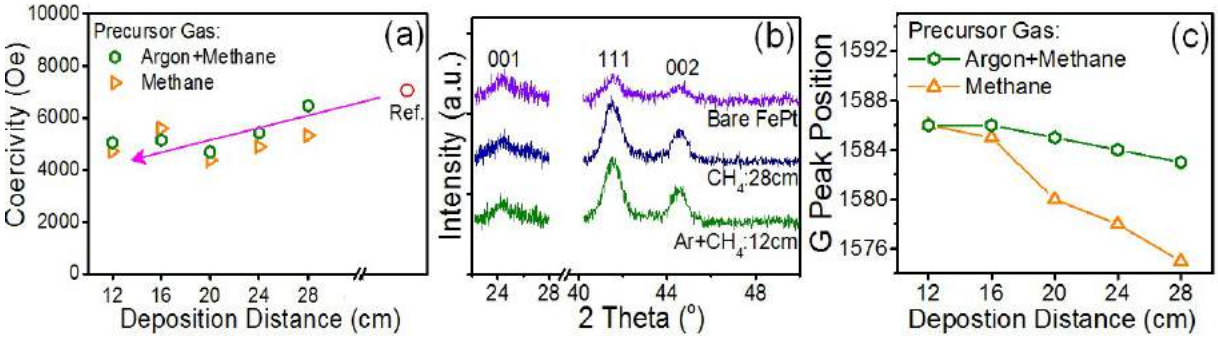

Fig. 1 (a) Coercivity of virgin and COC covered FePt samples prepared at different deposition distance. (b) XRD plot of bare and post COC deposited FePt samples. (c) G peak's position in Raman spectra of COC at different deposition Distance.

Table I XPS results for carbon type ratio in deposited COC

Carbon Type	COC at $Ar+CH_4$: 28 cm	COC at $Ar+CH_4$: 12 cm
sp^2	49.52	47.60
sp^3	39.72	42.43
sp^3/sp^2 %	44.50	47.12

CONTROLLING FePt GRAIN SIZE WITH A GRANULAR MgO-C INTERLAYER FOR HAMR

B. S. D. Ch. S. VARAPRASAD[1], B. ZHOU[1], T. MO[1], D. E. LAUGHLIN[1], and J.-G. (Jimmy) ZHU[1]

[1]Data Storage Systems Center, Carnegie Mellon University, Pittsburgh, PA, USA

INTRODUCTION

$L1_0$ FePt nano-hgranular media is uniquely positioned for heat assisted magnetic recording (HAMR) [1-3]. Currently (002) textured polycrystalline MgO is used as the underlayer for FePt to facilitate $L1_0$ ordering in perpendicular direction. Segregants like carbon or oxide or the mixtures of two have been used as to generate granular FePt microstructure [4-6]. Until now, the grain size of FePt is mainly controlled by the volume percentage of the segregant materials used during the deposition of the FePt layer. It is also known that the FePt grain grown across an MgO grain boundary of the underlayer could cause in-plane variants [6] and nucleation at the grain boundaries could result in (111) texture. In this paper, we present a systematic experimental investigation on developing a granular MgO-C interlayer deposited in between the MgO and FePt-X layers to control the FePt grainsize and distribution. We have experimentally demonstrated that FePt grain size and the corresponding microstructure in the FePt-C magnetic layer can be controlled by engineering the grain size and microstructure of the MgO-C interlayer.

EXPERIMENTAL RESULTS AND DISCUSSIONS

Experimental samples are fabricated on a naturally oxide surface of Si substrates with the following stack: MgO(10nm)/MgO-C(2)/FePt(0.2)/FePt-C(6). The MgO layer (referred to as underlayer), directly deposited at room temperature using RF sputtering with 50W sputtering power at 10mTorr Ar pressure. The MgO-C interlayer is deposited at room temperature using co-sputtering technique with RF sputtering for MgO and DC sputtering for C. The sputtering power is kept at RF100W for MgO and is varied for carbon deposition for various carbon concentrations. Interlayer deposition pressure has also been changed to optimize FePt-C layer grain size, microstructure and magnetic properties. After the deposition of MgO-C layer, the substrate temperature is raised to 600 ^{o}C. An approximately 0.2 nm thick FePt layer is then deposited on top of MgO-C interlayer using DC sputtering of 15W, followed by the deposition of FePt-C granular layer. For the FePt-C grainular layer, FePt and C are co-sputtered using DC with 20W and 300W sputtering power, respectively at 5 mTorr Ar pressure. The volume concentration of C in FePt-C layer is also varied in experiments. Modal experimental FePt-C media are also fabricated on (002) MgO single crystal substrate with the MgO-C (2nm) / FePt (0.2nm)/FePt-C (6nm) stack.

Figure 1 shows a TEM plan-view of a FePt-$C_{35vol\%}$ granular layer in which the volumetric percentage of carbon in the MgO-C interlayer is 40%. The micrograph shows that FePt grains are well separated by C grain-boundaries. The mean grain size of the FePt grains is 5.8 nm and the mean grain pitch is 7.8 nm. XRD analysis shows that the $L1_0$ order parameter of the FePt grain is S=0.79 with all correction factors considered [7]. Figure 2 shows the FePt grain sizes as a function of carbon concentration of the MgO-C interlayer while the carbon concentration of FePt-C layer is kept at 30% with the same deposition conditions (open

Bollapragada Varaprasad
sbollapr@andrew.cmu.edu

symbols). By solely varying the carbon concentrations in the MgO-C interlayer from 20% to 50%, the FePt grain size in the FePt-C layer changes from 11.5 nm to 6.5 nm. TEM study finds that the increase of carbon concentration in the MgO-C layer yields reduction of grain pitch of the MgO grains in the interlayer. The MgO grain pitch in the MgO-C layer is found to be similar to the FePt grain pitch of the FePt-C layer. The reduction of FePt grain pitch is well correlated with the reduction of FePt grain size, as shown in Fig. 3. All experimental results indicate FePt grains should have one-on-one growth on MgO grains in the MgO-C interlayer which also enables an additional means for controlling grain size and grain size distribution in the FePt-C magnetic layer. Correlations of in-plane ordered FePt grains as a function of MgO grain size of the MgO underlayer will be presented in the talk.

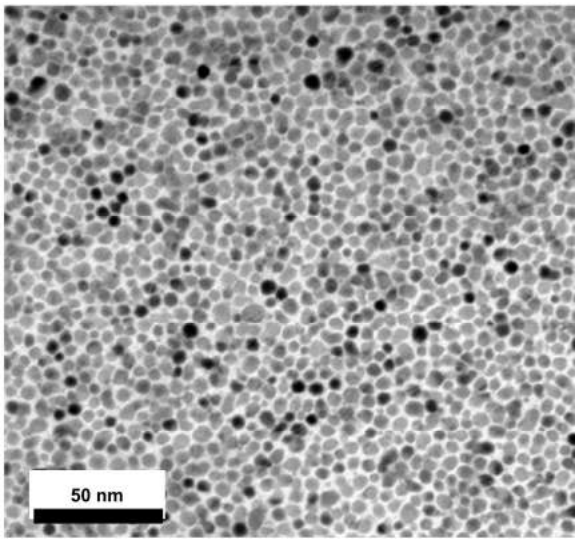

Figure 1. Plane-view transmission electron micrograph of granular FePt-$C_{35\%}$ layer of MgO(10)/MgO-C(2)/FePt(0.2)/FePt-C(6) film stack. The carbon volume percentage in the MgO-C inter layer is 40%. The average FePt grain size is 5.8 nm with average grain pitch of 7.8 nm.

1. D. Weller, A. Moser, L. Folks, M. E. Best, W. Lee, M. F. Toney, M. Schwickert, J. U. Thiele, and M. F. Doerner, IEEE Trans. Magn. 36, 10 (2000).
2. J.-U. Thiele, K. R. Coffey, M. F. Toney, J. A. Hedstrom, and A. J. Kellock, J. Appl. Phys. 91, 6595–6600 (2002).
3. A. Perumal, Y. K. Takahashi, T. O. Seki, and K. Hono, Appl. Phys. Lett. 92 132508 (2008).
4. T. Shiroyama, B. S. D. C. S. Varaprasad, Y. K. Takahashi, and K. Hono, IEEE Trans. Magn. 50(11) (2014).
5. Ram Acharya, Paper D3, The Magnetic Recording Conference, UC Berkeley, 2014.
6. H. Ho, J. Zhu, A. Kulovits, D. E. Laughlin, and J.-G. Zhu, J. Appl. Phys. 106, 193510 (2014).
7. E. Yang, D.E. Laughlin, and J.-G. Zhu, IEEE Trans. Mgn., vol. 48, No. 1, 7 (2012).

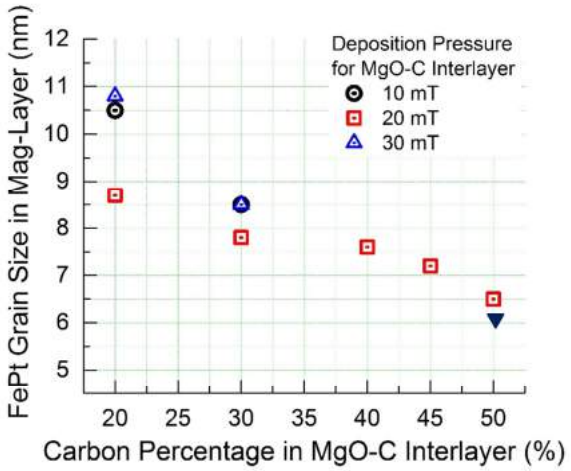

Figure 2. FePt grain size as a function of C-concentration in MgO-C layer. C-concentration in FePt-C layer is kept at 30% (open symbols) and 35% (the solid down-triangle symbol) cases, respectively.

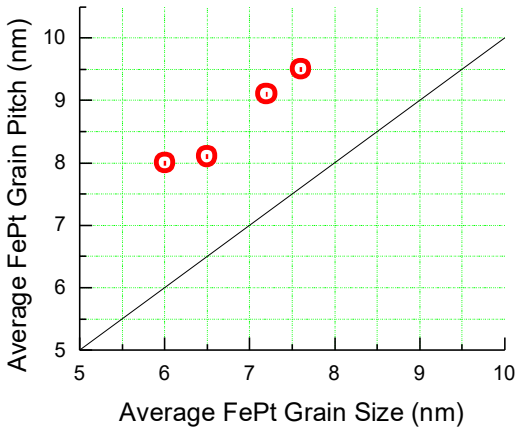

Figure 3. FePt grain pitch as a function of FePt grain size in the FePt-C granular magnetic layer.

COMPOSITE MEDIA FOR HIGH DENSITY HEAT ASSISTED MAGNETIC RECORDING

Randall H. VICTORA[1], and Zengyuan LIU[2]

[1)] University of Minnesota, Minneapolis, USA victora@umn.edu

[2)] University of Minnesota, Minneapolis, USA liux2310@umn.edu

I. INTRODUCTION

Exchange coupled composite media (ECC media) has been widely adopted by the hard disk drive industry for use in perpendicular magnetic recording. Important benefits include mitigation of the magnetic recording trilemma (balance of thermal fluctuations versus grain size and write field) and reduction of the switching field distribution. The resulting SNR improvements enable higher areal density. However, this media too is ultimately limited by the trilemma, and densities beyond 1 Tbit/in^2 (conventional system) or 1.5 Tbits/in^2 (systems incorporating shingled recording and/or TDMR) seem difficult to achieve. Heat assisted magnetic recording (HAMR) is the most promising candidate for next-generation magnetic recording technology: it breaks the trilemma by heat. L10 FePt media is usually considered for HAMR recording media that requires high anisotropy and small grain size. However, the recording temperature of HAMR is elevated to temperatures near the Curie temperature of FePt. Both magnetization and anisotropy of FePt are small at these temperatures. Therefore, thermal fluctuation and Curie temperature variance become two main noise sources owing to the resultant small Zeeman energy and poor thermal stability.

A composite media design with a superparamagnetic write layer and L10 FePt storage layer is proposed to mitigate the noise. The simulation results show that this structure can greatly decrease the transition noise and be insensitive to the Curie temperature variance in the L10 FePt storage layer. The areal density can reach as high as 4.7 Tb/in^2 for a Gaussian heat spot with a full-width-at-half-maximum of 30 nm, a 12 nm reader width, and an optimized bit length of 6 nm [1]. Further investigation also finds that the interlayer exchange coupling plays an important role in tuning the average write temperature and effects from thermal fluctuation.

II. MEDIA DESIGN AND MODEL

Micromagnetic simulation based on the Landau-Lifshitz-Gilbert (LLG) equation is implemented. A renormalization approach [2] with 1.5 nm renormalized cubic cells and parallel computing under NVIDIA GPU architecture are used to improve the simulation speed. The switching probability distribution (SPD) [1] is calculated to predict the optimal magnetic properties of the composite media. The average write temperature is defined as the one at which the switching probability is 50% during the dynamic cooling process. The full-width-at-half-maximum FWHM of the SPD curves provide an estimate of total noise. Based on these two parameter, the optimal structure is: $M_{s,wl}$=550 emu/cm^3, $K_{u,wl} = 7 \times 10^6\ erg/cm^3$ and $T_{c,wl}$=900K. The thickness of two layers is 4.5 nm (write layer) and 9.0 nm (storage layer). The temperature profiles of the write layer are scaled based on the magnetic profiles of FePt. [1] $M_{s,sl} = 922\ emu/cm^3$ and $K_{u,sl} = 4.11 \times 10^7\ erg/cm^3$ at 350 K. $T_{c,sl} = 700K$. Here, "sl" stands for the storage layer and "wl" represents the write layer. The head velocity is chosen to be 20 m/s. The applied magnetic field is 8000 Oe with uniform distribution inside the heat spot.

III. TRANSITION JITTER AND USER DENSITY

Transition jitter is defined as the standard deviation of zero-crossings of play-back signal along the down-track direction. It is proportional to transition noise. The recording simulation results under 5.5 nm grain pitch and various Tc variance of storage layer are shown in Fig. 1(a). Single FePt recording media suffers from Tc variance. Larger Tc variance causes more noise in single FePt media. However, the composite media is insensitive to Tc variance and greatly reduces the transition jitter. The magnetic recording system is optimized in terms of heat spot size, bit length and reader width. The track pitch is also optimized to enhance the user density without making any changes to the reader configuration. Fig. 1(b)

Randall H. Victora
E-mail: victora@umn.edu
Tel: 01-612- 6251825

shows the user density and effective bit ratio C/BL. Here, C is Shannon capacity calculated based on bit error rate (BER) [1]. BL is bit length. The BER is found statistically by repeatedly recording a pseudo random bit sequence on the composite media. The highest user density that can be achieved is 4.7 Tb/in^2.

IV. INTERLAYER EFFECTS

The strength of exchange coupling between both layers is tuned by $ILC = J_{ex}/J_o$. Here, $J_o \propto \sqrt{A_{ex,wl}A_{ex,sl}}$. Careful investigation shows that stronger interlayer exchange coupling increases the average write temperature and decreases the FWHM of the corresponding SPD defined in section II. FWHM only include the effects from thermal fluctuation with no Tc variance assumed in either layer. An analytic theory based on energy barrier calculation is proposed. These interesting trends are due to the linearity of energy barrier versus temperature at the high temperature region close to the Curie temperature [3].

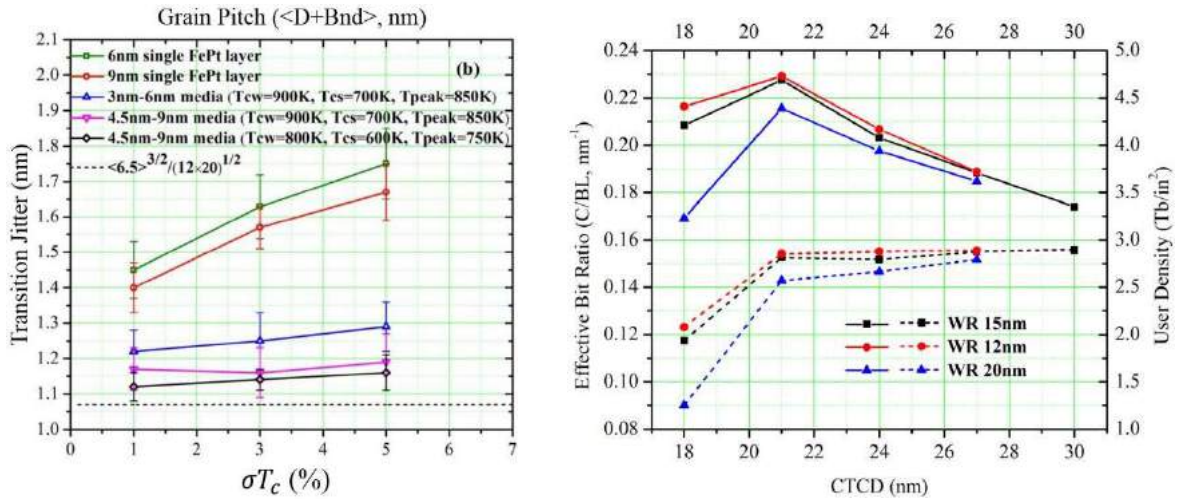

Fig. 1 (a) shows the transition jitter versus $\sigma T_{c,sl}$. (b) shows the C/BL (dashed) and user density (solid) versus track pitch.

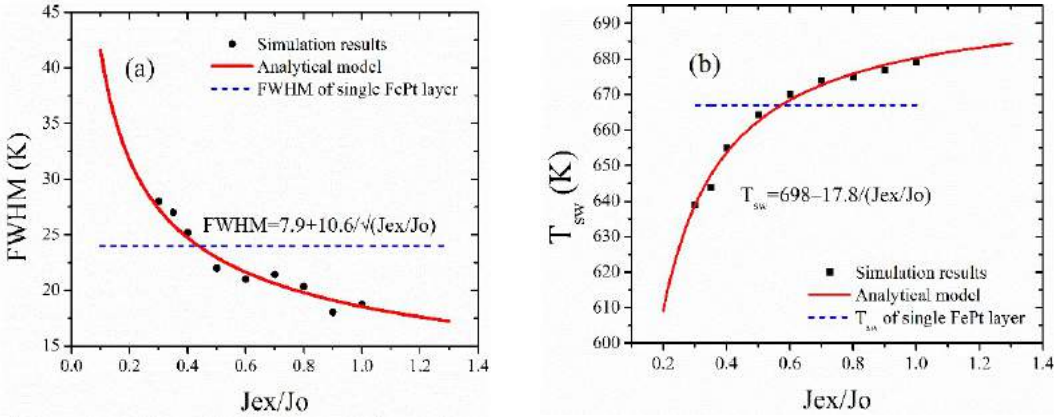

Fig. 2 (a) shows the FWHM versus ILC=Jex/Jo. (b) shows the average write temperature versue ILC.

REFERENCES

1) Zengyuan Liu, Yipeng Jiao and R. H. Victora, Appl. Phys. Lett. 108, 232402 (2016).

2) R. H. Victora and Pin-Wei Huang, IEEE Trans. Magn. vol. 49, no. 2 (2013).

3) Zengyuan Liu and R. H. Victora, AIP Advances 7, 056516 (2017).

B1

2D VISUALIZATION IN MAGNETIC RECORDING

Alexander TARATORIN[1], Maxim NIKIFOROV[2], Alexander SHTEYN[3], Rick SHI[4] and Michael ALEX[5]

1) Western Digital, San Jose, USA, alexander.taratorin@wdc.com

2) Western Digital, San Jose, USA, maxim.nikiforov@wdc.com

3) Western Digital, San Jose, USA, alexander.shteyn@wdc.com

4) Western Digital, San Jose, USA, rick.shi@wdc.com

5) Western Digital, San Jose, USA, michael.alex@wdc.com

I. INTRODUCTION

The quality of magnetic recording can be fully assessed from 2D distributions of the recorded read-back signal and noise (media and sensor). These signal and noise maps can be generated using digital signal processing and correlation analysis. Fast 2D mapping modules were developed that allow visualization of pole footprints, arbitrary data patterns, single-bit writing, and encroachment of the writer field onto adjacent tracks. These tests were integrated into a production test environment. Recently, we introduced the new SPAM (Switching Probability Averaging Measurement) method, which can detect the switching of media grains with unprecedented sensitivity (better than 1 out of 1000 grains). This 2D technique provides an experimental method for quantitative assessment of magnetic fields coming from the writer of read-write heads.

II. METHODOLOGY

The digital Guzik tester used for the measurements allows acquisition of high-resolution waveforms (up to 20 GS/s) synchronized with sector gates and synchronous write operation. However, read and write gates exhibit significant timing jitter (typically 10 ns RMS). In order to align traces captured in different cross-track locations, we used band-erased AC media noise waveforms as a reference in each data sector. This allows cross-correlation to a reference media location as long as the adjacent cross-track acquisitions are within the reader sensitivity window (typically < 15 nm). In order to avoid error accumulation during cross-track alignment, we used a least-squares offset reconstruction based on multiple adjacent signals. Alignment and averaging waveforms using multiple disk revolutions allowed accurate time-domain separation of media and sensor noise waveforms.

In order to analyze signal and noise statistics, we used correlation detection of data pattern periods in multiple data sectors. Synchronous averaging allowed high-resolution 2D imaging of the read-back signal. After the 2D average signal is calculated, the residual noise power is accumulated over multiple data periods, resulting in a 2D RMS noise distribution. In order to minimize effects of media velocity variations, the analysis window was limited to several microseconds immediately following the alignment area. Using optimized parallel data processing, we calculated the 2D average signal and RMS noise distributions of 100 cross-track locations and 10K data periods in 10 seconds, which makes these tests feasible for a production environment.

Using synchronous writing, the detailed 2D maps of adjacent- and cross-track interference (ATI/XTI) can be obtained. We developed a media noise cross-correlation technique (SPAM), which compares location-dependent waveforms before and after write operations. The cross-correlation method detects individual grain/cluster reversals of the recording medium, gaining about 3 orders of sensitivity over integral noise detection. The SPAM mapping test outputs high resolution images of logarithmic grain switching probability, allowing sensitive quantitative evaluation of ATI/XTI as well as the locations of write head structure causing erasure. High sensitivity to single grain switching allows extension of the SPAM method for media evaluation, such as thermal decay, media cluster size, HAMR erasure effects etc.

Alexander Taratorin
E-mail: alexander.taratorin@wdc.com
tel: +01-408-717-2216

III. RESULTS

Examples of read-back signal and RMS noise maps are shown in Fig.1. One full period of a pattern having transition bursts of 6T to 1T density shows distributions of cross-track amplitude, asymmetry and transition curvature. These parameters are automatically extracted from the images and reported as part of the production sequence. The RMS noise map shows the recording density dependence on media saturation (DC noise), jitter (transition noise) and track edge noise flip/flop structure caused by read sensor biasing. Small polarity dependent 45 degrees tilted structures on AC noise background indicate XTI erasure (domain wall activity).

Figure 2 illustrates a typical SPAM logarithmic switching probability map. Erasure “hot spots” are generated by magnetic transitions (center track). Cross-track switching probability graph (center) and ABS view of write head image (left) demonstrate that hot spots correspond to side shield boundaries (strong erasure with about one out of 10 grains reversed) and lower probability overhang erasure (about 1 out of 100 grains reversal) features. Overhang domains are mainly excited by lower frequency transitions.

REFERENCES

1) R. G. Lyons , "Understanding Digital Signal Processing", *Prentice Hall,* (2011)
2) M.Hashimoto. M.Salo, Y.Ikeda, A. Moser, R.Wood, H.Muraoka, ‘Analysis of Written Transition Curvature in Perpendicular Magnetic Recording From Spin-Stand Testing”, *IEEE Trans. Magn.,* 43(7) 3315-3319, (2007)

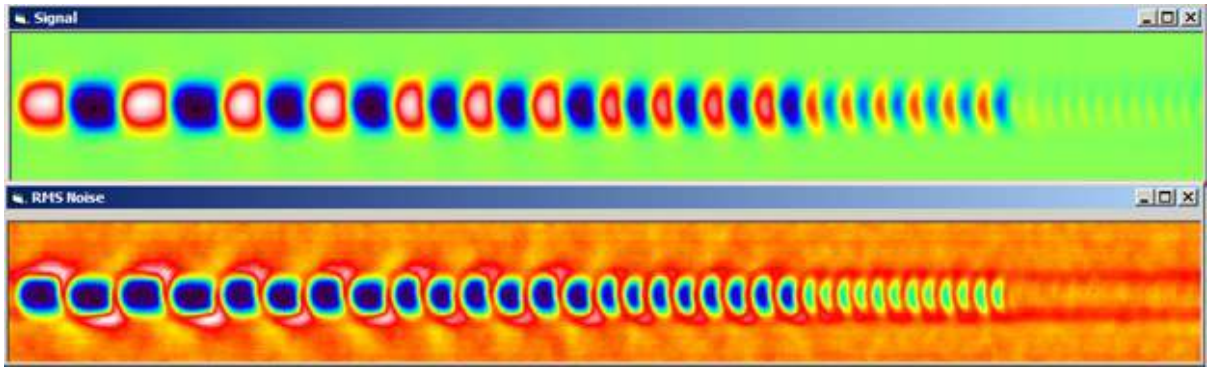

Fig. 1 Pseudo-color maps of 250*1500 nm area. Read-back signal (top) and RMS noise (bottom) of pattern consisting of 1T to 6T transition bursts recorded on AC band-erased media. Measurement time: 10 s.

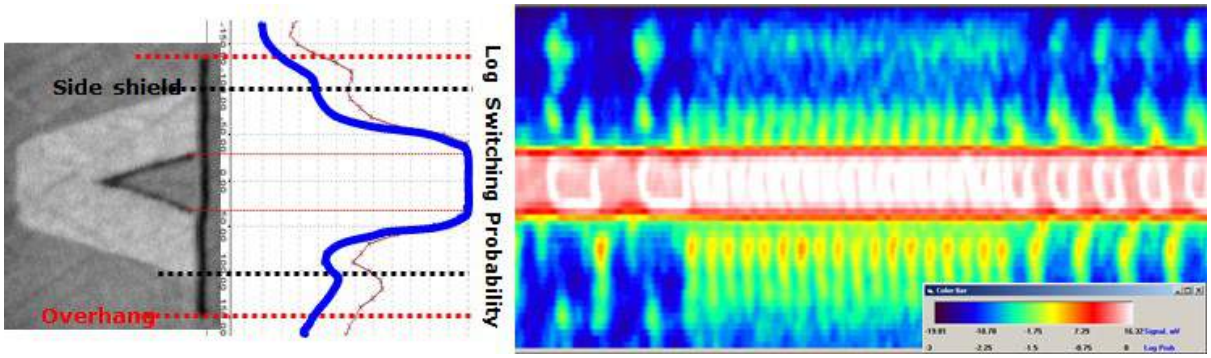

Fig. 2. 2D SPAM logarithmic switching probability map of 300*1000 nm area (right), cross-track integral graph (center) and ABS view of write head (left). Measurement time: 1 min.

ION BEAM BIT PATTERNED MEDIA USING MnGa ALLOY FILMS

D. OSHIMA[1], T. KATO[2] and S. IWATA[1]

1) Institute of Materials and Systems for Sustainability, Nagoya University, Nagoya, Japan

2) Department of Electronics, Graduate School of Engineering, Nagoya University, Nagoya, Japan

Bit patterned media (BPM) have attracted considerable interest as future high-density magnetic recording media because they provide a promising approach for solving the problem of the superparamagnetic limit, i.e., the thermal instability of recorded bits [1]. BPM are considered to extend the areal density of magnetic recording to more than 2 Tb/in^2, and further increase of the areal density to more than 5 Tb/in^2 is expected by combining with other recording techniques such as shingled magnetic recording and energy assisted magnetic recording. However, there are several issues to be solved for the practical use of BPM. One of the major issues is the development of a low-cost and high-yield fabrication process. Ion beam irradiation technique has been proposed to pattern magnetic materials without etching process. This technique provides a bit patterned media with minimal change in topography, which is referred to as planer BPM, and ion irradiation into Co/Pt [2]-[5] and Co/Pd [6], [7] multilayers has been first reported to realize planar BPM. However, in the Co/Pt and CoPd patterned by ion irradiation, the adjacent magnetic bits are not magnetically isolated due to the exchange coupling between the bits, which will limit the ultimate density of the media. In order to realize ultrahigh density planer BPM, magnetic materials exhibiting large perpendicular magnetic anisotropy and whose magnetization is suppressed by low dose ion irradiation are required. One of the candidate materials is $L1_0$ phase MnGa, and this paper reviews ion irradiation to MnGa films and fabrication of ion beam patterned MnGa films.

$L1_0$ phase MnGa (001) films were grown onto MgO (001) substrate with Cr buffer layer. The MnGa exhibited a large perpendicular anisotropy K_u of 7 x 10^6 erg/cc [8]. Figure 1 shows 30 keV Kr^+ ion dose dependences of saturation magnetization M_s and perpendicular anisotropy K_u of as-prepared MnGa film. Both the M_s and K_u monotonically decreased with ion dose and became almost zero at doses > 10^{14} ions/cm^2 [8]. The disappearance of the ferromagnetism is due to the phase change of MnGa from $L1_0$-ordered to A1 disordered phase, which was confirmed by X-ray diffraction. The MnGa films were patterned by uniform ion irradiation through micro-fabricated resist masks by electron beam lithography technique. Figure 2 shows (a) magnetic force microscope and (b) atomic force microscope images of the ion beam patterned MnGa films with a pitch size of 80 nm. The ion dose was set to be 1 × 10^{14} ions/cm^2 for the patterning. As seen in the figure, magnetic contrast was observed in “bit” areas while no contrast was seen in ion-irradiated “space” regions. In contrast to MFM image, the surface structure corresponding to ion-beam patterning was not seen in Fig. 2 (b). This suggests that the low-dose ion irradiation is a promising technique to fabricate high-density planar BPM.

X-ray magnetic circular dichroism (XMCD) and low-temperature *M-H* loop measurements of the irradiated samples were carried out in order to discuss the magnetic properties of bit boundary of planer patterned MnGa, which is crucial to control switching field distribution of BPM [9]. One of the interesting results is temperature dependence of the coercivity H_c shown in Fig. 3. The H_c of the MnGa irradiated with the doses of ~ 10^{13} ions/cm^2 significantly increased with decreasing measurement temperature while the H_c of as-prepared (non-irradiated) MnGa film slightly increased with decreasing the temperature. These results suggest that the ion irradiated MnGa film had a composite structure in which ferromagnetic $L1_0$-MnGa nano-crystals were separated by a non-magnetic A1-MnGa matrix [9]. A bit boundary of planer patterned MnGa is considered to have a composite structure with $L1_0$ and A1 phases but no intermediate structure from the discussion mentioned above, which is expected to decrease a switching field distribution of BPM.

Daiki Ohshima
oshima@nuee.nagoya-u.ac.jp

REFERENCES

1) A. Kikitsu, Y. Kamata, M. Sakurai, and K. Naito, "Recent Progress of Patterned Media," *IEEE. Tran. Magn*., vol. 43 (2007), pp. 3685-3688.
2) C. Chappert et. al., "Planar Pattened Magnetic media Obtained by Ion Irradiation," *Science*, vol. 280 (1998), pp. 1919-1922.
3) B. D. Terris et. al., "Ion-beam patterning of magnetic films using stencil masks," *Appl. Phys. Lett.,* vol. 75 (1999), pp. 403-405.
4) J. Ferré et. al, "Irradiation induced effects on magnetic properties of Pt/Co/Pt ultrathin films," *J. Magn. Magn. Mater.*, vol. 198–199 (1999), pp. 191-193.
5) R. Hyndman et. al., "Modification of Co/Pt multilayers by gallium irradiation – Part 1 : The effect on structural and magnetic properties," *J. Appl. Phys*., vol. 90 (2001), pp. 3843-3849.
6) E. Suharyadi et. al., "Microstructure and magnetic properties of the FIB irradiated Co/Pd multilayer films," *IEEE Trans. Magn*., vol. 41 (2005), pp. 3595-3597.
7) E. Suharyadi et. al., "Magnetic Properties of Patterned Co/Pd Nanostructures by E-Beam Lithography and Ga Ion Irradiation," *IEEE Trans. Magn.,* vol. 42 (2006), pp. 2972-2974.
8) D. Oshima et. al., "Control of magnetic properties of MnGa films by Kr^+ ion irradiation for application to bit patterned media," *IEEE Trans. Magn*., vol. 49 (2013), no. 7, pp. 3608–3611.
9) D. Oshima et. al., "Ion Irradiation-Induced Magnetic Transition of MnGa Alloy Films Studied by X-Ray Magnetic Circular Dichroism and Low-Temperature Hysteresis Loops," *IEEE Trans. Magn*., vol. 52 (2016), no. 7, 3201804.

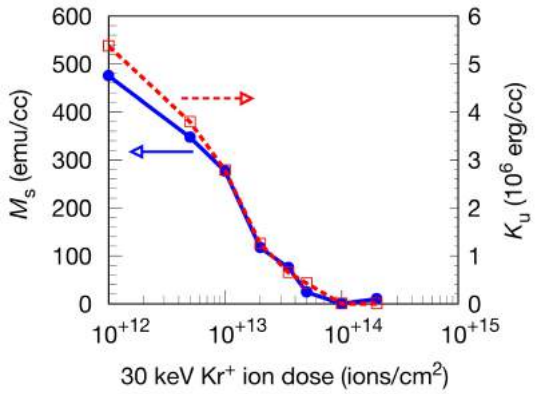

Fig. 1 30 keV Kr^+ ion dose dependence of M_s and K_u of MnGa film.

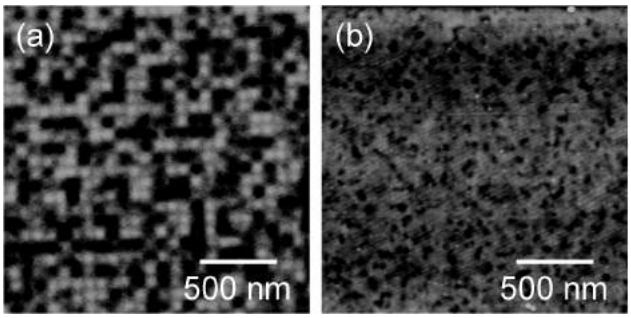

Fig. 2 (a) Magnetic force microscope and (b) atomic force microscope images of ion beam patterned MnGa film with a pitch size of 80 nm.

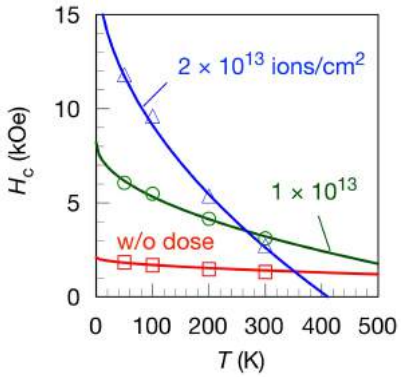

Fig. 3 Temperature dependence of the coercivity H_c of the MnGa films before and after ion doses of 1 × 10^{13} and 2 × 10^{13} ions/cm^2.

MICROSCOPIC ORIGINS OF ENHANCED OUTPUT OF HEUSLER ALLOY CPP-GMR READERS BY AMORPHOUS UNDERLAYER AND CONDUCTIVE OXIDE SPACER

T. NAKATANI[1], S. Li[1], Y. SAKURABA[1], T. T. SASAKI[1], X. D. XU[1], H. TAJIRI[2], T. FURUBAYASHI[1] and K. HONO[1]

1: National Institute for Materials Science

2: Japan Synchrotron Radiation Research Institute

I. INTRODUCTION

As the read sensor size is decreased, the sensor resistance increases and the electrical noise increases. Therefore, reducing the resistance-area product (*RA*) of sensor film is the central issue for realizing the read sensors for ultrahigh recording density HDDs. All-metallic current-perpendicular-to-plane giant magnetoresistance (CPP-GMR) using highly spin-polarized Co-based Heusler alloys have demonstrated large CPP-GMR ratio over 40% at low $RA < 0.05$ Ω μm^2 [1, 2]. This was achieved by annealing single-crystalline Heusler alloy films at high temperature above 500 °C to obtain a high degree of $L2_1$ or B2 chemical order of Heusler alloys. For the realization of CPP-GMR read sensors, however, achieving large CPP-GMR output using polycrystalline films annealed at a lower temperature (currently, ~300 °C) is important. Recently, Choi *et al*. [3] reported that CPP-GMR ratio of spin-valves using polycrystalline Heusler alloy layers could be improved by inserting thin (< 1 nm) amorphous CoFeBTa underlayer below the Heusler alloy layer. In addition, the non-magnetic spacer layer of CPP-GMR device has a great potential for improving the CPP-GMR value. Especially, a InZnO (IZO) conductive oxide-based spacer layer [5] is promising because of the slightly increased RA to ~0.1 Ω μm^2, which is optimal for read sensor application for 2 Tbit/in^2 [4], and the improved MR ratio ~25% achieved in practical spin-valve sensor structure.

In this presentation, we review our recent studies to understand the mechanisms of MR enhancements by (i) CoFeBTa amorphous underlayer inserted below Heusler alloy magnetic layer, and (ii) Ag/IZO/Zn spacer layer using synchrotron x-ray diffraction and electron microscopy.

II. EXPERIMENTAL PROCEDURES

CPP-GMR films were deposited by magnetron sputtering at room temperature. $Co_2(Mn_{0.6}Fe_{0.4})Ge$ (CMFG) Heusler alloy was used for the ferromagnetic layers. The films were annealed at 280 °C or 300 °C for 3 hours and pattered into CPP pillars. The degree of B2 ordering (site ordering between Co and (Mn,Fe)) was measured in 30 nm thick CMFG films by anomalous x-ray diffraction (XRD) near the x-ray energy of the Co-*K* absorption (~7.7 keV) in a synchrotron facility SPring-8.

III. RESULTS and DISCUSSION

Figure 1(a) shows the resistance change-area product (Δ*RA*) of Cu-lead/Ru(1)/CoFe(1)/CoFeBTa(0-1.2) /CMFG(5)/CoFe(0.4)/AgSn(4)/CoFe(0.4)/CMFG(5)/CoFe(1)/Ru cap (thickness in nm) pseudo spin-valve devices annealed at 300 °C. $(Co_{40}Fe_{40}B_{20})_{0.93}Ta_7$ amorphous underlayer was inserted below the bottom CMFG layer. Δ*RA* increased by inserting the CoFeBTa amorphous underlayer. As shown by the inset of Fig. 1(a), the CPP-GMR device with the CoFeBTa(1.2 nm) insertion showed $RA = 30$ mΩ μm^2 and MR ratio (Δ*R*/*R*) of 25%. As shown in Fig. 1(b), the degree of B2 order measured for 30 nm-CMFG films was higher for the CMFG films with thicker CoFeBTa insertion. Therefore, the increased Δ*RA* by the insertion of CoFeBTa should be originated from the enhanced B2 ordering of CMFG. It is also noteworthy that the degree of B2 order of the top CMFG deposited on the AgSn spacer layer (corresponding to the free layer of bottom-pinned spin-valve) was much lower (~46%) than those of the bottom CMFG deposited on the CoFeBTa underlayer (up to 76%). Thus, improving the degree of B2 order of the top CMFG layer is a key for further increase of CPP-GMR outputs.

Next, we studied the microstructure of CPP-GMR spin-valves with IZO-based spacer layers. Figure 2

Tomoya Nakatani
National Institute for Materials Science
E-mail: nakatani.tomoya@nims.go.jp
1-2-1, Sengen, Tsukuba, Ibaraki 305-0047, Japan
Phone: +81-29-859-2694

shows *RA vs*. Δ*R*/*R* of bottom-pinned spin-valves with Cu/Ta-lead/Ta(2)/Ru(2)/IrMn(6)/CoFe(2.6)/Ru(0.8)/CoFe(0.6)/CoFeBTa(0.8)/CMFG(2.5)/CoFe(0.4)/spacer/CoFe(0.4)/CMFG(4)/CoFe(1)/Ru cap structure annealed at 280 °C. By using Ag(Sn)/IZO/Zn spacer layers, both Δ*R*/*R* and *RA* increased compared to the spin-valve with the metallic AgSn(4) spacer layer. Figures 3 (a)-(b) shows the elemental mappings of In, Zn and Ag, respectively in the spin-valve film with Ag(0.4)/IZO(1.6)/Zn(0.8) spacer layer by energy dispersive x-ray spectrometry in scanning transmission microscopy, Ag shows an inhomogeneous concentration distribution in the position of the IZO layer. Thus, the distribution of the CPP electric current is expected to be inhomogeneous similar to that in current-confined-path spacer layer. Furthermore, as shown by the depth concentration profiles in Fig. 3(e), Mn is diffused into the spacer layer. The Mn impurity in spacer layer may cause a spin-flip scattering, thus it should reduce the CPP-GMR output. Therefore, suppressing the Mn diffusion to IZO-based spacer should improve the CPP-GMR sensor output.

References

[1] Sakuraba *et al*. Appl. Phys. Lett. 101, 252408 (2012). [2] Li *et al*. Appl. Phys. Lett. 103, 042405 (2013). [3] Choi *et al*. Appl. Phys. Express 10, 013006 (2017). [4] Nakatani *et al*. Appl. Phys. Express 8, 093003 (2015). [5] Takagishi *et al*. IEEE Trans. Magn. 46, 2086 (2010).

Figures

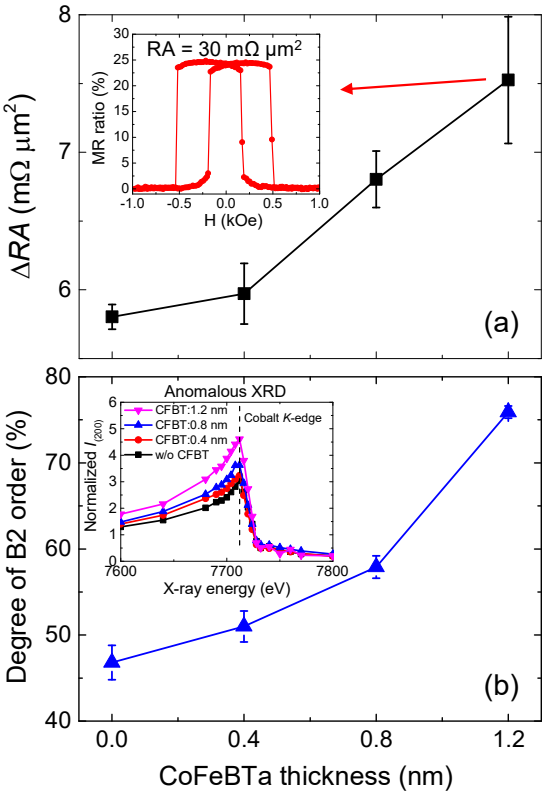

Fig. 1 (a) Δ*RA* and (b) degree of B2 order of CMFG film for various thickness of CoFeBTa underlayer.

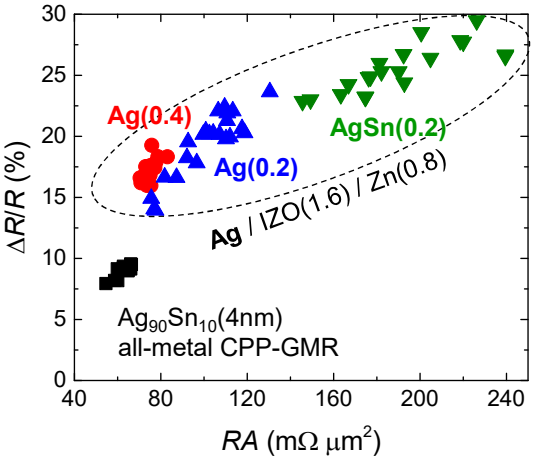

Fig. 2 *RA*-Δ*R*/*R* of spin-valves with Ag(Sn)/IZO/Zn and AgSn spacer layers.

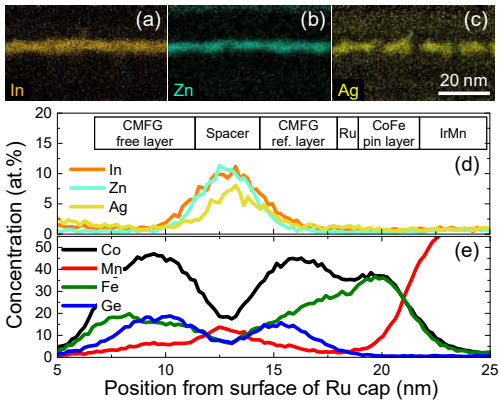

Fig. 3 Elemental concentration maps and profiles in spin-valves with Ag(0.4)/IZO(1.6)/Zn(0.8) spacer layer.

2-D EQUALIZATION WITH LOCATION DIVERSITY AND PRE-ADAPTATION TO HANDLE OFFTRACK IN ARRAY READER BASED HARD DISK DRIVES

George MATHEW[1], Scott DZIAK[2], Kurt WORRELL[2], Jeff E. SINGLETON[2], Bruce W. WILSON[1] and Haitao XIA[1]

[1] Broadcom Limited, San Jose, CA, USA, [2] Broadcom Limited, Longmont, CO, USA.

I. INTRODUCTION

The hard disk drive industry is transitioning into array-reader based magnetic recording (ARMR) to provide continued growth in recording density. A 2-D equalizer acts to electronically steer the array-reader to provide optimum signal pick-up from the track, thereby resulting in wider & deeper cross-track profile in error-rate performance. To realize this performance, the equalizer coefficients must be matched to the location of array-reader, which are not known precisely due to position errors during write and read. Two particularly challenging scenarios are reading shortly after seeking to a track and reading consecutive sectors which were not written sequentially. In both cases the offset between the array-reader and track cannot be inferred from previous sectors.

In this paper, we present a 2-D equalization strategy that uses location diversity and pre-adaptation to mitigate the mismatch between reader-location and equalizer coefficients. The data-decisions driving the various loops (timing/gain/dc, equalizer-adaptation) are generated using three 2-D equalizers (i.e. loop equalizer) that cover the range of expected offtrack. A delayed equalization strategy is used to mitigate the effect of offtrack in the 2-D equalizer (i.e. back-end equalizer) that is feeding the iterative detector. The proposed approach shows significantly improved read performance in the presence of large offtracks incurred by dual-reader.

II. 2-D EQUALIZER WITH LOCATION DIVERISTY AND PRE-ADAPTATION

Fig. 1 shows the schematic of the proposed 2-D equalization strategy [1].

The proposed structure uses three 2-D equalizers (LDF1, LDF2 & LDF3) and associated detectors for generating the detected data-bits (also called, loop decisions) necessary to drive the various loops. The equalizers LDF1, LDF2 & LDF3 are set based on positive offtrack location, track-center, and negative offtrack location, respectively, so as to get sufficient offtrack coverage. Final loop decisions are taken from the detector whose input signal best matches the chosen partial response (PR) equalization target. Coefficients of the equalizer whose output best matches the PR target are adapted. Because of loop latency considerations, different decision points and metrics may be used in determining the best detector for loop decisions and best loop equalizer for adaptation.

The back-end equalizer adopts a delayed equalization strategy. The first equalizer BDF-0 fast adapts over a block of the current sector to determine near-optimum coefficients for that sector, and the resulting coefficients are used to initialize the main equalizer BDF-1 that is feeding the back-end detector. Equalizer BDF-1 works on accordingly delayed version of the data samples. This strategy provides sufficient time to determine appropriate starting coefficients of BDF-1 so as to match the unknown location of the reader in each sector.

Performance evaluation of the proposed approach is done using a 2-D model of high-density magnetic recording (perpendicular, non-shingled) with 2050 KBPI, 460 KTPI, 55.22 nm magnetic write width, and dual-reader with 30 nm read width in each reader. The two read-sensors differ by 3dB in electronics noise. Fig.2 shows the bit error-rate (BER) performance of the individual fixed loop equalizers as well as performance of the overall diversity equalizer with adaptation, for reader-to-reader cross-track separation (CTS) of 20% and 40%. The individual equalizers LDF1, LDF2 and LDF3 are chosen based on offtrack locations {+25%, -5%, -30%} for 20% CTS and {+30%, -5%, -35%} for 40% CTS. Observe that the performance of diversity equalizer (black trace) is close to the optimum performance (solid red trace) over a large range of offtrack around track-center. Fig. 3 shows the corresponding detection performance from back-end detector (i.e. based on output BDF-1), with and without pre-adaptation, where the pre-adaptation block-length is chosen as 10000 bits. Observe that the use of pre-adaptation to initialize the coefficients of

GEORGE MATHEW
BROADCOM Limited
Tel: 408-433-7416
320 Ridder Park Dr, San Jose, CA 95131

BDF-1 (i.e. magenta trace) results in significantly improving the performance without pre-adaptation (i.e. cyan trace) over a large range of offtrack around track-center.

The data in Figs. 2 and 3, which are for the 1st sector in seek-arrival scenario, imply that by appropriately choosing the offtrack locations for the three loop equalizers and the pre-adaptation block-length for the back-end equalizer, the read channel in ARMR HDDs will be able to respond quickly to changes in reader-location without having to explicitly estimate the reader-location.

REFERENCES

[1] Patent application filed with USPTO, Apr 2017.

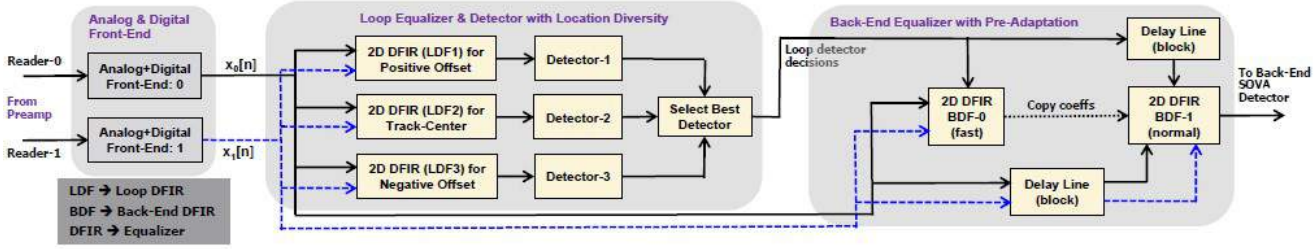

Fig. 1 ARMR 2-D equalization with location diversity in loop equalizer and pre-adaptation in back-end equalizer.

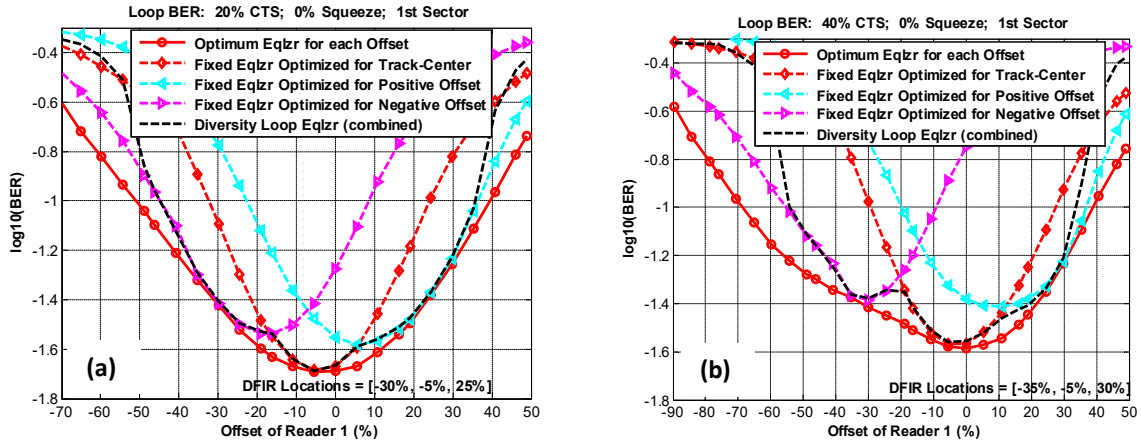

Fig. 2 BER performance of loop 2-D equalizer with location diversity: (a) 20% CTS, (b) 40% CTS.

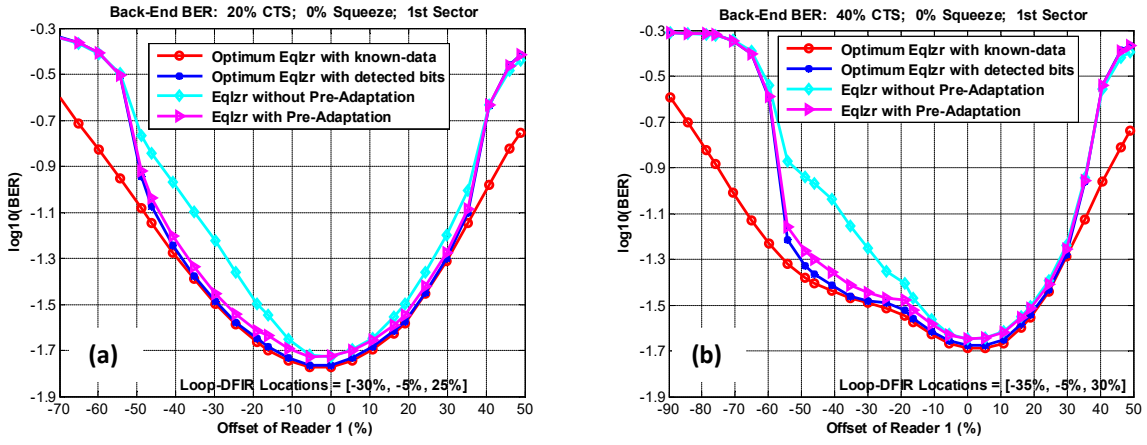

Fig. 3 BER performance of back-end 2-D equalizer pre-adaptation: (a) 20% CTS, (b) 40% CTS.

USER AREAL DENSITY OPTIMIZATION FOR CONVENTIONAL AND 2D DETECTORS/DECODERS

[1]Kheong Sann CHAN, [2]Ashish JAMES, [2]Sari SHAFIDAH, [1,4]Susanto RAHARDJA
[3]Jinlu SHEN, [3]Krishnamoorthy SIVAKUMAR, [3]Benjamin J. BELZER
[1]Nanjing Institute of Technology, Nanjing, China, kheongsann@ieee.org.
[2]Data Storage Institute, (ASTAR), Singapore, jamesa@dsi.a-star.edu.sg.
[3]Washington State University, Pullman, WA, USA, (jshen,siva,belzer)@eecs.wsu.edu
[4]Northwestern Polytechnic University, Xi'an, China, susantorahardja@ieee.org.

I. INTRODUCTION

Advances in the magnetic recording channel have the potential to detect and decode the stored data at lower SNRs, higher channel areal densities (CAD), lower code rates (R) and lower bit aspect ratios (BAR) than conventionally used in today's systems. The magnetic recording channel today optimizes at parameters in the vicinity of $R = 0.85$, BAR $= 3$, BL $= 12.5$nm, TP $= 38$nm, but it has been suggested in [1] that as the industry moves to shingled recording and starts using heads with multiple readers, the density could optimize at lower BAR's and code rates, and at a higher CADs. In the current work, we use the grain-flipping probability (GFP) model developed in [2], [3] together with conventional and advanced recording channels to determine the optimized user areal density (UAD) that can be delivered to the customer using conventional and advanced 2D detectors and decoders.

II. GFP DATA GENERATION MODEL

In this work, the GFP model is used to generate mass waveforms at various CADs, UADs, code rates (R) and BARs. In this study, we attempt to maximize the UAD over R and BAR. The metric that is observed is the frame error rate (FER) of the coded channel as a function of the UAD. The GFP model is trained from micromagnetic simulations. In this work, we started with a micromagnetic parameter set similar to that in [1] in which the target density is 4Tbpsi, but it was agreed that we would scale them down by $\sqrt{2}$ to a target density of 2Tbpsi, which is more appropriate given the state of today's head and media technology. The head and media parameters used in the micromagnetic simulations are shown below in Fig. 1.

Parameter		Value	Parameter		Value
Grain density	(Tgpsi)	11.4	σ_{gs}		20%
Grain boundary	(nm)	1.4			
K_u	(J/m^3)	450e3	σ_{Ku}		5%
M_s	(A/m)	750e3	σ_{Ms}		0%
H_k	(kOe)	12	σ_{Hk}		5%
exchange	(erg/cm^2)	2.5			
A_x	(J/m)	5.6e-12	σ_{Ax}		3%
e_z		0°	σ_{ez}		3°
media thickness	(nm)	14.1	HMS	(nm)	5.6

Parameter	Symbol	Value	Parameter	Symbol	Value
Main Pole trailing width	MPTW	70nm	Side shield gap	SSG	14nm
Main Pole height	MPH	130nm	Trailing shield gap	TSG	14nm
Main Pole angle	MPA	75°	Head Media spacing	HMS	5.6nm
Interlayer thickness	ILt	1.4nm	Media thickness	Mt	14nm

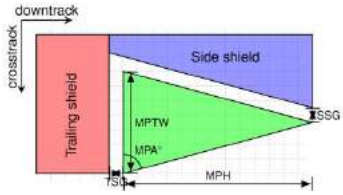

Fig. 1. Media parameters for the micromagnetic simulations are shown on the left, while the head parameters are on the right.

The micromagnetic simulations are used to characterize a GFP look-up table (LUT) which is then used to generate signals for simulations using conventional 1D LDPC coded channels and the FER is measured. The UADs, code rates and BAR's are the independent variables in our simulations. The UAD was varied from 1.35 to 2.2 Tbpsi in steps of 0.05, the code rate R was varied from 0.5 to 0.95 in steps of 0.05 while the BAR was varied from 1.0 to 3.1 in steps of 0.3. Results with the conventional 1D channel at representative BAR's are shown in Fig. 2 below.

Corresponding Author
E-mail:kheongsann@ieee.org
tel: +65-67149088
Work funded in part by ASTC.

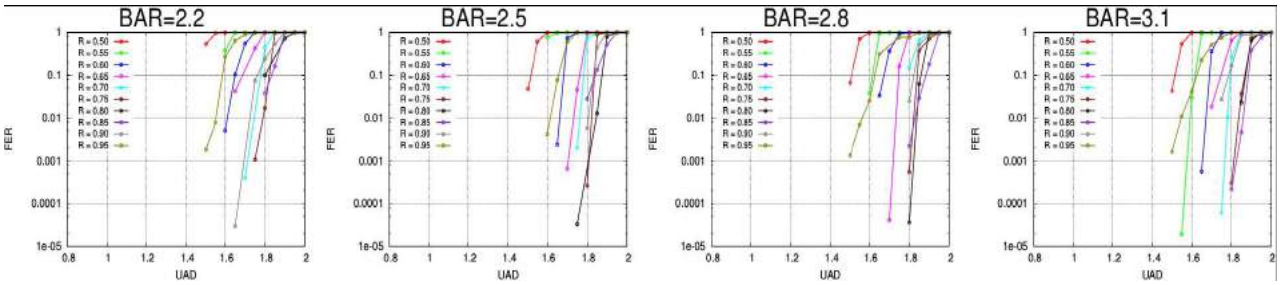

Fig. 2. FER vs UAD at different BARs and code rates.

The results from Fig. 2 show that for a conventional channel, the performance improves up to BAR=3.1 and an optimum code rate of 0.8 to 0.85 is observed at this BAR, with an achieved UAD of around 1.8 Tbpsi. It is noted here that the head/media are spec'd at 2Tbpsi. These results match closely with the HDD system parameters today.

III. 2D SIGNAL PROCESSING AND CODING SYSTEM

The system shown in Fig. *3* employs a three-input one-output 2D MMSE linear equalizer of size 3×15, for estimation of the coded data bits on the central track. This setup assumes a read head capable of simultaneously reading three tracks. The MMSE equalizer reshapes the channel to an 8+16D 1D PR target on the central track; processing three rows at a time enables equalization of the ITI from the outer two tracks. The equalizer output flows into a two-state 1D BCJR detector that uses the PR target to compute branch labels. The BCJR exchanges LLRs with an irregular repeat-accumulate (IRA) LDPC decoder to minimize the user BER. The main innovation is the use of three tracks to estimate the central track, within a relatively low-complexity system architecture.

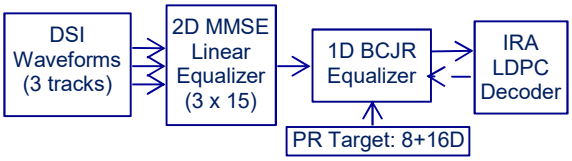

Fig. 3. 3-input / 1output MMSE/BCJR turbo detector

IV. SIMULATION RESULTS

Fig. 4 presents BER vs. user bits per grain for the system shown in Fig. 3. For a fixed BL of 11 nm, the best result of 2.289 Tbpsi is achieved at 21 nm track pitch (1.91 BAR). This is somewhat higher than the best results for the baseline one-track system in Fig. 2, which achieves 1.80 Tbpsi; the improvement is due to processing three tracks at once.

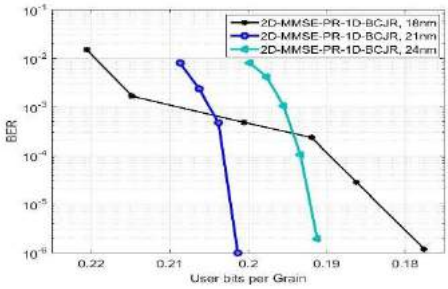

Fig. 4. Simulation results for the system in Fig. 3

REFERENCES

1) J. Barry, B. Vasic, M. Khatami, M. Bahrami, Y. Nakamura, Y. Okamoto, Y. Kanai, "Optimization of bit geometry and multireader geometry for TDMR", *IEEE Trans Magn.* Vol 52, No 2, Feb 2016.
2) K. S. Chan et al., "Channel Models and Detectors for Two-dimensional Magnetic Recording," *IEEE Trans. on Magn.*, vol. 46, no. 3, pp. 804–811, Mar. 2010.
3) K. S. Chan et al., "Comparison of Signals from Micromagnetic Simulations, GFP Model, and an HDD Readback," *IEEE Trans. on Magn.*, vol. 51, no. 11, pp. 1-4, Nov. 2015.
4) M. Mehrnoush, B. Belzer, K. Sivakumar, and R. Wood, "Signal Processing for Two Dimensional Magnetic Recording Using Voronoi Model Averaged Statistics," in *Proc. Conf. on Inform. Sci. and Syst.*, March 2015, pp. 1–6.
5) R. M. Todd, E. Jiang, R. Galbraith, J. R. Cruz, and R. W. Wood, "Two-dimensional Voronoi-based Model and Detection for Shingled Magnetic Recording," *IEEE Trans. on Magn.*, vol. 48, no. 11, pp. 4594–4597, Nov. 2012.

TEMPERATURE OF DATA IN STORAGE DEVICES AND DATA STORAGE SOLUTIONS FOR THE NEXT DECADE

Kai-Zhong GAO[1, 2], *Sr. Member IEEE*
[1]International Business and Technology Services, Kaizhong.Gao@intlbt.com
[2]Argonne National Laboratory, kgao@anl.gov

Magnetic data storage technology, such as HDD has tremendous growth over the past 60 years, and only until recently, the areal density capability (ADC) has slowing down [1-3]. It was until last couple of years, 3D NAND based SSD starts to take over some of the HDD markets [4]. In our recent study, a standard data "temperature" definition is determined and we show that this temperature of data is an intrinsic property of digital data for storage, which links both data storage capacity and access speed of a device together [5]. We show that this data temperature definition is consisted with "hot" and "cold" data concept utilized in the field of data storage system field.

Using this standard data temperature definition, we are able to analyze all digital data properties in a given device, such as in HDD. Fig. 2 shows an analysis of a given HDD used under different conditions, the results show that the maximum average data temperature capability for a given drive, regardless how to use it, depend only on the total number of files on that particular device. As shown in Fig. 3, the HDD drive capacity is increased by several orders of magnitudes over the past few decades. The average data temperature capability in the HDD is actually reduced, as illustrated in Fig. 4. The peak temperature of the drive does not change much, but the average data temperature is monotonically reduced as the drive capacity is increased. Further analysis shows that this trend is independent to the choice of applications, and only depend on the technology choice. In other words, for all HDD based technology, it follows a universal line for a given application. Further study also reveals how 3D NAND based SSD technology replaced HDD enterprise market over the past few years.

Based on this analysis, we further show that the digital universe evolution, to certain aspect, can be mapped to the physical world. As the size of digital universe increases, the amount of low temperature data also increase rapidly. This leads to a new opportunity for "cold" data storage, or data archive storage technology. Currently magnetic tape recording and Blu-ray based data archive systems are widely utilized for data achieve applications, as part of cloud based data centers, such as the one used in Amazon, Facebook etc. A comparison of these technologies shows its potential and limitations for the coming years, as the digital universe continue to grow. Using the same analysis, we will also show how STT-MRAM, as an emerging technology will join the field, and in what market it is likely to replace existing technology.

For data archive technology, one of the limitations is the time to first data, i.e. its peak data temperature capability. The storage archive system based on Blu-ray or magnetic tape recording has its intrinsic limitations which prevent many applications. Another limitation is associated with the method on how to achieve data and how to remove obsolete data. The technologies that enable magnetic tape recording and Blu-ray for data achieve system have certain limitations which raise additional concerns beyond technologic and economic perspectives. Based on the analysis, we show that being able to remove unwanted data, is the desired feature, even for data achieve systems. For a grand scale, this also has profound impact for the data center operations. Proper technology associated with new generations of data achieve system is desired, which enable opportunities in the coming decades.

With large capacity HDDs in the market with reduced cost, HDD based data archive system also plays a role in data archive system, despite its higher cost than Blu-ray and tape systems. Beyond the energy assisted technologies, recent enablers for drive capacity growth is mainly based on system architecture change, such as: Helium Drive with more platters, SMR, Dual Readers, IMR and BMR etc. One of the advantages of HDD based data archive system is its peak data temperature capability. We show that for a carefully designed hardware system, it is possible to further extend its capacity for a storage system, sometime even based on a given, fixed drive configurations. In addition, an optimized solution enables a lower power consumption for HDD storage system, which can be significantly more efficient than any of the existing systems, such as the one used in Facebook and google cloud data centers.

Kaizhong Gao
kgao@anl.gov

Based on the same theory, we study future HDD technology potential. We show that although more data will be saved on HDDs, the overall HDD potential is limited. On the other hand, the HDD based data archive system, if fully optimized, has its potential in the following decades. As the HDD industry fully explore assisted technology and trying to integrate them into product. An interesting situation may occur where the decades long development of Heat Assisted Magnetic Recording may eventually be suitable for "Cold" (data archive) storage system.

REFERENCES

1) Information Storage Industry Consortium (INSIC) Tape and HDD Technology Roadmap 2012-22 (Link), 2015-25 (Link).
2) ASTC Technology Roadmap (Link)
3) K. Z. Gao, Write Architectures and Their Impact on Hard Disk Drive Capacity, Intermag, 2017 DE03.
4) L. Mearian, Flash memory's density surpasses hard drives for first time, Feb. 2016, Computer World (Link)
5) K. Z. Gao, Temperature of Data, News and Views, International Business and Technology Service 2016 (Link)

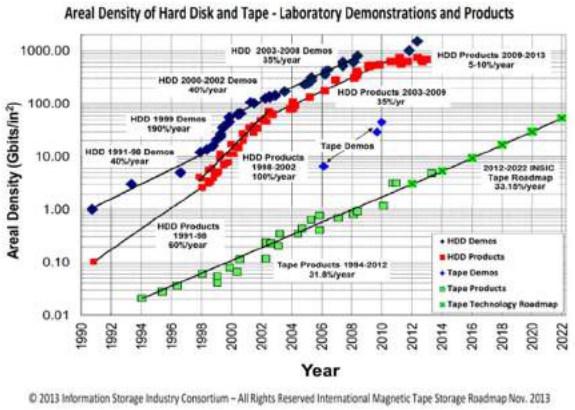

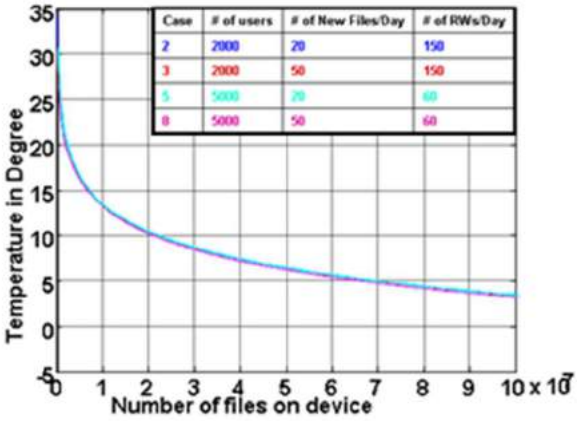

Figure 1 (left). Technology and product roadmap of HDD and Tape based on INSIC released study.

Figure 2 (right). Data temperature vs. number of files on a given device, for drive have different number of read and write attempt per day.

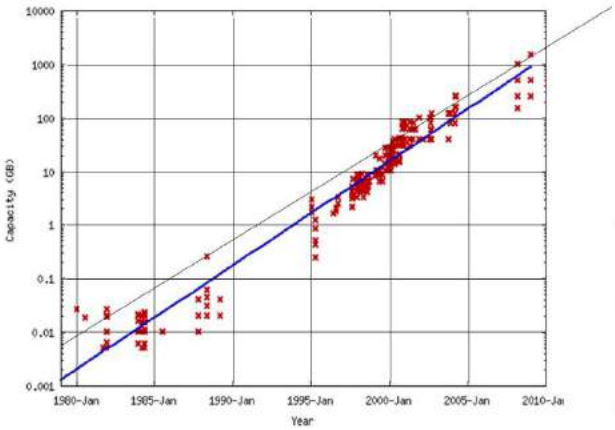

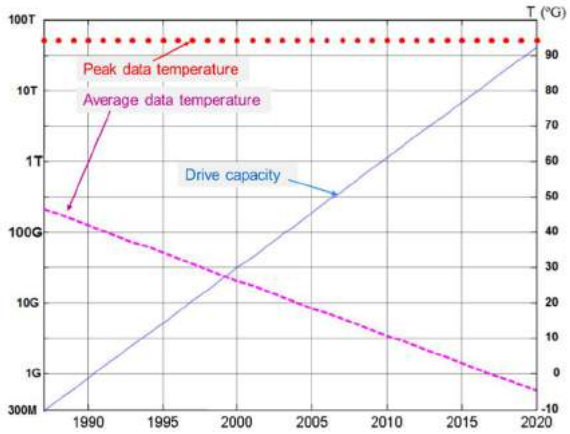

Figure 3 (left). HDD product capacity vs. time as listed on Wikipedia, with average 43% annual capacity growth rate over the past 3 decades.

Figure 4 (right). Peak data temperature, average data temperature capability and drive capacity vs. time. Data temperature capability for a given product is reduced with capacity increase.

B7

ROLE OF MICROSTRUCTURE ON ALL-OPTICAL SWITCHING AND THZ EMMISSION

E. E. FULLERTON[1]

1) Center for Memory and Recording Research, University of California San Diego, La Jolla, CA, 92093-0401, USA, eefullerton@ucsd.edu

I. INTRODUCTION

The possibilities of manipulating magnetization without applied magnetic fields have attracted growing attention over the last fifteen years. The low-power manipulation of magnetization, preferably at ultra-short time scales, has become a fundamental challenge with implications for future magnetic information memory and storage technologies. I will discuss recent experiments on the optical manipulation of magnetic materials and devices using 30-4000 fs optical pulses. We will discuss two related phenomena: (1) all-optical switching and control of magnetization without an external magnetic field (see Fig. 1) [1, 2] and (2) the emission of THz radiation (see Fig. 2) open laser excitation. All-optical switching has been observed for a broad range of materials, including ferrimagnetic alloys, multilayers, heterostructures as well as ferromagnetic films and granular recording media [1-5]. This discovery can enable breakthroughs for numerous applications since it exploits materials that are currently used in magnetic data storage and memory technologies. The observation of THz emission is believed to result from the generation of charge and spin currents generated from ultrafast demagnetization of magnetic materials [6, 7]. Generating and controlling of the spin currents in magnetic nanostructures using ultrashort laser pulses has may be the enabling technology for the spin based electronic devices operating at THz frequencies. In both cases integrating laser excitations with magnetic nanostructures in devices provides additional degrees of freedom in using intrinsic magnetic properties and their ultrafast response to laser pulses.

II. RESULTS

While both all-optical switching and THz emission have been experimentally observed in an increasing number of materials the mechanism or mechanisms involved are still under debate. To provide insight into these phenomena we have combined detailed temporally and spatially resolved measurements of a range of magnetic thin films and heterostructures which have a varying degree of structural disorder. These studies include FePt-based granular media [1, 2, 4, 5], Co/Pt-based thin-film heterostructures [1, 3] and FeRh/Pt bi-layers. Each system shows distinct behavior and dependence on structural disorder that challenge our current theoretical understanding.

For FePt-based magnetic recording media we find that the optical magnetic switching by circularly polarized light is an accumulative effect from multiple optical pulses [2] and can be described by a statistical model considering a small probability of switching magnetic grains for each light pulse, and these probabilities depend on the helicity of the light [2, 3]. It results in a high degree of alignment of FePt grains of approximately 75% achieved only with multiple circularly polarized optical pulses. This magnetic switching is found to be inhomogeneous throughout the material with some individual FePt grains neither switching nor demagnetizing. The origin of this behavior is identified as the near-field modification of the incident laser radiation around FePt nanoparticles [5] and the fraction of not-switching nanoparticles is influenced by the heat flow between FePt and a heat-sink layer. However, deterministic magnetization switching is achievable by the combination of circularly polarized light and modest external magnetic fields demonstrating that the circularly polarized light can aid the writing in a HAMR-like recording process.

For Co/Pt films time-resolved magneto-optical imaging reveals the dynamics of the helicity-dependent all-optical switching occurs on timescales from femtoseconds to seconds. Single femtosecond pulse demagnetizes the sample by 75% and aids the nucleation of a reverse domain. At the second stage circularly

E. E. FULLERTON
E-mail: efullerton@ucsd.eud
tel: +1-858-534-9639

polarized light breaks the degeneracy between the magnetic domains and promotes a preferred direction of domain wall motion. The growth of the reversed magnetic domain from the nucleation site, via deterministic displacement of the domain wall, leads to a full magnetization reversal [3].

Finally we have observed both helicity-dependent [6] and helicity-independent [7] THz emission in both Co/Pt and FeRh structures. By decoupling the horizontal and vertical components of the emitted THz-signals, we reveal the pump laser helicity-dependence in the emitted photocurrents in the ferromagnetic phase. We find the helicity dependent THz emission for Co/Pt structures increases dramatically with Co-Pt interfacial roughness and is strongly suppressed for epitaxial structure. Taking advantage of antiferromagnetic-to-ferromagnetic phase transition temperature in FeRh we distinguish a drastic change in the amplitudes of laser-induced emitted THz-signals upon heating the sample above transition temperature. Also, we can use 30 fs-laser pulses to force the material into its transition region, while the ultrafast magnetization dynamics are probed via THz-emission spectroscopy under the application of moderate external magnetic fields. Our results clearly reveal that the emitted electric fields show strong external magnetic field dependence (see Fig. 2) and the shape of the field dependence curve hints that the phase transition, in FeRh, occurs via super-paramagnetic-like behavior of the nucleated ferromagnetic phase.

III. ACKNOWLEDGEMENTS

This work is supported, in part, by the ONR MURI program and is in collaboration with R. Medapalli, C.-H. Lambert, Y. Quessab, M. Gottwald, R. Tolley, S. Patel, V. Uhlir, M. Menarini, L. Sham, V. Lomakin and Y. Fainman at UCSD, G. Malinowski and S. Mangin at Université de Lorraine, R. Mikhaylovskiy, G. Li, A. Kirilyuk, Th. Rasing, and A. V. Kimel, Radboud University, Nijmegen, The Netherlands and B. Varaprasad, Y.K. Takahashi, and K. Hono, National Institute for Materials Science, Tsukuba, Japan.

REFERENCES

1) Lambert *et al*., *Science* **345,** 1337-1340 (2014).
2) Takahashi *et al*. *Phys. Rev. Appl.* **6** (5) 054004 (2016).
3) Medapalli *et al*. arXiv: arXiv:1607.02505.
4) M.O.A. Ellis, E. E. Fullerton, R. W Chantrell, *Scientific Reports* **6**, 30522 (2016).
5) P. W. Granitzka et al., *Nano Letters*, **17** (04), 2426-2432 (2017).
6) J. Huisman *et al*., *Nature Nanotechnology* **11**, 455–458 (2016)
7) T. Kampfrath et al., *Nature Nanotechnology* **8**, 256–260 (2013)

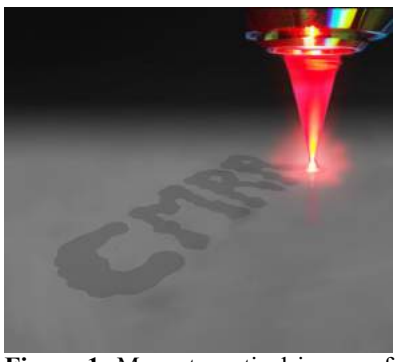

Figure 1: Magneto-optical image of CMRR written in a magnetic film using a circularly polarized 100-fs laser pulses where the orientation of the magnetic domains were controlled by sweeping circular polarized light over the film.

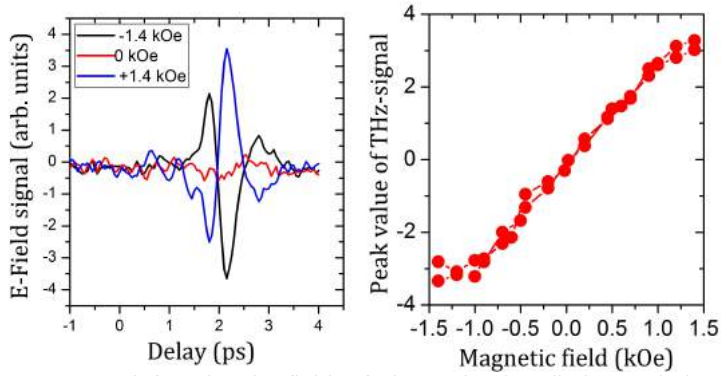

Figure 2: (left) Electric field of the emitted radiation polarized perpendicular to the applied magnetic field is shown for three different external magnetic field strengths. The emitted radiation changes sign with magnetization. (Right) The peak values of the E-field signals are plotted as a function of external magnetic field strengths.

4 GBIT DENSITY STT-MRAM USING PERPENDICULAR MAGNETIC TUNNEL JUNCTIONS WITH COMPACT BIT CELL STRUCTURE

S. M. SEO[1], S.-W. CHUNG[1], T. Y. LEE[1], J. B. PARK[1], T. KISHI[2], M. YOSHIKAWA[2], H. AIKAWA[2], T. NAGASE[2], K. SUNOUCHI[2], H. KANAYA[2], A. YAMAMOTO[2], K. TSUCHIDA[2], H. OYAMATSU[2], and S. J. HONG[1]

1) SK Hynix Inc., Icheon-si, Gyeonggi-do, Korea.ac.jp

2) Toshiba Electronics Korea Corporation, Seoul, Korea

Spin transfer torque Magnetic Random Access Memory (STT-MRAM) has attracted considerable attention as a potential replacement for Dynamic Random Access Memory (DRAM) because of its excellent performance such as infinite endurance, fast operation, and scalability beyond 30nm feature dimension [1-4]. Furthermore, STT-MRAM enable to overcome the excessive power consumption of DRAM by taking advantage of the non-volatility of magnetic tunnel junction (MTJ) storing data "1" or "0".

Both of the mature Si-based technology and the intensive progress on MTJ allow to develop *high-density* STT-MRAM. However, the critical challenges are still manifold because MTJ fabrication is based upon an extremely tight pitch. From the array operation point of view, high performance cell transistor and MTJ are essential. Also, the distribution of parasitic resistance should be significantly improved. In this work, we demonstrate 4Gbit density STT-MRAM with optimization of integration process and MTJ fabrication [5].

Fig. 1 shows the compact bit cell structure consisting of a NMOS transistor, a pair of bit line (B/L), a circle-shape MTJ, and source line (S/L). All perpendicular MTJ using CoFeB/MgO/CoFeB and the magnetic multilayer is on top of the bottom electrode (BEC). The bottom-storage layer is used to avoid the S/L bias degeneration resulting in the degradation of write current for a parallel-to-antiparallel switching. The top electrode contact (TEC) and source line contact (SLC) are successfully patterned within 90nm-pitch. The cell projection area using 3-dimensional transistor is estimated as $9F^2$ which is very close to that of DRAM. Fig. 2 is a floorplan of 4Gbit array. The chip is divided into 8 banks, and each bank contains 512Mb array. The quarter bank corresponds to the unit array blocks consisting of the unit cell array, a sub-wordline driver (SWD) for controlling a gate bias at the cell transistor, and a local Y-switch (LYSW) for selecting a B/L or a S/L which is connected to a sense amplifier (S/A) and write driver (WD).

In order to investigate the operation window of the bit cell array, V_{dd} is modulated in the range of 1.1~1.7V and the resistance of S/A was tuned by V_{ref}. The bit cell without MTJ structure was useful to evaluate the distribution of the parasitic resistance including cell transistor, B/L, S/L, and etc. Even though the resistance of MTJ is larger than the parasitic resistance, we found that the contact process is one of key factor for a reliable read operation. Write error rate (WER) evaluation was performed for several kbits with 10^6 cycles and tunable V_{dd}. With optimized fabrication process and MTJ stacks, the average WER could be sufficiently suppressed for a reliable write operation. The magnetic distribution of the MTJ array was evaluated under the external magnetic field. The magnetic distribution strongly depends on the MTJ stack, and it was critical to ensure a low WER. We compared the bit error rate between the bit-by-bit (BbB) read-write operation and all-by-all (AbA) read-write one so as to evaluate the retention performance. It was confirmed that the error rate is identical for both chip operations. This indicates that the stored data is retained for several minutes which is the time duration for AbA write operation. 4Gbit full-functional operation was performed after replacing failure bits with redundancy cells.

4Gbit density STT-MRAM was realized with all perpendicular MTJs and compact cell structure. Both of integration technology and MTJ fabrication were optimized to demonstrate the chip operation. This achievement paves the way toward stand-alone memory application of STT-MRAM.

S. W. Chung
E-mail: sungwoong.chung@sk.com
tel: +82-31-639-9189

REFERENCES

1) J. M. Slaughter et al., “High Density ST-MRAM Technology”, *IEDM Tech. Dig.*, 29.3.1-4, (2012).
2) C. Park, et al., “Systematic Optimization of 1 Gbit Perpendicular Magnetic Tunnel Junction Arrays for 28 nm Embedded STT- MRAM and Beyond”, *IEDM Tech. Dig*., 26.2.1-4, (2015).
3) H. Yoda et al., “High efficient spin transfer torque writing on perpendicular magnetic tunnel junctions for high density MRAMs”, *Current Appl. Phys*. vol.10, pp.e87-89 (2010).
4) T. Kishi et al., “Lower-current and fast switching of a perpendicular TMR for high speed and high density spin-transfer-torque MRAM”, IEDM Tech. Dig., 12-6, 2008.
5) S.-W. Chung et. al., “4Gbit density STT-MRAM using perpendicular MTJ realized with compact cell structure”, *IEDM Tech*. *Dig*., 27.1, (2016).
6) G. Jan et al., “Achieving Sub-ns switching of STT-MRAM for future embedded LLC applications through improvement of nucleation and propagation switching mechanisms”, Proc. of VLSI Tech. 2.4, 2016.

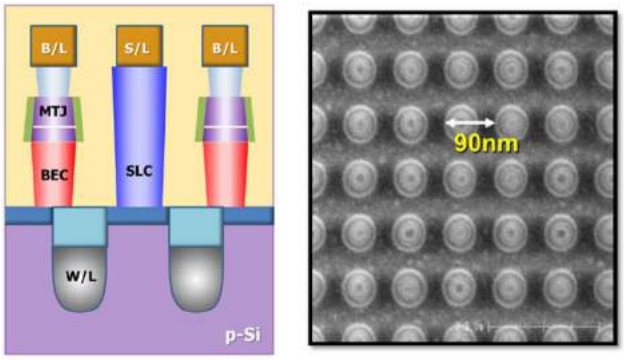

Fig. 1 (Left) Schematic diagram of bit cell and (Right) top-view SEM image after the contact patterning.

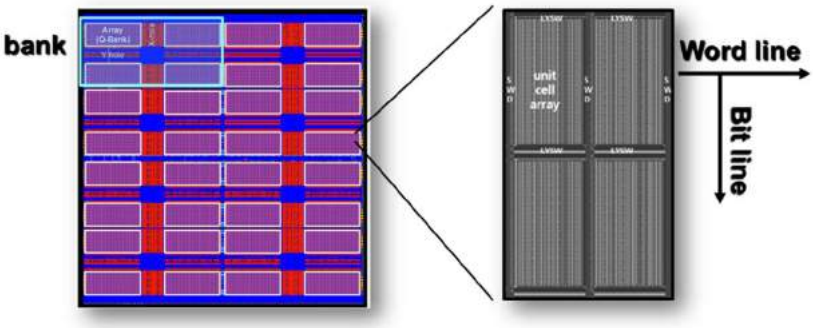

Fig. 2 (Left) 4Gbit STT-MRAM chip floor plan (Right) unit array blocks with error correction code.

SPIN-ORBIT TORQUE SWITCHING DEVICES FOR HIGH-SPEED MEMORIES AND ARTIFICIAL SYNAPSES

Shunsuke FUKAMI[1-4*], Chaoliang ZHANG[1,2], Aleksandr KURENKOV[1], William A. BORDERS[1], Samik DUTTAGUPTA[1,3], and Hideo OHNO[1-5]

1) Laboratory for Nanoelectronics and Spintronics, Research Institute of Electrical Communication, Tohoku University, Sendai, Japan

2) Center for Spintronics Integrated Systems, Tohoku University, Sendai, Japan

3) Center for Spintronics Research Network, Tohoku University, Sendai, Japan

4) Center for Innovative Integrated Electronic Systems, Tohoku University, Sendai, Japan

5) Advanced Institute for Materials Research, Tohoku University, Sendai, Japan

I. INTRODUCTION

Nonvolatile spintronics devices are expected as promising building blocks to realize high-performance and power-efficient integrated circuits [1]. While two-terminal devices with spin-transfer-torque (STT) switching is leading this field, interest has led to a consideration of three-terminal counterparts, which are in general implemented with two cell transistors for a unit cell [2]. The three-terminal cell architecture allows high-speed, typically GHz-class, operation, which is comparable to currently-used static random access memories. Spin-orbit torque (SOT) induced magnetization switching [3,4] offers a promising way for the writing scheme of the three-terminal devices. The SOT-induced switching takes place as a consequence of spin-orbit interactions, e.g., spin Hall effect and Rashba-Edelstein effect, when one applies a current to hetetostructures with broken inversion symmetry. Extensive studies carried out recently have revealed that the SOT switching offers new avenues for the spintronics-based integrated circuits. Here, we present SOT switching devices in two kinds of system and discuss their impact on integrated circuit technologies.

II. HIGH-SPEED MAGNETIZATION SWITCHING BY SPIN-ORBIT TORQUE

SOT-induced switching scheme can be divided into three categories, differing in the magnetic easy axis direction with respect to the applied current. Among them, a perpendicular easy axis scheme (Type Z) [3] and an in-plane collinear easy axis and current scheme (Type X) [5] are expected to be suitable for fast magnetization control, compared with an in-plane orthogonal easy axis and current scheme (Type Y) that is known to follow the conventional STT switching model. To investigate the magnetization dynamics of the different SOT switching schemes, we have fabricated the two types of in-plane magnetized (Types-X and -Y) devices from a Ta (or Ta/W)-CoFeB-MgO based stack on the same wafer and measured the switching properties by ns-long pulses. It has been found that Type-X scheme shows a favorable dependence of switching current density on pulse width as theory expected, allowing switching by 0.5-ns-long current pulse with a current density of 1.9×10^{11} A/m^2 [6]. We have also found that, while the application of perpendicular field is necessary to achieve bipolar switching for the Type-X scheme, this issue can be eliminated by slightly tilting the easy axis direction in the film plane [6]. The high-speed field-free magnetization switching driven by SOT demonstrated here is expected to realize high-performance and ultralow-power integrated circuits, which should expand the opportunities of IoT societies.

III. ANALOG SWITCHING AND ITS APPLICATION TO ARTIFICIAL NEURAL NETWORKS

For bipolar switching in the Type-Z scheme, necessity of an application of in-plane external field collinear with the current to break the rotational symmetry of SOT had been an obstacle for practical use. One possible way to overcome this challenge is a utilization of an antiferromagnet/ferromagnet heterostructure, in which the exchange bias at the interface takes the role of the in-plane field and SOT

Shunsuke Fukami
E-mail: s-fukami@riec.tohoku.ac.jp
tel: +81-22-217-5555

generated in the structure drives the switching. To achieve the field-free switching following this scenario, we have used a heterostructure with an antiferromagnetic PtMn and ferromagnetic Co/Ni multilayer [7]. It has been found that when the film stack is properly designed, perpendicular magnetization of the Co/Ni layer can be switched at zero fields due to the exchange bias and SOT arising from the PtMn. Moreover, in case of moderately large exchange bias, the switching evolves in an analog fashion, which may be attractive for applications to neuromorphic computing as an artificial synapse. A detailed analysis has clarified that this property is caused by the fact that a number of small magnetic domains behave independently, among which the direction of exchange bias varies inside the device [8].

Taking advantage of the analog nature of the SOT devices with antiferromagnet-ferromagnet structure, we have shown a proof-of-concept demonstration of neuromorphic computing [9]. In this work, we have developed an artificial neural network using 36 SOT devices with a field-programmable gate array and software implemented on a PC, and have tested an associative memory operation. The Hopfield model [10] has been employed to associate memorized patterns from randomly generated noisy patterns. The learning operation is performed by changing the Hall resistance of analog SOT devices, which represents a synaptic weight between neurons. We have confirmed that the SOT devices have the expected learning ability, resulting in a successful associative memory operation [9]. Since the spintronics devices have virtually infinite endurance and nonvolatility, the spintronics-based artificial neural networks are expected to open a paradigm of *edge* artificial intelligence with an on-chip learning capability.

ACKNOWLEDGEMENTS

We thank T. Anekawa, H. Akima, S. Moriya, S. Kurihara, S. Sato, and Y. Horio for fruitful discussion and technical supports. This work is partly supported by the ImPACT Program of CSTI and the R&D Project for ICT Key Technology of MEXT.

REFERENCES

1) H. Ohno et al., “Magnetic Tunnel Junction for Nonvolatile CMOS Logic,” **2010** IEDM Technical Digest p. 9.4.1 (2010).
2) S. Fukami et al., “Domain Wall Motion Device for Nonvolatile Memory and Logic — Size Dependence of Device Properties,” IEEE Transactions on Magnetics **50**, 3401006 (2014).
3) I. M. Miron et al., “Perpendicular switching of a single ferromagnetic layer induced by in-plane current injection,” Nature **476**, 189 (2011).
4) L. Liu et al., “Spin-Torque Switching with the Giant Spin Hall Effect of Tantalum,” Science **336**, 555 (2012).
5) S. Fukami et al., “A spin–orbit torque switching scheme with collinear magnetic easy axis and current configuration,” Nature Nanotechnology **11**, 621 (2016).
6) S. Fukami et al., “A sub-ns three-terminal spin-orbit torque induced switching device,” **2016** VLSI Symposia, Digest of Technical Papers, p. T06-05 (2016).
7) S. Fukami et al., “Magnetization switching by spin–orbit torque in an antiferromagnet–ferromagnet bilayer system,” Nature Materials **15**, 535 (2016).
8) A. Kurenkov et al., “Device-size dependence of field-free spin-orbit torque induced magnetization switching in antiferromagnet/ferromagnet structures,” Applied Physics Letters **110**, 092410 (2017).
9) W. A. Borders et al., “Analogue spin–orbit torque device for artificial-neural-network-based associative memory operation,” Applied Physics Express **10**, 013007 (2017).
10) J. J. Hopfield, “Neural networks and physical systems with emergent collective computational abilities,” Proc. Natl. Acad. Sci. USA **79**, 2554 (1982).

MATERIAL DEVELOPMENTS AND NANOSECOND-SCALE SWITCHING PROCESS IN PERPENDICULARLY MAGNETIZED STT-MRAM CELLS

T. DEVOLDER[1], J. SWERTS[2], S. COUET[2], W. KIM[2], G. KAR[2], V. NIKITIN[3], J.-V. KIM[1], P. BOUQUIN[1], T. LIN[2], S. MERTENS[2], and G. KAR[2]

1) C2N, Centre for Nanoscience and Nanotechnology, CNRS, Univ. Paris-Sud, Université Paris-Saclay, Orsay, France, thibaut.devolder@u-psud.fr

2) IMEC, Kapeldreef 75, B-3001 Leuven, Belgium

3) Samsung Electronics Corporation, 601 McCarthy Blvd Milpitas, CA 95035, USA

Spin transfer torque (STT)-based magnetic random access memory (MRAM) with perpendicular magnetization are seen as possible new memory elements thanks to their non-volatility, scalability, high endurance and low power requirement. The core of an STT-MRAM stack is a magnetic tunnel junction (MTJ) composed of FeCoB/MgO/FeCoB. One of the FeCoB layer is pinned to a high anisotropy synthetic ferrimagnet to create a fixed reference layer (RL) system while the second FeCoB acts as a free layer (FL). In this perpendicular technology, the requirements for the free layer (FL) include a high anisotropy and a low damping. In addition, reference layers (RLs) have to be insensitive to magnetic fields and spin-torques and are usually constructed in a synthetic ferrimagnet configuration to avoid the generation of stray fields that would destabilize the free layer.

I. MATERIAL RESEARCH

Historically, the FL is capped with amorphous Ta and more recently capped with a second MgO layer to benefit from a second interface anisotropy in the so-called 'dual MgO' configuration. We have studied the influence of the Ta spacer deposition condition on the thermal robustness, anisotropy and damping of the single and dual MgO free layers embedded in a state of the art perpendicular MTJ stack and we benchmark it to optimized single MgO FL devices. Controlling interface quality around the spacer of the free layer is a key requirement to maintain perpendicular anisotropy up to 400°C annealing. The key degradation mechanism is the diffusion of the spacer material that starts as soon as the annealing temperature triggers the crystallization of the FeCoB of the free layer. This crystallization can be postponed almost until the BEOL annealing conditions by increasing the Boron content in the FeCoB parts of the free layer. If interdiffusion occurs, the nature of the spacer material then also influences the damping. Altogether, we will explain how we can obtain a damping factor as low as 0.0035 in a dual MgO free layer and demonstrate it by vector network analyzer ferromagnetic resonance (Fig. 1). Complementary material optimizations concern the coupling of the different functional blocks within the reference layer [1-3] and the proper choice of buffer layers [4] to promote the right texture and the corresponding high perpendicular anisotropy. Altogether, we demonstrate a fully stable double MgO free layer structure up to 90 minutes of annealing at 400°C.

II. STT SWITCHING AT THE NS SCALE

We have then studied the nanosecond-scale STT switching in devices. We first looked at samples in which the fixed system comprises a hard synthetic antiferromagnet coupled to a FeCoB spin-polarizing layer through weak ferrocoupler [4]. The electrical signatures of the reversal indicate non-uniform magnetization reversal with the presence of a domain wall in junctions of various sizes. In the antiparallel to parallel switching, the reversal proceeds within 3-4 nanoseconds. A nucleation phase is followed by an irreversible flow of a wall through the sample at an average velocity of 40 m/s. Conversely, the P to AP transition has a complex dynamics with dynamical back-hopping that worsen at larger applied voltages. We attribute this back hopping to the instability of the nominally fixed layers [4].

We then studied samples in which the fixed system is harder and consequently free of dynamical

T. Devolder
E-mail: thibaut.devolder@u-psud.fr

back-hopping [5]. When the field and the spin-torque concur to both favor the P to AP transition, the reversal yields monotonic resistance ramps that can be interpreted as a domain wall propagation through the device; smaller cells switch faster, and proportionally to their diameter. At the largest sizes, transient domain wall pinning can occasionally occur. When the field hinders the P to AP transition triggered by the spin-torque, the P to AP switching is preceded by repetitive switching attempts, during which the resistance transiently increases until successful reversal occurs. At 50 nm, the P to AP switching proceeds reproducibly in 3 ns, with a monotonic featureless increase of the device resistance.

In the reverse transition (AP to P), the variability of reversal is not restricted to stochastic variations of incubation delays before the reversal: several reversal paths are possible even in the smallest junctions. Besides, the non-uniform nature of the magnetic response seems still present at the nanoscale, with sometimes electrical signatures of strong disorder during the AP to P reversal. The AP to P transition is preceded by a strong instability of the AP states in devices larger than 100 nm, indicative of fluctuations likely at the pillar edge. The switching asymmetry is related to the non uniformities of the stray field emanating from the reference layers of the tunnel junction, which affects the zones in which nucleation is favored.

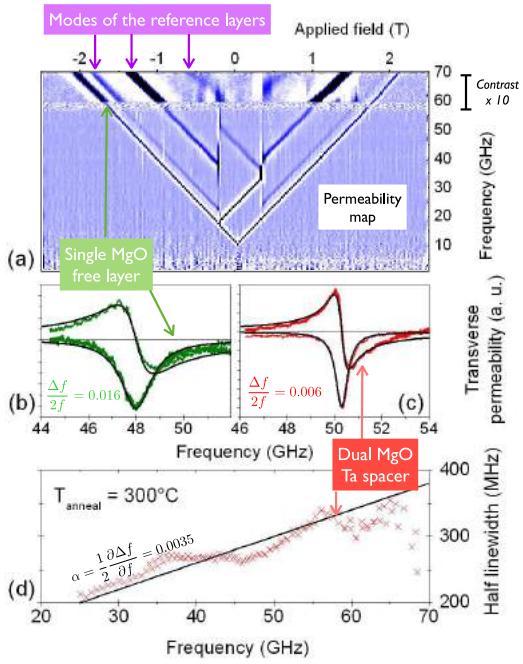

Figure 1: Examples of dynamical properties. (a) Permeability versus out-of-plane field and frequency for an MTJ with a single MgO free layer. The apparent vertical bars are the eigenmode frequency jumps at the different switching fields of the MTJ. (b) Real and imaginary parts of the experimental (symbols) and modeled (lines) permeability for an out-of-plane field of 1.54 T for the same MTJ. The model is for an effective damping that includes the contribution of the inhomogeneity. (c) Same but for a dual MgO free layer based on a Ta spacer (d) Cross symbols: FMR half frequency linewidth versus FMR frequency for a dual MgO free layer based on a Ta spacer. The line is a guide to the eye corresponding to a Gilbert damping of 0.0035.

REFERENCES

1) Thibaut Devolder, et al., "Evolution of perpendicular magnetized tunnel junctions upon annealing", *Appl. Phys . Lett.* 108, 172409 (2016).
2) T. Devolder et al. "Annealing stability of magnetic tunnel junctions based on dual MgO free layers and [Co/Ni] based thin synthetic antiferromagnet reference system" *J. Appl. Phys.* 121, 113904 (2017).
3) Enlong. Liu et al. "Effect of the seed layer on the damping constant of [Co/Ni] multilayers with perpendicular magnetic anisotropy "*J. Appl. Phys*. 121, 043905 (2017)
4) T. Devolder et al., "Time-resolved spin-torque switching in MgO-based perpendicularly magnetized tunnel junctions" *Phys. Rev. B* 93, 024420 (2016).
5) T. Devolder, et al. "Size-dependence of nanosecond-scale spin-torque switching in pMTJ", *Phys. Rev. B,* 93, 224432 (2016).

FURTHER TECHNOLOGIES FOR STT-MRAM

K. YAKUSHIJI, H. TAKAGI, N. WATANABE, K. Kikuchi, Y. KURASHIMA, A. SUGIHARA, H. KUBOTA and A. FUKUSHIMA

National Institute of Advanced Industrial Science and Technology (AIST), Tsukuba 305-8568, Japan
k-yakushiji@aist.go.jp

I. 3D Integration Technology for STT-MRAM

Three-dimensional (3D) integration technology based on direct wafer bonding and backside silicon removal processes is a key technology not only for 3D stacking of MTJ cells for ultrahigh-density MRAM but also for integrating epitaxial MTJs with a single-crystal tunnel barrier and a novel magnetic material in MRAM chips during the back end of line (BEOL) process. In this study, for the first time, we aimed to develop a 3D integration technology for perpendicularly-magnetized MTJs (p-MTJs) [1].

A p-MTJ film (poly-crystal in this study) was fabricated on a 6” bare Si wafer by sputtering. On an 8” counter wafer, a lead electrode layer (based on low-resistance Cu-N layers) was stacked. Note that the counter wafer corresponds to a CMOS wafer with copper lines on top in an MRAM application. Tantalum was used for the cap layer both in the p-MTJ and counter wafers. The 6”-p-MTJ and 8”-electrode wafers were bonded by a room-temperature bonding apparatus as shown in Fig. 1. In the HRTEM image of the bonded wafers, the two Ta cap layers are bonded almost perfectly. Next step was the removal of the backside Si in the 6”-p-MTJ wafer by a high-speed (yet damage-less) process. Photograph of the grinded and etched wafer is shown in Fig. 2. Because the backside Si was completely removed, the surface of the wafer is a Ta layer, which was originally the seed layer of the MTJ film. After the 3D process, Spin-transfer-torque (STT) switching properties were studied for p-MTJ nano-pillars (φ = 35 nm). Higher MR ratio (143%) was obtained when 3D process was applied, while STT switching properties changed only slightly. The p-MTJ showed average switching current of 62 μA and average Δ of 98 (i.e., switching efficiency of 1.6).

It can be concluded that the p-MTJ nano-pillars exhibited favorable STT switching properties and no serious degradations after the wafer bonding and silicon removal. STT-MRAM technology incorporating direct wafer bonding and removal of backside silicon will make it possible to integrate epitaxial MTJs with a single-crystal tunnel barrier and novel materials.

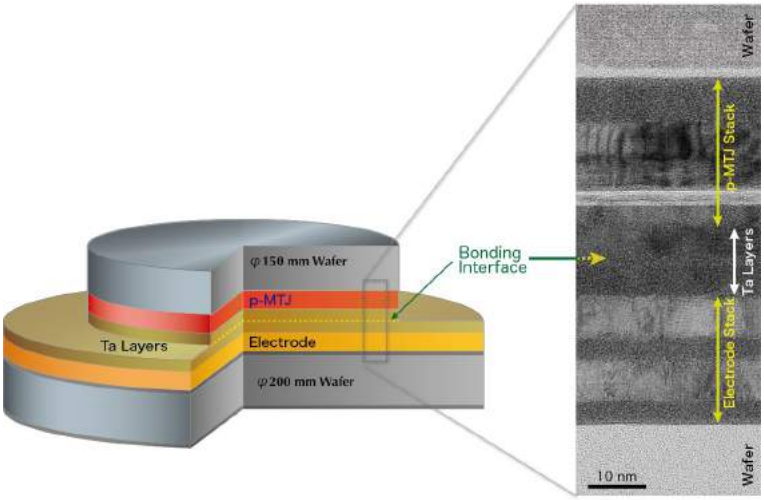

Fig. 1 Schematic illustration of a bonded sample and the HRTEM image of the cross-section around the bonding interface.

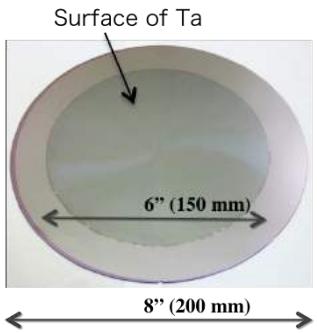

Fig. 2 Photograph of a sample after the Si removal process.

K. Yakushiji
E-mail: k-yakushiji@aist.go.jp
tel: +81-29-861-3251

II. Materials Research on Reference Structure

One of the important properties for STT-MRAM is the stability of the reference layer for stable read/write operations. Recent studies demonstrated perpendicularly magnetized synthetic antiferromagnetic (p-SAF) structures with an even stronger antiferromagnetic (AF) interlayer exchange coupling (IEC) effect: the plot of the IEC coupling energy density (J_{ex}) versus Ru spacer thickness displays oscillations the largest being the first one, which appears at 0.45-0.50 nm [2]. Other candidate materials for the SAF spacer include Rh and Ir, but they have not been extensively investigated. In this study, we investigated an IEC property for Co/Pt-based p-SAF structures with an Ir or a Rh spacer layer [3].

For Ir spacer, J_{ex} peak is broader and higher than the case of Ru spacer, and the peak is at a slightly thicker spacer layer as shown in Fig. 3. This broad peak enables us to obtain a high J_{ex} exceeding 2 erg/cm^2 over a wide spacer layer thickness range between 0.40 to 0.54 nm. The range is twice that of the Ru case. This feature will be a great advantage for the manufacturability of STT-MRAMs because it tolerates the thickness variations of the spacer layer. We also fabricated p-MTJ nano-pillars and evaluated their magnetoresistance and STT switching properties. Figure 4 shows typical R-H minor loops of a p-MTJ pillar with φ = 25 nm for t_{Ir} = 0.48 nm and T_a = 350ºC. It retains a large AF-coupled field exceeding ±8 kOe. Figure 5 shows the STT switching properties for the same pillar. The average I_{c0} and Δ were 43 μA and 85, resulting in a switching efficiency of about 2.

We can conclude that the Ir spacer is superior to the conventional Ru spacer in various aspects and has no disadvantages, and it enables us to make a very stable reference layer for p-MTJs in STT-MRAM.

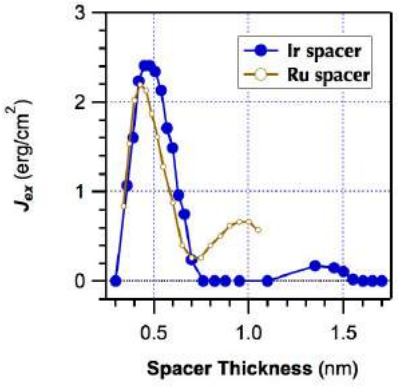

Fig. 3 J_{ex} vs. spacer thicknesses for p-SAFs.

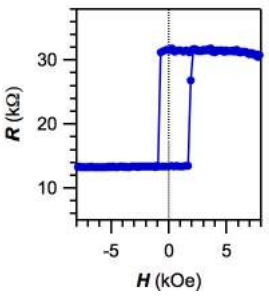

Fig. 4 *RH* minor loop for a p-MTJ with an Ir spacer.

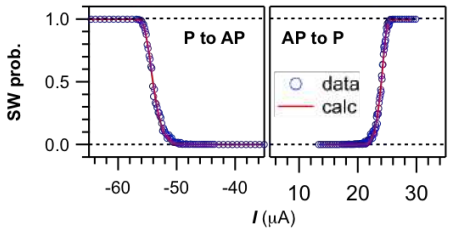

Fig. 5 STT switching properties for a p-MTJ with an Ir spacer (φ = 25 nm).

ACKNOWLEDGEMENT

This work was supported by the ImPACT Program of the Council for Science, Technology and Innovation.

REFERENCES

1) K. Yakushiji et al., "Three-dimensional Integration Technology of Magnetic Tunnel Junctions for Magnetoresistive Random Access Memory Application ", *Appl. Phys. Express,* **10**, (2017) *in press*.
2) K. Yakushiji et al., "Perpendicular Magnetic Tunnel Junctions with a Strong Antiferromagnetic Interlayer Exchange Coupling at First Oscillation Peak", *Appl. Phys. Express,* **8,** 083003 (2015).
3) K. Yakushiji et al.., "Very Strong Antiferromagnetic Interlayer Exchange Coupling with Iridium Spacer Layer for Perpendicular Magnetic Tunnel Junctions", *Appl. Phys. Lett.,* **110,** 092406 (2017*)*.

INVESTIGATION FOR HIGH-DENSITY STT-MRAM

Hiroyuki TOMITA[1], Yoshitsugu TANAKA[1], Keiichi NAGASAKA[1], Kanto NAKAMURA[1], Shinji FURUKAWA[1], Hitoshi KUBOTA[2], Akio FUKUSHIMA[2], Kay YAKUSHIJI[2], Hiroki MAEHARA[3] and Naoki WATANABE[1]

1) Tokyo Electron Yamanashi Limited, Nirasaki, Japan, hiroyuki.tomita@tel.com

2) National Institute of Advanced Industrial Science and Technology (AIST), Tsukuba, Japan

3) Tokyo Electron Limited, Nirasaki, Japan

Perpendicularly magnetized magnetic tunnel junctions (pMTJs) have been studied for many kinds of applications such as spin-transfer-torque random access memory (STT-MRAM), random number generator (Spin Dice) [1], radio-frequency (rf) detector (spin-torque-diode) [2], holographic display [3] and neuromorphic devices [4]. In these applications, STT- MRAM is the most actively studied device, because it is next generation non-volatile and fast operation memory with “more than moore” technology. In order to commercialize the STT-MRAM, it is necessary to develop for higher capacity of the device. For the higher capacity STT-MRAM, we have to develop not only micro-fabrication process but also pMTJ film property. Before miniaturizing the pMTJ bit size, we improved the stability of reference layer magnetization for stable read-write operation by using Ir spacer layer in antiferro-magnetized coupling structure. Then we tried miniaturizing pMTJ bit, and realized 10 nm order ultra-small sized pMTJ with high magneto-resistance (MR) ratio over 140% which value is the same as blanket one measured by CIPT. But resistance of pMTJ becomes huge in this case around 100 kΩ. Then we also tried evaluation of lower resistance-area (RA) products pMTJs.

The pMTJ films were prepared using Tokyo Electron EXIM™ sputtering system. The film structure was buffer layer/ [Co/Pt] and CoFeB based synthetic anti-ferromagnetic reference layer/ MgO barrier/ [CoFeB/ spcer (W, Mo)/ CoFeB] free layer/ MgO capping layer/ metal capping layer. Metallic layers were deposited by DC magnetron sputtering and the MgO barrier layer was formed by oxidizing an Mg layer. All the pMTJ films were annealed 400 degC for 1 hour after film deposition. Then pMTJ films were patterned into nano-pillars by using an EB lithography, Ar ion etching and conventional liftoff process. For the first experiment, we improved reference layer’s magnetic property. So far, typical pMTJ reference layer has perpendicular magnetized synthetic anti-ferromagnetic structure with Ru (t ~ 0.8 nm, second peak) spacer layer. To obtain stronger anti-ferromagnetic coupling, we applied other spacers Ru (t ~ 0.45 nm, first peak) and Ir (t ~ 0.55 nm, first peak). Figure 1 shows *M-H* curves with different spacer layers, Ru 2nd peak, Ru 1st peak and Ir 1st peak. We obtained strong coupling with Ir spacer. We confirmed that MR ratio does not fall even if Ir spacer was used. Then we patterned pMTJ film (MR ratio 142% and RA value 7.3 Ωμm^2 by CIPT) into minute dot size pillar. In this study, we obtained a device with a minimum electric diameter of 10.4 nm (physically about 15 nm from the TEM image). As shown in figure 2, 10 nm order pMTJ shows still large MR value as blanket film. In order to increase the capacity of the STT-MRAM, it is necessary to miniaturize the pillar size. However, with the miniaturization, the resistance rapidly increases, as shown in figure 2(a) 10 nm pMTJ’s resistance became around 100 kΩ. Then we also investigated pMTJ properties with lower-RA values. Figure 3 shows MR curves with low RA pMTJ pillars (design size of pillar are 50 nm). As shown these results, we succeed high MR values with low RA values. In the talk, we will also discuss the size dependence of pMTJ include STT-switching properties.

REFERENCES

1) A. Fukushima, *et. al*., *Appl. Phys. Express* **7** 083001 (2014).
2) K. Aoshima, *et. al*., *J. Appl. Phys*. **111**, pp07C911.1-07C911.3 (2012).
3) A. A. Tulapurkar, *et. al*., *Nature*, **438**, 339 (2005)

Hiroyuki Tomita
Hiroyuki.tomita@tel.com

4) N. Locatelli, *et. al*., *Nature Mat* **13**, 11 (2014)
5) K. Nakamura, *et. al.*, in *61st MMM Conference* (2016), p. AF-03.
6) K. Yakushiji, *et. al*., *Appl. Phys. Express* **11**, 092406 (2017).

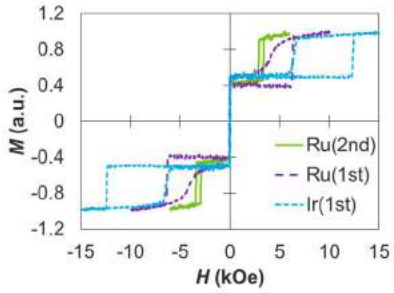

Fig.1 Magnetization loops of pMTJs having synthetic anti-ferromagnetic structure with Ru (2nd peak), Ru (1st peak) and Ir (1st peak) spacer layers.

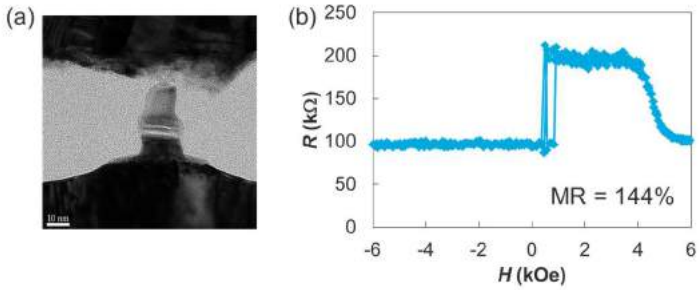

Fig. 2 (a) TEM image and (b) *R*-*H* loops of minimum 10 nm-order diameter pMTJ.

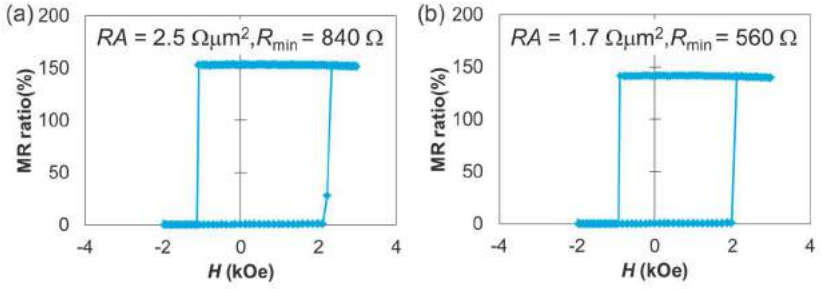

Fig 3 MR loops of low-RA pMTJs.

RECENT PROGRESS IN VOLTAGE-CONTROLLED MAGNETIC ANISOTROPY ~TOWARDS THE REALIZATION OF VOLTAGE-TORQUE MRAM~

T. NOZAKI[1], Y. SHIOTA[1], A. KOZIOŁ-RACHWAŁ[1, 2], M. TSUJIKAWA[3,4], X. XU[5], T. OHKUBO[5], T. TSUKAHARA[6], S. MIWA[6, 7], M. SUZUKI[8], S. TAMARU[1], H. KUBOTA[1], A. FUKUSHIMA[1], K. HONO[5], M. SHIRAI[3,4], Y. SUZUKI[1, 6, 7]

1) National Institute of Advanced Industrial Science and Technology, Spintronics Research Center, Tsukuba, Ibaraki, 305-8568

2) AGH University of Science and Technology, Faculty of Physics and Applied Computer Science, Al. Mickiewicza 30, 30-059 Kraków, Poland

3) Research Institute of Electrical Communication, Tohoku University, Sendai, Miyagi 980-8577, Japan

4) Center for Spintronics Research Network, Tohoku University, Sendai, Miyagi, 980-8577, Japan

5) National Institute for Materials Science, Research Center for Magnetic and Spintronic Materials, Tsukuba, Ibaraki 305-0047, Japan

6) Graduate School of Engineering Science, Osaka University, 1-3 Machikaneyama, Toyonaka, Osaka 560-8531, Japan

7) Center for Spintronics Research Network, Osaka University, 1-3 Machikaneyama, Toyonaka, Osaka 560-8531, Japan

8) Japan Synchrotron Radiation Research Institute (JASRI), Sayo, Hyogo 679-5198, Japan

I. INTRODUCTION

A magnetoresistive random access memory (MRAM) is expected to realize the ultra-low stand-by power of future computing system using a non-volatile feature of magnetism. However, one of crucial technical challenges is the reduction in operation power, because the magnetization control using electric-current consumes high energy due to Ohmic dissipation. To overcome this fundamental issue, the development of electric-field manipulation of magnetism is strongly demanded. The voltage-controlled magnetic anisotropy (VCMA) effect in an ultrathin ferromagnetic metal layer [1,2] is one of the most promising and practical approaches, because it can be applied in an MgO-based magnetic tunnel junction (MTJ) with high-speed response [3,4]. An important remaining issue of the VCMA effect is to enhance its efficiency to demonstrate the scalability. For example, for giga-bit class memory applications, VCMA coefficient of more than a few hundreds or even 1000 fJ/Vm is required [5,6]. However, the VCMA effect with high speed response is limited to be 100 fJ/Vm at present. In this talk, we'll introduce recent progresses in the materials research for the large VCMA effect and in the voltage-induced dynamic magnetization switching, and also discuss future prospects and challenges for the realization of voltage-torque MRAM.

II. EXPERIMENTAL RESULTS

To investigate the VCMA effect in a high-quality ultrathin ferromagnetic metal layer, we prepared fully-epitaxial MTJs consisting of MgO seed (3 nm)/Cr buffer (30 nm)/Fe-based ultrathin ferromagnetic metal layer (t < 1 nm)/MgO (2.3 nm)/Fe(10 nm)/Ta(5 nm)/Ru(7 nm). The bottom ultrathin Fe-based layer is the perpendicularly magnetized free layer, whose perpendicular magnetic anisotropy (PMA) can be controlled by voltage application. The top 10 nm-thick Fe is the in-plane magnetized reference layer. Tunneling magnetoresistance (TMR) curves were measured under in-plane magnetic fields and various bias voltage applications. The polarity of the bias voltage was defined relative to the top Fe layer. Two ferromagnetic layers takes orthogonal magnetization

Takayuki Nozaki
E-mail: nozaki-t@aist.go.jp
tel: +89-29-8699822

configuration under zero magnetic field. An application of in-plane magnetic field tilts the magnetization of the free layer in the in-plane direction and its behavior can be observed as a gradual decrease of tunneling resistance. Figure 1 (a) shows the bias voltage dependence of normalized TMR curves for the MTJ with the free layer of t = 0.82 nm. Voltage applications cause clear shift in saturation field, suggesting the voltage-induced PMA change. Effective PMA energy density, K_{eff} (J/m^3) was evaluated from tunneling conductance curves with saturation magnetization value under each bias condition. Figure 1(b) summarizes applied electric-field dependence of the K_{eff} t. Large VCMA coefficient of 320 fJ/Vm was observed under the positive electric-field applications. This value satisfies the required specifications for ultra-large last-level cache voltage-torque MRAM.

In the presentation, we'll also introduce the evaluation of write error rate (WER) of precessional magnetization switching induced by VCMA effect [7] and discuss future strategy to achieve the practical low WER value for memory applications.

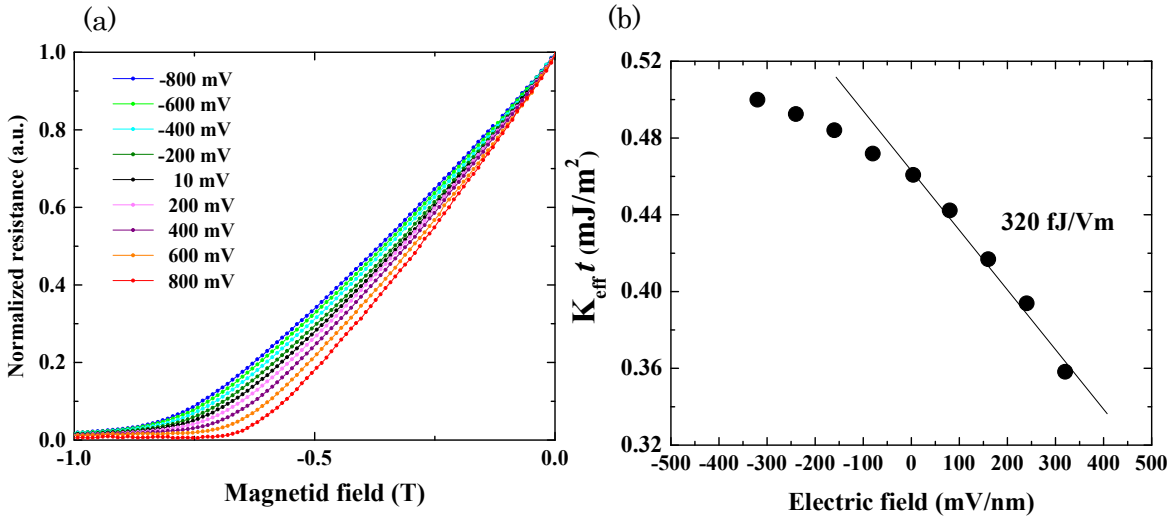

Fig. 1 (a) bias voltage dependence of normalized TMR curves for the voltage-driven MTJ and (b) Applied electric-field dependence of perpendicular magnetic anisotropy energy, K_{eff} t.

IV. ACKNOWLEDGEMENT

This work was supported by ImPACT Program of Council for Science, Technology and Innovation, and a Grand-in-Aid for Scientific Research (No. 26709046).

REFERENCES

1) M. Weisheit *et al*. *Science* **315**, 349 (2007).
2) T. Maruyama *et al. Nature Nanotech*. **4**, 158 (2009).
3) Y. Shiota *et al. Nature Mater.* **11**, 39 (2012).
4) T. Nozaki *et al. Nature Phys.* **8**, 491 (2012).
5) P. Khalili Amiri, *et al. IEEE Trans. Magn.* **51**, 3401507 (2015).
6) T. Nozaki *et al. Phys. Rev. Appl*. **5**, 044006 (2016).
7) Y. Shiota *et al. Appl. Phys. Exp.* **9**, 013001 (2016).

D1

JITTER IN HEAT ASSISTED MAGNETIC RECORDING

J. HOHLFELD[1], P. SUBEDI[1], P.J. CZOSCHKE[1], M. BENAKLI[1]
1) Seagate Technology, Bloomington, USA

I. INTRODUCTION

The linear density capability of magnetic hard disk drives is fundamentally limited by transition jitter. Conventionally, jitter is understood and attributed to two independent sources: i) the random distribution of the location and size of magnetic grains, and ii) the ratio of the switching field distribution and the gradient of the effective write field. Heat assisted magnetic recording (HAMR) is developed to extend the linear density capability of conventional perpendicular recording on the promise that it can reduce both sources of jitter simultaneously. The thermo-magnetic writing process of HAMR not only allows for media comprising much smaller grains but also yields much larger effective write field gradients [1,2].

II. MEDIA SATURATION vs WRITE FIELD

The temperature at which HAMR patterns are written, T_W, is governed by the temperature dependence of the magneto-crystalline anisotropy field, $H_K(T)$, and by the externally applied magnetic write field via: $H_K(T_W) \sim H_{eff}$, where H_{eff} denotes the effective Stoner-Wolfarth write field [3]. This implies that small write fields will not be able to control the magnetization against the impact of strong thermal fluctuations while strong write fields, competing with smaller thermal fluctuations, might yield perfect alignment of all grains. We checked this conjecture by measuring track-averaged amplitudes of 70 nm wide tracks as function of the applied write current (used to control H_{eff}) for media with and without soft magnetic underlayer (SUL). To keep the track-width constant at 70 nm we slightly adjusted the laser power for each write current. The experimental results are compared calculated values of H_{eff} in Figure 1.

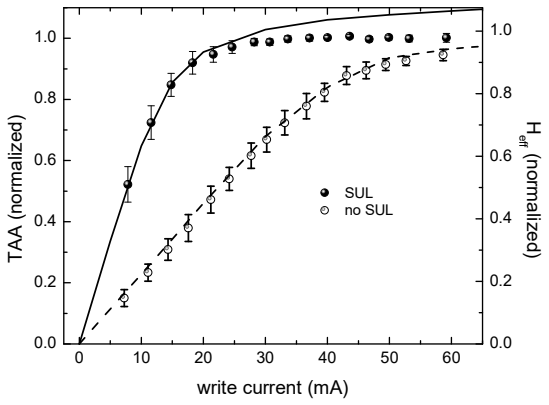

Fig. 1 Comparison of track-averaged amplitudes (TAA, symbols) measured as function of write current for constant track width of 70 nm on media with and without SUL to calculated variations of H_{eff} (solid and dashed line, respectively).

III. JITTER vs MEDIA SATURATION

When measuring transition jitter as function of the applied write field we always find a steep increase of jitter at low write fields that eludes conventional interpretation and mirrors the variations of the media saturation. This finding triggered extensive theoretical investigations on the impact of the media saturation

Julius Hohlfeld
E-mail: Julius.Hohlfeld@seagate.com
tel: +1-952-4027285

on jitter. These studies revealed that jitter indeed depends on the remanent state of the media and should be expressed as sum of squares of three terms:

$$jitter = \sqrt{GS^2 + SFD^2 + (c \cdot NSR_{REM})^2} \quad (1)$$

The first two terms are the conventional contributions due to the grain size- and switching field distributions, whereas the new term depends on the noise-to-signal ratio for the remanence of the media with the prefactor c = (20 ± 1) nm. Figure 2 a) shows the excellent agreement between measured and calculated jitter that can be obtained via Eq. (1), when the write current dependent variations of the remanence shown in Fig. 2 b) are taken into account.

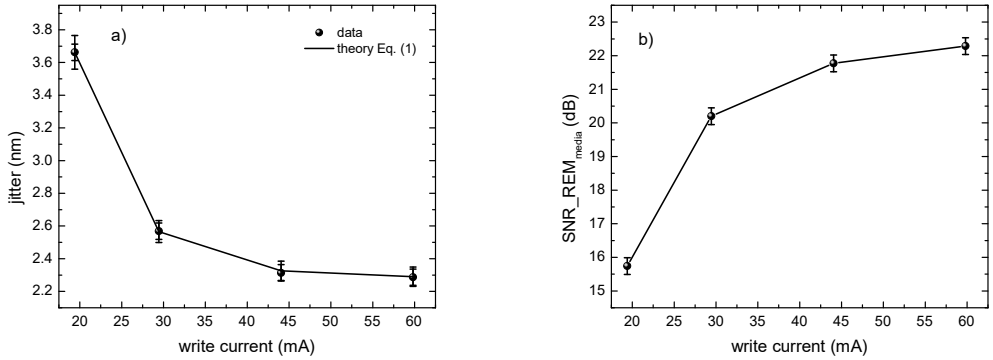

Fig. 2 a) Variations of measured jitter with write current are perfectly reproduced by Eq. (1), when the write current dependent variations of the remanence shown in panel (b) are taken into account.

In our forthcoming paper, we will show that Eq. (1) is generally valid as long as the field rise time is fast enough to ensure that the write field in the vicinity of transitions is equal to the write field governing the remanent state of the media. We will also show that failures of Eq. (1) to reproduce measured jitter can be used to rank field rise-times.

REFERENCES

1) R. E. Rottmayer et al. , "Heat-Assisted Magnetic Recording", *IEEE Trans. Magn.,* 42(10) 2417-2421, (2006).
2) A. Q. Wu et al., "HAMR Areal Density Demonstration of 1+ Tbpsi on Spinstand", *IEEE Trans. Magn.,* 49(2) 779-782, (2013).
3) J. Hohlfeld, X. Zheng, and M. Benakli, "Measuring temperature and field profiles in heat assisted magnetic recording", J. Appl. Phys. 118, 064501, (2015)

NOISE SOURCES AND MECHANISMS IN HEAT-ASSISTED MAGNETIC RECORDING

G.J. PARKER and Lei XU
Western Digital, San Jose, CA, gregory.parker@wdc.com, lei.xu@wdc.com

I. INTRODUCTION

As Heat-Assisted Magnetic Recording (HAMR) approaches commercialization, there are outstanding challenges that need to be addressed for a reliable and robust non-volatile storage device. One such challenge is noise sources due to the HAMR write process. We address this through dynamic micro-magnetic simulations of the HAMR write process. Every grain is assumed to obey the stochastic dynamics of the ensemble average of classical magnetic spins of Ref. [1]. Magneto-crystalline anisotropy temperature dependence from renormalization theory, $Hk(T) = Hk(0)\ (1\text{-}T/Tc)^{\beta}$, was assumed in order to close the implementation. Ab-initio [2] and recent experimental study [3] suggests $\beta = 0.36$ for $L1_0$ FePt. We note in [1] the stochastic LLB equation is similar to [4] except here stochastic effects along the ensemble average magnetization direction are allowed. Finally, [1] deterministic LLB equation is identical to [5] up to model dependent constants.

Noise sources during HAMR write process can be categorized by their physical origin: stochastic magnetization dynamics, optical/thermal variations and material distributions. We address each in turn in the following sections.

II. STOCHASTIC MAGNETIZATION DYNAMICS

Stochastic or "thermal" effects arise due to the finite temperature and size of the magnetic grains. Using a realistic thermal profile and a uniform write field Fig. 1 shows the mean and standard deviation of perpendicular magnetization of the same media sample for 640 low frequency write simulations. The only difference between the simulations is the realization of the stochastic effects. Both field magnitude and direction influence this noise source. Temporal history of write field and temperature of a grain also influences the dynamics.

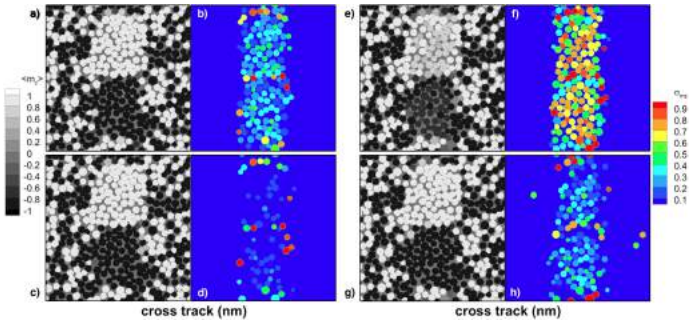

Figure 1 Media sample, 640 writes with a uniform field. a,c) are average perpendicular magnetization, b,d) are standard deviation of perpendicular magnetization, a,b) for 7kOe normal field, c,d) 10kOe normal field e-h) are the same as a-d) except field is 65^0 from normal.

III. OPTICAL AND THERMAL

During HAMR writing, optical power is deposited into the recording medium. Optical coupling variations can arise due to distributions in grain geometry and optical response. Similarly, geometry, material and thermal property distributions can result in a variation of recording grain temperature. A 'lumped element' thermal model was constructed to allow for such variations. Fig.2 shows an instantaneous temperature profile without (a) and with (b) thermal property distributions. These distributions give rise to noise in the recording metrics; e.g. transition jitter which is shown in (c) for the same media ensemble, but for various peak absorption values and thermal property variations. This thermal model can also estimate the noise source induced by power fluctuations arriving at the recording medium.

G.J.PARKER
E-mail: gregory.parker@wdc.com
tel: 1 408 717 7583

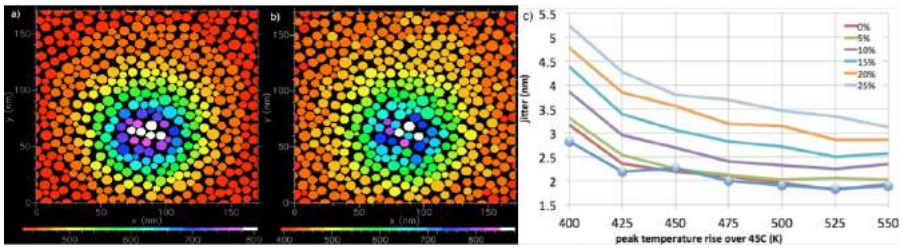

Figure 2: Instantaneous temperature (K) of grains from lumped element thermal model. a) has no distribution in absorption or thermal properties while b) has a 20% variation in thermal properties. c) resulting jitter as a function of peak temperature for multiple variations in thermal properties; blue circles is standard thermal model

IV. MEDIA DISTRIBUTIONS

Granular magnetic grains and their distributions (grain volume and pitch, saturation magnetization, Hk-both orientation and magnitude, etc.) are noise sources in both conventional and heat-assisted magnetic recording. The Curie temperature distribution, mainly due to grain volume and crystalline ordering distributions, can adversely affect recording metrics. Fig. 3 shows simulated easy axis hysteresis loops [6] of two realized recording layers differing in Hk distributions. A data track followed by two neighboring tracks were simulated for these media types for various track pitch and three constant laser powers.

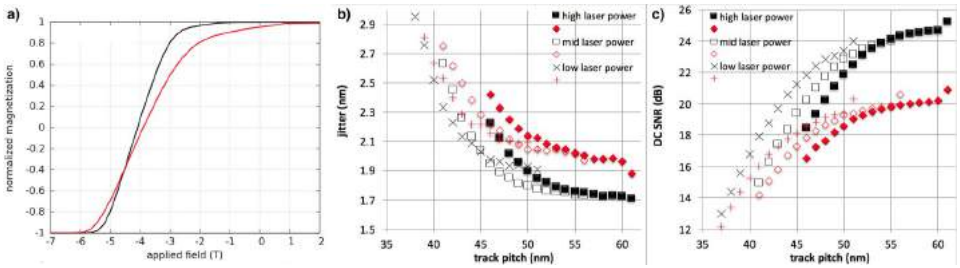

Figure 3: Two media types (red and black) are similar except for Hk distribution; a) simulated half hysteresis loop at 40 Oe/s at 300K, b) transition jitter and c) DC SNR as a function of track pitch for the two media types and three different laser powers based on 640 ensemble members. The last point in each series (largest track pitch) is for an isolated track.

V. CONCLUSION

Simulations of the HAMR write process have given insights into the sources and contributions of noise typically seen in experimental investigations. Noise arising from stochastic effects can be mitigated by controlling the write field and cooling rate. Optical/thermal distributions give rise to a variation of peak temperature and therefore different write locations degrading recording metrics. Material media distributions also give rise to noise sources, requiring identification of process conditions which control these distributions, particularly as grain size is reduced. Finally, the geometry of the magnetic patterns (e.g. BAR), including any possible curvature, affect the relative weights of these noise sources at the recording system level.

REFERENCES

1) M.Tzoufras and M.K.Grobis , "Dynamics of single-domain magnetic particles at elevated tempertaures", *New Journal of Physics,* **17** 103014, (2015).
2) D.Garanin, "Fokker-Plank and Landau-Lifshitz-Bloch equations for classical ferromagnetic bodies", *Phys. Rev. B*, **55** 3050, (1997).
3) O.N.Mryasov, U.Nowak, K.Y.Guslienko and R.W.Chantrell, *Europhys. Lett.* **69** 805, (2005).
4) H.J. Richter and G.J. Parker, "Temperature dependence of the anisotropy field of $L1_0$ FePt near the Curie temperature", Intermag 2016 invited talk, accepted to *J. of Appl. Phys.*
5) L.Xu and S.Zhang, "Magnetization dynamics at elevated temperatures", *Physica E*, **45** 72, (2012).
6) G.J.Parker and W.N.G.Hitchon, "A kinetic theory of micromagnetic time evolution", *Physics Lett. A*, **377** 2388, (2013).

HEAT ASSISTED INTERLACED MAGNETIC RECORDING

Steven GRANZ[1], Wenzhong ZHU[1], Chris REA[2], Ganping JU[3], Jan-Ulrich THIELE[3], Tim RAUSCH[1] & Edward GAGE[1]

1) Seagate Technology, 1280 Disc Drive, Shakopee, MN 55379, USA
2) Seagate Technology, 7801 Computer Avenue, Bloomington, MN 55435, USA
3) Seagate Technology, 47488 Kato Road, Fremont, CA, 94538, USA

I. INTRODUCTION

Heat Assisted Magnetic Recording (HAMR) is the next generation hard disk drive technology which enables continued and significant areal density growth [1]. There are currently two common architectures for the layout of tracks in hard disk drives: Conventional Magnetic Recording (CMR) and Shingled Magnetic Recording (SMR). In CMR, any track can be written at any time and neighboring tracks do not intentionally overlap. In SMR, the tracks are written sequentially in bands with the tracks intentionally overlap like shingles on a roof. In this paper, we introduce a novel track layout, Interlaced Magnetic Recording (IMR)[2] and apply it with a HAMR recording system.

II. HEAT INTERLACED MAGNETIC RECORDING

Heat Interlaced Assisted Magnetic Recording (HIMR) is an alternative recording architecture where tracks are recorded in an interlaced order with different linear densities. In IMR, there are two different types of tracks: bottom and top tracks. Bottom tracks are written first at every other track location whereas top tracks are written second at every other track at an offset as seen in Figure 1. IMR is convenient with HAMR since the linear density can be adjusted based on the linear density tradeoff with laser current. Bottom tracks can be written wide with a higher laser power and top tracks can be written narrow with a lower laser power. Bottom tracks are double sided squeezed by the top tracks whereas top tracks are non-squeezed. Since the top tracks squeeze the bottom tracks, the top track laser current defines the trackpitch of the HIMR system. HIMR ADC gain is from three main sources: bottom track linear density gain from increased laser current (which reduces curvature and increases the thermal gradient), top track linear density gain from non-squeezed conditions (top tracks do not suffer from adjacent track write interference since the next top track is two tracks away) and trackpitch is defined by the top track laser current which is lower and gives a narrow track enabling high kTPI. IMR has one system performance penalty. Top tracks can be re-written as many times as needed but to overwrite a bottom track with top tracks present, the adjacent top tracks need to be read and then re-written after the bottom track. A band structured like with SMR may be desired but the system performance penalty for IMR will be similar or less than SMR depending on the workload of the drive.

II. EXPERIMENTAL DETAILS

We investigated the areal density capability for HAMR, HAMR SMR and HIMR on a spinstand using the ASTC areal density metric [3]. Ten HAMR heads were used. The heads and media were similar to those used in previous studies [3-4]. Spinstand measurements were with writer current 55mA, active reader and writer clearance of 1 nm, radius of 23 mm, skew 0^o and 5400 rpm with linear velocity of 13.21 m/s. Channel areal density (Tflux/in^2) was measured. A code rate of 0.88 was used to calculate user areal density (Tbit/in^2).

III. RESULTS

The areal density capability of the ten HAMR heads yielded an average HAMR ADC of 1.15 Tbit/in^2 with 32x adjacent track writes, HAMR SMR ADC of 1.46 Tbit/in^2 and HIMR ADC of 1.5 Tbit/in^2 as seen in Figure 2a. HIMR observed a 31% increase in areal density over HAMR whereas HAMR SMR observed a 27% increase in areal density over HAMR. For HAMR, HAMR SMR and HIMR, the bit aspect ratio was measured as seen in Figure 2b. For HAMR SMR and HIMR, the track density was significantly higher than HAMR due to the single adjacent track write. HAMR SMR had the highest track density because of the single-sided adjacent track interference (ATI) when shingling the tracks. For HIMR, the linear density and bit aspect ratio was significantly higher than HAMR and HAMR SMR due to the increase in laser current for the

Steven Granz
Seagate Technology: ART Lab
E-mail: steven.d.granz@seagate.com
tel: +952-402-7239
1280 Disc Drive, Shakopee, MN 55379

IMR bottom tracks and the adjacent track interference reduction for top tracks.

It should be noted that the best components from this design at a more aggressive clearance achieved a channel density around 2 Tbit/in^2 when combined with SMR and MSMR (Multiple Sensor Magnetic Recording).

IV. CONCLUSION

This novel interlaced track layout architecture enables further increases in HAMR areal density capability (HIMR) which is favorable for the hard disk drive markets with a system performance penalty less than shingled magnetic recording.

REFERENCES

1) M. Kryder, E. Gage, T. McDaniel, W. Challener, R. Rottmayer, G. Ju, Y. Hsia, F. Erden, "Heat Assisted Magnetic Recording" *Proc. IEEE* **96** 1810-1835 (2008). *IEEE Trans Magn*., **53**, NO. 4 (2017).
2) E. Hwang, J. Park, R. Rauschmayer, B. Wilson, "Interlaced Magnetic Recording"
3) S. Granz, T. Ngo, T. Rausch, R. Brockie, R. Wood, G. Bertero, E. Gage, "Definition of an Areal Density Metric for Magnetic Recording Systems" *IEEE Trans Magn*., **53**, NO. 2 (2017).
4) C. Rea, P. Subedi, H. Zhou, D. Saunders, M. Cordle, P. Lu, S. Granz, P. Czoschke, S. Hernandez, J. Jury; Y. Peng, J. Thiele, A. Wu, G. Ju, T. Rausch, M. Seigler, E. Gage "High Track Pitch Capability for HAMR Recording", *IEEE Trans Magn.,* **53** NO. 2 (2017).

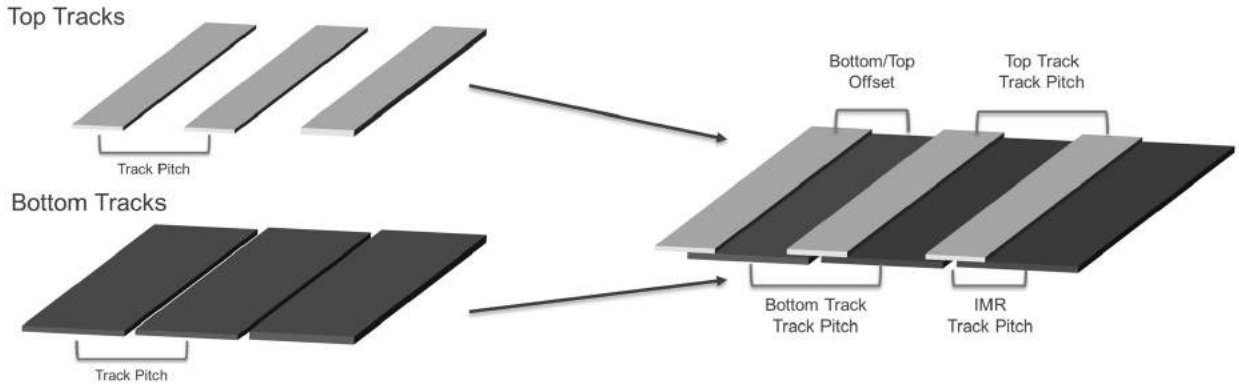

Figure 1: Heat Assisted Interlaced Magnetic Recording Track Layout

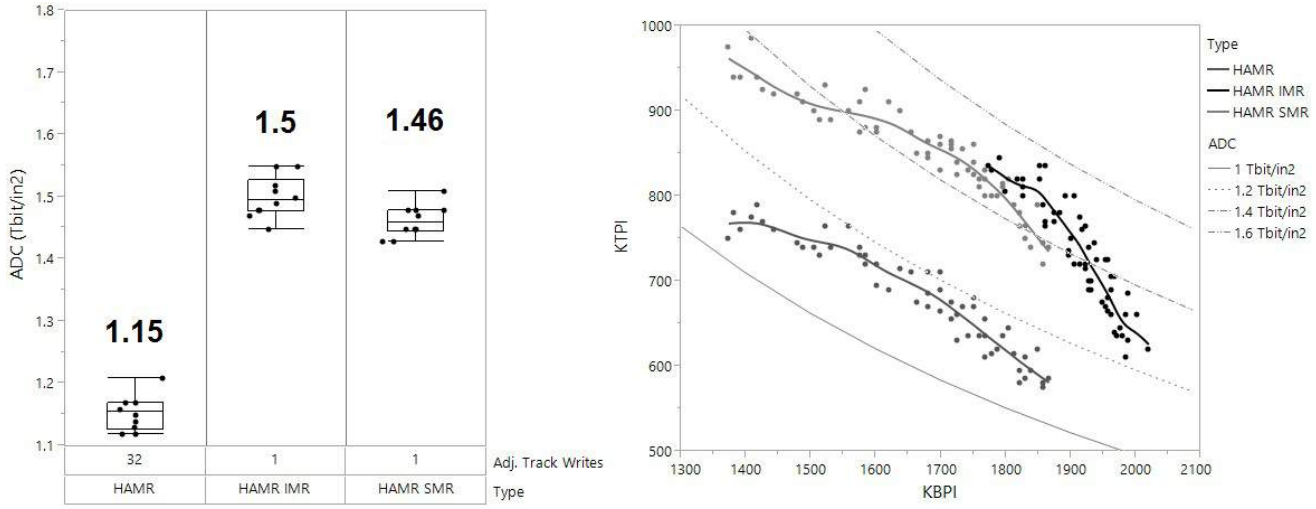

Figure 2: HAMR, HAMR SMR and HIMR: ASTC ADC and VBAR

DISTRIBUTION-BASED RECORDING MODEL FOR HAMR

T. MALETZKY[1], M. STAFFARONI[1], and M.M. DOVEK[1]
1) Headway Technologies, Milpitas, California, USA, tobias.maletzky@headway.com

I. BACKGROUND

Landau-Lifshitz-Gilbert (LLG) and Landau-Lifshitz-Bloch (LLB) based recording simulations are the gold standard in judging the performance and the impact of various parameters in Heat Assisted Magnetic Recording (HAMR). While these models include the full dynamics of the recording process, they do not readily allow identification of performance-limiting factors. Furthermore, these simulations are often too time consuming to allow thorough investigation of all input parameters. The standard approach in LLG and LLB recording simulations utilizes a finite number of grains which are chosen based on known recording media distributions. These grains represent only a subset of the entire distribution of grains. For achieving results which are independent of this subset, a sufficiently large number of transitions with different grain configurations has to be simulated. The final result of a recording simulation is then based on averaging over all of the aforementioned simulations.

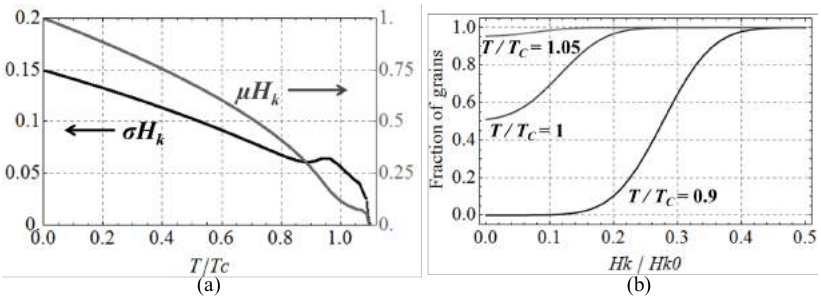

(a) (b)

Fig. 1 (a) temperature dependence of the mean and the standard deviation of the normalized H_k distribution, (b) cumulative distribution function for H_k at different normalized temperatures

In HAMR, the impact of grain to grain interactions is reduced by operating around the Curie temperature of the recording medium. At high temperature, the demagnetization field and the exchange coupling are small compared to the applied magnetic field of the recording head. This opens the opportunity to perform all calculations with distributions of grain properties directly, rather than on the basis of single grains and their interactions with their neighbors. The recording-modeling approach presented here has the advantage that no detour via grain subsets is required: the obtained results already represent the average over an infinite number of grains. This allows for short calculation time and a higher resolution of variations among recording impacting parameters, e.g. different thermal distributions in the recording medium.

II. BASICS OF THE DISTRIBUTION-BASED RECORDING MODEL

Most important for determining the recording transition length is the distribution of the anisotropies H_k at the different normalized temperatures $x = T/T_C$. It is defined by the distribution of the anisotropy H_{k0} at 0 K with relative standard deviation σH_{k0}=15%, the distribution of the Curie temperature T_C with relative standard deviation σT_C=3%, and the temperature dependence of the normalized anisotropy field

$$H_k(x)/H_{k0} = (1- x)^{\beta} \qquad (1)$$

with the exponent β~0.5 for FePt [1]. Assuming Normal distributions for the anisotropies H_k>0 for every x and taking the accumulation at H_k =0 into account when approaching T_C, a cumulative distribution function $F_x(y)$ for the normalized anisotropy $y = H_k/H_{k0}$ at the normalized temperature x can be derived:

$$F_x(y) = \Phi(\sigma T_C(x-1)) + (1-\Phi(\sigma T_C(x-1))) \cdot F_{\mathcal{N}(\mu(x),\sigma(x))}(y) \quad \text{with} \quad \Phi(x) = \frac{1}{2}\left(1+\operatorname{erf}\left(\frac{x}{\sqrt{2}}\right)\right), \qquad (2)$$

where erf (x) is the error function and $F_{\mathcal{N}(\mu,\sigma)}$ denotes the cumulative distribution function of the Normal distribution with mean $\mu(x)$ and standard deviation $\sigma(x)$.

Tobias Maletzky
E-mail: tobias.maletzky@headway.com
tel: +1-408-934-5318

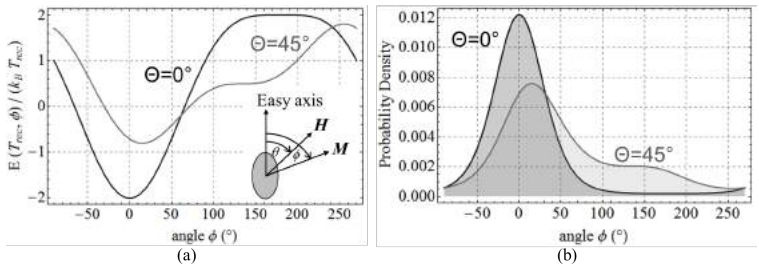

(a) (b)

Fig. 2 (a) To the thermal energy $k_B T_{rec}$ normalized Stoner-Wohlfarth energy at the recording point for T_{rec}/T_C=0.997 and a weak head field with H_{eff}/H_{k0}=0.04, (b) corresponding probability density

Fig. 1a shows the temperature dependence of the mean μH_k and the standard deviation σH_k of the normalized anisotropy y, which can be numerically derived by a random number simulation based on (1) assuming a $\mathcal{N}(1, \sigma T_C)$ distribution for x and a $\mathcal{N}(1, \sigma H_{k0})$ distribution for y itself, which multiplies the right hand side of (1). Fig. 1b shows the cumulative distribution function $F_x(y)$ according to (2) based on the μH_k and σH_k curves shown in Fig. 1a.

Applying (2) to the spatial temperature distribution in the middle of the recording layer gives the H_k distribution at every point in the layer. According to the Stoner-Wohlfarth model [2], switching of a grain occurs if its H_k is smaller than the effective head field given by

$$H_{eff}(T) = |H(T)| \frac{\sqrt{1-\tan^{\frac{2}{3}}\theta + \tan^{\frac{4}{3}}\theta}}{1+\tan^{\frac{2}{3}}\theta} \cdot \mathrm{sign}(H_{perp}), \tag{3}$$

where H_{perp} denotes the component of the head field perpendicular to the recording layer and θ is the angle between the easy axis of the grain and the head field. Therefore, if the spatial H_{eff} distribution in the recording layer is known, $F_x(y)$ with y= H_{eff} /H_{k0} gives at every point in the layer the percentage of switchable grains, i.e. the percentage of grains for which $H_k < H_{eff}$.

Although the $H_k < H_{eff}$ map obtained according to the procedure outlined above can be used to evaluate the quality, i.e. thermal gradient and curvature, of thermal distributions and their interplay with the media distributions and read-back width, this approach does not include thermal fluctuations. Therefore, this model delivers reliable results if the head field is assumed to be sufficiently high, such that the impact of thermal fluctuations on the recording can be ignored. Extension of the model to incorporate thermal erasure can be achieved by estimating the probability of stable switching for switchable grains in the recording layer with the Stoner-Wohlfarth energy

$$E(T,\phi) = \mu_0 M_s(T) V\left[\tfrac{1}{2} H_k(T) \sin^2(\phi) - H\cos(\theta-\phi)\right], \tag{4}$$

where M_s is the saturation magnetization, V is the grain volume, H is the head field magnitude, and ϕ is the angle between the magnetization and the grain's easy axis, which can also be understood as the grain's state.

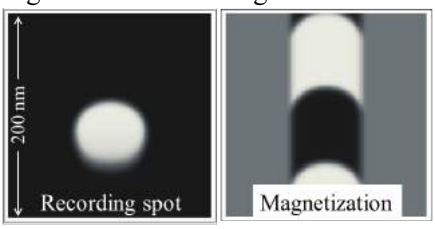

Fig. 3 Recording spot and track-map based on distributions with max. T/T_C=1.14 and max. H_{eff}/H_{k0}=0.04

Assuming that the explicit time dependence of the switching process is less dominant than the change of the energy barrier between the two stable states at room temperature, a stationary switching model can be formulated. Inserting the energy (4) at the recording point (Fig. 2a), i.e. H_{eff}=H_k, in a Boltzmann factor and normalizing by the integral of this factor over all grain states, gives the probability density function of the grain states ϕ (Fig. 2b). For a sufficiently long bit-length and assuming the worst case, all switchable grains freeze at the (H_{eff}=H_k, T=T_{rec}) pair determined by (1) with the highest temperature T and therefore with the lowest H_k. Weighting all grains with this switching probability results in an approximation for the fraction of stable switched grains that are not thermally randomized. Fig. 3 shows a recording spot and a resulting magnetization probability track-map derived by the model presented here using a representative thermal spot with a thermal gradient of ~7 K/nm.

REFERENCES

1) J.-U. Thiele et al., *J. Appl. Phys.*, **91**, NO. 10, 6595 (2002)
2) E.C. Stoner and E. P. Wohlfarth, *Philos. Trans. R. Soc. London*, Ser. A **240**, 599 (1948)

INTERFERENCE FROM ADJACENT TRACKS IN HAMR RECORDING SYSTEMS: SIDE-READING AND ENCROACHMENT

Peter CZOSCHKE[1], Victor SAPOZHNIKOV[2], Nuttapon CHAIDAUNGSRI[3] and Douglas SAUNDERS[4]

1) Seagate Technology, Bloomington, MN, USA, peter.j.czoschke@seagate.com

2) Seagate Technology, Bloomington, MN, USA, victor.b.sapozhnikov@seagate.com

3) Seagate Technology, Samut Prakan, Thailand, nuttapon.chaidaungsri@seagate.com

4) Seagate Technology, Bloomington, MN, USA, douglas.a.saunders@seagate.com

I. INTRODUCTION

The linear density capability of a head-media combination in a drive environment will deviate necessarily from its intrinsic capability due to factors such as readback interference from adjacent tracks, the existence of pre-existing data on the medium, and encroachment from subsequently written tracks. Due to the differences in head structure, media composition and structure, and recording physics of heat-assisted magnetic recording (HAMR), the influences of these various factors on recording performance differ substantially compared to conventional or shingled perpendicular magnetic recording (PMR).

II. RESULTS

In this study, the effects of pre-existing data ("background tracks") and subsequently written data ("foreground tracks") are examined separately to understand the relative contributions due to encroachment and side-reading. The effects of side-reading are measured by comparing the bit-error-rate (BER) of a data track written on a high-frequency AC background (band erased), which presumably has a minimal amount of readback interference, with data tracks written on a pair of background tracks at various distances off-track from where the main data track is then written. The difference in BER is attributed to background interference effects, which are due to side-reading and any written-in interference [1]. The effects of encroachment are measured by comparing BER of a track before and after the writing of two foreground tracks written at a full track width to either side of the data track. The foreground tracks themselves will also cause interference during readback due to side-reading, much as the background tracks.

Figure 1 shows the average data from 20 heads measured at seven different datarates ranging from approximately 65% to 100% of the nominal datarate for the head design. In all cases, the BER after the foreground tracks are written is the same, regardless of the background condition, indicating that the background condition does not significantly affect the write process for HAMR recording. The data labelled "Full BG" have the background tracks written at the same location as the later foreground tracks. Since the two conditions (before and after writing of the foreground tracks) should have similar degrees of side-reading, the difference between them can be attributed primarily to encroachment.

For the HAMR system, the data indicate that encroachment and side-reading result in a similar amount of on-track performance degradation compared to the intrinsic BER of the track. Similar measurements on a PMR system show a lower effect due to side-reading. The effects of both decrease at higher datarates, due in part to the higher bit density of the tracks, which results in lower and more localized stray fields from the media, but also due to the higher base error rate, which makes the channel detector less sensitive to additional noise sources.

PETER CZOSCHKE
Seagate Technology, Recording Heads Group
7801 Computer Avenue South
Bloomington, MN 55435 USA
E-mail: peter.j.czoschke@seagate.com
tel: +952-402-8694

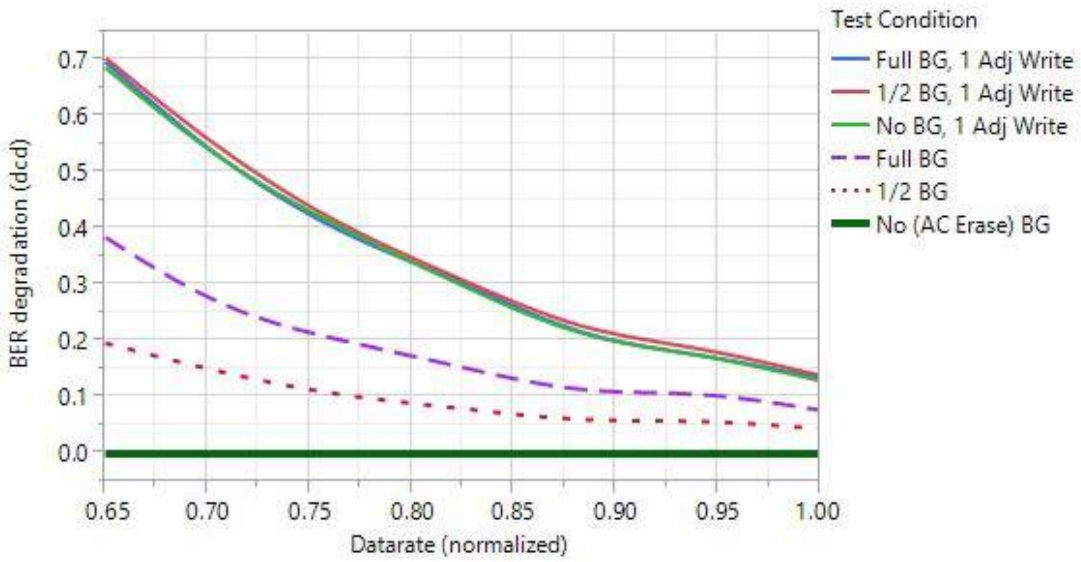

Fig. 1. Performance degradation due to background data and adjacent tracks in a HAMR recording system. "Full BG" indicates the background data is at a full track spacing from the center position where the main data track is written. "1/2 BG" indicates the background data was written at approximately 40% track spacing from the center position. Foreground tracks (labelled with "1 Adj Write") are always written at a full track spacing offset. For conditions with foreground tracks, all three lines overlap, indicating the background condition has no effect in these cases but the foreground tracks data have the same side-reading effect as the background data.

A micromagnetic model of a read sensor of similar structure as the one used in the experiment is also constructed to better understand the empirical data. Various different recording and media properties are varied, such as head-media spacing (which is larger in present HAMR systems due to thicker head and media overcoats), storage layer geometry, and the placement/existence of a soft underlayer in the media. It was shown that differences in these factors between HAMR and PMR recording systems can account for the large side-reading effect in HAMR.

REFERENCES

1) J. Fernandez-de-Castro, et al., "Measuring and understanding write width and off-track as a function of linear density in perpendicular recording", *J. App. Phys.,* 111, 07B702 (2012).

MAGNETIC HEAD DESIGN FOR TRANSITION CURVATURE CORRECTION IN HAMR

Jian-Gang (Jimmy) ZHU, Yuwei QIN, and James BAIN, Cheng-Ming CHOW

Data Storage Systems Center, Carnegie Mellon University, Pittsburgh, PA, USA

INTRODUTION

In heat assisted magnetic recording (HAMR), curved recording thermal profile creates transitions with pronounced curvature and significantly limits linear density capability [1]. With write head field being spatially uniform, transition fronts of recorded bits essentially follow the temperature contour of the thermal profile at recording, or "freeze", temperature. Consequently, the recording thermal gradient degrades at cross track positions away from track center, allowing increased medium noise in the presence of grain-to-grain Curie temperature variation [2]. Furthermore, at small transition spacing, the curved transition fronts yields severer erasure-after-write away from track center, causing significant track narrowing at high linear densities [2].

The key to correcting transition curvature is to have recording occurs at different "freeze" temperatures across track width such that transition front can be straight with curved temperature contours of recording thermal profile. This can be achieved by designing write heads to produce head field with varying amplitude adequately across the recording track [2, 3]. The cross-track varying field should have the lowest amplitude at the center of the track where the peak temperature occurs and the highest amplitude at track edges to lower the "freeze" temperature for straightening transition front. Thus, for a straight transition front, the "freeze" temperature decreases from the center to the edges and this temperature varying range is essentially determined by the maximum field amplitude available from the write head and the lowest field amplitude which needs still sufficiently high to yield magnetization saturation [3]. If the head field maintains its amplitude beyond track edges, wing-like recording patterns will be created beyond the edges of straightened transitions and the evolve into erase bands at high linear densities [4]. Field reduction beyond track edges will reduces the erase band width.

In this paper, we present a modeling study which combines write head design, near field transducer design, and micromagnetic simulation of the HAMR recording process to understand the potential as well as the limit of practical implementation for correcting transition curvature.

SIMULATION RESULTS AND DISCUSSIONS

Figure 1 shows a head design, referred to as dual-rail design, which is formed by two magnetic poles, semi-infinite along the recording track direction both are magnetized in the same direction perpendicular to the ABS. The produced head field at middle of a 10nm thick magnetic medium is used for recording simulations with the center of the head (middle of the gap) aligned with the center of the circular thermal profile. Recording 1T transition patterns at four different linear densities are shown in Fig. 3(b) with the results of spatially uniform head field shown in comparison (Fig. 3(a)). The degree of the transition curvature for recording with the dual-rail write head is significantly reduced comparing to that for recording with the spatially uniform head filed with optimized head field amplitude 10.5kOe.

Pr. Jimmy Zhu

E-mail: jzhu@cmu.edu

At 2500 KFCI, the transitions for recording with uniform write field are all percolated whereas the transitions for recording with the dual-rail head field still remains intact. Figure 2 shows the calculated SNR for both recording cases. In the talk, more detailed head design and analysis will be presented.

REFERENCES
[1] Rea, C, Subedi P, Zhou H. "High Track Pitch Capability for HAMR Recording," IEEE Trans. Magn. (2016)
[2] Zhu, J.-G. and Li H. "Correcting Transition Curvature in Heat Assisted Magnetic Recording". IEEE Trans. Magn., vol. 53, No. 2, 3100507 (2016).
[3] Zhu, J.-G., Li, H, "Write head field design for correction transition curvature in heat assisted magnetic recording," AIP Advances, 7 (5), 056505 (2017).
[4] Qin, Y. and Zhu, J.-G. "Curvature Correction Head Field Design and Track Edge Characteristics in Heat Assisted Magnetic Recording," Intermag 2017, Paper BE-04 (2017).

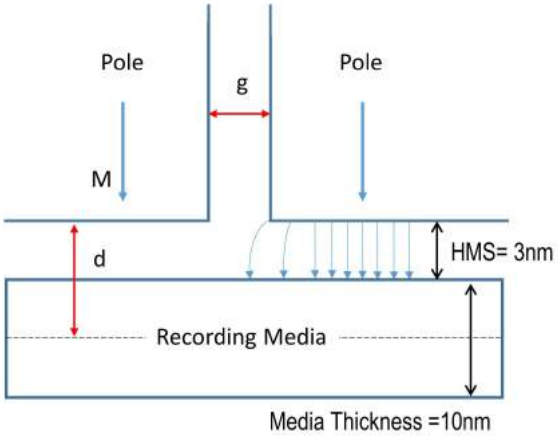

Fig. 1 Illustration of the write head design and recording geometry in the cross-track direction. The head gap of 15 nm is assumed for the simulation results presented here.

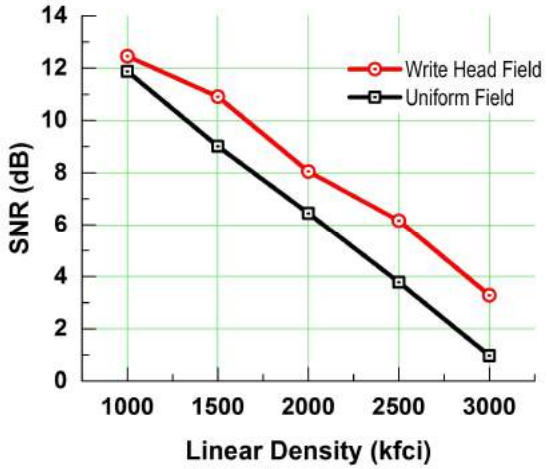

Fig. 2 Calculated medium 1T signal-to-noise ratio (SNR) as a function of linear density for recording with the write head shown in Fig. 1 (*Red*) and with the spatially uniform field (*Black*).

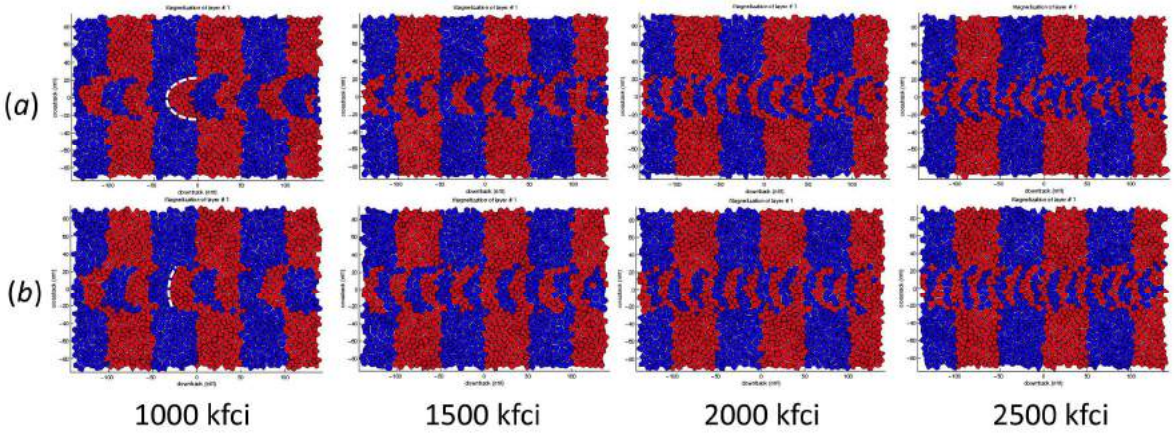

Fig. 3. Simulated 1T recording patterns at four different linear densities for (*a*) recording with the write head shown in Fig. 1 and (*b*) recording with spatially uniform head field.

D7

ENERGY-ASSISTED RECORDING: SYSTEM ARCHITECTURE & APPLICATIONS

Bernd LAMBERTS, Classica JAIN and Remmelt PIT
Western Digital, San Jose, California, USA

I. Introduction

The introduction of energy-assisted recording technologies changes the way rotating magnetic storage systems have been perceived in a fundamental way. Traditionally recording devices have been treated as bimodal regarding reliability and durability. The designs consider only two states, the Head & Media components perform as measured during manufacturing or are defective. Energy-assisted recording introduces the need to manage components over the used lifetime [1].

For energy-assisted recording, the achievable performance is a function of the parameters which limit component lifetime. This introduces the need to understand workload distributions of modern storage architectures such as distributed file systems and hyper-scale applications. Another key aspect of the device use is related to the transition from direct static mapped disk layouts like PMR recording, to systems using indirection mapped layouts such as SMR recording. In the second part of the paper we discuss solutions to manage component lifetime while maximizing the recording system performance.

II. SYSTEM CHALLENGES

For systems with a finite lifetime of the head disk interface, a detailed understanding of the access statistics is crucial. The total volume of data and the temporal distribution as well as the spatial distribution are all important. We used device logs and detailed system traces to analyze the workload distributions. Our results show dramatic differences in data consumption as function of the application [see charts 1 & 2]. We find that hyper-scale workloads show significantly higher utilization than traditional enterprise applications [chart 2]. This result is consistent with other studies on access density requirements [2]. We investigated the time dependency of the workload via categorizing device logs into age classes. Our results indicate that almost no systems experience increased write workload over time. Typical use cases show an increased workload in the 1st 12 months followed by stabilization and a decline towards the end of the warranty life. This is consistent with the observation of data “aging” over time.

Details of the access statistics were investigated via analysis of device logs and trace analysis of setups in our System Integration Group. One of the key findings is that file system choices and device driver selection have similar impact to the overall results as the choice of applications. We find that poor choices in the Host software stack may lead to excessive write amplification for individual components. In some cases, 30% of all I/O’s over 24 hours are associated with less than 1% of the LBA’s [chart 3].

The reasons for this behavior are related to check-pointing by the application layer and/or the use of special meta-data index systems to facilitate synchronization across processes. A contributing effect is the fact that modern disk drives can store typical ‘iNodes’ of file systems such as Ext4 [3] on a few dozen tracks. Depending on the device format layout, this may lead to excessive use of individual heads.

III. DEVICE SOLUTIONS

There are three areas of opportunity where some of the impact of finite lifetime can be mitigated:

1) **Component lifetime management:** We present an integrated component lifetime management approach that aims to maximize the utilization of the given hardware. As shown in the previous paragraphs, only a few devices experience the maximal workload. Since the lifetime of energy-assisted recording devices is inversely proportional to their energy output, we use a reinforcement learning [4] approach to optimize component lifetime.

2) **Workload distribution opportunities:** As outlined in chapter II, challenging situations may occur for systems which feature excessive use of single components or localized areas in the device. This situation is challenging for statically mapped designs like traditional PMR recording arrangements. One solution

Bernd Lamberts
E-mail: Bernd.Lamberts@wdc.com
tel: +1-408-717-8761

of this problem is the use of an intermediate de-staging buffer or cache. This technique is well known from write cache designs in computer science.

3) **Workload management opportunities:** Even considering the options discussed in 1) & 2) ultimately true wear leveling similar to solid state devices [5] may be required. A major challenge to this objective is the fact that the true component lifetime is known. Hence most approaches are limited to workload balancing. Even for this objective we find a significant difference between systems based on full indirection like HA-SMR[6] and statically mapped systems such as PMR. For SMR systems it will be significantly easier to insure balanced use of all components.

REFERENCES

1) Budaev, Bair V., and David B. Bogy. "On the lifetime of plasmonic transducers in heat assisted magnetic recording." *Journal of Applied Physics* 112.3 (2012): 034512.
2) Cisco, “Cisco global Cloud Index 2015-2020”, http://www.cisco.com/c/dam/en/us/solutions/collateral/service-provider/global-cloud-index-gci/white-paper-c11-738085.pdf
3) Aneesh Kumar et al, “Ext4 block and inode allocator improvements”, Proceedings of the Linux Symposium, (2008)
4) Sutton, Richard S.; Barto, Andrew G. (1998). *Reinforcement Learning: An Introduction*. MIT Press.
5) Yang, Ming-Chang, et al. "Garbage collection and wear leveling for flash memory: Past and future." *Smart Computing (SMARTCOMP), 2014 International Conference on*. IEEE, 2014.
6) Feldman, Tim, and Garth Gibson. "Shingled magnetic recording areal density increase requires new data management." *USENIX; login: Magazine* 38.3 (2013).

IV. ILLUSTRATIONS

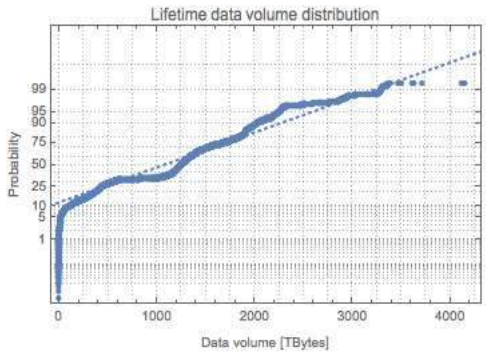

Fig. 1 Observed population data Volume distribution

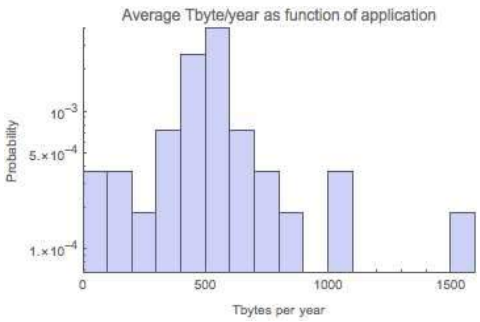

Fig 2. Data volume by application

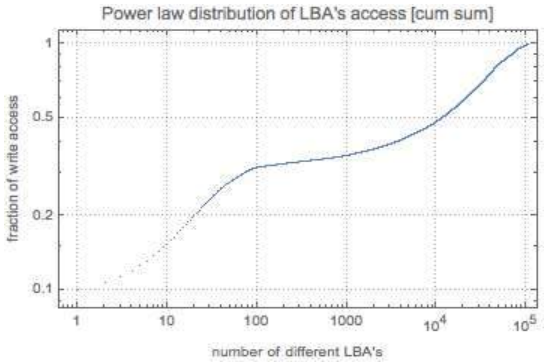

Fig. 3 File system 24h access distribution by LBA

THEORETICAL LIMITS OF MICROWAVE ASSISTED MAGNETIC RECORDING (MAMR) EFFECTIVE FIELD GRADIENT

Kirill RIVKIN[1] and Mourad BENAKLI[2]

1) Seagate Technology, Edina MN, USA, kirill.rivkin@seagate.com

2) Seagate Technology, Edina MN, USA, mourad.benakli@seagate.com

Microwave Assisted Magnetization Reversal (MAMR) is a phenomenon where RF frequency field is applied to magnetic material and by resonantly exciting large angle precessions succeeds in lowering its coercivity. There was a wealth of publications that offered a reasonably accurate theoretical prediction of the coercivity reduction expected from such an effect[1], for a uniform linearly or circularly polarized RF field with a constant amplitude and frequency. Most modern implementations of MAMR system however rely on using an STO (Spin Torque Oscillator) for the purpose of field generation, which produces a highly non-uniform field, and which is further combined with non-uniform low frequency or essentially DC field, generated by a magnetic write pole. It is possible to extend the theoretical treatment to such scenario[2], however with the emphasis on estimating the parameters enabling the maximum possible reduction of coercivity. The question arises whether this approach can realistically predict the optimal performance of a real system. The areal density is going to be determined by the best linear achievable for the selected track density, which is usually determined by the STO width. The gating factor is a jitter parameter, if this parameter exceeds about 15% of the total bit length, there is a substantial probability of an event where on both sides of the "bit" the transitions will be shifted by thrice the value of standard deviation, and therefore the bit will disappear altogether. At this point, the number of errors is bound to be very considerable. In zeroth order approximation, the jitter value, a, depends (Eq.1) on the media grain diameter D, write width W, dynamic gradient smearing and timing jitter, together represented as velocity of the media ϑ multiplied by time constant τ, switching field distribution SFD, and the effective gradient of the writer's field along the downtrack direction dH/dx, with what we assume to be a constant c.

$$a \sim \vartheta\tau + \sqrt{\frac{D}{W}}\sqrt{cD^2 + \left(\frac{SFD}{dH/dx}\right)^2} \tag{1}$$

When *a* is measured in nanometers, the peak linear density (in kilobits per inch) will then be close to:

$$KBPI = 25400\,\frac{0.15}{a} \tag{2}$$

For the maximum media anisotropy that can be written with a MAMR system, we previously deduced the following formula (Eq.3), under typical assumptions of a single spin model[2]:

$$H_k \approx H_{SW} + 5.8H_{RF}\left|\cos\Delta a\right| \tag{3},$$

where H_{SW} is the amplitude of low frequency or DC Stoner-Wolfarth effective field, and Δa is the difference between the angle at which the RF field is applied and the optimal value, which depends on the value of the H_{SW} angle. In case of three dimensional (with x and yz plane components[2]) STO generated RF field:

$$\mathbf{H}_{RF} = \mathrm{Re}\left(e^{-i2\pi\omega t}\cdot\left(\hat{y}H_{yz}\sin a - \hat{z}H_{yz}\cos a \pm i\hat{x}H_x\right)\right) \tag{4},$$

Kirill Rivkin

E-mail: kirill.rivkin@seagate.com

this can be further extended to yield the following equations for the maximum writeable anisotropy and corresponding optimal (maximum) operating frequency[2], where H_z is the component of DC field parallel to the anisotropy:

$$H_k \approx H_{SW} + \left|5.8\left(H_{yz}\left|\cos\Delta a\right| \pm 0.8H_x\right)\right| \quad (5)$$

$$\omega = 0.72\gamma(H_k - H_z) \quad (6).$$

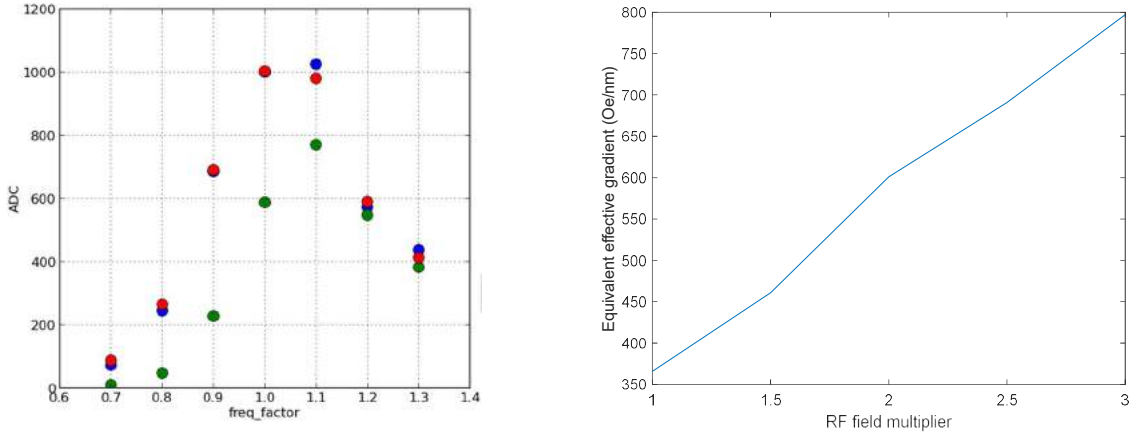

Figure 1. Modeled areal density for a single layer media with three writer designs, and equivalent effective field gradient versus the amplitude of the RF field generated by the STO.

The question is then whether these values actually define the optimal performance point of a real system, which includes non-uniform DC and STO fields. We performed an ADC estimation by modeling three writer designs (Fig. 1), with different gaps between the write pole and the trailing shield (determining the gradient of the DC field), and different write pole width. In each case we optimized the frequency, measuring the latter as a ration to the value provided by the (Eq.6) for the anisotropy value of (Eq.5). In our second run, we attempt to estimate the value of the effective gradient produced by the system, in a method similar to the one published[3] previously. We start by modeling an artificial conventional writer design with a constant gradient of the effective field, thus allowing us to produce a jitter number as a function of gradient. Then, we model a number of MAMR cases, including the one with relatively uniform DC field (i.e. very wide write gap), and the STO RF field multiplied by an arbitrary parameter. This allows us to consider the relationship between the RF field generated and the effective gradient (Fig. 2). Considering a single spin predicted the effective gradient of the order of 1500 Oe/nm for the multiplier of 1, one can see the value with a more realistic media to be just about 15% of the theoretical maximum. The difference can be shown to be driven by the modification of (Eq.1) that needs to be adopted to account for the MAMR physics. The effectiveness of conversion of the RF field to the effective gradient can then be manipulated by the MAMR system design.

REFERENCES:

1. S. Okamoto,I. Igarashi, N. Kikuchi and O. Kitakami, J. Appl. Phys. **107**, 123914 (2010).
2. K. Rivkin, M. Benakli, N. Tabat and H. Yin, J. Appl. Phys. **115**, 214312 (2014).
3. S. Greaves, T. Katayama, Y. Kanai, H. Muraoka, IEEE Trans. Magn. **51**, 2507 (2015).

DESIGN AND DEVELOPMENT OF SPIN-TORQUE-OSCILLATOR FOR MICROWAVE ASSISTED MAGNETIC RECORDING

H. SEPEHERI-AMIN[1], S. BOSU[1], C. ABERT[2], Y. SAKURABA[1], S. KASAI[1], M. HAYASHI[1], D. SUESS[2], and K. HONO[1]

1) Research Center for Magnetic and Spintronic Materials, National Institute for Materials Science, Tsukuba, Japan

2) Christian Doppler Laboratory - Advanced Magnetic Sensing and Materials, University of Vienna, 1090 Vienna, Austria

I. Introduction

Microwave assisted magnetic recording (MAMR) is a promising technology to overcome the stagnated areal density increase of hard disk drives. However, its most essential part, spin-torque-oscillator (STO), has not been realized. The STO device for MAMR should have a size of 30-40 nm and be able to generate large $\mu_0 H_{ac} > 0.1$ T with a frequency over 20 GHz at a small current density $J<1.0\times10^8$ A/cm^2 [1]. In addition, large oscillation cone angle of free layer is desired to maximize the $\mu_0 H_{ac}$. Such a device has not been realized experimentally due to the lack of fundamental understandings on the desired materials and structure of the STO. We have combined micromagnetic simulations to propose the desired material/design of STO for MAMR. The designed STO is developed and analyzed experimentally [2,3]. In this talk, we will first address how we developed STO device with size of below 40 nm that can oscillate OOP with frequency of over 20 GHz and large H_{ac} over 0.1 T. Thereafter, we will present desired material parameters to develop all-in-plane mag-flip STO.

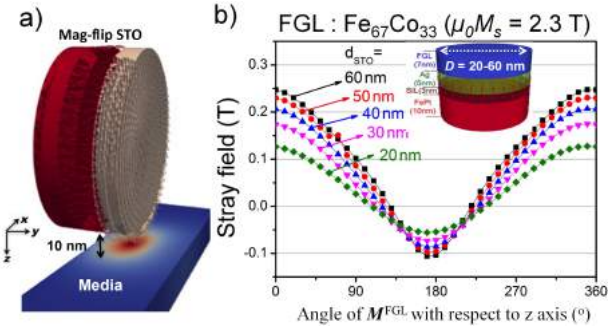

Figure 1: (a) Schematic illustration of STO and perpendicular recording media setup for ac field calculation $\mu_0 H_{ac}$, (b) calculated stray field distributions from STO's with different sizes, D = 20 to 60 nm.

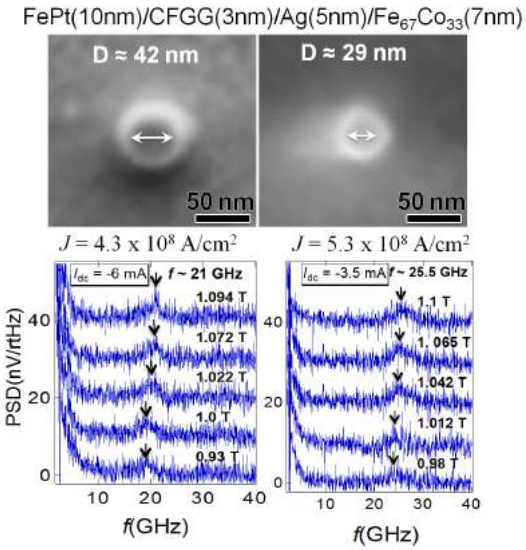

Figure 2: SEM image from two different STO device with $Co_2FeGa_{0.5}Ge_{0.5}$ SIL and $Fe_{67}Co_{33}$ FGL with diameters of 42 and 29 nm and corresponding rf power spectrum obtained at $J = 4.3 \times 10^8$ and 5.3×10^8 A/cm^2, respectively. Applied $\mu_0 H_{ext}$ at tilting angle $\theta_H \sim$ 4-5° are shown in each spectrum. $f \sim 21$ GHz and $f \sim 25.5$ GHz has been observed for $D = 42$ nm and $D = 29$ nm, respectively at $\mu_0 H_{ext} \sim 1.1$ T.

II. Experimental procedure and purpose of the study

We employed a micromagnetic simulation code, *magnum.fe*, which solves the coupled dynamics of magnetization (***m***) and spin accumulations (***s***) simultaneously using the time dependent 3D spin diffusion equations and the Landau-Lifshitz-Gilbert (LLG) equation, respectively [4]. This will allow us to directly simulate the effect of locally varying spin accumulations on the magnetization dynamics. We first designed the required materials for a mag-flip STO device. Mag-flip STO device consists of out-of-plane magnetized spin injecting layer (SIL) and in-plane magnetized field generating layer (FGL). We have shown that use of high spin polarized materials such as half metallic Heusler alloys in SIL is necessary to reduce bias current density required for oscillation of FGL [2]. However, developed device had large size of ~ 60nm, not suitable for MAMR. In this work, we designed the STO that can produce large H_{ac} with size of smaller than 40nm. The designed STO device was developed experimentally and oscillation behavior was studied by measuring the power spectra using a spectrum analyzer for the frequency range from 1 to 40 GHz. In order to reduce total thickness of the STO

H. Sepehri-Amin
E-mail: h.sepehriamin@nims.go.jp
tel: +81-29-859-2739

device, we also designed materials for another type of STO device, all in-plane mag-flip STO device, consisting in-plane magnetization SIL and FGL, that can generate large $\mu_0 H_{ac}$ with a frequency over 20 GHz in a small bias current density.

III. Results and discussion

Figure 1 shows calculated stray field produced from an STO device located 10nm far from center of perpendicular recording media. The STO device has $Fe_{67}Co_{33}$ as FGL with $\mu_0 M_s$ ~ 2.3 T. The stray field from this STO is shown in Fig. 1(b) for diameters of ~ 20 to 60 nm. $\mu_0 H_{ac}$ varies from 0.12 T for D ~ 20 nm to 0.25 T for D ~ 60 nm when the angle of OPP mode is considered its maximum, i.e, φ = 90°. Therefore, as of requirement for MAMR, $Fe_{67}Co_{33}$ FGL with even D ~30 to 40 nm could generate substantially large $\mu_0 H_{ac}$ ~ 0.15 to 0.2 T. Figure 2 shows SEM images of developed STO devices with diameters of ~42 and 29 nm. These mag-flip STO contain $Co_2FeGa_{0.5}Ge_{0.5}$ (CFGG) SIL to reduce the bias current density required for oscillation [2]. $Fe_{67}Co_{33}$ was used as FGL. The rf power spectrums obtained at applied external magnetic fields of ~1.0 T, shown in Fig. 2, indicates that these devices can oscillate with f ~ 21 and 25.5 GHz around $\mu_0 H_{ext}$ ~ 1.1 T for D~ 42 and 29 nm, respectively. However, required current density for these oscillations *are* still higher than the requirements for practical MAMR, which could be reduced by improving the chemical ordering as well as spin polarization of SIL. Nevertheless, increase of spin polarization of 3nm thick SIL is one challenge. Recently, Zhu et al. proposed by all-in-plane mag-flip STO, one can reduce the critical current density for oscillation [5]. We designed the optimum materials parameters for all-in-plane mag-flip STO device that can result in reduced current density for out-of-plane oscillation. Figure 3 (a) shows our designed all-in-plane mag-flip STO device consisting a thin SIL and 14nm thick FGL. Electrons are pumped from bottom to top and due to the reflection of electrons from FGL/Ag, the SIL switches and transmitted down-spin electrons lead to oscillation of FGL. Unlike the conventional mag-flip STO device, we found that the spin polarization of FGL play very important role in J_c required for switching of SIL and OOP oscillation of FGL. As shown in Fig. 3, by increase of spin polarization of FGL, J_c can be substantially reduced. The underlying mechanism is shown in Fig. 4. Fig. 4 (a) shows the STO device and 3D spin accumulation in Z direction in the model when all the layers are magnetized OOP under 1 T external magnetic field. Fig. 4 (b) shows distribution of $\boldsymbol{S}_z$ from SIL toward FGL for different spin polarization of FGL. It was found that by increase of β^{FGL}, we get more reflected down spins from FGL/Ag interface that will be beneficial for switching of SIL and OOP oscillation of FGL, resulting in smaller J_c. In this talk, we will introduce optimum material parameters for SIL and FGL that can minimize bias current density for OOP oscillation of FGL. In addition, we will introduce our recent experimental results on development of all-in-plane mag-flip STO device.

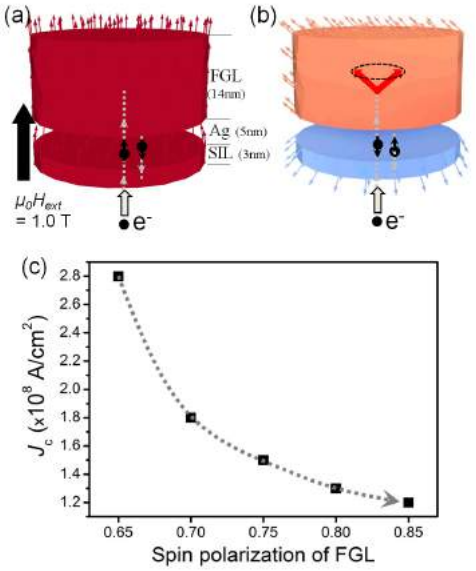

Figure 3: (a) and (b) Schematic illustration of all-in-plane mag-flip STO and OOP oscillation of FGL while magnetization of SIL is switched, (b) calculated critical current density for switching of SIL and OOP oscillation of FGL versus spin polarization of FGL.

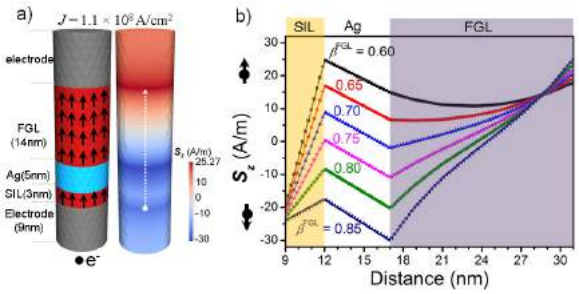

Figure 4: (a) All-in-plane mag-flip STO device magnetized OOP upon applying 1T external magnetic field and spin accumulation in Z direction ($\boldsymbol{S}_z$) for J = 1.1×10^8 A/cm²(b) calculated line contour of $\boldsymbol{S_Z}$ from SIL toward FGL for different spin polarization of FGL.

Acknowledgement: This work is in-part supported by ASRC MAMR project and GrantinAids for Young Scientific Research B (17K14802).

References: [1] Takeo A. *et al*., Intermag Conference 2014 (AD-02). [2] Bosu S. *et al.,* Appl. Phys. Lett. **108**,072403 (2016). [3] Bosu S. *et al.,* Appl. Phys. Lett. **108**,072403 (2017). [4] Abert C. *et al*., Sci. Rep. **5**, 14855 (2015). [5] Zhu J. *et al.,* MMM-Intermag 2016, San Diego.

3D MAGNETIC RECORDING BASED ON MAMR TECHNOLOGY

R. SATO, H. SUTO, T. KANAO, T. NAGASAWA, and K. MIZUSHIMA
Corporate Research & Development Center, Toshiba Corporation, Kawasaki, Japan.
riz.sato@toshiba.co.jp

I. BACKGROUND

Conventionally, hard disk drives (HDDs) store data in 2D pattern of the magnetization direction in magnetic recording media. To increase the recording density beyond the limit of 2D, 3D magnetic recording that uses a media with multiple recording layers will be required. In response to this situation, we have proposed and been working on 3D magnetic recording based on ferromagnetic resonance (FMR) excitation in a microwave field [1-6]. When each of multiple recording layers is designed to have a different FMR frequency, FMR excitation can be induced in a specific recording layer by tuning the frequency of the applied microwave field, and this FMR excitation can be utilized for layer-selective read/write operations. Our 3D magnetic recording is compatible with the structure of conventional HDDs consisting of a spinning recording medium and a flying head element. The major challenge, however, is how to generate a microwave field from a head element. This issue can be solved by employing microwave-assisted magnetic recording (MAMR) technology. MAMR uses a microwave field in inducing FMR excitation of the media magnetization to write in a high-anisotropy media material and has been extensively studied as a candidate writing method for next-generation 2D magnetic recording.

II. LAYER-SELECTIVE WRITING BASED ON MAMR

Figure 1(a) shows a schematic of layer-selective writing based on MAMR technology. A write head element has a spin-torque oscillator (STO) integrated in the gap between the write pole and the trailing shield. By applying a current to the STO, the STO magnetization oscillates and generates a microwave field. Note that this microwave field is a stray field from the oscillating STO magnetization and confined near the STO. No electromagnetic radiation is involved. Each recording layer consists of antiferromagnetically coupled (AFC) two magnetic layers (soft layer and hard layer) having a different perpendicular magnetic anisotropy (PMA). The AFC strength and PMAs are designed as follows. The soft layer has a PMA low enough to realize a spontaneous antiferromagnetic configuration in the remanent state, and the hard layer has a PMA high enough to ensure thermal stability. By employing the AFC structure, the dipolar interaction between the recording layers can be suppressed. Switching of the hard layer is induced by the head field and microwave field. After that, switching of the soft layer occurs spontaneously to make an AFC configuration. Switching behavior in a microwave field has been studied, and it has been shown that switching field decreases almost linearly as microwave-field frequency increases and abruptly increases at a critical frequency. Figure 1(b) schematically shows switching condition when the hard layer of three recording layer has a different FMR frequency, which suggests that layer-selective switching is possible by tuning microwave-field frequency.

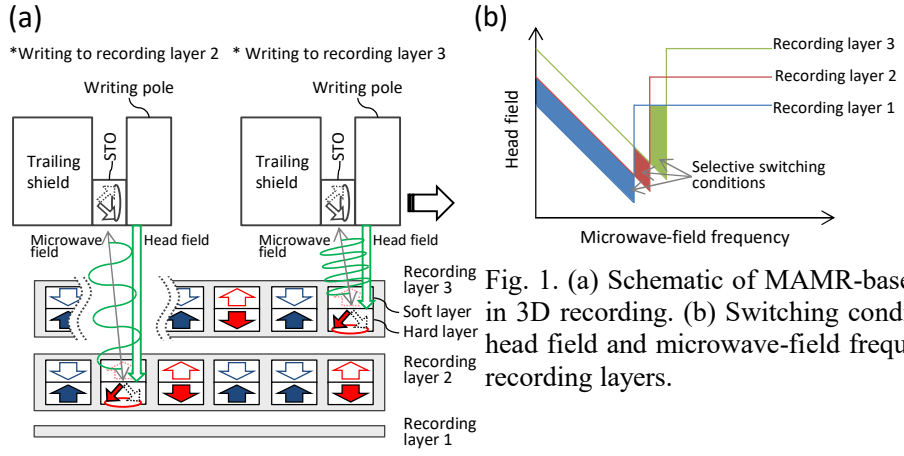

Fig. 1. (a) Schematic of MAMR-based layer-selective writing in 3D recording. (b) Switching condition as a function of the head field and microwave-field frequency in the case of three recording layers.

riz.sato@toshiba.co.jp

III. READING BASED ON INTERACTION BETWEEN MEDIA MAGNETIZAION AND STO

Figure 2(a) shows a schematic of reading based on interaction between media magnetization and an STO. When the STO comes close to a recording magnetization (RM) in the media, they interact through microwave stray field, and magnetization oscillation is resonantly excited in the RM when the oscillation frequency of the STO is close to the FMR frequency of the soft layer. Different from the case of writing, this excitation does not induce switching but leads to a change in magnetization oscillation of the STO, which is used to read magnetization direction in RM. Because this method is based on FMR excitation and does not require a static stray field, it is applicable in 3D magnetic recording, and a recording layer can be selected by FMR frequency. Here, to investigate basic aspects of this method, readout from a sequence of single-layer 6 RM with staggered magnetization configuration is demonstrated by using a micromagnetic simulation. The oscillation frequency of the STO is set near to the FMR frequency of the soft layer with downward magnetization direction (down state). Figure 2(b) shows y-components of magnetizations as a function of time. That of the STO corresponds to a readout signal since the magnetization of the STO fixed layer is directed in y-direction. When the STO comes near to RM in down state, the magnetization oscillation of RM is excited, and the amplitude of STO oscillation is decreased owing to increased effective damping. On the other hand, when the STO is near RM in up state, the magnetization of RM is excited little, and the STO oscillation amplitude recovers. The changes of the STO oscillation occur in a few nanoseconds. By detecting these differences of oscillation change, the magnetization direction of RM can be distinguished.

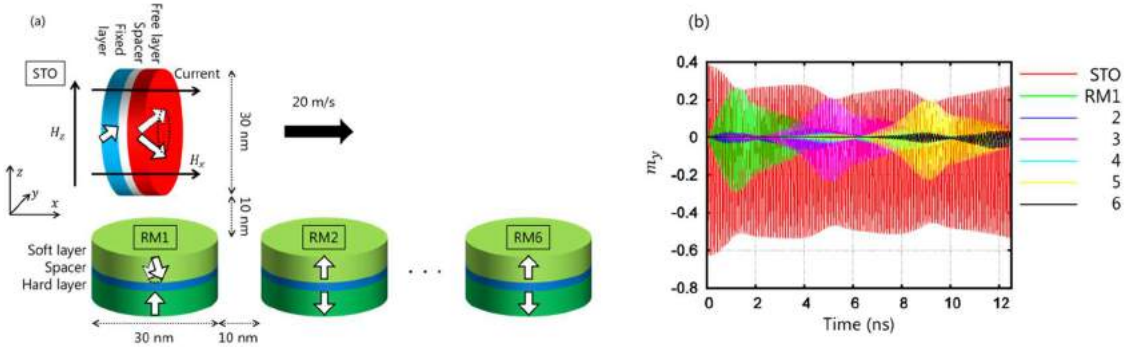

Fig. 2 (a) Schematic of reading based on interaction between recording magnetization (RM) and spin-torque oscillator (STO). At 0 ns, the STO is placed with its right surface at 10 nm left from the left edge of the first RM and moves rightward at a velocity of 20 m/s. (b) y-components of magnetizations as a function of time.

REFERENCES

[1] T. Yang, H. Suto, T. Nagasawa, K. Kudo, K. Mizushima, and R. Sato, “Readout method from antiferromagnetically coupled perpendicular magnetic recording media using ferromagnetic resonance”, J. Appl. Phys. **114**, 213901 (2013).

[2] H. Suto, T. Nagasawa, K. Kudo, K. Mizushima, and R. Sato, ”Nanoscale layer-selective readout of magnetization direction from a magnetic multilayer using a spin-torque oscillator”, Nanotechnology **25**, 245501 (2014).

[3] K. Kudo, H. Suto, T. Nagasawa, K. Mizushima, and R. Sato, ”Resonant magnetization switching induced by spin-torque-driven oscillations and its use in three-dimensional magnetic storage applications”, Appl. Phys. Express **8**, 103001 (2015).

[4] H. Suto, T. Nagasawa, K. Kudo, T. Kanao, K. Mizushima, and R. Sato, “Layer-selective Switching of a double-layer perpendicular magnetic nanodot using microwave assistance”, Phys. Rev. Appl. **5**, 014003 (2016).

[5] H. Suto, K. Kudo, T. Nagasawa, T. Kanao, K. Mizushima, and R. Sato, “Three-dimensional magnetic recording using ferromagnetic resonance”, Jpn. J. Appl. Phys. **55**, 07MA01 (2016).

[6] T. Kanao, H. Suto, K. Kudo, T. Nagasawa, M. Yamagishi, K. Mizushima, and R. Sato, “Magnetization dynamics of resonantly interacting spin-torque oscillator and recording media: readout method using magnetic resonance” 61st Conference on Magn. Magn. Mater. (MMM), New Orleans, 2016.

This work is supported by Strategic Promotion of Innovative Research and Development from Japan Science and Technology Agency, JST.

ANTI-FERROMAGNETICALLY COUPLED MEDIA FOR MICROWAVE ASSISTED MAGNETIC RECORDING

Simon GREAVES[1], Yasushi KANAI[2] and Hiroaki MURAOKA[1]
1) RIEC, Tohoku University, Sendai, Japan, simon@riec.tohoku.ac.jp
2) IEE, Niigata Institute of Technology, Kashiwazaki, Japan, kanai@iee.niit.ac.jp

I. INTRODUCTION

Microwave-assisted magnetic recording (MAMR) technology can increase the effective head field gradient and reduce the switching field of a recording medium [1]. It may also allow selective recording on multiple-layer media [2]. In a MAMR system a high frequency (HF) field is generated by a spin-torque oscillator (STO). One issue is the dependence of the optimum HF field frequency on the magnetic state of the medium, e.g. the optimum HF field frequency may differ depending on whether the medium is AC-demagnetised or saturated. This behaviour originates in the magnetostatic field interactions between media grains. In this talk we present the results of simulations of anti-ferromagnetically coupled (AFC) media, in which such interactions can be reduced.

II. RESULTS

AFC and single layer (SL) perpendicular media were compared. Both media had an 11 nm thick recording layer; in the AFC media the recording layer had a 4 nm hard / 1 nm Ru / 6 nm soft structure. The non-magnetic Ru layer provided anti-ferromagnetic exchange coupling of -1 erg/cm^2 between the hard and soft layers [3]. The soft layer had M_s of 400 emu/cm^3 whilst the hard layer and SL media M_s was 600 emu/cm^3. The soft layer K_u was 2×10^6 erg/cm^3 whilst the hard layer K_u and SL media K_u was varied. Fig. 1 shows an example of MH loops for SL and AFC media with an average grain size of 8 nm and an average grain pitch of 9 nm. In zero field the remanence of the AFC medium was almost zero due to the anti-parallel alignment of the magnetisation in the hard and soft layers. The remanence was not exactly zero due to distributions of M_s among grains. The coercivity of the SL medium and the average switching field of the hard layer of the AFC medium was about 20 kOe in both media.

Fig. 2 shows the SNR of 635 kfci tracks written on media with various K_u using a range of HF field frequencies. Peaks in the SNR were clear in some cases but, particularly in the case of high K_u AFC media, the optimum HF field frequency extended over a wide range. As K_u increased the peak SNR decreased and the optimum HF field frequency increased. The maximum SNR gain over a non-MAMR system ranged from 8-10 dB when recording on AFC media to 9-16 dB when using SL media.

Fig. 3 shows the SNR versus linear density for two SL and two AFC media. Significant differences between the two media can be seen. The SNR of SL media decreased linearly with increasing linear density, dropping below zero dB at around 1450 kfci. The SNR of AFC media was much less sensitive to linear density and although the SNR was lower at 635 kfci, for linear densities exceeding 1200 kfci the AFC media had higher SNR. The AFC media had a small output signal at low linear density, about 1/7th that of the SL media at 635 kfci. However, the AFC output signal (and noise) were almost independent of linear density, whereas the SL media output signal decreased rapidly with linear density. Head output waveforms at 1693 kfci are shown in fig. 4. The waveforms are the average of five tracks, with the average output signals of the AFC and SL media indicated by the horizontal lines. The SL media output signal was about 1.7 times that of the AFC media, but the noise was much higher. Fluctuations in the AFC media waveform were much smaller than in the SL waveform, resulting in higher SNR for the AFC media.

Although the remanence of the AFC media was close to zero the read head was still able to detect a small signal from the written tracks. The higher M_s hard layer was nearest to the read head and spacing loss reduced the contribution to the signal from the soft layer. By reducing the thickness of the AFC media it may be possible to introduce a second recording layer and this will be explored in the talk,

Simon Greaves
RIEC, Tohoku University,
Katahira 2-1-1, Aoba ku,
Sendai, 980-8577
E-mail: simon@riec.tohoku.ac.jp
Tel: +81-22-217-5458

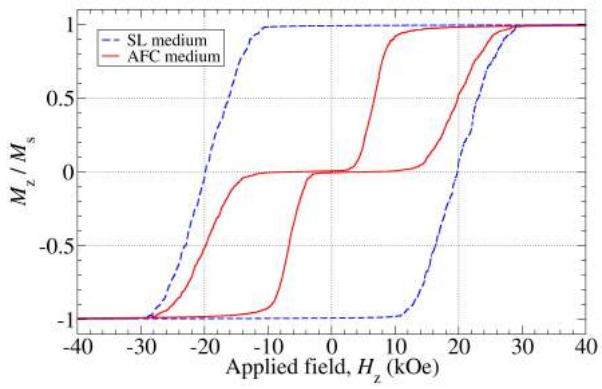

Fig. 1 Hysteresis loops of single layer (SL) and AFC media. K_u hard / SL = 8×10^6 erg/cm^3.

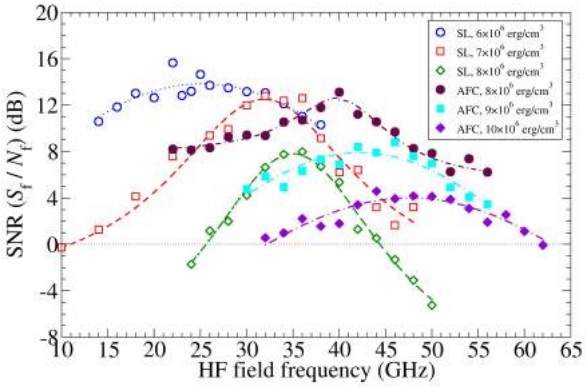

Fig. 2 SNR of 635 kfci tracks vs. HF field frequency and media K_u.

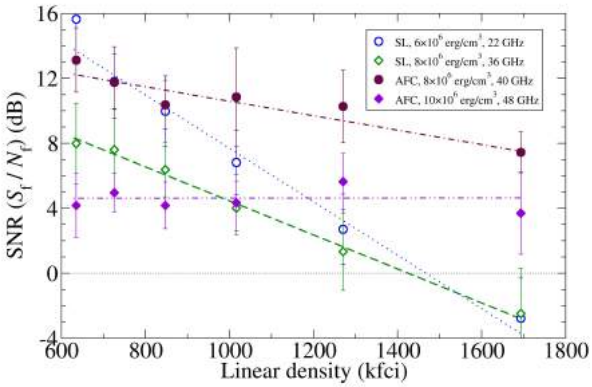

Fig. 3 SNR vs. linear density for SL and AFC media with various K_u.

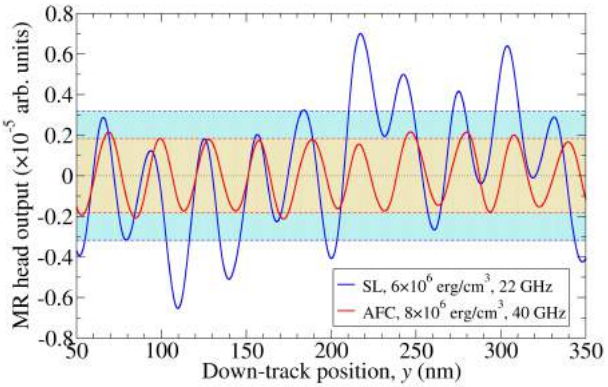

Fig. 4 MR head output signal for 1693 kfci tracks written on SL and AFC media.

REFERENCES

[1] J. G. Zhu and Y. Wang, IEEE Trans. Magn. 46, p751, (2010).
[2] S. J. Greaves, Y. Kanai and H. Muraoka, IEEE Trans. Magn. 53, 3000510, (2017).
[3] P. J. H. Bloemen, H. W. van Kesteren, H. J. M. Swagten and W. J. M. de Jonge, Phys. Rev. B. 50, p13505, (1994).

DEVELOPMENT OF MICROWAVE INTERFEROMETER BASED ULTRA-HIGH SENSITIVITY FERROMAGNETIC RESONANCE MEASUREMENT APPARATUS FOR CHARACTERIZING DYNAMICAL PROPERTIES OF MAGNETIC NANODOT

S. TAMARU[1]*, H. KUBOTA[1], and A. FUKUSHIMA[1]

1) National Institute of Advanced Industrial Science and Technology, Spintronics Research Center, Tsukuba, Ibaraki, 305-8568, Japan,

*shingo.tamaru@aist.go.jp

I. INTRODUCTION

Microwave Assisted Magnetic Recording (MAMR) technology is one of the promising candidates for increasing the recording densities of hard disk drives (HDDs). In the MAMR technology, a spin torque oscillator (STO) embedded right next to the write pole generates a microwave field, which is applied to the storage layer of the HDD media to temporally decrease the coercivity during the magnetization switching process. Because this technology takes advantage of cooperative phenomena between high frequency magnetic fields and spin dynamics, it is crucial to thoroughly characterize dynamical properties of both the STO and magnetic storage layer. The high frequency characterization of the STO is particularly challenging due to its small dimension and multilayer structure that complicate the behavior at high frequencies, thus making it difficult to come up with a clear understanding of the results obtained by the standard oscillation spectrum measurement. Therefore, it is desirable to have other means for measuring high frequency dynamics of a magnetic nanostructure as a complementary measurement technique to independently characterize the magnetic layer of interest in the STO structure. For this purpose, we have explored a microwave interferometer based ferromagnetic resonance (FMR) measurement technique. As an initial feasibility study, a vector network analyzer ferromagnetic resonance (VNA-FMR) apparatus combined with a Mach-Zehnder type microwave interferometer was built, and its FMR sensitivity was examined. This combination successfully demonstrated an enhancement of the FMR sensitivity by as large as more than 40 dB compared with that of the standard VNA-FMR, with which we could clearly detect a FMR signal on as small as 100 nm diameter and 5 nm thick CoFeB single nanodot. We named this technique as Interferometric FMR (I-FMR) [1].

While the first feasibility study of the I-FMR technique showed a very significant sensitivity enhancement, the I-FMR apparatus itself was not ready for use as a practical characterization tool, as it required a manual adjustment of the microwave interferometer every time when the frequency is changed, which is a very tedious and time consuming step, thus seriously spoiling the usability of the I-FMR. In order to overcome this difficulty, we developed a second version of the I-FMR apparatus, in which the phase shifter and variable attenuator are motor controlled, thus the microwave interferometer can now be automatically adjusted without human intervention.

II. OVERVIEW OF THE NEW I-FMR APPARATUS

Fig. 1 shows the block diagram of the I-FMR technique. The stimulus signal generated by the VNA's built-in oscillator is split into two paths. The stimulus signal propagating along one path is coupled into a coplanar waveguide (CPW), on which a magnetic dot is fabricated. This CPW is placed in the gap of an electromagnet that can generate a bias magnetic field H_B of up to 21 kOe as well as a low frequency modulation field of about a few tens of Oe. The stimulus propagating along the other path goes through a phase shifter (PS) and continuously variable attenuator (VA). These two stimuli are combined by a power combiner (PC), which is a reversely connected Wilkinson power divider. The PS and VA are adjusted such that these two stimuli have the same amplitude and 180° opposite phase. Therefore, these two stimuli destructively interfere with each other so no stimulus signal should exit at the PC output under the ideal condition when no magnetic activity is excited in the magnetic dot. When a H_B satisfying the FMR

Shingo Tamaru
E-mail: shingo.tamaru@aist.go.jp
tel: +81-29-861-3007

resonant condition is applied, FMR is excited in the magnetic dot, absorbing the stimulus power, thus changing the transmission property of the CPW. This breaks the balance between the two stimuli, so the difference corresponding to the FMR signal exits the PC, which is amplified by a low noise amplifier and eventually detected by the VNA receiver.

The most important feature of the second version of the I-FMR apparatus is that a high precision stepping motor is attached to both the PS and VA, allowing the host computer to remotely control these two components. Using this, we implemented a program to automatically adjust the interferometer by iteratively adjusting the PS and VA such that the leakage of the stimulus is minimized.

Fig. 2 shows the comparison of the FMR spectra taken with the conventional VNA-FMR, first (manual adjustment) and second (automatic adjustment) versions of the I-FMR apparatuses. This figure shows that the sensitivities of the I-FMR for the first and second versions are about 41 dB and 36 dB higher than that of the conventional VNA-FMR. The second version of I-FMR shows about 5 dB lower sensitivity than the first version, which is considered to be caused by the thin flexible cables directly attached to the probes that attenuate the microwave stimulus. The development of the second version of the I-FMR apparatus is in the final phase, meaning that it is undergoing the system optimization to maximize the sensitivity, thus expected to be fully up and running shortly. Also, a new batch of samples have just been fabricated with an improved microfabrication process. The new samples are expected to solve the problem with the first batch of samples that had some redeposited magnetic residue during the dry etching process, which were also detected by the I-FMR measurement, thus obscuring the FMR signal of interest.

In this talk, the features and capabilities of the new I-FMR apparatus are presented, as well as some new measurement results taken on the new batch of sample to demonstrate the powerfulness of this new tool for characterizing magnetization dynamics of magnetic nanostructures.

REFERENCES

1) S. Tamaru et al., " Ultrahigh Sensitivity Ferromagnetic Resonance Measurement Based on Microwave Interferometer", *IEEE Magn. Lett.,* (5) 1-4, (2014).

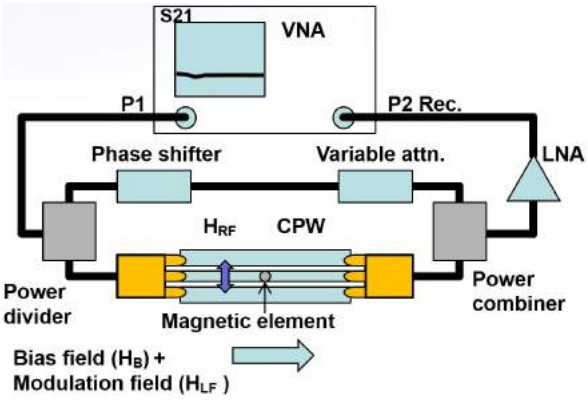

Fig. 1, Block diagram of the I-FMR apparatus

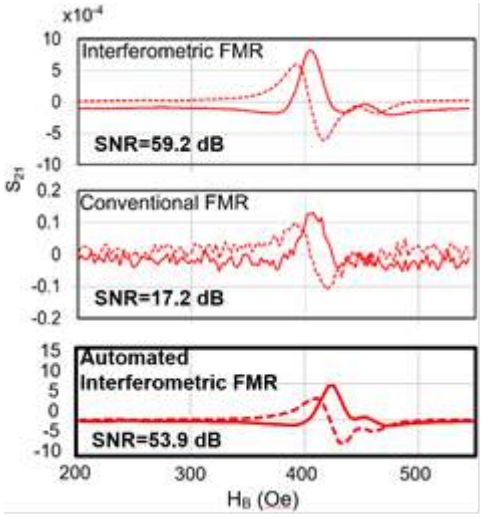

Fig. 2, Comparison of the FMR spectrum measured on a 800 nm diameter and 5 nm thick CoFeB single nanodot taken by the conventional VNA-FMR, first and second versions of I-FMR.

TIME AND SPATIALLY RESOLVED XMCD-FMR MEASUREMENT ON A Co/Pt MULTILAYER DOT EXCITED BY RF MAGNETIC FIELD IN THE GHz REGIME

Nobuaki KIKUCHI[1], Hitoshi OSAWA[2], Motohiro SUZUKI[2], Osamu KITAKAMI[1]

1) IMRAM Tohoku University, Sendai, Japan, kikuchin@tagen.tohoku.ac.jp

2) Japan Synchrotron Radiation Research Institute (JASRI), Sayo, Japan

I. INTRODUCTION

Understanding of magnetization dynamics in nanostructures is a crucial issue for further development of magnetic devices. X-ray magnetic circular dichroism (XMCD) using synchrotron lights has advantages against conventional magneto-optic Kerr effect (MOKE), which is widely used to perform time and spatial resolved magnetic measurement. One major advantage is that XMCD can realize element resolved measurement by selecting proper X-ray energy. Another advantage is its shorter wavelength allowing to focus into spot with well below 100 nm. Synchrotron X-ray is suitable also for time resolved measurement because the lights are formed as pulses with typical duration below 100 ps. In this study, we have performed time and spatial resolved XMCD ferromagnetic resonance (FMR) measurement on Co/Pt multilayer dot previously studied by the anomalous Hall effect FMR [1]. Magnetization behavior under rf field with GHz frequency was studied by detecting MCD of polarized Pt layer at the interface with hard X-ray.

II. SAMPLE DETAILS

A gold line of 3 μm in width and 100 nm in thickness was fabricated on a MgO(100) substrate for rf field application. After depositing a SiO_2 layer of 100 nm in thickness for insulation, a Co/Pt multilayer with structure of MgO sub./Ta(0.5)/Pt(1)/Ru(24)/$[Pt(0.5)/Co(1.3)]_4$/Pt(0.5)/Ru(2) was deposited by magnetron sputtering. The numbers in brackets are thickness of each layer in nanometers. The effective perpendicular anisotropy of continuous film was evaluated to be -1.2 kOe. The multilayer was patterned into a circular dot of 2.6 μm in designed diameter by electron beam lithography and ion etching. The dots were located on the gold line therefore the rf magnetic field was applied parallel to the film plane. The sample was mounted on a PTFE printed circuit borad and connected to a rf signal source through SMA connectors and cables. Co/Pt dots with electrodes for anomalous Hall effect (AHE) was also fabricated on the same substrates for comparison.

III. XMCD MEASUREMENT

XMCD measurements was carried out at the hard X-ray beam line BL39XU of SPring-8 [2]. The energy of X-ray was selected to be 11.57 keV of Pt-L_3 edge. X-ray absorption signals were measured by fluorescence mode using a silicon drift detector (SDD). Since the excitation depth of the X-ray in the energy range reaches a few micrometers, the measured signal is averaged one from all Pt layers including the underlayer. The X-ray incident angle was set to be 60 degrees from the film normal to be able to detect in-plane magnetization component by XMCD. Dc magnetic field was applied along film normal using a permanent magnet to saturate magnetization perpendicularly. The dc field strength was set to about 2 kOe so that FMR frequency is in the frequency range of 2-4 GHz. Figure 1 describes the geometry of X-rays, rf and dc fields in this study. The X-ray beam was focused into a spot with dimension of 100 × 250 nm^2 defined by full width at half maximum (FWMH) by using a the Kirkpatrick-Baez (KB) mirror. The duration of X-ray pulse was 60 ps in FWMH. The repetition frequency of X-ray pulse was set to 208 kHz by inserting a chopper [3]. The rf field were applied as pulse trains so that magnetization was reset before each rf field pulse application. The pulse duration and the repetition rate were 100 ns and 208 kHz, respectively. Time and position dependent XMCD measurement were carried out by performing one dimensional scan along z-axis shown in Fig. 1 and

Nobuaki KIKUCHI
E-mail: kikuchin@tagen.tohoku.ac.jp
tel: +81-22-2175359

varying delay of rf field against X-ray pulse. Figure 2 shows relative XMCD signal as functions of delay time and z-axis position measured (a) before applying rf field and (b) 4 ns after applying rf field of 2.5 GHz in frequency. The scanning steps of delay and position are 50 ps and 100 nm, respectively. Before applying rf field, XMCD contrast is uniform in the dot and no time dependence is observed. By applying rf field, clear periodic pattern corresponding to rf field frequency appears against delay. The obtained XMCD contrast does not show significant position dependence. This result indicates uniform precession motion of magnetization was excited over a whole dot within 4 ns.

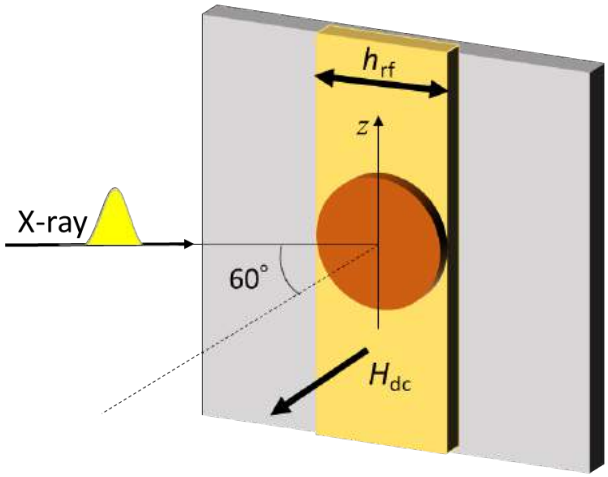

Fig. 1 The geometry of experimental set-up

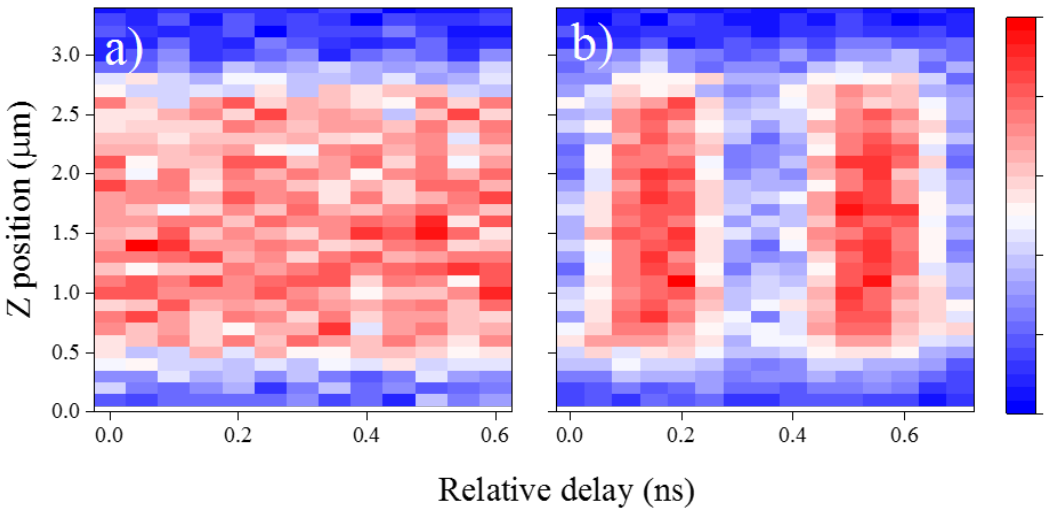

Fig. 2 Relative XMCD signal as functions of position and delay measured (a) before applying rf field and (b) 4 ns after applying rf field of 2.5 GHz in frequency.

REFERENCES

1) N. Kikuchi *et al*., "Quantized spin waves in single Co/Pt dots detected by anomalous Hall effect based ferromagnetic resonance", Applied Physics Letters 105, 242405-1~4 (2014).
2) M. Suzuki *et al*., "A hard X-ray nanospectroscopy station at SPring-8 BL39XU", Journal of Physics: Conference Series 430, 012017~1-4 (2013).
3) H. Osawa *et al*., "Development of high-repetition-rate X-ray chopper system for time-resolved measurements with synchrotron radiation", Japanese Journal of Applied Physics 56, 048001-1~3 (2017)

VOLTAGE-CONTROL SPINTRONICS MEMORY HAVING POTENTIALS FOR HIGH-DENSITY AND HIGH-SPEED APPLICATIONS

H. YODA, N. SHIMOMURA, Y. OHSAWA, Y. SAITO, Y. KATO, T. INOKUCHI, S. SHIROTORI, K. KOI, M. SHIMIZU, H. SUGIYAMA, S. OIKAWA, B. ALTANSARGAI, M. ISHIKAWA, Y. KAMIGUCHI, K. IKEGAMI, and A. Kurobe

Corporate R & D Center, Toshiba Corporation, Kawasaki, Japan

I. INTRODUCTION

In order to reduce energy consumption of memory hierarchy, several non-volatile memories have been developed. However all of the candidates consume more energy in active modes than save in stand-by modes for busy mobile applications. Therefore, usage of non-volatile memories has been limited to storage of data. This is a historical dilemma that all the candidates have not solved.

In this paper, developments and performances of voltage-control spintronics memories (VoCSM) cell are explained and a potential of reduction in writing-charge, Q_w is discussed.

II. FUNDAMENTAL WRITING PROPERTY OF THE VoCSM CELL

In its writing mode, voltage is applied to the top-electrodes of the MTJs to control the switching energy-barrier by changing surface perpendicular anisotropy, K_s of the storage-layer due to VCMA-effect. The write-current, I_w flows in the bottom spin-Hall electrode made of 5d heavy metal such as Ta to write data due to spin-Hall effect.

The fundamental writing property of the cell is shown in Fig.1. In case of the CoFeB/MgO/ CoFeB/Ta junction, positive voltage lowers K_s and the switching current-density, J_{csw}, increases. On the contrary, negative voltage heightens K_s and J_{csw} decreases as shown in Fig.1. This properties is the necessity for VoCSM cell must possess.

III. DEMONSTRATION OF VoCSMS

(a) High-density VoCSM

The high-density VoCSM memory architecture employs a string of MTJs as memory cells as shown in Fig. 1 (a). The string consists of eight MTJs (bits) located on the bottom-electrode.

In writing-mode, a set of two writing-currents, I_w, flow in the electrode to apply spin-Hall torque while voltage is applied to the bits to control the switching energy-barrier. In order to select bits to write data, negative voltage referred to as activating voltage (V_a) is applied, while positive voltage referred to as deactivation voltage (V_{da}) is applied to non-selected bits that heightens the switching energy-barrier to avoid write-disturbance.

In reading mode, positive voltage is applied to avoid read-disturbance.

The write error-rate curve is shown in Fig.2 (b). The curves are the typical deterministic spin-transfer-torque curve. Selective-writing scheme was applied to MTJs and the results are shown in Fig.2 (c). There observed no writing-errors for total of 160 sets of writing-pulses. This indicates that selective-writing scheme does work.

(b) High-speed VoCSM

The high-speed VoCSM architecture employs a string-structure of two MTJs as shown in Fig.3 (a).

In its reading mode, differential reading is employed to compensate relatively large RC delay of the order of nsec. due to large resistance of MTJs.

In its writing mode, acceleration voltage, V_a , is applied to the MTJs to accelerate switching speed.

The write-currents, I_w flow in the bottom-electrode at the same timing in opposite directions for the two MTJs to be applied spin-torques in opposite directions. Then, magnetizations of the two MTJs switch to opposite polarities with each other. The writing scheme is called complementary flash-writing. Fig. 3 (b) shows the results of the complementary flash-writing with V_a=−0.8V. The flash-writing does work.

I_w pulsewidth dependences of I_{csw} are shown for both conventional spin-Hall writing and VoCSM in Fig.3 (c). If the same write current-density, J_w, for example J_w= 0.6 J_{co} is fed for the both cases, tconventional spin-Hall writing may have switching speed of 1000nsec. but VoCSM may have switching speed of 10nsec. A potential to have ultra-high-speed writing of the VoCSM is proved

IV. DISCUSSION ON REDUCTION IN Q_w

I_{csw} scales with the junction area as shown in Fig.4. All we should do to lower I_w is to scale the area, as

HIROAKI YODA
E-mail: hk.yoda@toshiba.co.jp
tel: +81-44-549-2130

far as the switching energy-barrier is bigger than the retention energy-barrier, to achieve small Q_w.

V. CONCLUSION

The VoCSMs were proved to work and the I_w scales with the junction area. Therefore, it is concluded that the VoCSMs have a potential to solve the historical dilemma.

ACKNOWLEDGMENT

This work was partly supported by the ImPACT Program of the Council for Science, Technology and Innovation (Cabinet Office, Government of Japan). We acknowledge Prof. M.Sahashi for guidance of this research.

REFERENCES

1) H. Yoda, et al., "Voltage-Control Spintronics Memory (VoCSM) Having Potentials of Ultra-Low Energy-Consumption and High-Density," *Digests of 62th IEDM*, 27.6 (2016)
2) H. Yoda, et al., "High-Speed Voltage-Control Spintronics Memory," to be presented at IMW 2017 in Monterey CA,USA
3) S. Shirotori, et al., "Voltage-Control Spintronics Memory (VoCSM) with a self-aligned heavy-metal electrode," presented at INTERMAG 2017 Europe in Dublin, Ireland

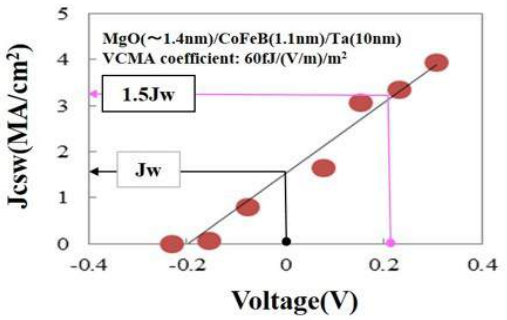

Figure 1. Voltage dependence of Critical switching current density of a VoCSM cell

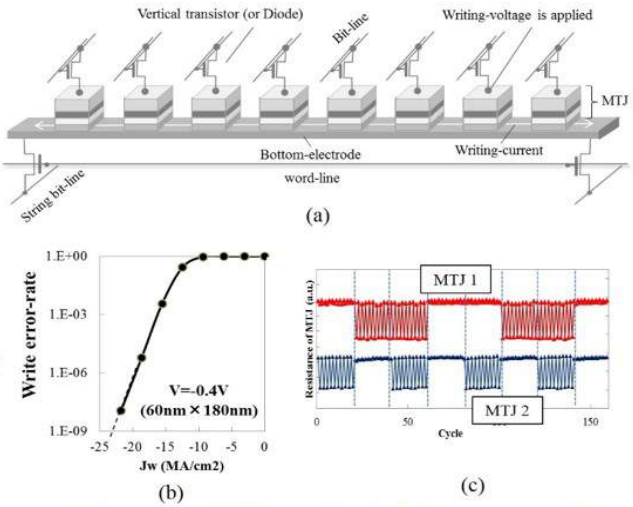

Figure 2. High density VoCSM demonstration[1] A schematic drawing of the unit-cell (b)WER of the VoCSM (c) Demonstration of Flash-writing

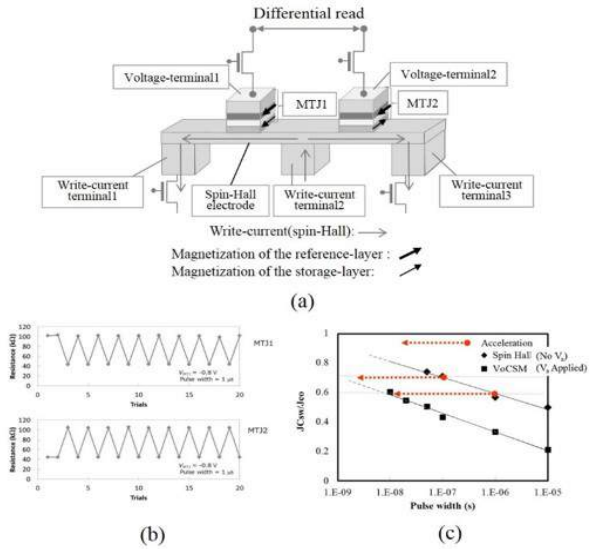

Figure 3. Demonstration of high-speed VoCSM [2]
(a) A schematic drawing of the unit-cell
(b) Demonstration of complementary flash-writing
(c) Pulsewidth dependence of Icsws for spin-Hall writing and VoCSM

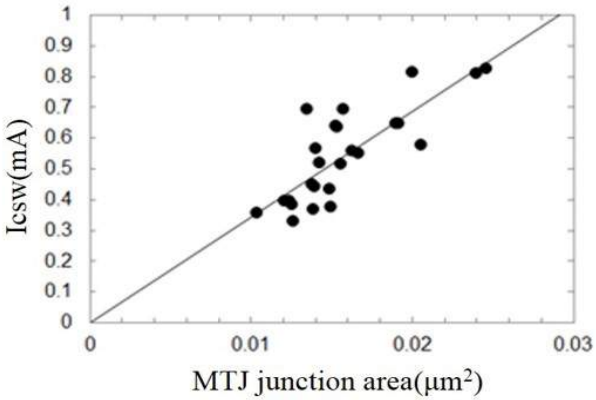

Figure 4. Junction area dependence of Critical switching current of a VoCSM cell[3]

ADVANCED MAGNETIC TUNNEL JUNCTIONS USING SPINEL OXIDE BARRIERS

Hiroaki SUKEGAWA
National Institute for Materials Science (NIMS), Tsukuba, Japan, sukegawa.hiroaki@nims.go.jp

I. BACKGROUND

Magnetic tunnel junctions (MTJs) consisting of a ferromagnet (FM)/barrier/FM trilayer structure are used a read head of hard disc drives (HDDs), and has made a great contribution to the increase in HDD capacity. MTJs are also used as memory cells of non-volatile magnetoresistive memories (MRAMs). In recent years, great attention has been paid to researches on high-sensitive magnetic sensors using MTJs for automotive and medical uses. For such new practical applications, further improvement of the performance of MTJs are required.

In MTJs, tunneling resistance changes with the relative magnetization direction of the two FM layers. The proportion of the resistance change is called a tunnel magnetoresistance (TMR) ratio, and this determines the device output performance. Therefore, obtaining large TMR ratios are desirable for practical uses of MTJs. Nowadays MgO is commonly used as a barrier material of MTJs since large TMR ratios exceeding 100% at room temperature (RT) are easily obtained by the spin-dependent coherent tunneling effect [1]. However, it is difficult to tune the barrier properties such as a lattice constant and a barrier height beyond the MgO physical parameters. Therefore, to widen the application range of MTJs further, tuning the MTJ properties by introducing new barrier materials could be a promising way.

In this presentation, I would like to introduce recent research progress in MTJ barrier design using spinel-based oxides. Especially, I will talk about achievement of large TMR ratios and improvement of bias voltage dependence of TMR due to lattice-constant tuning by an $MgAl_2O_4$ barrier. Furthermore, I will introduce achievement of a barrier height tuning by developing a Ga-based spinel barrier, $MgGa_2O_4$.

II. LATTICE-MATCHED MTJ USING $MgAl_2O_4$ BARRIER

$MgAl_2O_4$ (spinel) has a spinel structure with a lattice constant of ~0.809 nm [2]. Although the structure of $MgAl_2O_4$ is much more complicated than that of the rock-salt type MgO, the lattice-spacing of $MgAl_2O_4$ is 4% smaller than that of MgO; therefore, the $MgAl_2O_4$ lattice matches well with lattices of CoFe(B) alloys and Co-based Heusler alloys [3]. Moreover, the lattice-spacing of $MgAl_2O_4$ can be further tuned by controlling the Mg-Al composition, enabling us to obtain perfect lattice-matched interfaces with various bcc-based FM layers. In addition, as observed in MgO-based MTJs, large TMR ratios due to the occurrence of the coherent tunneling through the Δ_1 Bloch states are achievable in $MgAl_2O_4$-based MTJs [4].

An $MgAl_2O_4$ barrier layer can be fabricated by post-oxidation of an Mg-Al alloy layer [3] and direct RF sputtering from a sintered $MgAl_2O_4$ target [5]. Especially, an excellent quality of the $MgAl_2O_4$ barrier and lattice-matched flat interfaces with Fe electrodes were demonstrated by the direct sputtering method as shown in Fig. 1(a) [5]. TMR ratios of the prepared epitaxial Fe/$MgAl_2O_4$/Fe(001) MTJ reached 245% and 436% at RT and 3 K, respectively, which are very large values as an MTJ using Fe electrodes. A TMR ratio can be improved using Co-based Heusler alloy Co_2FeAl electrodes, and a value up to 342% at RT was demonstrated in a $Co_2FeAl/MgAl_2O_4/Co_2FeAl$(001) MTJ [6].

In general, a TMR ratio reduces with increasing bias voltage, and this causes reduction of electric output of MTJ based devices. The lattice-matching by $MgAl_2O_4$ significantly improves this bias voltage dependence of a TMR ratio due to suppression of inelastic scattering at the barrier interface. A V_{half}, the bias voltage where the TMR ratio is halved, of the Fe/$MgAl_2O_4$/Fe MTJ was around 1.0-1.3 V, which is much larger than that of general MTJs (V_{half} ~ 0.4-0.8 V) [3,5].

An ultra-thin FM/$MgAl_2O_4$ interface showed strong perpendicular magnetic anisotropy (PMA), similar to FM/MgO interfaces [7]. Especially, at an ultra-thin $Co_2FeAl/MgAl_2O_4$(001) interface, it was demonstrated that the perfect lattice-matching resulted in very small Co_2FeAl lattice distortion, leading to

Hiroaki SUKEGAWA
E-mail: sukegawa.hiroaki@nims.go.jp
tel: +81-29-860-4642

a large PMA energy [8]. Therefore, the use of $MgAl_2O_4$ is also advantageous to obtain perpendicularly magnetized MTJs, necessity for high-density MRAM applications.

III. MTJ WITH WIDE-GAP SEMICONDUCTOR SPINEL: $MgGa_2O_4$

According to the theoretical reports, spinel oxides (AB_2O_4 type) with (001) orientation are expected to show TMR enhancement due to the coherent tunneling effect [4,9]. In addition, the band gap of spinel oxides can be reduced by substituting heavy elements for *A* and *B* sites, which results in reduction in a barrier height [9]. Recently, an MTJ with a wide-gap semiconductor spinel $MgGa_2O_4$ barrier was prepared by the direct sputtering [10]. As shown in Fig. 1(b), a lattice-matched epitaxial Fe/$MgGa_2O_4$/Fe structure was successfully obtained. The MTJ showed a relatively large TMR ratio of 121% at RT (196% at 4 K). More importantly, the resistance area product of the MTJ was approximately 50 times smaller than that of an Fe/$MgAl_2O_4$/Fe MTJ at a given barrier thickness due to a low barrier height of $MgGa_2O_4$. This result suggests that a barrier height can be tuned while achieving a large TMR ratio through composition control of a spinel oxide barrier.

IV. SUMMARY AND PROSPECTS

The achievement of lattice-matched interfaces by introducing an $MgAl_2O_4$-based barrier resulted in improvement of MTJ performances such as TMR ratios and PMA characteristics. Recently, excellent time-dependent dielectric breakdown properties of $MgAl_2O_4$ barriers were also demonstrated [11], indicating high reliability of $MgAl_2O_4$-based MTJs suitable for practical uses. Additionally, the study of a new spinel barrier, $MgGa_2O_4$, demonstrated that spinel oxides can tune not only lattice constants but also barrier heights as MTJ barriers. These results indicate the possibility of creating new MTJ applications by the “barrier design” using various spinel oxides.

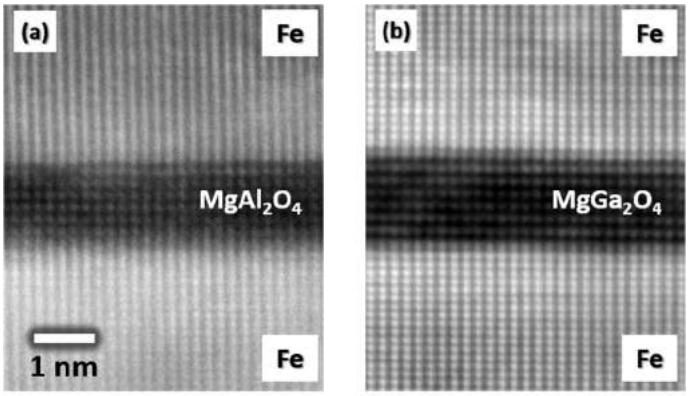

Fig. 1 Cross-sectional scanning transmission electron microscopy images of (a) Fe/$MgAl_2O_4$/Fe(001) and (b) Fe/$MgGa_2O_4$/Fe(001) MTJs fabricated by direct sputtering.

This work was done in collaboration with Y. Kato, T. Daibou, N. Shimomura, Y. Kamiguchi, J. Ito, H. Yoda, K. Hono, S. Mitani, T. Ohkubo, K. Inomata, Z. C. Wen, J. P. Hadorn, M. Belmoubarik, T. Scheike, and P.-H. Cheng. This work was partly supported by the ImPACT Program of Council for Science, Technology and Innovation, Japan, and JSPS KAKENHI Grant Nos. 16H06332 and 16H03852.

REFERENCES

1) S. Yuasa and D. D. Djayaprawira, J. Phys. Appl. Phys. **40**, R337 (2007). 2) S. M. Hosseini, Phys. Status Solidi B **245**, 2800 (2008). 3) H. Sukegawa *et al.*, Appl. Phys. Lett. **96**, 212505 (2010). 4) Y. Miura *et al.*, Phys. Rev. B **86**, 24426 (2012). 5) M. Belmoubarik *et al.*, Appl. Phys. Lett. **108**, 132404 (2016); AIP Adv. **7**, 055908 (2017). 6) T. Scheike *et al.*, Appl. Phys. Express **9**, 053004 (2016). 7) J. Koo, H. Sukegawa, and S. Mitani, Phys. Status Solidi RRL **8**, 841 (2014). 8) H. Sukegawa *et al.*, Appl. Phys. Lett. **110**, 112403 (2017). 9) J. Zhang, X.-G. Zhang, and X. F. Han, Appl. Phys. Lett. **100**, 222401 (2012). 10) H. Sukegawa *et al.*, Appl. Phys. Lett. **110**, 122404 (2017). 11) C. M. Choi *et al*., Electronics Lett. **53**, 119 (2017).

NANO-LAYER OF TETRAGONAL Mn-BASED ALLOYS FOR MRAM APPLICATIONS

Shigemi MIZUKAMI and Kazuya SUZUKI
Advanced Institute for Materials Research, Tohoku University, Sendai, 980-8577, Japan,
shigemi.mizukami.a7@tohoku.ac.jp

A magnetic tunnel junction with a perpendicular magnetic easy-axis (p-MTJ) is a key device for non-volatile magnetoresistive random access memory (MRAM). The CoFeB/MgO-based p-MTJ has been developed and applied to the current-induced spin-transfer-torque (STT) MRAM application. Currently, STT-MRAM for a working memory with a large memory capacity up to 4 Gbit has been demonstrated [1]. Beside, a new spintronic memory has been also proposed and demonstrated, namely voltage controlled spintronic memory (VoCSM) in which magnetization switching is achieved by the current-induced spin-orbit torque (SOT) and voltage-controlled magnetic anisotropy (VCMA) [2]. The CoFeB/MgO is now one of the standard material combinations in those spintronic memories. However, the emergence of new materials for spintronic memories are also demanded because CoFeB has a large saturation magnetization of more than 1000 kA/m and CoFeB/MgO shows moderate perpendicular magnetic anisotropy (PMA) below 1 MJ/m^3. The materials with smaller saturation magnetization and larger PMA are crucial for MRAM with higher memory capacity fabricated with the sub-20 nm semiconductor technology node.

Various ordered magnetic alloys with a large uniaxial magnetic anisotropy have been examined for p-MTJs. Among those alloys, the ordered tetragonal Heusler-like Mn-based alloys, such as Mn_3Ga and its derivatives, have attracted much attention for STT-MRAM because they have high spin-polarization of 88%, related to the Heusler structure and low saturation magnetization of 100-300 kA/m due to ferrimagnetism. A high bulk PMA ~ 1 MJ/m^3 and low Gilbert damping constant < 0.008 also originate from the special property of Mn, *i.e.*, it has nearly half-filled 3*d* electron orbital states in a crystal field with tetragonal symmetry [3]. One technological challenge is to realize p-MTJs with an *ultrathin* Mn-based alloy layer with a large PMA and a typical thickness of 1–3 nm. This is crucial for devices driven by the current-induced torque. However, this has not yet been achieved, because growth of Mn-based alloy nano-layers on conventional buffer layers, such as Cr, has deteriorated their PMA.

Quite recently, this issue has been resolved by our finding of the low temperature crystal growth of MnGa nano-layer [4]. The film deposition was performed by the commercial ultra-high vacuum magnetron sputtering technique, and the point was to use a unique buffer material, CoGa, that is paramagnetic at room temperature for Co concentration of about 50%. Perpendicular magnetization for the epitaxial MnGa films grown on CoGa has been clearly observed even though its thickness was 1 nm. Interestingly, this low-temperature growth technique can be also applied to the polycrystalline growth and the highly (001)-textured MnGa nano-layer can be obtained [5].

Subsequently, we have demonstrated a p-MTJ with a 1-3 nm thick MnGa nano-layer epitaxially grown on a CoGa buffer [6]. The transmission electron microscopy (TEM) showed an atomically flat interface of the MnGa and CoGa buffer layer which promotes an epitaxial strain of MnGa so as to fit CoGa buffer with a lattice mismatch of 4 % [Fig. 1(a)]. This MnGa layer exhibited a PMA of about 0.6 MJ/m^3, magnetization of about 300 kA/m, and those magnetic properties may be suited for advanced MRAM with the large memory capacity. First principles calculations confirmed that the epitaxial strain-induced crystal lattice distortion in this p-MTJ modifies the band dispersion of MnGa and leads a large tunnel magnetoresistance (TMR) effect due to the orbital symmetry filtering effect similar to the Fe/MgO case [7]. Therefore, the large TMR ratio is expected by further optimization of interfaces qualities even though the experimentally observed TMR ratio has not been high yet at the present [Fig. 1(b)].

The above-mentioned low temperature growth process also enables us to investigate the current-induced switching effect for the Mn-based nano-layer, which has never been reported before. To investigate the current-induced SOT switching, we prepared the micron sized Hall bar consisting of Pt-capped 2.5-nm-thick MnGa film grown on CoGa buffer layer. This trilayer film exhibited a low saturation magnetization of 150 kA/m and a large PMA effective field of 2.5 T. The current-induced magnetization

Shigemi Mizukami
shigemi.mizukami.a7@tohoku.ac.jp

switching of MnGa nano-layer induced by an in-plane electrical current was clearly observed, as show in Fig. 1(c), and the switching phase diagram was qualitatively consistent with the damping-like torque due to the spin-Hall effect for the Pt layer having the positive spin-Hall angle [8].

In this talk we will overview the above-mentioned results and recent progress of Mn-based nanolayer p-MTJs developments for MRAM applications, including low Gilbert magnetic damping properties for their films [9]. This work was partially supported by the ImPACT program and KAKENHI.

REFERENCES

1) S.-W. Chung, T. Kishi, J. W. Park, M. Yoshikawa, K. S. Park, T. Nagase, K. Sunouchi, H. Kanaya, G. C. Kim, K. Noma, M. S. Lee, A. Yamamoto, K. M. Rho, K. Tsuchida, S. J. Chung, J. Y. Yi, H. S. Kim, Y. S. Chun, H. Oyamatsu, and S. J. Hong, "4Gbit density STT-MRAM using perpendicular MTJ realized with compact cell structure" in *2016 IEEE Int. Electron Devices Meet. (IEEE, 2016)*, p. 27.1.1-27.1.4.
2) H. Yoda, N. Shimomura, Y. Ohsawa, S. Shirotori, Y. Kato, T. Inokuchi, Y. Kamiguchi, B. Altansargai, Y. Saito, K. Koi, H. Sugiyama, S. Oikawa, M. Shimizu, M. Ishikawa, K. Ikegami, and A. Kurobe, "Voltage-control spintronics memory (VoCSM) having potentials of ultra-low energy-consumption and high-density", in *2016 IEEE Int. Electron Devices Meet. (IEEE, 2016)*, p. 27.6.1-27.6.4.
3) S. Mizukami, A. Sakuma, A. Sugihara, K. Z. Suzuki, and R. Ranjbar, "Mn-based hard magnets with small saturation magnetization and low spin relaxation for spintronics", *Scr. Mater.* 118, 70 (2016), and reference herein.
4) K. Z. Suzuki, R. Ranjbar, A. Sugihara, T. Miyazaki, and S. Mizukami, "Room temperature growth of ultrathin ordered MnGa films on a CoGa buffer layer", *Jpn. J. Appl. Phys.* 55, 10305(R) (2016).
5) A. Ono, K. Z. Suzuki, R. Ranjbar, A. Sugihara, and S. Mizukami, "Ultrathin films of polycrystalline MnGa alloy with perpendicular magnetic anisotropy", *Appl. Phys. Express* 10, 23005 (2017).
6) K. Z. Suzuki, R. Ranjbar, J. Okabayashi, Y. Miura, A. Sugihara, H. Tsuchiura, and S. Mizukami, "Perpendicular magnetic tunnel junction with a strained Mn-based nanolayer", *Sci. Rep.* 6, 30249 (2016).
7) S. Yuasa, T. Nagahama, A. Fukushima, Y. Suzuki, and K. Ando, "Giant room-temperature magnetoresistance in single-crystal Fe/MgO/Fe magnetic tunnel junctions", *Nat. Mater.* 3, 868 (2004).
8) R. Ranjbar, K. Z. Suzuki, Y. Sasaki, L. Bainsla, and S. Mizukami, "Current-induced spin–orbit torque magnetization switching in a MnGa/Pt film with a perpendicular magnetic anisotropy", *Jpn. J. Appl. Phys.* 55, 120302(R) (2016).
9) K. Z. Suzuki, A. Kamimaki, Y. Sasaki, and S. Mizukami, *in-preparation.*

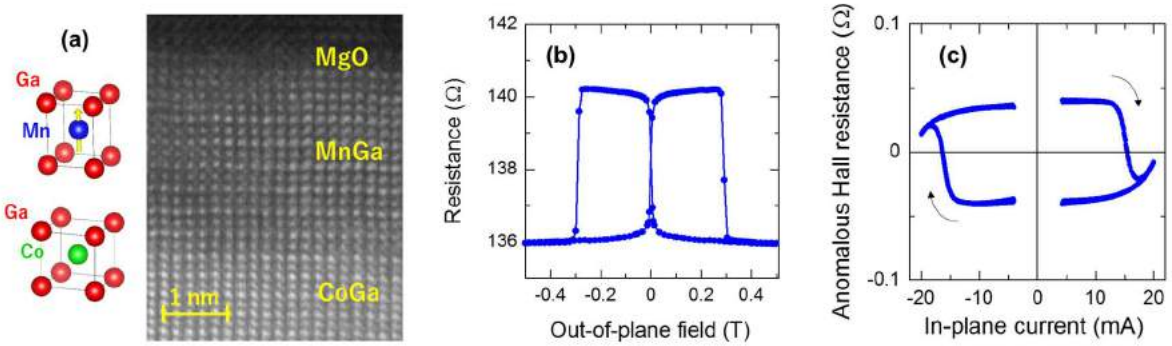

Fig. 1 (a) The cartoon of crystal structures of MnGa and CoGa and the TEM image of the cross section of CoGa buffer / MnGa / MgO /CoFeB p-MTJ. (b) Typical magnetoresistance curve of this p-MTJ. (c) The current-induced magnetization switching for the CoGa/MnGa/Pt trilayer film, which has been measured by the anomalous Hall effect as a function of in-plane applied current under a small in-plane magnetic field.

STORING OR PROCESSING DATA WITH ANTIFERROMAGNETS?

X. MARTÍ[1,2], I. FINA[3]

1) Institute of Physics, Academy of Sciences of the Czech Republic, Czech Republic xmarti@fzu.cz
2) IGS Research, La Pobla de Mafumet, Spain, xavi.marti@igsresearch.com
3) Institut de Ciència de Materials de Barcelona (CSIC), Bellaterra, Spain, ignasifinamartinez@gmail.com

I. INTRODUCTION

Information technologies are nowadays especially receptive for novel building blocks that could help the transit beyond the Moore's law era. On these grounds, a plethora of candidate technologies have raised their proposals to stand in for covering specific portions of the ubiquitous Silicon technologies that nowadays are fairly covering from data storage (whilst in tight competition with magnetic media) up to data processing. At this moment of change, antiferromagnetic-based devices have emerged with quite an unprecedented momentum from the fundamental theories up to the academic sphere success in less than a decade. Now that the first round of academic demonstrations has been delivered [1,2,3], the moment to carefully choose where to focus the subsequent efforts and prevent an excessive economical and intellectual divergence has come.

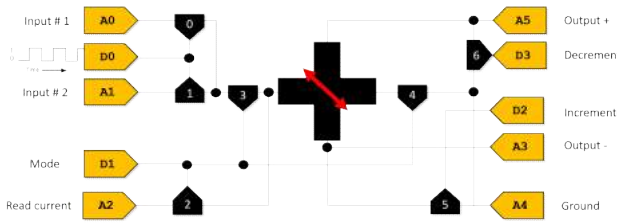

Figure 1. Schematic of an antiferromagnetic cross-shaped device in the center surrounded by contact pins (gold) and transistors (black). This building block fed with a clock signal input can be set to realize OR, XOR, AND, NOT, and a gradient of an analog input signal.

In this talk, we will first review the main features demonstrated so far by antiferromagnetic-based devices. Namely: the electrical switching at room temperature [4]; the realization of a USB-based desktop device capable of read/write intermediate resistive states and perform basic operations such pulse-counting and signal integration [5]; pushing the switching speed well into the picosecond regime by contact-less means [6].

After the state-of-the-art revision, we will present our core building block from which we will try to realize logic operations such as OR, XOR, AND, NOT and also some complex real-time operations such as the gradient of an analogic input signal. The schematic of the starting circuit geometry is shown in Figure 1. By setting the "mode", "incrementer" and "decrementer" pins to specific values, one can toggle among several functions. While this schematic does not represent a standalone device to be integrated immediately, it does represent the seed to initiate a dialogue with further integration steps.

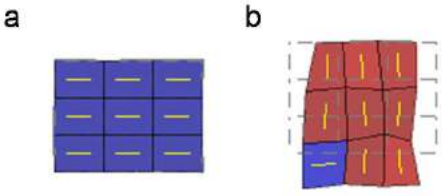

Figure 2. Scheme of the two perpendicular magnetic states after applying magnetic field along (a) north-south direction and (b) west-east direction in a magnetostrictive antiferromagnet. The difference between a and b can be sensed by electrical resistance measurements but the stray fields remain identical in both panels.

In the next section of the talk, we will compare the pros and cons of setting the heading of the antiferromagnetic spintronics field towards data storage, to data processing or to both – or to none.

Before concluding the talk, we will say a word on the progress of more fundamental aspects of the field that could also meet practical applications. Among these: the exploitation of magnetic invisibility of antiferromagnets for low-density security applications; the magnetoelastic coupling

Xavier Marti
E-mail: xmarti@fzu.cz

present in numerous materials that could be used for storing, encoding or even cloaking information (see Figure 2); and the state of the art of the magnetoelectric devices [7].

REFERENCES

1) T. Jungwirth, et al., “Antiferromagnetic spintronics” *Nat. Nanotechnology* 11, 231 (2016)
2) V. Baltz, et al., “Antiferromagnetism: the next flagship magnetic order for spintronics?”, submitted to *Rev. Mod. Phys.*, arXiv: 1606.04284
3) X. Marti, et al., “Prospect for antiferromagnetic spintronics”, *IEEE Trans. Magn.* 51, 2900104 (2015)
4) P. Wadley, et al. "Electrical switching of an antiferromagnet." *Science* 351, 587 (2016).
5) V. Schuler, et al., “Antiferromagnetic multi-level memory cell.”, *Nature Commun.* (in press), arXiv:1608.03238
6) K. Olejnik, et al., “Switching of an antiferromagnet by picosecond electrical-radiation pulses”, in preparation
7) See, for instance, T. Kosub, et al., “Purely antiferromagnetic magnetoelectric random access memory.” *Nat. Commun.* 8, 13985 (2017).

Cr_2O_3 BASED MAGNETOELECTRIC FERRIMAGNET TOWARD MRAM APPLICATIONS

Tomohiro NOZAKI[1] and Masashi SAHASHI[1,2]

1) Department of Electronic Engineering, Tohoku University, Sendai 980-0845, Japan

2) ImPACT Program, Japan Science and Technology Agency, Tokyo 102-0076, Japan

I. INTRODUCTION

Recently the voltage control of a magnetization direction has received considerable attentions as the technology to achieve an ultra-low power consumption magnetic random access memory (MRAM). One of the promising technologies is the voltage control of a magnetic anisotropy (VCMA) in ferromagnetic metals. Since the dynamic switching of magnetization was demonstrated by utilizing the VCMA effect[1,2] in MgO-based magnetic tunnel junctions (MTJ), it has been intensively investigated. It is called "voltage torque MRAM". VCMA value of as large as ~300 fJ/Vm was already reported[3]. Thus it is expected to realize voltage torque MRAM in the not-too-distant future.

The other candidate is that using magnetoelectric (ME) antiferromagnet Cr_2O_3. When we apply parallel (anti-parallel) electric (E) and magnetic field (H), the antiferromagnetic domain of Cr_2O_3 align as ↑↓↑↓ (↓↑↓↑). If we apply fixed positive H, by changing the direction of E from positive to negative, we can switch the direction of surface spin of Cr_2O_3 from up (↑) to down (↓). In addition, the surface spin information can be transferred to neighbor ferromagnet via exchange coupling. Thus by combining both the ME effect and exchange coupling, we can achieve electric control of magnetization. The concept of so called "magnetoelectric random access memory (MERAM)" was proposed in 2006[4]. After that, its primitive operations were demonstrated for Cr_2O_3 bulk[5,6] and thin film[7,8] systems. Recently the reduction of the large switching energy was proposed[9]. In additions, ferromagnet free purely antiferromagnetic random access memory was demonstrated[10]. These reports make the MERAM more realistic and more interesting. Although Cr_2O_3 is an antiferromagnet, sometimes finite magnetization has been observed for Cr_2O_3 films. We found relative large parasitic magnetic moment, which comparable to the ferrimagnet, for doped Cr_2O_3. In this study, we investigated the parasitic magnetic moments of Al- and Ir-doped Cr_2O_3 film and discussed the usability.

II. EXPERIMENTAL PROCEDURES

The non-dope, Al-doped, and Ir-doped Cr_2O_3 films are fabricated by RF reactive sputtering method. The Al and Ir contents and lattice parameters of the films were confirmed by X-ray fluorescence (XRF) and X-ray diffraction measurements, respectively. Magnetic and magnetoelectric properties were measured by using a superconducting quantum interference device (SQUID) magnetometer or anomalous Hall effect (AHE). The detail of the magnetoelectric properties measurements are described in[11]. Uncompensated surface spin of Cr_2O_3 film was measured by X-ray magnetic circular dichroism (XMCD) spectroscopy. The XMCD measurements were carried out at beam line BL25SU of the SPring-8 synchrotron radiation facility.

III. RESULTS AND DISCUSSIONS

By Al- and Ir-doping, relative large volume magnetization were obtained. The Cr_2O_3 volume magnetization increase with increasing both Al- and Ir-contents; by about 3.7% Al-(Ir-) dope, volume magnetization of as large as 59 (4.9) emu/cc were obtained, which correspond to 0.61 (0.05) μ_B/Cr. Interestingly, the doped Cr_2O_3 film still exhibit ME properties, and the parasitic magnetization is coupled with the ME order parameter of Cr_2O_3. Fig. 1 shows the ME coefficient α of (a) Al-doped and (b) Ir-doped Cr_2O_3 film against H at 170 K. With increasing applied H, the parasitic magnetization reverse and simultaneously the ME order parameter also reverse. Fig. 1 indicate that in Al-doped sample case, Cr_2O_3 parasitic magnetization is coupled with F^+ state (↑↓↑↓), while in Ir-doped sample case, Cr_2O_3 parasitic magnetization is coupled with F^- state (↓↑↓↑). These fact were confirmed by combined study of

Tomohiro NOZAKI
E-mail: nozaki@ecei.tohoku.ac.jp
tel: +81-22-795-7067

magnetization measurements, measurements of Cr_2O_3 surface spin by XMCD, and ME coefficient measurements. These results suggest the parasitic magnetic moment can be controlled by magnetic and electric fields through the ME effect. That is "magnetoelectric ferrimagnet". XRD results indicate both *a* and *c* value expansion for Ir-doped sample, and *a* and *c* value compression for Al-doped case. These different kind of lattice strain may related to the difference in Cr_2O_3 volume magnetization direction, since similar magnetization direction change was also observed for Cr_2O_3 films with various buffer layers[10]. In this study, we clarified the co-existence of ME and ferrimagnetic properties in doped Cr_2O_3 films. Such an electrically controllable magnetization have a great potential for developing new electric field controlled memory concepts, in additions to the utilization of reduction of ME switching energy[9].

ACKNOWLEDGEMENTS

This work was partly funded by ImPACT Program of Council for Science, Technology and Innovation (Cabinet Office, Japan Government) and JSPS KAKENHI Grant Number 16H05975.

REFERENCES

1) Y. Shiota et al., "Induction of coherent magnetization switching in a few atomic layers of FeCo using voltage pulses", *Nat. Mater.*, 11, 39 (2012).
2) S. Kanai et al., "Electric field-induced magnetization reversal in a perpendicular-anisotropy CoFeB-MgO magnetic tunnel junction", *Appl. Phys. Lett.*, 101, 122403 (2012).
3) T. Nozaki et al., "Large Voltage-Induced Change in the Perpendicular Magnetic Anisotropy of an MgO-Based Tunnel Junction with an Ultrathin Fe Layer" *Phys. Rev. Appl.*, 5, 044006 (2016).
4) X. Chen et al., "Magnetoelectric exchange bias systems in spintronics", *Appl. Phys. Lett.*, 89, 202508 (2006).
5) P. Borisov et al., "Magnetoelectric Switching of Exchange Bias", *Phys. Rev. Lett.,* 94, 117203 (2005).
6) X. He et al., "Robust isothermal electric control of exchange bias at room temperature", *Nat. Mater.*, 9, 579 (2010).
7) T. Ashida et al., "Observation of magnetoelectric effect in Cr_2O_3/Pt/Co thin film system", *Appl. Phys. Lett.*, 104, 152409 (2014).
8) T. Ashida et al., "Isothermal electric switching of magnetization in Cr_2O_3/Co thin film system", *Appl. Phys. Lett.*, 106, 132407 (2015).
9) M. Al-Mahdawi et al., "Low-energy magnetoelectric control of domain states in exchange-coupled heterostructures", *Phys. Rev. B*, accepted.
10) T. Kosub et al., "Purely antiferromagnetic magnetoelectric random access memory", *Nat. Commun.*, 8, 13985 (2017).
11) M. Al-Mahdawi et al., "Apparent critical behavior of sputter-deposited magnetoelectric antiferromagnetic Cr_2O_3 films near Neel temperature", *J. Phys. D: Appl. Phys.*, 50, 155004 (2017).

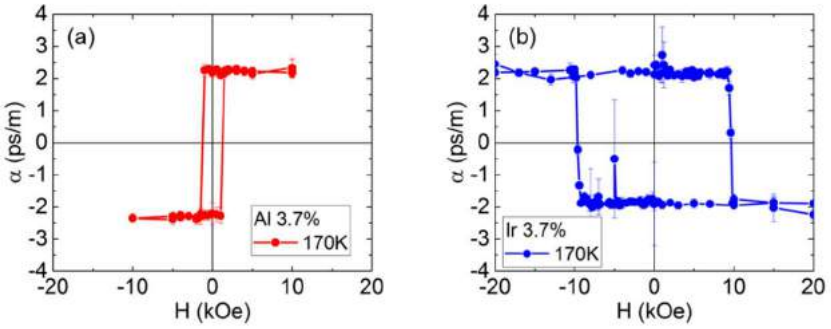

Fig. 1 *H* dependence of ME coefficient α of (a) Al-doped and (b) Ir doped samples measured at 170K.

ULTRA-LOW MAGNETIC DAMPING IN METALLIC AND HALF-METALLIC MATERIALS FOR DATA-STORAGE AND MRAM

Justin M. SHAW[1§], Martin SCHOEN[1], Danny THONIG[2], Eric EDWARDS[1], Hans NEMBACH[1], Tom SILVA[1], Michael SCHEIDER[1], Matt PUFALL[1], Charlie KARIS[2], Olle ERIKSSON[2]

1) Quantum Electromagnetics Division, National Institute of Standards and Technology, Boulder, Colorado 80305, USA

2) Department of Physics and Astronomy, University of Uppsala, S-75120 Uppsala, Sweden

§justin.shaw@nist.gov

The phenomenology of magnetic damping is of critical importance to devices which seek to exploit the electronic spin degree of freedom since damping strongly affects the energy required and speed at which a device can operate. However, theory has struggled to quantitatively predict the damping, even in common ferromagnetic materials. This presents a challenge for a broad range of applications in data storage, magnonics, spintronics and spin-orbitronics that depend on the ability to precisely control the dynamics of a device. Complicating the situation is the need to simultaneously control many other magnetic properties, such as anisotropy and saturation magnetization, that may or may not be independent of the damping.

I will discuss our recent work to precisely measure the intrinsic damping in several metallic and half-metallic material systems and compare experiment with several theoretical models.[1-7] This investigation uncovered a metallic material composed of Co and Fe that exhibit ultra-low values of damping that approach values found in thin film YIG.[8-10] Such ultra-low damping is unexpected in a metal since magnon-electron scattering dominates the damping in conductors. However, this system possesses a distinctive feature in the bandstructure that minimizes the density of states at the Fermi energy $n(E_F)$. This behavior can be seen in Figure 1 which shows the compositional dependence of the intrinsic damping in Fe-Co alloy system. $n(E_F)$ is also included in the figure and exhibits a proportionality with the damping. These findings provide the theoretical framework by which such ultra-low damping can be achieved in metallic ferromagnets and may enable a new class of experiments where ultra-low damping can be combined with a charge current.

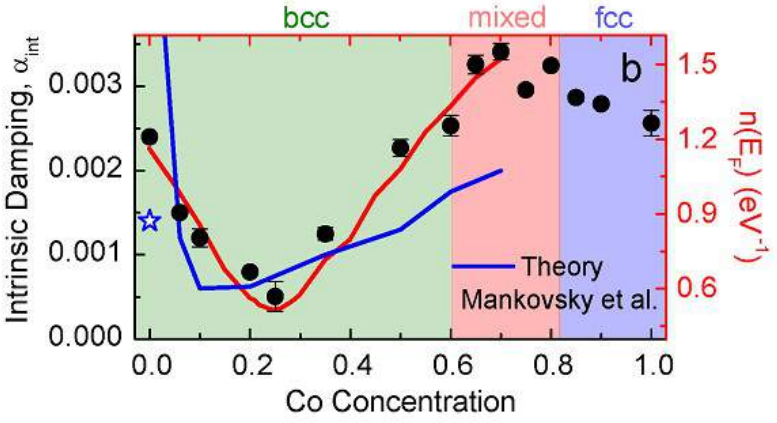

Figure 1. The intrinsic damping parameter (black circles) and density of states (red line) at the Fermi energy as a function of the Co concentration. [8]

Half-metallic Heusler compounds by definition have a bandgap in one of the spin channels at the Fermi energy. This feature can also lead to exceptionally low values of the damping parameter as a result of the reduced number of scattering channels. Co_2MnGe is a particularly promising Heusler material for

Justin Shaw
Justin.shaw@nist.gov

applications in MRAM due to its low ordering temperature.[11] We show that an intrinsic damping parameter as low as 0.0008 can be achieved in B2 ordered, polycrystalline Co_2MnGe films. Our results show a correlation of the damping with the order parameter and resistivity in Co_2MnGe.

.

REFERENCES

[1] Mankovsky et al. "First-principles calculation of the Gilbert damping parameter via the linear response formalism with application to magnetic transition metals and alloys" *Phys. Rev. B,* 87, 014430 (2013)

[2] Turek et al. "Nonlocal torque operators in *ab initio* theory of the Gilbert damping in random ferromagnetic alloys" *Phys. Rev. B,* 92, 214407 (2015).

[3] Gilmore et al. "Identification of the Dominant Precession-Damping Mechanism in Fe, Co, and Ni by First-Principles Calculations" *Phys. Rev. Lett.*, 99, 027204 (2007)

[4] Thonig et al. "Gilbert damping tensor within the breathing Fermi surface model: anisotropy and non-locality" *New J. Phys.*, 16, 013032 (2014)

[5] Brataas et al. "Scattering Theory of Gilbert Damping" *Phys. Rev. Lett.,* **101**, 037207 (2008)

[6] Starikov et al. "Unified First-Principles Study of Gilbert Damping, Spin-Flip Diffusion, and Resistivity in Transition Metal Alloys" *Phys. Rev. Lett.*, 105, 236601 (2010)

[7] Liu et al.," First-principles calculations of magnetization relaxation in pure Fe, Co, and Ni with frozen thermal lattice disorder" *Phys. Rev. B* **84**, 014412 (2011)

[8] Schoen et al, "Ultra-low magnetic damping of a metallic ferromagnet" *Nature Physics* (2016)

[9] Schoen et al, "Magnetic properties of ultrathin 3d transition-metal binary alloys. I. Spin and orbital moments, anisotropy, and confirmation of Slater-Pauling behavior" *Phys. Rev. B*, 95 , 134410 (2017)

[10] Schoen et al, "Magnetic properties in ultrathin 3d transition-metal binary alloys. II. Experimental verification of quantitative theories of damping and spin pumping" *Phys. Rev. B*, 95 , 134411 (2017)

[11] M.J. Carey et al, "Co2MnGe-based current-perpendicular to the plane giant magnetoresistance spin-valve sensors for recording head applications" *J. Appl. Phys.,* 109, 093912 (2011)

NOTE

ADSORPTION PROPERTY OF ULTRA-THIN PFPE LUBRICANT WITH IONIC END-GROUPFOR DLC SURFACE

H. TANI[1], R. LU[1], S. KOGANEZAWA[1], and N. TAGAWA[1]
1) Kansai Univ., Osaka, Japan, hrstani@kansai-u.ac.jp

I. INTRODUCTION

Ionic liquids have low vapor pressure and high thermal resistance. Therefore, an ionic liquid may be a candidate as a lubricant material for magnetic disks used in heat-assisted magnetic recording (HAMR) drives. Liu et al. previously compared the tribological properties and thermal stability of an ionic liquid with those of perfluoropolyether (PFPE) lubricants Krytox and X1P; the ionic liquid showed better friction behavior and thermal stability than the other lubricants [1]. The thermal stability of a lubricant film is needed in the head-disk interface (HDI) of HAMR drives. Kondo et al. synthesized a novel perfluoropolyether (PFPE) ionic liquid whose terminal group is an ammonium salt with a carboxylic group and confirmed that it exhibited superior frictional properties when compared to the conventional PFPEs [2]. Hatsuda et al. developed a new thermally stable protic ionic liquid (PIL) or PIL-type lubricants and found that a higher ΔpKa—the difference in pKa value between an acid and a base—is effective at improving thermal stability [3]. Gong et al. evaluated room-temperature ionic liquids for HAMR application and concluded that the ionic lubricants were considerably more thermally stable than Zdol and Zteraol [4].

In this study, we focused on the adsorption properties of a PFPE lubricant with ionic end-groups and a diamond-like carbon (DLC) surface in order to apply the lubricant to improve the thermal stability for HAMR media. The study also compared two types of PFPE lubricant films in terms of their affinities to DLC surfaces. One lubricant material (SNH2) was Demnum main-chain with single ionic end-group and the other lubricant material (Z-tetraol) was Fomblin main-chain with double hydroxyl end-groups.

II. EXPERIMENT

A PFPE lubricant with a Demnum main-chain and an amine salt end-group called SNH2 was prepared as shown in Fig. 1-(b). Z-tetraol was prepared as a reference, shown in Fig. 1-(a). Normal dip coating and electric-field-assisted dip (EFAD) coating were applied to the lubrication [5]. A photographic image of the EFAD coating tool is shown in Fig. 2. Cu electrode plates in the lubricant solution were placed parallel to each side of the disk surface. Electrode pins contacted the edge of disks. A DC voltage was applied between the disk and electrode plates while dipping the disk and the electrodes in the lubricant solution, resulting in an electric field between the electrode plates and disk surfaces. In this experiment, the dipping duration was 180 s, the withdrawal speed was 2 mm/s, and the distance between each electrode plate and the center of the disk was 12.5 mm. A voltage of 10 V corresponds to an electric field of 0.8 kV/m.

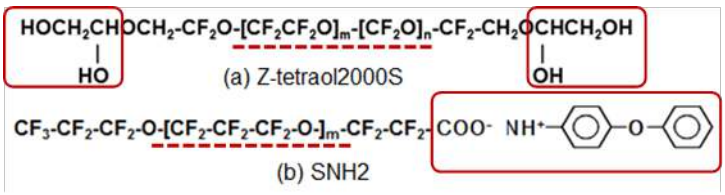

Fig. 1 Lubricant chemical structure used in this study.

Hiroshi Tani
E-mail: hrstani@kansai-u.ac.jp
tel: +81-6-6368-0771

III. RESULTS AND DISCUSSION

The lubricant thickness as a function of varying lubricant concentration in its solution is shown in Fig. 3. At lower lubricant concentration, the lubricant thickness of SNH2 was the same (10 Å @ 0.001 wt%) as that of Z-tetraol (10 Å @ 0.01 wt%). In addition, the thickness of SNH2 was found to increase in the positive electric field; however, it did not increase in the negative electric field. This is probably because the main-chain side on the SNH2 structure has a negative charge, which creates an attractive force between the lubricant molecules and the disk surface, thus helping the SNH2 main-chains to adsorb on the DLC surface.

Figure 4 shows the surface free energy of SNH2 films. The polar surface energy of the SNH2 film was much higher than that of the Z-tetraol film; this was thought to be because the ionic functionalities of mobile molecules had large polarity.

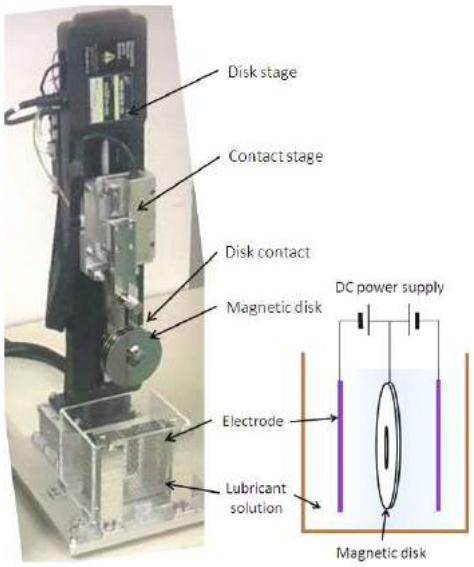

Fig. 2 Electric-field-assisted dip coating tool [5].

IV. CONCLUSION

We concluded that the PFPE lubricant with ionic end-groups needed UV treatment, although it had a large electrostatic interaction with the DLC surface.

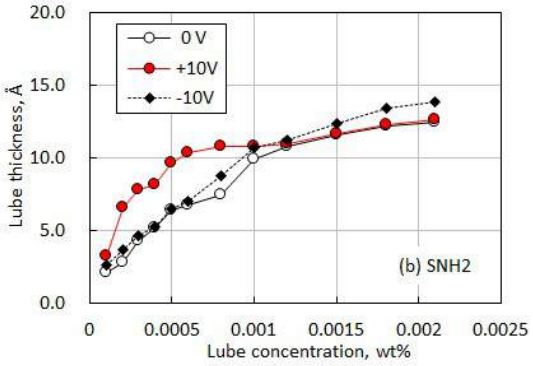

Fig. 3 Electric field assisted dip coating tool [5].

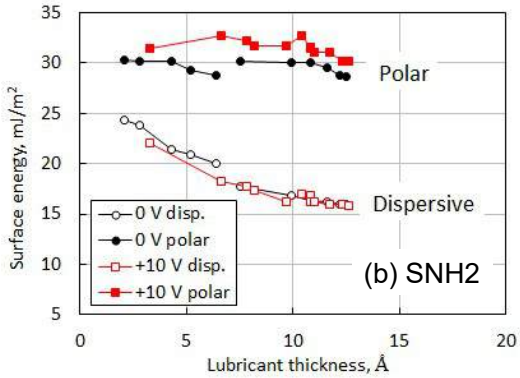

Fig. 4 Electric field assisted dip coating tool [5].

REFERENCES

1) W. Liu et al. "Tribological Behavior of Sialon Ceramics Sliding against Steel Lubricated by Fluorine-Containing Oils", Tribo. Inter., 35, 503–509, (2002).
2) Hirofumi Kondo, "Tribochemistry of Ionic Liquid Lubricant on Magnetic Media", Advances in Tribology,
Volume 2012, Article ID 526726, (2012).
3) Kouki Hatsuda et al., "Friction Properties of Ionic Liquid Lubricants under High Temperature", International Tribology Conference ITC2015, 18pG-05, (2015).
4) Xiao Gong et al., "Room-temperature Ionic Liquids (RTILs): Media Lubricants for Heatassisted Magnetic Recording (HAMR)? ", IEEE Trans. on Magn., DOI 10.1109/TMAG.2015.2438253, (2015).
5) Hiroshi Tani et al., "Electric-Field-Assisted Dip Coating Process of Ultrathin PFPE Lubricant Film for Magnetic Disks", IEEE Trans. on Magn., 45(10), 3636–3639, (2009).

201 GB/IN^2 RECORDING AREAL DENSITY ON SPUTTERED MAGNETIC TAPE

Simeon FURRER[1], Mark A. LANTZ[1], Peter REININGER[1], Angeliki PANTAZI[1], Hugo E. ROTHUIZEN[1], Roy D. CIDECIYAN[1], Giovanni CHERUBINI[1], Walter HAEBERLE[1], Evangelos ELEFTHERIOU[1], Junichi TACHIBANA[2], Noboru SEKIGUCHI[2], Takashi AIZAWA[2], Tetsuo ENDO[2], Tomoe OZAKI[2], Teruo SAI[2], Ryoichi HIRATSUKA[2], Satoshi MITAMURA[2] and Atsushi YAMAGUCHI[2]

1) IBM Research - Zurich, CH-8803 Rueschlikon, Switzerland

2) Sony Storage Media Solutions Corporation, Tagajo-shi, Miyagi-ken 985-0842 Japan

I. INTRODUCTION

Magnetic tape systems are currently the most cost effective solution for the storage of large volumes of infrequently accessed data. However, for tape systems to remain competitive, it is essential to maintain this cost advantage by continuing to scale areal density. State of the art commercial linear-tape drives operate at an areal density of 5-7 Gb/in2. In this work, we demonstrate the viability of continuing to scale the tape roadmap for another decade [1] by performing a single-channel tape areal density demonstration of 201 Gb/in2 on a prototype sputtered magnetic tape.

II. TECHNOLOGIES AND EXPERIMENTAL RESULTS

The linear tape recording performance of a prototype perpendicularly oriented sputtered tape sample was investigated using a 48 nm wide tunneling-magnetoresistive (TMR) hard disk drive read head and a prototype tape write head. The sputtered tape media has a structure depicted in Fig. 1 that consists of the following layers: a diamond-like carbon (DLC) overcoat (5 nm), a CoPtCr-SiO_2 magnetic layer (14 nm), a Ru intermediate layer consisting of two films formed under different sputtering conditions (#1:18 nm/#2:5 nm), NiW (10 nm)/TiCr (2 nm) seed layers, and a CoZrNb (14 nm) soft under-layer deposited onto a polyaramide substrate. The surface roughness measured by AFM over 30 μm^2 is characterized by an average roughness Ra = 0.9 nm and a ten-point average roughness Rz = 16 nm. The average grain size in the CoPtCr-SiO_2 recording layer is 6.6 nm with a standard deviation of 1.2 nm. The magnetic properties, measured using Kerr magnetometer are: coercivity = 3880 Oe, Mrt = 0.57 memu/cm^2, and squareness = 0.97. The coercivity of the prototype media is larger than that of commercial tape and provides a room temperature thermal stability: K_uV/k_BT = 67.7, measured using the technique described in [2]. In order to fully saturate the media, we used a prototype ring-type tape writer with $Ni_{45}Fe_{55}$ poles and an additional 200 nm layer of Fe_xCo_{1-x} deposited between the 160 nm write gap and the trailing edge pole. This high B_s layer enables the production of larger write fields and provides sharper field gradients.

To explore the recording potential of the sputtered media, we recorded a repeating 255-bit pseudorandom binary sequence (PRBS) at linear densities from 569 kbpi to 900 kbpi using the prototype tape writer and a reel-to-reel tape transport. The recorded PRBS data was read back using a 48 nm wide hard disk drive TMR read head and the captured waveforms were processed by a software read channel that implements all the functions of an in-drive read channel. We set a target threshold error rate performance based on our previous work in which we analyzed the performance of iterative decoding of a product Reed-Solomon code with N1 = 240, N2 = 192 and a code rate of 0.83, similar to the codes implemented in current commercial tape drives [3]. In this work we found that with a byte-error rate (BER) of ≤ 4.5e-2 at the output of the detector a user error rate of less than 1e-20 can be achieved after two consecutive C1 and C2 decoding steps. Hence we set a performance target of a raw byte-error rate of < 4.5e-2 at the output of the detector, assuming a reverse concatenation architecture. The BER performance of the read-back waveforms was analyzed using four detection algorithms: 1) 8-state extended partial-response class 4 (EPR4) detection, 16-state noise-predictive maximum-likelihood (NPML) detection, 16-state data-dependent NPML (DD-NPML) detection and 4) and an extended version of the DD-NPML detector that tracks the mean of the data-dependent noise (D3-NPML). Figure 2(a) depicts the channel SNR versus linear density at the input of the EPR4 detector and Fig. 2(b) compares the BER performance of the four detectors. At a linear density of 818 kbpi the channel SNR is 10.7 dB and the BER performance of all four detectors is below the target of less than 4.5e-2. The best performing detector, D3-NPML, crosses the BER target at an interpolated linear density 893 kbpi where the

M. A. Lantz
IBM Research – Zurich
Saeumerstr. 4, Rueschlikon, Switzerland
tel: +41 44 724 8232
e-mail: mla@zurich.ibm.com

channel SNR is estimated to be 9.9 dB. Hence, an operating point of 818 kbpi in combination with the D3-NPML detector provides an operating margin of about 0.8 dB.

To explore the potential track density achievable with this media we performed track-following experiments using an experimental low noise reel-to-reel tape transport and a prototype TMR tape read head equipped with two, 1-µm-wide servo readers mounted in a commercial tape head actuator. The media was formatted with an experimental timing-based servo pattern with a 24° azimuth angle and a 51 µm sub-frame length that enables the generation of servo estimates at a high rate and nano-scale position estimation resolution. The read-back signals from the two servo readers were processed using a pair of synchronous servo channels implemented in an FPGA-based prototyping platform. The position estimates from the two servo channels were then averaged and used for feedback control. An H_∞-based track-following controller was implemented in the same FPGA to enable real-time closed-loop track-following experiments. The control loop hardware and FPGA implementation were optimized to reduce delay in the control system and enable the synchronous operation of the controllers. Because of the speed dependence of both the delay in the servo signal and the frequency characteristics of the lateral tape motion, a set of track-following controllers were designed with each controller optimized for a specific tape speed. The low estimation noise in the averaged estimated position signal enables the use of high-bandwidth track-following controllers characterized by a closed-loop bandwidth derived from the sensitivity transfer function that ranges from approx. 478 Hz at 1.2 m/s tape speed to approx. 1380 kHz at 4.1m/s tape speed. Figure 2(c) shows an example of the closed-loop position-error signal (PES) measured at a tape speed of 3.1 m/s. Figure 2(d) depicts the standard deviation of the PES (σ-PES) as a function of tape velocity demonstrating a σ-PES ≤ 6.5 nm over the speed range of 1.2 to 4.1 m/s. The minimum reliable track width can be estimated using the model described by the Information Storage Industry Consortium [1] as: track width = $2\sqrt{2}$ *$3\sigma_{PES}$ + reader width. Taking a reader width of 48 nm and the worst case measured σ_{PES} = 6.5 nm leads to an estimated track width of 103 nm and a track density of 246.2 ktpi. Combining this track density with the linear density of 818 kbpi achieved within the error rate target with the 48 nm reader corresponds to a potential areal recording density of 201.4 Gb/in^2.

REFERENCES

1) International Magnetic Tape Storage Roadmap, Information Storage Industry Consortium, 2012 and 2015.
2) J. Tachibana et al. IEEE Trans. Magn., vol. 50, 3202806, 2014
3) S. Furrer et al. IEEE Trans. Magn., vol. 51, 3100207, 2015

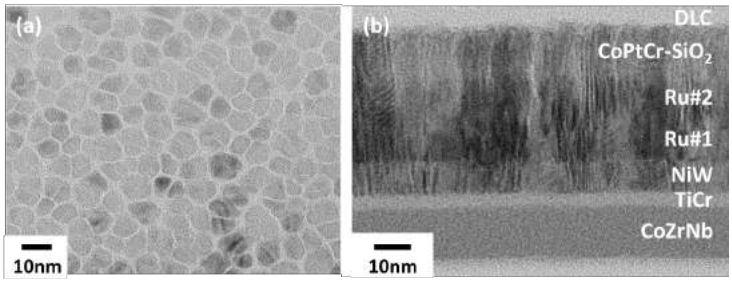

Figure 1 (a) TEM Plan view and (b) TEM cross-section images of the prototype sputtered tape media.

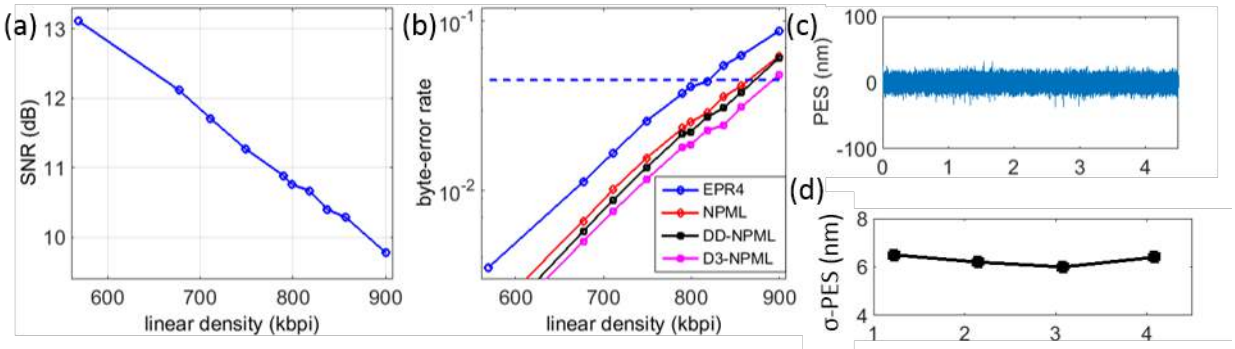

Figure 2 (a) Data channel SNR and (b) byte-error rate versus linear density. The dashed line shows the demo byte-error rate target. (c) PES during track following at 3.1 m/s. (d) Standard deviation of the PES versus tape speed.

VOLTAGE CONTROL Of MAGNETIZATION DIRECTION OF MULTIFERROIC THIN FILMS FOR APPLICATION TO NOVEL MAGNETIC RECORDING DEVICES WITH ELECTRIC-FIELD WRITING METHOD

Satoru YOSHIMURA
Akita University, Akita, Akita, 010-8502 JAPAN

I. INTRODUCTION

Electric field writing magnetic recording is a prospective technology for future recording devices due to its lower power consumption and easier writing. For example, in the case of hard-disk drives (HDDs), magnetic field writing will gradually become more difficult due to increase of needed magnetic field. On the other hand, in the case of HDDs with multiferroic recording media which can use the electric field writing method, the power requirement is very low for switching the magnetization direction, the structure of the writing head is simple such as a needle-shape conductive element, and a very high electric field can be applied to the multiferroic layer easily due to its thinness. Therefore, in these days, control of magnetization by electric field was widely studied. In these days, suitable multiferroic materials such as Bi-based ferrite[1-3] with ferromagnetism and ferroelectrisity at room temperature were reported. In this study, I propose a novel electric field writing magnetic recording technology using a multiferroic $(Bi_{1-x}Ba_x)FeO_3$ thin film with ferromagnetism and ferroelectricity for new magnetic recording devices with low power consumption.

II. RESULTS AND DISCUSSION

The multilayer of Ta(5 nm)/Pt(100 nm)/ $(Bi_{1-x}Ba_x)FeO_3$(100 nm) were deposited onto a thermally oxidized Si wafer by UHV sputtering system. The Ba concentration, x was varied at 0, 0.1, 0.2, 0.4. The Ta seedlayer, Pt underlayer, and $(Bi_{1-x}Ba_x)FeO_3$ layer were deposited at room temperature, 300 ℃, and 400-500 ℃, respectively. The film thickness and deposition temperature of Ta seedlayer and Pt underlayer were optimized to obtain strong (111) orientation of Pt underlayer[4]. The VHF (40.68 MHz) plasma irradiation process during RF (13.56 MHz) sputter deposition[5] of $(Bi_{1-x}Ba_x)FeO_3$ films was performed with the electric power of 5 W to obtain crystal grain growth of $(Bi_{1-x}Ba_x)FeO_3$ thin films at lower substrate temperature. By increasing the Ba concentration, the saturation magnetization M_s increases with maintaining the saturation electric polarization P_s, and then, in the $(Bi_{0.6}Ba_{0.4})FeO_3$ film, the clear hysteresis in the magnetization curve and ferroelectric loops was measured, and the M_s of about 60 emu/cm^3, the P_s of about 6 μC/cm^2, the coercivity H_c of about 2.5 kOe, and the squareness ratio M_r/M_s of about 0.6 were obtained, respectively (see Fig. 1). The magnetization curve of the $(Bi_{0.6}Ba_{0.4})FeO_3$ film at the measuring temperature of 250 ℃ showed clear hysteresis and the ferromagnetic transition (Curie) temperature T_c was about 400 ℃ (see Fig. 2).

The magnetization reversal with micrometer size on the $(Bi_{0.6}Ba_{0.4})FeO_3$ film by applying local electric field was demonstrated using scanning probe microscopy. Fig. 3 (a), (b), and (c) show the topographic, electric force microscopy (EFM), and magnetic force microscopy (MFM) images of the $(Bi_{0.6}Ba_{0.4})FeO_3$ film before applying DC voltage. In the case of MFM image (c), demagnetized domain structure was observed. In the case of EFM image (b), the domain structure which is same as the case of MFM image was observed. As the local electric field writing process to the $(Bi_{0.6}Ba_{0.4})FeO_3$ film, the surrounding area (3 μm square) was scanned by the conductive tip which was applied the DC voltage of +6.5 V, and the center area (1 μm square) was scanned by the conductive tip which was applied the DC voltage of -6.5 V, respectively. Fig. 3 (d), (e), and (f) show the topographic, EFM, and MFM images of the $(Bi_{0.6}Ba_{0.4})FeO_3$ film after applying DC voltage. In the center area of these images, ferroelectric and ferromagnetic single domain structure was imaged with negative electric and positive magnetic charge contrast by surrounding positive electric and negative magnetic charge contrast. This indicates that the clear ferroelectric domains with micrometer size were formed by local electric field writing, and the magnetization direction of center

Satoru YOSHIMURA
fax: +81-18-837-0409
tel: +81-18-889-2459
syoshi@gipc.akita-u.ac.jp

and surrounding area is upward and downward to film surface. From these results, the present multiferroic film is thought to be useful for novel magnetic recording devices driven by electric field.

REFERENCES

1) D. H. Wang, W. C. Goh, M. Ning, and C. K. Ong, *Appl. Phys. Lett.*, **88**, 212907 (2006). 2) D. G. Barrionuevo, S. P. Singh, R. S. Katiyar, and M. S. Tomar, *MRS Proceedings*, 1256 (2010). 3) H. Hojo, R. Kawabe, H. Yamamoto, K. Mibu, and M. Azuma, *1st Seminar of Ferroic-ordering and their manipulation D-1*, Campus Innovation Center Tokyo, 4th Jan (2016). 4) Y. Takeda, S. Yoshimura, M. Takano, H. Asano, and M. Matsui, *J. Appl. Phys.*, **101**, 09J514 (2007). 5) S. Yoshimura, H. Kobayashi, G. Egawa, H. Saito, and S.Ishida, *J. Appl. Phys.*, **109**, 07B751 (2011).

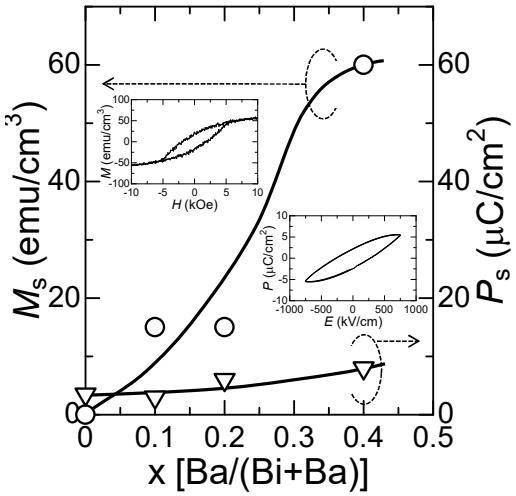

Fig. 1 Dependence of saturation magnetization and saturation electric polarization on Ba concentration for $(Bi_{1-x}Ba_x)FeO_3$ films.

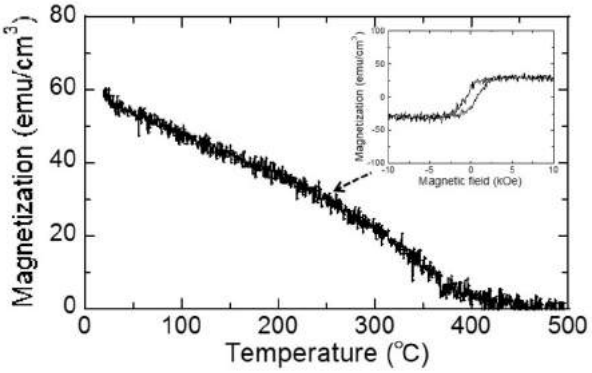

Fig. 2 Dependence of saturation magnetization on measuring temperature and the magnetization curve at the measuring temperature of 250 ℃ for $(Bi_{0.6}Ba_{0.4})FeO_3$ film.

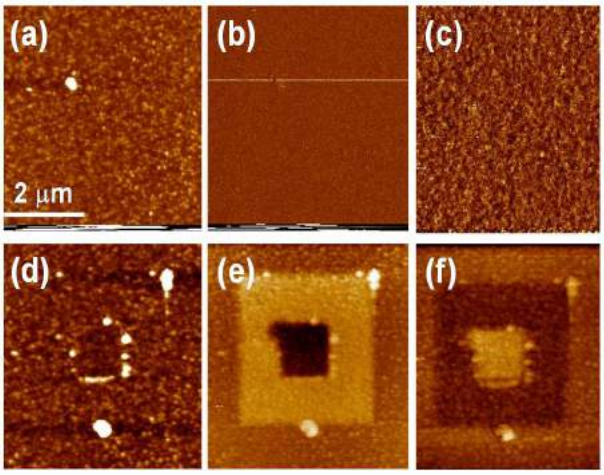

Fig. 3 (a) topographic, (b) EFM, and (c) MFM images of $(Bi_{0.6}Ba_{0.4})FeO_3$ film before applying DC voltage, and (d) topographic, (e) EFM, and (f) MFM images of $(Bi_{0.6}Ba_{0.4})FeO_3$ film after applying DC voltage.

BP-04

IN-SITU OBSERVATION OF DEVELOPMENT OF INTERNAL STRESS AT THE INITIAL STAGE OF FILM GROWTH

Shigeki NAKAGAWA, Masanari Nakagome, Hisanori HAYASHIBARA and Yota TAKAMURA
Tokyo Institute of Technology, O-okayama, Meguro, Tokyo, Japan, nakagawa@ee.e.titech.ac.jp

I. INTRODUCTION

It is important to clarify origins and mechanism of an internal stress induced in a film during the film formation, because the development of the internal stress is strongly related to the properties of films which are used for magnetic storage media and spintronic devices. Facing targets sputtering (FTS) system can form various functional ferromagnetic thin films owing to its unique configuration of substrate and targets. Ru/FeCo(B) thin films prepared by the FTS system shows large uniaxial magnetic anisotropy along the facing targets direction in the film plane.[1] Structural analysis using in-plane X-ray diffraction measurements clarified that the in-plane anisotropy was caused by an anisotropic residual stress formed during deposition process. However, the origin of the anisotropic residual stress has not been understood yet. We developed an in-situ stress observation system of an anisotropic internal stress at the initial stage of film growth by detecting displacement of cantilever substrate during the film deposition process to clarify initiation and accumulation of the internal stress σ.

II. EXPERIMENTAL

Fig. 1 shows in-situ stress observation system installed in the FTS system. Two rectangular thin glass substrates with a size of 45 mm x 5 mm x 30 μm were set at the film deposition region as cantilevers to detect internal stress σ along the cross-targets (facing) and the orthogonal direction to the cross-targets direction, respectivel. Internal stress σ formed along facing and orthogonal directions is evaluated using Stoney's law [2,3] from the displacement of the cantilevers measured by laser displacement sensors.

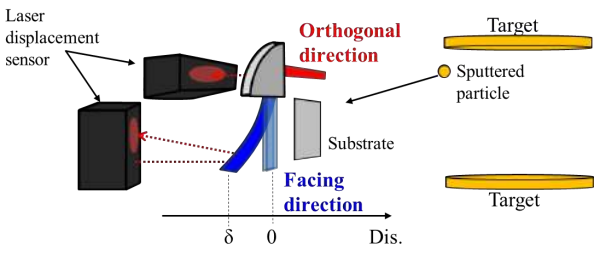

Fig.1 In-situ stress observation system installed in FTS

III. RESULTS AND DISCUSSION

It is well known that low and high Ar gas pressure cause compressive and tensile internal stress, respectively, to the films prepared by sputter-deposition method. However, the σ of all the films prepared at various Ar gas pressure shows tensile stress at the initial stage of the film growth. The tensile stress at the early stage of the film growth is caused by the formation of island structure and their agglomeration on the substrate. The critical thickness of the film t_p where the stress changes from tensile to compressive is around 1.5 to 8 nm depending on the surface energies of the film materials and that of the substrate.

Figure 2 (a), (b) and (c) show changes of a product of stress σ and nominal film thickness t as a function of t for Ti, Ru and FeCo, respectively. Ti, Ru and FeCo were deposited with Ar gas pressure of 0.04 Pa. Deposition rates for Ti, Ru, and FeCo were 0.066, 0.083 and 0.11 nm/s, respectively. It is recognized that the σ formed along facing and orthogonal directions are different. Positive and negative slope of $\sigma \cdot t$ - t curves indicate that tensile and compressive stress developed more dominantly than the other. $\sigma \cdot t$ - t curves for Ti (a) and Ru (b) can be divided into two zones: tensile stress growth (Zone-1), and compressive stress growth (Zone-2). The critical thickness between Zone-1 and Zone-2 is defined as t_{P1}. In Zone-1 ($t < t_{P1}$), the film growth mode is considered to be island growth, and the tensile stress would be caused by the surface tension or van der Waals's force [4] among the islands. In Zone-2 ($t > t_{P1}$), the compressive stress would be caused by the

Shigeki Nakagawa
E-mail: nakagawa@ee.e.titech.ac.jp
tel: +3-3726-3564

peening effect [5] that is observed in continuous layers prepared at relatively low sputtering gas condition. Thus, t_{P1} is considered to be the critical thickness that growth mode changed from island to layer-by-layer growth. t_{P1} of Ru was thicker than that of Ti as shown in Fig. 2 (a) and (b). This result is consistent with that the surface energy of Ru is larger than Ti.

A $\sigma \cdot t$ - t curve for a ferromagnetic FeCo film, shown in Fig. 2(c), was slightly different from those of Ti and Ru. The curve showed two peaks at t = 3.3 nm and 7.8 nm, and a dip was observed at t = 4.2 nm.

In-situ measurement of a resistivity ρ of the film is appropriate method to detect continuity of the film during the deposition. Fig.3 shows the change of $\sigma \cdot t$ and $\rho \cdot t$. as a function of nominal thickness of the FeCo film at the early stage of the film growth. Plane-view TEM images are also indicated for t of 3, 4.5 and 10 nm, respectively. The dip appeared at t of 4.2 nm corresponds to the phase transition from amorphous to crystalline stage, since the drastic change of the ρ and the lattice image in the TEM view are clearly observed at the thickness. In-situ observation system of the internal stress developed in this study is a powerful tool to detect the change of the phase transition and crystallization and as well as macroscopic deformation of the film structure.

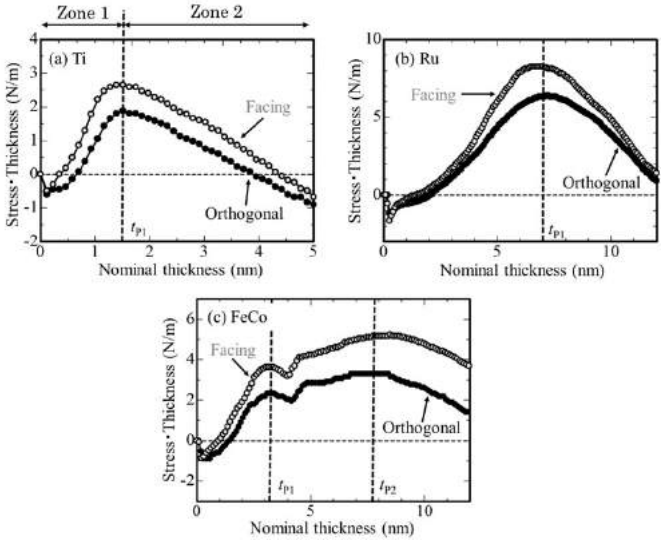

Fig.2 $\sigma \cdot t$ - t curves for (a) Ti (b) Ru and (c) FeCo films.

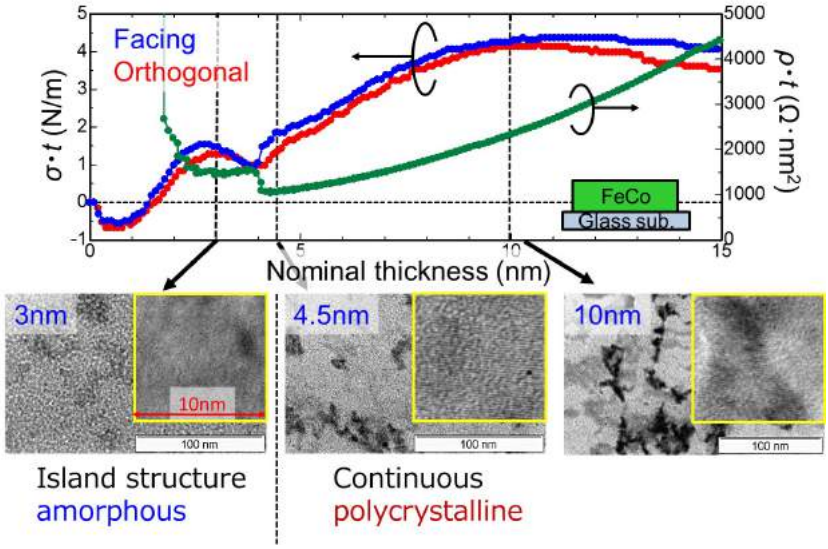

Fig.3 . change of $\sigma \cdot t$ and $\rho \cdot t$. as a function of nominal thickness t of the FeCo film. Plane-view TEM images for t of 3, 4.5 and 10 nm

REFERENCES

[1] A. Hashimoto, K. Hirata, T. Matsuu, S. Saito, and S. Nakagawa, IEEE Trans. Magn. 44, 3899 (2008).
[2] G.G.Storney, Proc. R. Soc. London Ser. A 82, 172 (1909).
[3] D. Sander, A. Enders, and J. Kirschner, Rev. Sci. Instrum. 66, 4734 (1995).
[4] M. Itoh, M. Hori, and S. Nadahara, J. Vac. Sci. Technol. B 9, 149 (1991).
[5] C. T. Wu, Thin Solid Films 64, 103 (1979).

BP-05

TWO-DIMENSIONAL MAGNETIC RECORDING SCHEMES USING CHANNEL POLARIZATION

Hidetoshi Saito
Department of Applied Physics, School of Advanced Engineering, Kogakuin University
1-24-2 Nishi-shinjuku, Shinjuku-ku, Tokyo, 163-8677, Japan

I. INTRODUCTION

Two-dimensional magnetic recording (TDMR) schemes have been one of important element technologies of the recent or future magnetic recording systems and expected to extend the storage density of the magnetic recording systems towards 10 terabits per square inch (Tb/in^2). In any TDMR schemes, it is desirable to apply a two-dimensional (2D) signal processing schemes to two-dimensional (2D) data sequences recoded on the magnetic recording medium. But, if we use 2D maximum likelihood (ML) sequence detectors to decode 2D data sequences optimally, there is a difficult computational complexity problem related to NP-hard for ML decoding complexity [1]. Therefore, if we design any 2D modulation code or error-correction code (ECC), we cannot help restricting code rate, encoding or decoding complexity from the view point of signal processing. In this research, it shows the new signal processing system for TDMR. In this proposed system, the design method of 2D modulation codes are based on channel polarization techniques for polar encoding [2]. As a result, these designed 2D modulation codes are equivalent to specific systematic polar codes [3]. Especially, using the fast transform methods in signal processing, it is known that complexity of polar encoding/decoding for the block size n is $O(n \log n)$. This characteristic of complexity is preferable for a TDMR scheme because a 2D modulation codeword is decoded by a realistic calculation.

II. TWO-DIMENSIONAL MODULATION CODES USING SYSTEMATIC POLAR CODES

It is known that polar codes are linear block codes which are introduced by Arıkan for effective channel coding [2]. In polar encoding, the polar transform is to apply the transform matrix $\boldsymbol{G}_n \equiv \boldsymbol{G}_2^{\otimes n}$, the n-th Kronecker power of $\boldsymbol{G}_2 = (\boldsymbol{g}_1 \boldsymbol{g}_2), \boldsymbol{g}_1 = (1\ \ 1)^T, \boldsymbol{g}_2 = (0\ \ 1)^T$, to the block of 2^n bits. The polar encoder chooses a set of ℓ rows of the matrix $\boldsymbol{G}_2$ to a form of $\ell \times 2^n$ matrix which is used as the generator matrix in the encoding procedure. In this encoding process, the information bits which correspond to this set is called “frozen bits”. The way of choosing this set is dependent on the channel W and uses a phenomenon called “channel polarization”. Channel polarization is an operation which produces 2^nchannels $\{W_2^{(i)}: 1 \le i \le 2^n\}$ from 2^n independent copies of a symmetric binary discrete memoryless channel such that the new parallel channels are polarized in the sense that their mutual information is either close to 0 (completely noisy channels) or close to 1 (perfectly noiseless channels). Every frozen bits are set to dummy symbols “0”. That is, these frozen bits are considered to be parity symbols in a codeword. In this research, the 2D modulation code is defined as follows. In polar encoding, $\boldsymbol{Y}_{2^n} = \boldsymbol{G}_{2^n} \times \boldsymbol{U}_{2^n}$, where $\boldsymbol{Y}_{2^n}, \boldsymbol{U}_{2^n}$ are a codeword and a binary information sequence with length of 2^n bits, respectively. Here, it satisfies that $\boldsymbol{G}_{2^n} \times \boldsymbol{G}_{2^n} = \boldsymbol{I}_{2^n}$, where $\boldsymbol{I}_{2^n}$ is the $2^n \times 2^n$ identity matrix. That means that systematic encoding with bit-reversal is assumed using a cascade of two non-systematic polar encoder circuits [3]. If a dummy symbol is inserted periodically into a codeword, these dummy symbols give a $(0, k_x, k_y; N)$ constraint, where a $(0, k_x)$-RLL constraint is defined for the down-track direction of each track and a k_y constraint is defined for the cross-track direction of every N tracks. In decoding, a codeword without dummy symbols is decoded by a successive cancellation decoder which decodes the bits $\hat{\boldsymbol{Y}}_{2^n}$ in order. If $\hat{\boldsymbol{U}}_{2^n} = \boldsymbol{G}_{2^n} \times \hat{\boldsymbol{Y}}_{2^n}$, it is able to obtain estimated information bits.

Hidetoshi Saito
E-mail: h-saito@cc.kogakuin.ac.jp
tel: +81-3-3340-2831
fax: +81-3-3348-3486

III. PROPOSED TDMR SCHEME USING BIT PATTERNED MEDIA

Fig. 1 shows the block diagram of the TDMR scheme. In this TDMR scheme with bit-patterned media (BPM), it uses the 2D generalized partial response (GPR) equalization system and one-dimensional (1D) *channel level log-likelihood ratio* (LLR) [3] detector. In Fig.1, $2N+1$-track recording is assumed for the TDMR scheme. For the readback TDMR channel, the readback signal of BPM is represented by the 2D Gaussian pulse response given by [4] and the normalized peak of the pulse amplitude is A_p. The noise sequence is additive white Gaussian noise (AWGN) with zero mean and variance σ_n^2.

IV. ERROR RATE PERFORMANCE OF TDMR SCHEMES

Fig. 2 shows the block error rate (BER) performances of the coded GPR systems. In Fig.2, the solid line show the BER performance of the proposed coding scheme with the (0,3,0,3) run-length limited (RLL) constraint using four-track recording. The dashed line shows the performance of the conventional binary low-density parity-check (LDPC) coding scheme [5] with the (0,9) RLL constraint using single-track recording. These coding scheme have the effective transmission rate η_e= 2.6, 0.92, respectively. The recording condition corresponds to the areal density of 4.0 Tb/in^2 given by [4]. In this simulation, the SNR is defined as SNR = $20\log_{10}A_p/\sigma_n$[dB]. As can be seen Fig. 2, the proposed coding scheme using four tracks outperforms that of the conventional coding scheme using a single track by about 5.0 dB of SNR gains at a BER of 10^{-5}.

V. CONCLUSIONS

In this research, new TDMR schemes based on channel polarization are proposed. These proposed schemes have 2D modulation codes which codewords are generated by systematic polar encoding method. Concatenated coding schemes between the 2D modulation code and non-binary LDPC code for four-track recording have the superior performance compared with the conventional 1D high rate binary LDPC coding scheme.

REFERENCES

1) E. Ordentlich and R. M. Roth, *IEEE Tran. Inf. Theory*, vol.57, no.12, pp.7661-7670, Dec. 2011.
2) E. Arikan, *IEEE Trans. Inf. Theory*, vol.55, no.7, pp.3051-3073, July 2009.
3) G. Sarkis, et al., *IEEE J. Sel. Areas Commun*., vol.32, no.5, pp.946-957, May 2014.
4) T. Wu, M. A. Armand and J. R. Cruz, *IEEE Trans. Magn*., vol.50, no.1, pp.1-11, Jan. 2014.
5) H. Zhong, T. Zhong and E. F. Haratsch, *IEEE Trans. Magn*., vol.43, no.7, pp.1118-1123, Mar. 2007.

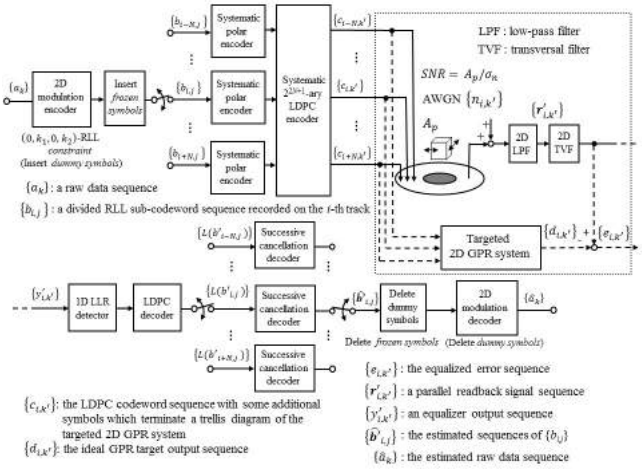

Fig. 1 Block diagram of TDMR scheme using BPM.

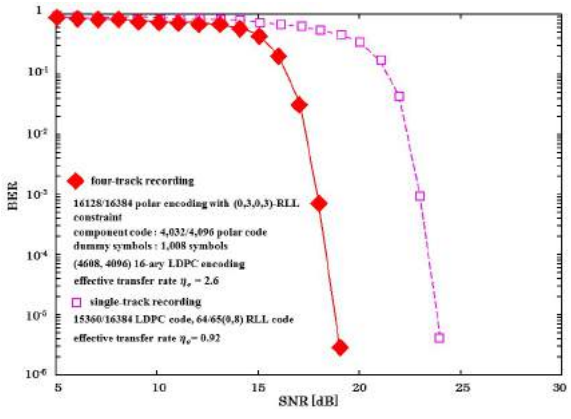

Fig. 2 Evaluated BER performances.

DEVELOPMENT OF BARIUM FERRITE TAPE MEDIA WITH HIGH SNR AND THERMAL STABILITY

Eiki OZAWA, Atsushi MUSHA, Atsushi MOROOKA, Masahito OYANAGI, Toshio TADA, and Hiroyuki SUZUKI

Recording Media Research Laboratories, FUJIFILM Corporation, Odawara 250-0001, Japan

I. INTRODUCTION

The total volume of digital data is increasing at an explosive pace and is projected to reach 44 zetabytes (ZB) by 2020—10 times the volume of data estimated for 2013 [1]. Particulate media-based tape storage systems are widely used for data backup and archiving applications because of their low cost, stability of the recording media for long-term data retention, and the reliability of information retrieval and reproduction. Therefore, it is important to continuously increase the storage capacity of magnetic tapes. Achieving a higher areal recording density, requires the volume size of magnetic particles to be reduced. However it is a cause of deterioration of thermal stability. In this study, we investigated whether high thermal stability can be obtained with magnetic tapes in fine barium ferrite (BaFe) particles.

II. EXPERIMENTS AND RESULTS

We have developed a magnetic tape medium (test tape) using BaFe particles as small as 1360 nm^3, which is approximately 30% smaller than those used in LTO7 tape. In addition, we improved the KuV/kT (by increasing the Ku) by adjusting the amount of substitution element.

(i) Parametric properties: The recording performance of the test tape and LTO7 tape was evaluated using a loop tester at a linear velocity of 2 m/s with an enhanced field tape write head (described in reference [2]), consisting of conventional $Ni_{45}Fe_{55}$ poles with an additional 200-nm-thick liner layer of CoFe deposited between the write gap and the trailing pole, and a giant magnetoresistive head. The broadband SNR was calculated from the root mean square voltage of the read-back signal corresponding to a written data pattern of a period of $2T$ (where T is the channel bit period) and the noise, which was the integral value of the power spectral density from 0 to $1/T$ Hz, as measured with a spectrum analyzer.

Fig.1 shows the dependence of the output of the test tape and LTO7 tape on the recording linear density. The test tape exhibited a higher output and an improved frequency response than the LTO7 tape. The higher output of the test tape is attributed to both the high degree of perpendicular orientation (perpendicular squareness ratio: 0.79, 0.66 for test tape and LTO7 tape respectively) and a reduction in the surface roughness (AFM Ra: 1.7 nm, 2.0 nm for test tape and LTO7 tape respectively).

Fig.2 shows the signal and modulation noise spectrum at a linear density of 350 kfci (kfci = 1000 flux changes per inch). Since the surface roughness is smooth, it is conceivable that the media noise of the test tape increases with the output as compared with the LTO7 tape, but the same media noise as the LTO7 tape is obtained. This is primarily thought to result from the reduction in the magnetic particle volume from 1950 nm^3 to 1360 nm^3. As a result, the BB-SNR of the test tape was 4.0 dB higher than that of the LTO7 tape at a linear density of 350 kfci.

(ii) Thermal stability: In order to investigate the effect of enhancing the thermal stability by improving the KuV/kT, we compared the decay rates of the test tape both before and after KuV/kT improvement of the test tape. Fig.3 shows the signal degradation of the test tape and that of the tape before KuV/kT improvement. The decay rate of the test tape was 0.029 dB/decade. This value was lower than that of the tape before KuV/kT improvement (0.071 dB/decade) and corresponds to maintaining the bit error rate, which is permitted to be less than 1×10^{-4} when using the GPR4ML-AR model that is implemented in an actual tape drive after 10^9 seconds (approximately 30 years) storage at 24 °C [3-5].

Eiki Ozawa
E-mail: eiki.ozawa@fujifilm.com
Tel: +81-465-32-9514

III. SUMMARY

We successfully developed a BaFe particulate tape of which the BB-SNR was 4.0 dB higher than that of a commercially available LTO7 tape at a linear density of 350 kfci and of which the thermal stability was acceptable for long-term archiving over approximately 30 years. We believe this advanced BaFe particulate tape is a promising candidate for next-generation magnetic particulate tapes. Furthermore, we expect tape-storage systems using BaFe particulate media to continue to provide sufficient storage capacity at a low total cost of ownership for many years to come.

REFERENCES

1) IDC, "The Digital Universe of Opportunities: Rich Data and the Increasing Value of the Internet of Things," http://www.emc.com/collateral/analyst-reports/idc-digital-universe-2014.pdf.
2) S. Furrer et al., "85.9 Gb/in^2 Recording Areal Density on Barium Ferrite Tape," *IEEE Trans. Magn.* 51 (4) 1-7, (2015).
3) Y. Kurihashi et al., "Effect of thermal conditions on bit error rate for barium-ferrite particulate media," *IEEE Trans. Magn.* 49 3760-3762, (2013).
4) Y. Kurihashi et al., "Influence of Thermal Stability factor Distribution for Barium Ferrite Magnetic Tape," *ITE technical report* 37(30) 25-29, (2013).
5) O. Shimizu et al., "Development of advanced barium ferrite tape media," *J. Magn. Magn. Mater.,* 400(2) 365-369, (2016).

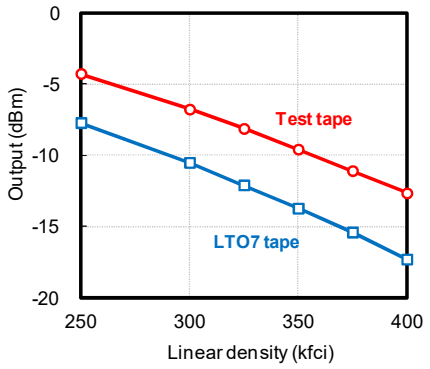

Fig. 1 Recording linear density vs. 2T output.

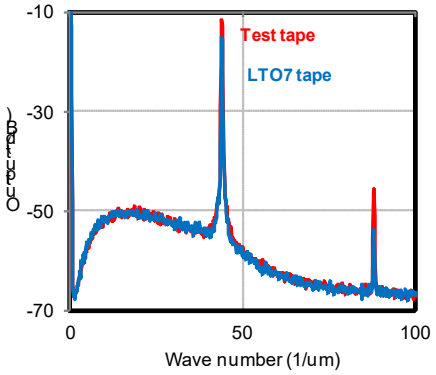

Fig. 2 Signal and modulation noise spectrum at a linear density of 350 kfci.

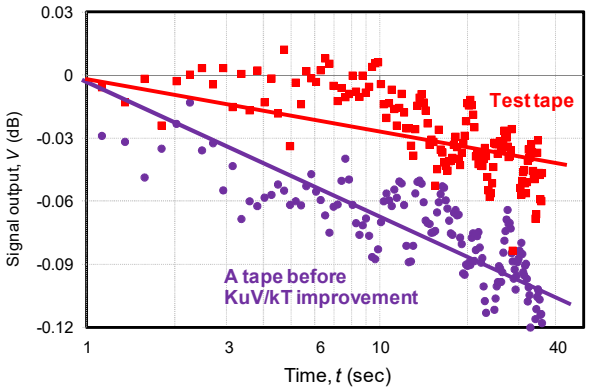

Fig. 3 Signal decay of test tape and the tape before KuV/kT improvement. Solid lines are results fitted with 0.029 [dB/decade] (test tape), and 0.071 [dB/decade] (tape before KuV/kT improvement).

MAGNETIC PROPERTIES OF EPITAXIAL BARIUM HEXAFERRITE (0001) THIN FILMS DEPOSITED BY RADIO FREQUENCY MAGNETRON SPUTTERING

R. PATEL*[1], Y. IKEDA[1], H. ONADA[1], T. TAINOSHO[1], Y. HISAMATSU[1],
S. SHARMIN[1], E. KITA[1, 2], and H. YANAGIHARA[1]
1) Division of Applied Physics, Graduate School of Pure and Applied Sciences,
University of Tsukuba, Tsukuba, Ibaraki 305-8573, Japan
2) National Institute of Technology Ibaraki College, Hitachinaka, Ibaraki 312-8508, Japan

Barium hexaferrite epitaxial thin films is a potential candidate for microwave devices and data storage application, due to its uniaxial magnetic anisotropy, moderate saturation magnetization, high curie temperature, and low microwave losses [1-5]. Previous studies showed that the barium hexaferrite thick films with buffer layer grown by liquid phase epitaxy, pulsed laser deposition, and radio frequency sputtering methods have the lower saturation magnetization and squareness ratio [5-8]. Therefore, the high quality thin film growth technique to achieve large magnetization comparable to the bulk is required for the above purpose. Thus, the purpose of this research is to understand the effect of thickness and composition on magnetic behavior of the barium hexaferrite (0001) thin films.

The epitaxial growth of barium hexaferrite (0001) thin films was performed with two different target composition (stoichiometric: $BaFe_{12}O_{19}$, and barium rich: $BaFe_{10}O_x$) on an α-Al_2O_3 (0001) substrate via radio frequency (RF) magnetron sputtering. Hereafter, we refer the samples grown with the stoichiometric target as BaM1(0001) and with the Ba-rich target as BaM2(0001). The flow rate of Ar was 10 sccm; total pressure inside the sputtering chamber was maintained at 0.4-0.5 Pa. The RF power of the stoichiometric and barium rich target was set at 100 W and 50 W. The barium hexaferrite (0001) thin films were post annealed in atmosphere at 1000 °C for 10 minute. The BaM1(0001) thin films of 25, 53, 83, 100, and 135 nm thicknesses were deposited, similar thicknesses is also deposited with BaM2(0001) thin films.

The RHEED image after deposition indicates the epitaxial growth of barium hexaferrite thin films. The XRD was used to characterize the structural properties for all samples. The dominant reflection peaks are (006), (008) and (0014), which indicate excellent c-axis orientation. It is found that the value of the lattice constant c of the barium hexaferrite deviates from its bulk value 23.2 Å [ICDD PDF 01-084-0757]. In all samples of BaM1(0001) thin films using the position of (008) bragg peak, the obtained value is lower in the range of 23.0 to 23.1 Å, but in case of BaM2(0001) thin films for all sample, the obtained value range from 23.1 to 23.2 Å. This indicates the crystallites of the thin films are under some strain.

The magnetic properties of BaM1(0001) and BaM2(0001) thin films deposited on α-Al_2O_3 (0001) substrate are shown in fig 1(a-b). The barium hexaferrite (0001) thin films grown under the optimal conditions exhibit magnetic anisotropy with the easy axis of magnetization perpendicular to the films with a high squareness ratio of 0.7. The BaM1(0001) thin film of thickness 101 nm shows saturation magnetization M_s (out-of-plane) of 304 emu/cm^3, while the BaM2(0001) thin film (thickness 104 nm) shows M_s (out-of-plane) of 379 emu/cm^3, which is comparably equal to the bulk value of $BaFe_{12}O_{19}$ (380 emu/cm^3)[2].While the effective uniaxial magnetic anisotropy K_u^{eff} of the BaM1(0001) thin film of 25 nm is $K_u^{eff} = 3.12 \times 10^6$ erg/cm^3. On the other hand, BaM2(0001) thin film of 23.5 nm is $K_u^{eff} = 2.3 \times 10^6$ erg/cm^3. Although the saturation magnetization in case of BaM1(0001) thin films is almost constant for all film thickness, the magnetic anisotropy constant decreases with increasing film thickness and becomes almost constant over 100 nm. But in case of BaM2(0001) thin films, the saturation magnetization get closer to the bulk value with increasing the film thickness.

Rutherford backscattered spectroscopy (RBS) was performed to evaluate the composition of the BaM1(0001) thin film of 100 nm. The experimentally obtained ratio of BaM1(0001) thin film is off-

s1530111@u.tsukuba.ac.jp

stoichiometric Ba:Fe = 1:9, suggesting that some defects exists in the obtained hexaferrite films. The crystal structure of barium hexaferrite is close-packed layers form with four fundamental blocks, S, S*, R and R*, among which the S* and R* blocks can be obtained simply through the rotation of the S, and R blocks respectively, by 180° with respect to the c axis. A pair of S and R or S* and R* conserves charge neutrality and Ba ions occupies in R (or R*) block. Therefore, an off-stoichiometric M-type hexaferrite may involve the other oxide block such as T-block. The estimated T-block is about 23%, which affects neither magnetization nor magnetic anisotropy. The rest of S R S* R* block influence the M_S and $\boldsymbol{K_u^{eff}}$, which is 292 emu/cm^3 and 2.46 Merg/cm^3 and it is close to the experimental value. Therefore, such reduction of M_s and $\boldsymbol{K_u^{eff}}$ in BaM1(0001) thin films could be explained by an existence of T-block.

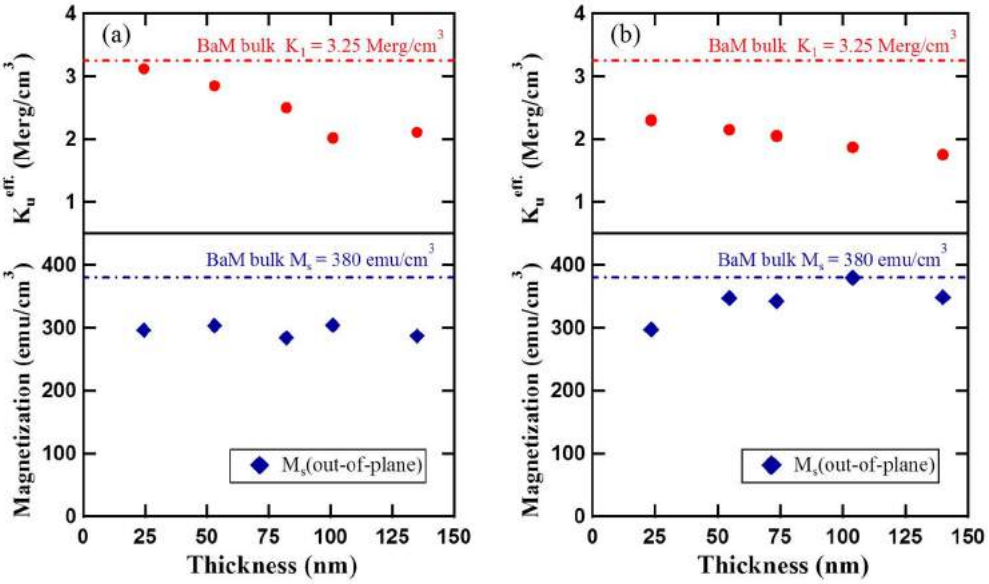

Fig. 1(a-b) Plot of saturation magnetization (out-of-plane) and effective uniaxial magnetic anisotropy ($\boldsymbol{K_u^{eff}}$) of BaM1(0001) and BaM2(0001) thin films vs different thicknesses.

References

1. B. T. Shirk, W. R. Buessem, Temperature dependence of M_S and K_1 of $BaFe_{12}O_{19}$ and $SrFe_{12}O_{19}$ single crystals, J. Appl. Phys. 40, 3 (1969).
2. R. O. Handley, Modern Magnetic Materials (Wiley, New York, 2000).
3. L. Zhang, X. D. Su, Y. Chen, Q. F. Li, and V. G. Harris, Radio-frequency magnetron sputter-deposited barium hexa-ferrite films on Pt-coated Si substrates suitable for microwave applications, Scripta Mater. 63, 492–495 (2010).
4. R. D. Weir, Carl W. Nelson, Vertical-Magnetic-Recording medium with barium ferrite magnetic layer, United States Patent 6110557, 29 (2000).
5. S. D. Yoon and C. Vittoria, Thick M-type barium hexaferrite films grown on garnet substrates, J. Appl. Phys., 96, 4 (2004).
6. X. H. Liu, M. H. Hong ,W. D. Song , G. X. Chen, H. M. J. Lam, J. P. Wang, T. C. Chong, Barium ferrite ($BaFe_{12}O_{19}$) thin films prepared by pulsed laser deposition on MgO buffered Si substrates, Appl. Phys. A 80, 611–614 (2005).
7. H. Xu, W. Zhang, B. Peng, W. Zhang, Properties of barium hexa-ferrite thin films dependent on sputtering pressure, Appl. Surf. Sci. 257, 2689–2693 (2011).
8. Z. Chen, A. Yang, K. Mahalingam, K. L. Averett, J. Gao, G. J. Brown, C. Vittoria, and V. G. Harris, Structure, magnetic, and microwave properties of thick Ba-hexaferrite films epitaxially grown on GaN/Al2O3 substrates, Appl. Phys. Lett. 96, 242502 (2010).

PROPOSAL OF GRAIN BOUNDARY OXIDES FOR HIGH K_u $Co_{80}Pt_{20}$ GRANULAR MEDIA WITH SMALL GRAIN SIZE

Ryosuke KUSHIBIKI [1,2], Kim Kong THAM[1], Shintaro HINATA[2], and Shin SAITO[2]

[1]Tanaka Kikinzoku Kogyo K.K., 22, Wadai, Tsukuba, Ibaraki 300-4247, Japan
[2]Department of Electronic Engineering, Graduate School of Engineering, Tohoku University, 6-6-05, Aoba, Aramaki, Aoba, Sendai 980-8579, Japan

I. INTRODUCTION

CoPt-oxide granular media with columnar grain growth have been widely used for perpendicular magnetic recording. To further increase the recording density of the media, enhancement of magnetocrystaline anisotropy (K_u) and reduction of magnetic grain diameter (*GD*) are required. In the previous study, it was found that a granular medium with high K_u can be obtained when oxide with low melting point (T_m), especially B_2O_3, was utilized due to the promotion of columnar grain growth[1)]. However, the effect of T_m of the oxide on the *GD* is still unclear. Therefore, in this report, after examining the influence of various grain boundary oxides on *GD*, we will discuss about the guiding principle of choosing grain boundary oxide materials.

II. RESULTS AND DISCUSSION

Figure 1 show dependence of (a) magnetocrystalline anisotropy (K_u) and (b) grain diameter (*GD*) for $Co_{80}Pt_{20}$ −30vol% single oxide granular media with d_{mag} of 16 nm on melting point (T_m) of the grain boundary oxides materials. The inset shows the definition of *GD*, which is evaluated from CoPt (11.0) diffraction from the XRD in-plane profiles by Scherrer's equation[2,3)]. Here, from the result of out-of-plane XRD profiles for the granular media with grain boundary oxide materials with various T_m (the result are not shown here), these granular structure magnetic grains are considered to have *c*-plane sheet texture orientation. When T_m of oxide increases from 450 to 2410℃, K_u and *GD* decrease from 7.7 to 4.1×10^6 erg/cm^3 and from 5.6 to 3.0 nm, respectively. From this result, it suggests that a granular medium with both high K_u and low *GD* cannot be realized by only employing single oxides.

We consider that a granular medium with reasonably high K_u and small *GD* may be achievable by utilizing double grain boundary oxides with moderate T_m which consist of high and low T_m oxides. To verify the effect of double oxides, second oxides with T_m ranging from 450 to 2330℃ and first oxide of low T_m (B_2O_3) were added to $Co_{80}Pt_{20}$ alloy ($Co_{80}Pt_{20}$-15vol% B_2O_3-15vol% second oxides). Figure 2 shows dependence of K_u and *GD* on T_m of various second oxides. When T_m of the second oxide is lower than 1857℃ (TiO_2), K_u is almost comparable with that of B_2O_3. For T_m higher than 1857℃, K_u decreases. In the case of *GD*, it is almost constant for T_m of the second oxide lower than 1723℃ (SiO_2). When T_m is higher than 1723℃, *GD* decreases. From this result, the addition of TiO_2 for the second oxide is effective to realize a granular medium with high K_u and small *GD*.

Figure 3 shows in-plane-view TEM of $Co_{80}Pt_{20}$-15vol% B_2O_3-15vol% typical second oxide (second oxide: (i) B_2O_3 (T_m: 450℃), (ii) SiO_2 (T_m: 1723℃), (iii) TiO_2 (T_m: 1857℃) and (iv) Cr_2O_3 (T_m: 2330℃)). Observing the detailed in-plane-view TEM of high T_m second oxides such as TiO_2 and Cr_2O_3, grain boundaries with different thicknesses are confirmed. The thick grain boundaries are similar to that of the second oxide of B_2O_3. Inside some magnetic grains thin grain boundaries can also be observed. It is considered that the existence of the thin grain boundaries induces the *GD* reduction. Generally, the variation of the grain boundary thickness will lead to a wide grain size distribution. The application of underlayer with smaller grains size than current one may be effective to obtain a granular medium with homogeneous grain size.

Ryosuke KUSHIBIKI
fax: +81-29-864-8176
tel: +81-29-864-8175
r-kushibiki@ml.tanaka.co.jp

REFERENCES

1) K. K. Tham, R. Kushibiki, S. Hinata, and S. Saito, *Jpn. J. Appl. Phys*., **55**, 07MC06 (2016).
2) P. Scherrer, *Göttinger Nachrichten Gesell*., **2**, 98 (1918).
3) D. M. Smilgies, J. Appl. Cryst. **42**, 1030 (2009).

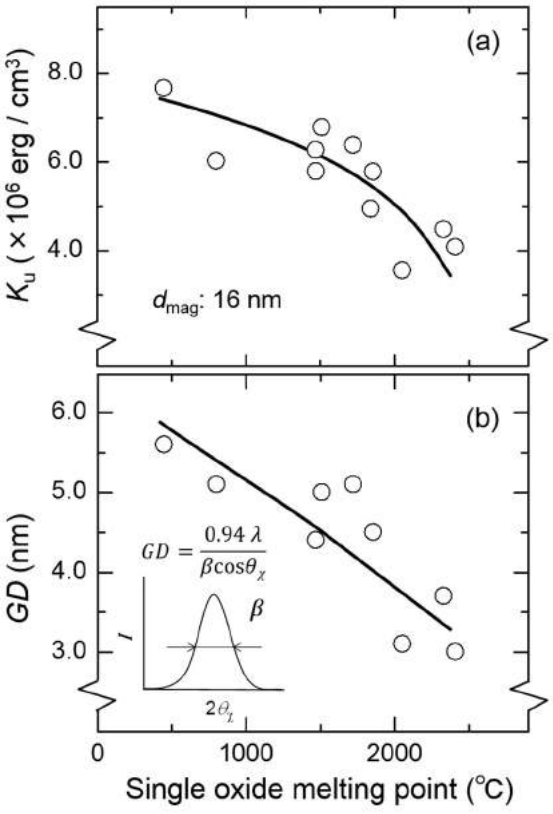

Fig. 1. Dependence of (a) magnetocrystalline anisotropy (K_u) and (b) grain diameter (GD) for $Co_{80}Pt_{20}$−30vol% single oxide granular media with d_{mag} of 16 nm on melting point (T_m) of the grain boundary oxides materials. The inset shows the definition of GD, which is evaluated from CoPt (11.0) diffraction from the XRD in-plane profiles by Scherrer's equation[2,3].

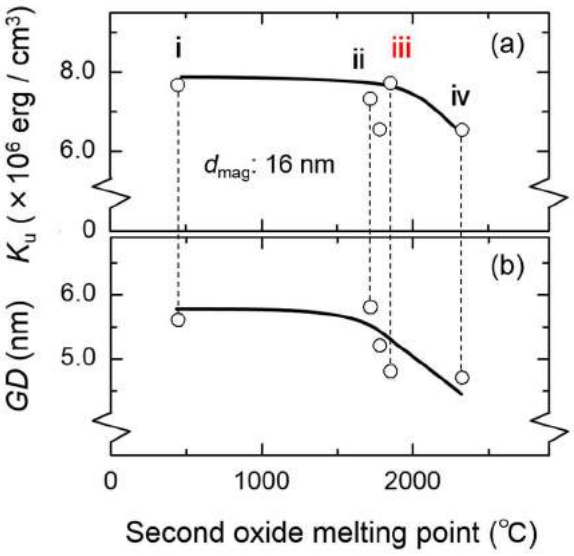

Fig. 2. Dependence of (a) K_u and (b) GD of various oxides in $Co_{80}Pt_{20}$-15vol% B_2O_3-15vol% second oxide granular media with d_{mag} of 16 nm on T_m of the grain boundary oxides materials. In-plane-view TEM of these samples (second oxide: (i) B_2O_3 (T_m: 450℃), (ii) SiO_2 (T_m: 1723℃), (iii) TiO_2 (T_m: 1857℃) and (iv) Cr_2O_3 (T_m: 2330℃)) are shown in Figure 3.

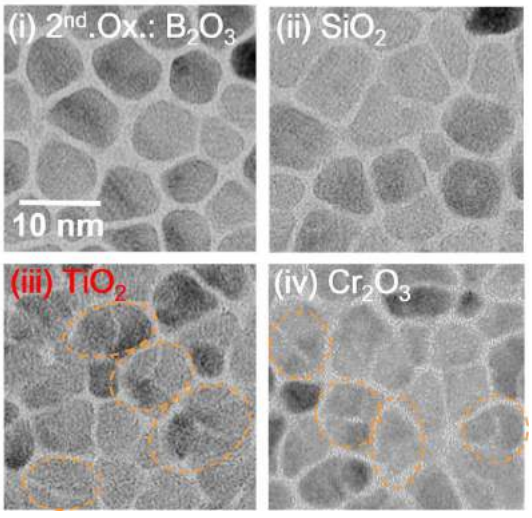

Fig.3 In-plane-view TEM of granular media shown in Figure 2.

FERROMAGNETIC RESONANCE FOR EXCHANGE-COUPLED TWO-DIMENSIONAL ASSEMBLY OF NANO-COLUMNS

Shintaro HINATA, Daiji HASEGAWA and Shin SAITO,
Tohoku University, Sendai, Miyagi, 980-8579 JAPAN

I. INTRODUCTION

The influence of intergranular exchange coupling (J_g) between columns and the magnetic anisotropy field (H_k) distribution (ΔH_k) on the ferromagnetic resonance (FMR) of the magnetic nano-column assembly is numerically investigated using the Landau–Lifshitz‐Gilbert equation. The nano-column assembly is assumed to represent granular perpendicular magnetic recording (PMR) media. The FMR measurements of the PMR media with $J_g > 1$ erg/cm^2 can be used to evaluate the intrinsic values of H_k and the damping constant (α) despite the existence of ΔH_k. In case of PMR media with $J_g = 0$ erg/cm^2, the intrinsic value of α can be evaluated. However, H_k will be underestimated depending on the degree of ΔH_k.

II. RESULTS AND DISCUSSION

Fig. 1 shows the schematic diagram of the computational model for the magnetic nano-column assembly supposed for the granular PMR media. The assembly was assumed to consist of 32 × 32 columns. In addition, a single column comprised four computational units of size 8 × 8 × 4 nm. The magnetic easy axes of all units were assumed to align with the z–direction. Each unit was assumed to have an M_s of 616 emu/cm^3, γ of 1.936 × 10^7 Oe^{-1}s^{-1}, and α of 0.032 corresponding to $Co_{74}Pt_{16}Cr_{10}$–8 mol (SiO_2) [1]. H_k of each column had a Gaussian distribution with an average (H_k^{ave}) of 16.2 kOe and full width at half maximum (ΔH_k) of 0–2 kOe. The intergranular exchange coupling acting between contiguous columns (J_g) was changed from 0 to 5 erg/cm^2.

A. FMR for PMR media without intergranular exchange coupling

Fig. 2 (a) shows χ" curves for PMR media with various ΔH_k. The resonance field (H_{res}) increased from 2.6 to 2.8 kOe with increase in ΔH_k from 0.0 to 2.0 kOe. The line width as given by the full width at half maximum (ΔH_{res}) took constant value of 0.71 kOe, even with changes in ΔH_k. When M_s was increased to 1000 emu/cm^3 and H_k to 15 kOe, H_{res} showed a similar shift to the higher field side with increase in ΔH_k (details not shown in figure). For reference, values of H_{res} and ΔH_{res} were estimated from the conventional Kittel equation [2]. The estimated values of H_{res} (H_{res}^{Kittel}) and ΔH_{res} (ΔH_{res}^{Kittel}) are 2.6 kOe and 0.71 kOe, respectively. The aforementioned behavior of H_{res} cannot be explained by the Kittel mode. To discuss the aforementioned behavior of H_{res} and ΔH_{res} against an increase in ΔH_k, the χ" curve of each column is shown in Fig. 2 (b) and (c). In this figure, black lines show the χ" curve for each column and the red line shows the χ" curve for the medium. In the case of (b) $\Delta H_k = 0.0$ Oe, the χ" curves of all columns were in good agreement. This indicates that the magnetic moment of each column was resonating in the parallel arrangement. On the other hand, in the case of (c) $\Delta H_k = 2.0$ kOe, the χ" curve for each column had one large maximum at the same H_{bias} of 2.8 kOe, and had countless local maxima and minima in the range $H_{bias} < 2.8$ kOe. These local maxima and minima canceled between columns. As a result, clear resonances did not appear on the χ" curve of the media, and a long tail by the lower field side of the H_{res} of 2.8 kOe was observed on the χ" curve of the media. This suggests that the parallel arrangement of the magnetic moment of each column cannot be maintained at resonance (hereafter, called as the incoherent mode).

B. FMR for PMR media with intergranular exchange coupling

In figure 3 (a), χ" curves for FMR media with ΔH_k of 2.0 kOe and various J_g of 0.0, 1.0, and 5.0 erg/cm^2 are shown. In the case of $J_g > 1.0$, the χ" curves completely overlapped and H_{res} values of 0.71 kOe were in agreement with H_{res}^{Kittel}. The value of ΔH_{res} did not depend on ΔH_k. This result suggests that the resonance of the magnetic moment of each column changes from the incoherent mode to the Kittel mode with increase in J_g.

Figure 3 (b) and (c) shows the χ" curve of each column for these media. In the case of (c) $J_g = 5.0$ erg/cm^2, almost all of the local maxima and minima and the maximum at the 2.6 kOe as observed for

Shintaro HINATA
s_hinata@ecei.tohoku.ac.jp

H_{res}^{Kittel} mainly remained. This indicates that the resonance changed from the incoherent mode to a state near the Kittel mode, because of the increase in intergranular exchange coupling.

III. CONCLUSION

From the viewpoint of evaluating the intrinsic magnetic properties, the FMR measurement of PMR media with $J_g > 1$ erg/cm^2 can help in evaluating the intrinsic values of H_k and α despite the existence of ΔH_k. In the case of PMR media with $J_g = 0$ erg/cm^2, the intrinsic value of α can be evaluated. On the other hand, H_k is underestimated depending on the degree of ΔH_k, even if the H_k distribution has a large value of 2 kOe. However, the difference of the evaluated and intrinsic values of H_k is 0.2 kOe at most. In the presentation, FMR for more simple assembly is considered to understand the relationship between H_{res} and J_g.

REFERENCES

[1] S. Hinata, et al., *J. Appl. Phys.*, **105**, 07B718 (2009).
[2] C. Kittel, *Phys. Rev.*, **73**, 155, (1948).

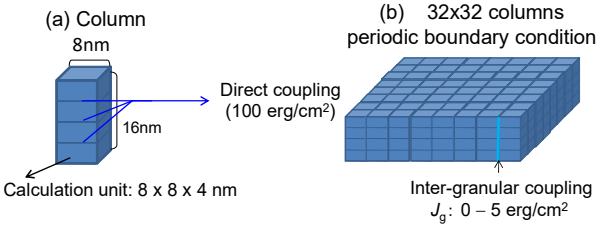

Fig. 1 Schematic views of the computational model for PMR media. (a) Each crystalline column was assumed to be composed of four computational units of 8 × 8 × 4 nm size. (b) Media was assumed to be composed of 1024 columns.

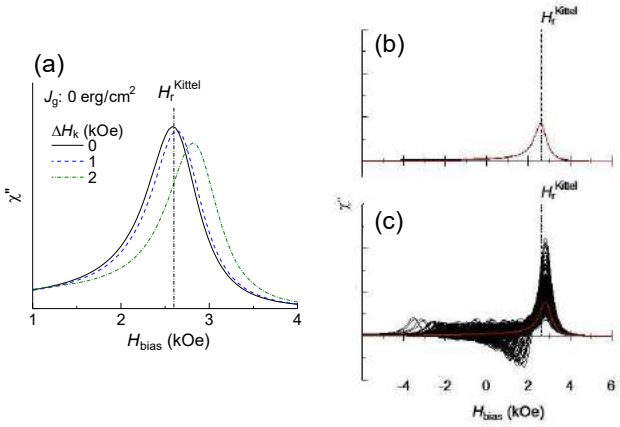

Fig. 2 (a) H_{bias} dependence of the χ" of PMR media with no intergranular exchange coupling (J_g) and various ΔH_k. Dependence of χ" on H_{bias} for each nano-column with (b) ΔH_k = 0 and (c) 2 kOe.

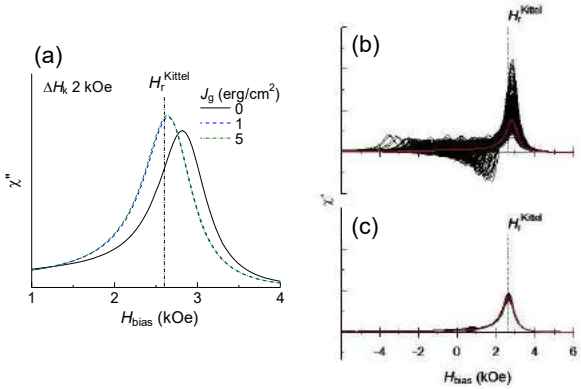

Fig. 3 (a) H_{bias} dependence of the χ" of PMR media with ΔH_k of 2.0 kOe and various J_g. Dependence of χ" on H_{bias} for each column in the PMR media with (b) J_g = 0 and (c) 5.0 erg/cm^2.

ENHANCEMENT OF $L1_0$ ORDERING IN ELECTRODEPOSITED FePt NANODOT ARRAYS

S. WODARZ[1], S. HASHIMOTO[1], M. KAMBE[1], G. ZANGARI[2], and T. HOMMA[1]

[1] Waseda University, Tokyo, Japan, t.homma@waseda.ne.jp

[2] University of Virginia, Charlottesville, USA, gz3e@eservices.virginia.edu

I. INTRODUCTION

Electrodeposition processes have been widely used to fabricate magnetic thin films and micro/nano structures. In this work, we have attempted to utilize this process to fabricate ferromagnetic nanodot arrays [1] by combining electron beam lithography (EBL) and electrodeposition for use in bit patterned media (BPM) [2]. The equiatomic FePt alloy with $L1_0$ order phase has been considered as one of the most promising candidates for use in BPM due to its high magnetocrystalline anisotropy, K_u [3], which enables recording density beyond several Tbit/in^2. In previous work, we have succeeded in achieving structural ordering and magnetic hardening of electrodeposited FePt films [1], however, high temperature annealing up to 650 ºC was needed for the phase transition to $L1_0$ ordered structure, which caused degradation of uniform geometry of nanodot arrays; lowering of annealing temperature of FePt was therefore strongly needed to enhance the $L1_0$ ordering. In order to solve this problem, in this work, we have attempted to fabricate uniform $L1_0$-FePt nanodot arrays by synthesizing a multilayer FePt structure [4] and FePt-Cu alloy structure [5] to enhance the ordering process of FePt under lower annealing temperature or heating time requirements.

II. EXPERIMENTAL METHODS

Nanopore patterned substrates were prepared by EBL, which has a high resolution for fabricating single nanometer-sized pores onto sputter deposited Ru (60 nm thick) / Ti (5 nm thick) / n-Si (100) substrate. Electrodeposition of FePt was carried out into the nanopores to fabricate nanodot arrays with 15 nm diameter and 35 nm pitch under the conditions summarized in Table 1. Post annealing treatment of deposited FePt was carried out using a rapid thermal annealing system under forming gas (Ar 90 % and H_2 10 %). The multilayer structure consisted of Fe- and Pt-rich layers with various thickness, deposited sequentially in the same electrolyte by changing the applied potential and deposition duration for each layer; pulse deposition of Fe- and Pt-rich layer was performed with -1.4 and -0.8 V (vs. Ag/AgCl), respectively. Single layer FePt films were deposited with constant potential of -1.0 V (vs. Ag/AgCl). For the fabrication of FePt-Cu alloy, $CuSO_4$ was added into the bath condition of Table1. The composition of FePt-Cu alloy was controlled with applied potential and concentration of $CuSO_4$ to achieve near-equiatomic composition of (FeCu)Pt and Cu composition of 20-30 at%.

III. RESULTS AND DISCUSSION

To investigate the phase transformation of the multilayer and single layer FePt films, crystal structure of 20 nm-thick films was characterized after annealing at 450 ºC for 1 h by x-ray diffraction (XRD). Upon annealing, single layer film showed no peaks of $L1_0$ structure, whereas multilayer films showed (111), (200), and (001) peaks of $L1_0$ structure. To further investigate the phase transformation, degree of $L1_0$ ordering of the annealed films was evaluated from the lattice constant of c-axis from XRD patterns. The c-lattice constants of multilayer and single layer films were evaluated to be 3.62 and 3.74 Å, respectively upon annealing at 450 ºC, which suggested the enhancement of $L1_0$ ordering in multilayer structure to shrink the c-lattice constant. In addition, the out-of-plane coercivity of multilayer film after annealing at 450 ºC was 6.6 kOe, whereas single layer film showed 1.0 kOe. Furthermore, coercivity increased up to 9.0 and 12.3 kOe for multilayer and single layer upon annealing at 650 ºC, suggesting that the phase transformation and magnetic hardening was strongly facilitated in the multilayer structures. Based on these

Takayuki Homma
E-mail: t.homma@waseda.ne.jp
Tel: +81-3-5286-3209

results, fabrication of FePt nanodot arrays with multilayer structure was attempted by depositing FePt into nanopore patterned substrate with 15 nm diameter and 35 nm pitch, and uniform nanodot arrays without deterioration were successfully formed after post annealing process. Furthermore, phase transformation of nanodot arrays was successfully achieved to form FePt nanodot arrays with $L1_0$ structure; a TEM image shows uniform fringes in the perpendicular direction from the substrate without grain boundaries (Fig. 1), suggesting a formation of a single crystal.

Subsequently, enhancement of $L1_0$ ordering was attempted by addition of Cu to form FePt-Cu alloy. Upon annealing at 450 ºC, XRD patterns of FePt-Cu showed peaks of $L1_0$ structure, and (001) peak shifted to higher 2θ angle compared to FePt alloy, which provides evidence of FePt-Cu alloying. In addition, magnetic hardening was observed with FePt-Cu films upon annealing at 450 ºC, whereas the binary alloy showed no magnetic hardening under annealing at 450 ºC. Furthermore, coercivity of FePt-Cu films increased up to 6.0 kOe by controlling the c/a lattice ratio with optimization of the alloy composition. In addition, fabrication of FePt-Cu nanodot arrays with single crystal of $L1_0$ structure was successfully demonstrated due to the facilitation of $L1_0$ ordering by addition of Cu. These results demonstrate successful fabrication of uniform $L1_0$-FePt nanodot arrays with Tbit/in^2 level density, by applying a multilayer structure or addition of Cu to enhance the $L1_0$ ordering.

REFERENCES

1) T. Homma, S. Wodarz, D. Nishiie, T. Otani, S. Ge, G. Zangari, “Fabrication of FePt and CoPt Magnetic Nanodot Arrays by Electrodeposition Process”, *Electrochem. Soc. Trans.,* 64(31) 1-9, (2015).
2) B. D. Terris, T. Thomson, “Nanofabricated and self-assembled magnetic structures as data storage media”, *J. Phys. D: Appl. Phys.*, 38 R199-R222, (2005).
3) D. Weller, et al., “High Ku Materials Approach to 100 Gbits/in^2”, *IEEE Trans. Magn.,* 36(1) 10-15, (2000).
4) Y. Endo, N. Kikuchi, O. Kitakami, Y. Shimada, *J. Appl. Phys.*, 89(11) 7065-7067, (2001).
5) T. Maeda, T. Kai, A. Kikitsu, T. Nagase, J. Akiyama, *J. Appl. Phys.*, 80(12) 2147-2149 (2002).

Table 1 Electrodeposition conditions

Chemicals	Concentration / mM
$(NH_4)_2C_6H_6O_7$	150
$Fe_2(SO_4)_3$	50
NH_2CH_2COOH	150
$NaNO_2$	100
$(NH_4)_2SO_4$	100
$Pt(NO_2)_2(NH_3)_2$	15
Bath temperature	75 °C
pH	8
Reference electrode	Ag / AgCl
Counter electrode	Pt mesh

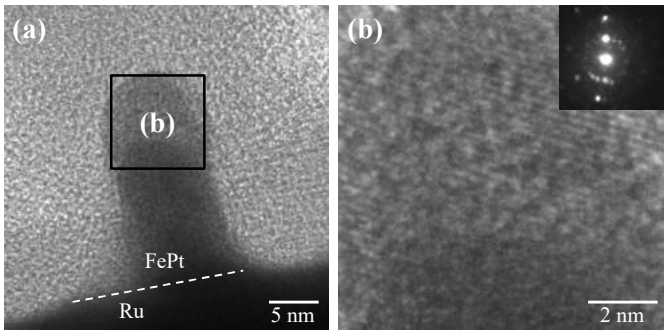

Fig. 1 Cross-sectional TEM image of FePt nanodot arrays with 15 nm diameter and 35 nm pitch. (a) low magnification and (b) high magnification image. Inset shows selective area electron diffraction of nanodot.

Ru ALLOY-OXIDE BUFFER LAYER FOR INTERGRANULAR EXCHANGE DECOUPLING FOR CoPt-B_2O_3 GRANULAR MEDIA

Kim Kong THAM[1], Ryosuke KUSHIBIKI[1, 2], Tomonari KAMADA[1], Shintaro HINATA[2], and Shin SAITO[2]

1) Tanaka Kikinzoku Kogyo K. K., Tsukuba, Ibaraki 300-4247, JAPAN
2) Tohoku University, Sendai, Miyagi 980-8579, JAPAN

I. INTRODUCTION

CoPt-oxide granular media have been widely used for perpendicular magnetic recording. To further increase recording density of the media, reduction of media noise through the promotion of intergranular exchange decoupling is essential[1)]. Generally, to exchange decouple magnetic grains of the media, oxides with amorphous phase which do not dissolve into CoPt alloy have been employed as the grain boundary materials. The oxide is expected to segregate into the trench of Ru underlayer so that CoPt grains can grow heteroepitaxially on the bump of Ru underlayer. Previously, we had found that a granular medium with high magnetocrystalline anisotropy (K_u) was successfully realized when B_2O_3 was applied for the grain boundary material[2)]. However, the separation between magnetic grains at the initial growth region in the Ru trench by low melting point oxide such as B_2O_3 is not sufficient[3)]. Therefore, we have carried out an investigation on the deposition of a buffer layer (BL) with non-ferromagnetic metal and oxide on the Ru underlayer to grow the non-ferromagnetic metal and oxide on the Ru bump and trench, respectively, aiming to intergranular decouple the magnetic grains. In this paper, we will discuss about the effect of utilizing BL on the intergranular exchange decoupling in relation with magnetic properties.

II. RESULTS AND DISCUSSION

Samples structure used in this study: Sub./ Ta (5 nm)/ $Ni_{90}W_{10}$ (6 nm)/ Ru (0.6 Pa, 10 nm)/ Ru (8.0 Pa, 10 nm)/ BL/ $Co_{80}Pt_{20}$-30vol%B_2O_3 (4-16 nm)/ C (7 nm). $Ru_{50}Co_{25}Cr_{25}$-30vol%TiO_2 (0-3 nm) was used for the BL. Here for the BL, a non-ferromagnetic Ru alloy which consists of the metal element of underlayer (Ru) and granular media (Co) was adopted for the metal material to maintain hetero-epitaxial growth of CoPt alloy on Ru. While TiO_2 was chosen as a typical material used for the grain boundaries in the granular media.

Fig. 1 shows *m-H* loops for CoPt-B_2O_3 granular media (a) without and (b) with RuCoCr-TiO_2 BL (1 nm) at various media thicknesses. When a BL is introduced, larger coercivity (H_c) and smaller slope (α) at around H_c for each media thickness can be observed.

Fig. 2 shows dependence of H_c on the BL thickness (d_{BL}). When d_{BL} is increased from 0 to 1.5 nm, a large increase of H_c around 20%, from 7.5 to 9.0 kOe can be observed. Further increase of d_{BL} to 3.0 nm will decrease H_c from 9.0 to 8.7 kOe. This indicates that the employment of the BL is quite effective to increase H_c of the medium.

To find out the origin of H_c variation according to various BL thickness, anisotropy field (H_k), thermal stability and degree of intergranular exchange coupling were investigated. Here, thermal stability and degree of intergranular exchange coupling are determined from $v_{act}K_u^{grain}/kT$ and α, where v_{act} is the activation volume measured from time dependence of remanence coercivity[4)] and K_u^{grain} is evaluated from K_u of the granular media when 30vol% B_2O_3 is excluded. Fig. 3 shows dependence of (a) H_k and K_u, (b) $v_{act}K_u^{grain}/kT$ and (c) α on d_{BL}. When d_{BL} is varied from 0 to 1.5 nm, H_k remains constant at around 19 kOe, $v_{act}K_u^{grain}/kT$ decreases from 160 to 140, and α decreases from 1.7 to 1.2, which reveals that the granular medium is thermally stable and the intergranular exchange decoupling is promoted. Further increase of d_{BL} to 3.0 nm will decrease H_k from 19 to 17 kOe. This result suggests that the decrease of degree of intergranular exchange coupling when d_{BL} is increased from 0 to 1.5 nm induces larger H_c. Furthermore, the reduction of H_c for d_{BL} thicker than 1.5 nm is caused by the reduction of H_k which is originated from K_u reduction.

From these results, the introduction of RuCoCr-TiO_2 BL underneath the high K_u CoPt-B_2O_3 granular media is quite effective to increase H_c through reduction of intergranular exchange coupling.

Kim Kong Tham
Tanaka Kikinzoku Kogyo K.K.
fax: +81-22-795-7134
tel: +81-80-8490-7311
6-6-05 Aoba, Aramaki, Aoba-ku, Sendai 980-8579 JAPAN

REFERENCES

1) Gun Choe et al., *J. Magn. Mag. Mater.*, **287**, 159 (2005).
2) Kim Kong Tham et al., *Jpn. J. Appl. Phys*., **55**, 07MC06 (2016).
3) Ryosuke Kusibiki et al, *AIP Advances*, **7**, 056512 (2017).
4) K. Yamanaka et al., *J. Magn. Magn. Mater.*, **145**, 255 (1995).

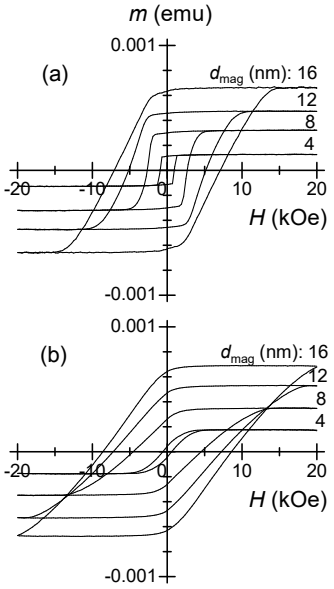

Fig. 1 *m*-*H* loops for CoPt-B_2O_3 granular media (a) without and (b) with RuCoCr-TiO_2 buffer layer (1 nm) at various granular layer thicknesses.

Fig. 2 Dependence of coercivity (H_c) on the buffer layer thickness (d_{BL}).

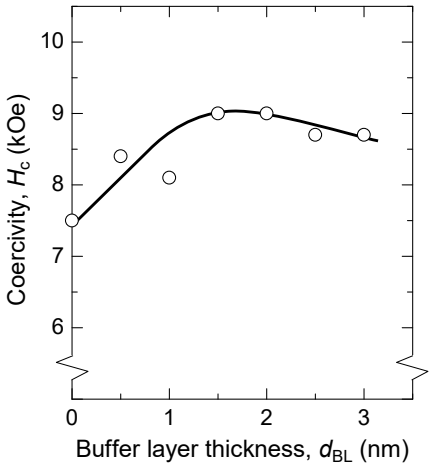

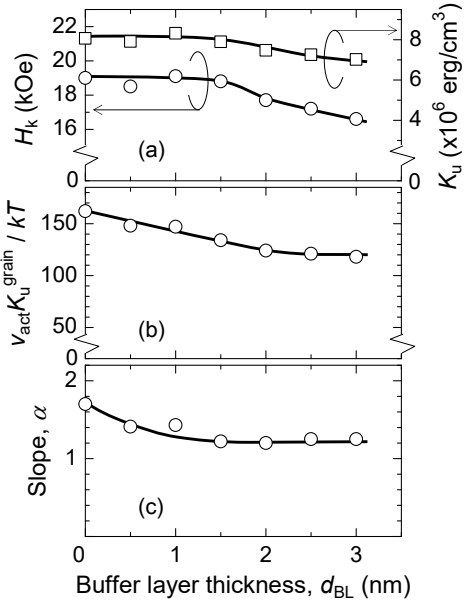

Fig. 3 Dependence of (a) H_k and K_u, (b) $v_{act}K_u^{grain}/kT$ and (c) Slope (α) on buffer layer thickness (d_{BL}).

CONTROL OF ISOLATED FePt GRAINS FORMATION BY MULTIPLE NANO-PARTICLE NUCLEATION WITH RAPID THERMAL ANNEALING METHOD

M. TANAKA[1], K. MIYOSHI[2], A. OGASAWARA[3] and A. TSUKAMOTO[4]

1) Nihon Univ., Chiba, Japan, csma16006@g.nihon-u.ac.jp

2) Nihon Univ., Chiba, Japan, cski17027@g.nihon-u.ac.jp

3) Nihon Univ., Chiba, Japan, ogasawara_aki@inl.ecs.cst.nihon-u.ac.jp

4) Nihon Univ., Chiba, Japan, tsukamoto.arata@nihon-u.ac.jp

I. INTRODUCTION

For the fabrication of high density magnetic recording medium, we studied about fabrication of isolated FePt grains formation with Rapid Thermal Annealing and Rapid Cooling Process (RTA)[1],[2]. As one of the issues in this method, grains density and grain diameter depend on the thickness of pre-stacked metal thin films, so they can not be controlled independently in single RTA process. Generally, particle nucleation phenomena have important role during FePt grain formation process under RTA. Therefore, we focused that control of FePt grains formation by multiple particles nucleation procedure. In this report, it was shown that the multiple particles nucleation with RTA is effective for independent control of grain density and diameter, furthermore grains formation position.

II. EXPERIMENT

Metal thin films were fabricated using DC magnetron sputtering on flat thermally oxidized Si substrates. Fe and Pt layers were fabricated in 0.18 Pa pressure ArH (H_2: 3 vol. %) gas atmosphere. For particlize, metal films were annealed by RTA process in the vacuum chamber at 2.0×10^{-3} Pa with infrared lamp. At the end of RTA, metal films were quenched by RCP. The average temperature elevation rate was about 120 ℃ / sec. At the maximum temperature of 600 ℃, the optical pass was closed then N_2 gas was flowed for RCP. The size and the shape of isolated particles were observed by Scanning Electron Microscope (SEM) and Transmission Electron Microscope (TEM).

III. RESULTS&DISCUSSION

Pt thin films {A: 1.0 nm, B: 1.88 nm} were particlized by RTA. Fig.1 shows SEM and TEM planer view images, number of particles (N_p) and particles average diameter (D_a) in each samples. Isolated Pt particles were emerged in both samples. Sample B was obtained as areal particles density of 10 T particles/ inch^2 over. Next, Pt (0.69 nm)/ Fe (1.31 nm) continuous multilayer thin film was additionally deposit on these samples and then RTA was performed. Fig.2 shows SEM planer view images of FePt grains. Sample B retained the particles density and particles formation position of Pt particles. Sample A is decreased areal particles density.

For fabrication of high density particles, it is favorable that metallic film is stacked as thin as possible. Fig.3 shows particles density is higher than FeCuPt particles formed with the same or thin film that already reported[3]. From These results, The first tiny grain formation is effective for control of grains areal density. Second grains formation is effective for grain growth. Therefore, multiple particles nucleation is effective for independent control of grain density and diameter, furthermore grains formation position. In same deposited amount of FePt, the particle density was increased with double nucleation procedure than single RTA process.

Masahiro Tanaka,
Graduate School of Science and Technology, Nihon University,
7-24-1 Narashinodai, Funabashi, Chiba 274-8501 Japan.
E-mail: csma16006@g.nihon-u.ac.jp
Tel.: +81-47-469-5455

REFERENCES

[1] Y.Itoh, T.Aoyagi, A.Tsukamoto, K.Nakagawa, A.Itoh and T.Katayama:*Jpn. J.Appl.Phys.*,**43,**12,8040(2004).
[2] A. Itoh, A. Tsukamoto, S. Okame and K. Mizusawa, "*J. Magn. Soc. Jpn.* ", 36, 62-65(2012)
[3] J. Tsukioka, T. Ubana, A. Tsukamoto, and A. Itoh: *J. Magn. Soc. Jpn*., 38, 143-146(2014).

Acknowledgment: This work is partially supported by Storage Research Consortium and MEXT-Supported Program for the Strategic Research Foundation at Private Universities2013-2017.

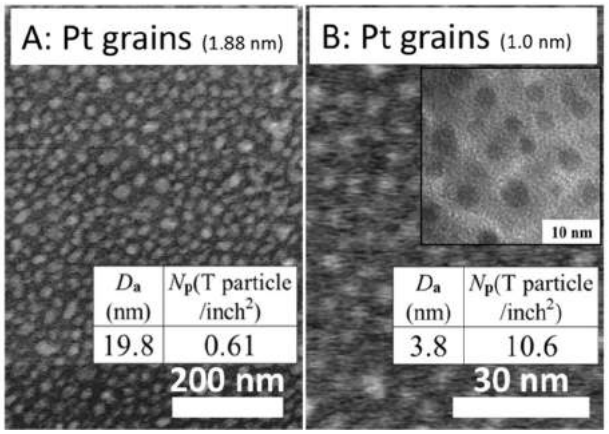

Fig.1 SEM and TEM planer view images, D_a and N_p in each samples. A: Pt thickness is 1.0 nm, B: Pt thickness is 1.88 nm.

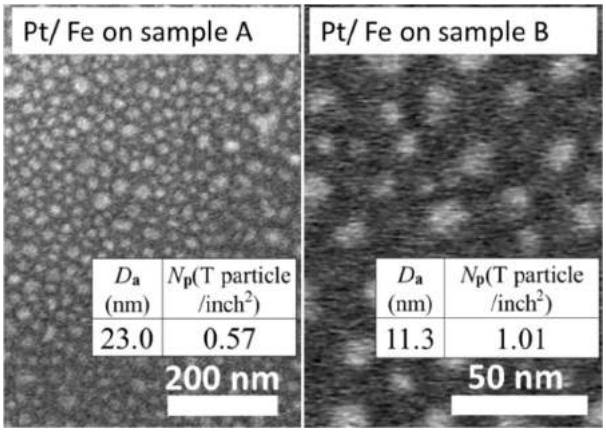

Fig.2 SEM planer view images, D_a and N_p in each samples. left: Pt/ Fe thin film on Sample A. right: Pt/ Fe thin film on Sample B.

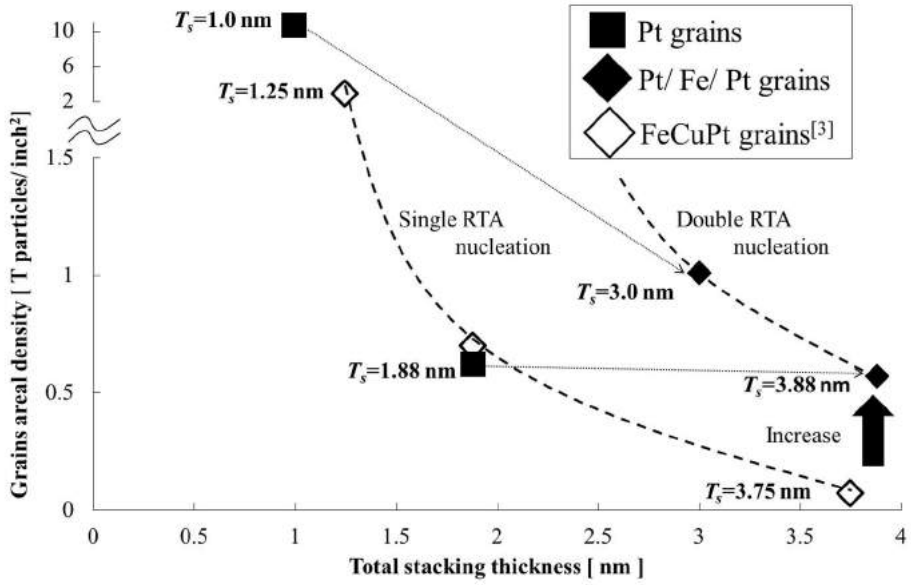

Fig.3 Dependence of total stack thickness on grain density.

ALL-OPTICAL MAGNETIZATION SWITCHING ON GdFeCo/METAL FILMS TRRIGERED BY FEMTOSECOND PULSED LASER

H. YOSHIKAWA[1], S. EL MOUSSAOUI[2], Y. KASATANI[3] and A. TSUKAMOTO[4]

1) Nihon Univ., Chiba, Japan, cshr15001@g.nihon-u.ac.jp

2) Nihon Univ., Chiba, Japan, souliman.el-moussaoui@inl.ecs.cst.nihon-u.ac.jp

3) Nihon Univ., Chiba, Japan, kasatani_yuichi@inl.ecs.cst.nihon-u.ac.jp

4) Nihon Univ., Chiba, Japan, tsukamoto.arata@nihon-u.ac.jp

I. FEMTOSECOND LASER PULSE EXCITED MAGNETIZATION SWITCHING

In order to realize faster recording, we research the magnetic recording by femtosecond laser pulse. All-Optical magnetization Switching (AOS) phenomenon is excited by single femto-second laser pulse without any external magnetic field. This switching is not limited by Ferro-Magnetic Resonance limit unlike conventional magnetic field driven magnetization switching. Additionally, AOS can direct overwrite recording with polarization [1]. It means AOS faster switching and magnetic recording in prospect. Only tens femtosecond laser pulse are sufficient to induce the non-adiabatic and non-equilibrium energy dissipation processes of electron, lattice and spin in metallic thin films and AOS is occurred via these processes [2]. In particular, electronic heating in short time range has important role for it [3]. From this idea, we considered controlling the efficiency of GdFeCo switching with different designed stacked structure which has different electronic energy dissipation character in this short time scale. In this research, we designed GdFeCo/"different electronic specific heat C_{el} metal" films for high efficient AOS recording.

II. EXCITATION OPTICAL SYSTEMS AND FILMS

The GdFeCo thin films were grown on atomically flat glass substrate by magnetron sputtering (DC sputtering for metallic layer and RF reactive sputtering for dielectric SiN layer) following the sequence hereafter: SiN (60 nm) / GdFeCo (10 nm) / metal X (5 nm) / glass sub., (where X = A: GdFeCo, B: AlTi, C: Cu). GdFeCo is one of the famous metal for AOS and magneto-optical (MO) effect. The obtained all the samples had an out-of-plane magnetic anisotropy (squareness ratio ~1). We know the interesting dependency of AOS on the different structured samples as following like GdFeCo (l nm) / SiN (m nm) / AlTi (n nm) ({l, m, n} = {20, 0, 10}, {20, 5, 0}, {20, 10, 0} and {30, 5, 10}) [3]. AOS has different dependency from thermo-magnetic nucleated domains, it doesn't simply depend on the total absorbed energy and continuous GdFeCo/AlTi thickness. It suggests AOS especially depends on the electronic energy dissipation process after the absorption as not like usual laser heating process. From this result, we designed the sample A, B and C. The designed GdFeCo thickness, 10 nm is designed similar penetration depth. The GdFeCo surface have twice of absorbed energy at 10 nm from surface after the irradiation. Additionally, we chose different metals which have different electronic specific heat C_{el}. C_{el} depends on γ ($C_{el} = \gamma T$) and γ is 5 mJ/mol·K^2 for Fe, 4.7 for Co 1.35 for Al, 3.5 for Ti and 0.688 for Cu [4]. On the other hand, the specific heat C of Fe is 444 J/kg·K, Co is 434, Al is 900, Ti is 519, and Cu is 385 [4].

For AOS excitation, a regenerative amplified laser pulses from a Ti: sapphire laser at a wavelength of λ = 800 nm and the pulse width of 90 fs (FWHM) was used. We shot a femtosecond pulsed laser to these samples perpendicularly. After this excitation, we measured the size of AOS created domains. It was performed by placing a sample under a polarizing microscope, where domains with magnetization "up" and "down" could be observed as "dark" and "bright" regions, respectively.

III. CREATED MAGNETIC DOMAIN SIZE OF METALLIC FILMS WITH SPECIFIC HEAT

As a result, we found that AOS could triggered with lower irradiate laser power in GdFeCo film stucked on smaller C_{el} metal. Fig. 1 shows the irradiated power dependency of the created domain sizes by AOS on each samples. In this figure, open circles means the domains created by AOS and the size of the created domain can be deduced by considering the scale in the inset of the figure. Each AOS on each films increase the size with the irradiated power, because AOS create magnetic domains in the area above an absorbed fluency threshold [5]. Furthermore, the most important result of this experiment is the AOS

HIROKI YOSHIKAWA
E-mail: cshr15001@g.nihon-u.ac.jp
tel: + 81-47-469-5455

created domain size is different on these samples and it realize the relation to C_{el}. The smaller C_{el} metal "Cu" sample C has the smaller threshold than the bigger C_{el} metals. The C dependency didn't is noticed in this result, clearly. If AOS depends on the electronic thermally energy dissipation process in short time scale, we can think the models as follows. After the irradiation by a laser pulse and the absorption at each point of this film. It is thermally equilibrated in metallic layers following the electronic specific heat C_{el} by hot electrons. Therefore, GdFeCo get energy from smaller C_{el} metallic layer. From these, we suggest AOS is able to be triggered by lower irradiate laser power in GdFeCo film stucked on smaller C_{el} metal with short time scale electronic energy dissipation.

ACKNOWREDGEMENT

This work was partially supported by MEXT-Supported Grant-in-Aid for Scientific Research on Innovative Area "Nano-Spin Conversion Science" (Grant No.26103004), MEXT-Supported Program for the Strategic Research Foundation at Private Universities, 2013-2017 (S1311020) and Grant-in-Aid for JSPS Fellows (16J01232).

REFERENCES

1) C. D. Stanciu, F. Hansteen, A. V. Kimel, A. Kirilyuk, A. Tsukamoto, A. Itoh and Th. Rasing, "All-optical magnetic recording with circularly polarized light", *Phys. Rev. Lett.*, 99, 047601 (2007).
2) Radu, K. Vahaplar, C. Stamm, T. Kachel, N. Pontius, H. A. Dürr, T. A. Ostler, J. Barker, R. F. L. Evans, R. W. Chantrell, A. Tsukamoto, A. Itoh, A. Kirilyuk, Th. Rasing & A. V. Kimel, "Transient ferromagnetic-like state mediating ultrafast reversal of antiferromagnetically coupled spins", *Nature*, 472, 205–208 (2011).
3) H. Yoshikawa, S. El Moussaoui, S. Terashita, R. Ueda and A. Tsukamoto, "Magnetic layer thickness dependence of all-optical magnetization switching in GdFeCo thin films", *Jpn. J. Appl. Phys*, 55 07MD01 (2016).
4) The Japan Institute of Metals and Materials, "revised 4th edition Metals data book", p17 [in Japanese] (2004)
5) H. Yoshikawa, S. Kogure, S. Toriumi, T. Sato, A. Tsukamoto, and A. Itoh, "Ultrafast heat pulse magnetization switching near compensation condition in GdFeCo", *J. Magn. Soc. Jpn*, 38, 139 (2014).

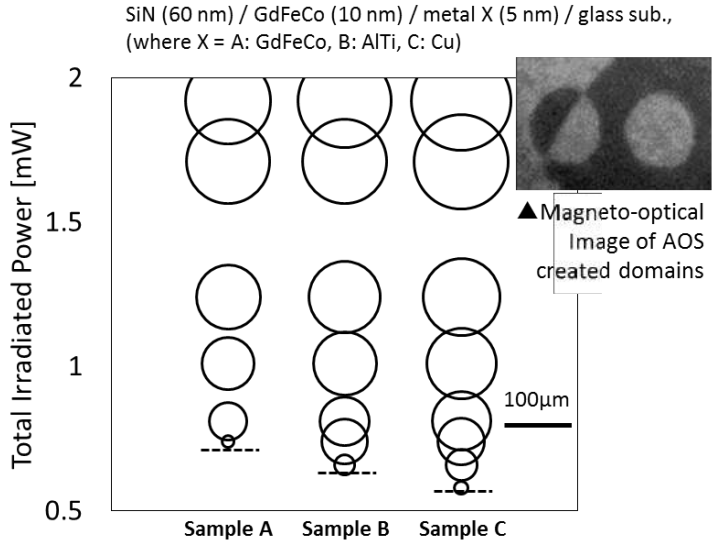

Fig. 1 Irradiated laser power dependence of the created domain size for different sample design A, B, and C. The sizes of circles shows the domains created by AOS and it is deduced by considering the scale in the inset of the imaging.

ISOLATED $L1_0$-FePt GRAINS AND FORMATION PROCESS FABRICATED BY RAPID THERMAL ANNEALING

A. TSUKAMOTO[1], R. KOBAYASHI[2] and M. IMAZATO[3]

1) Nihon Univ., Chiba, Japan, tsukamoto.arata@nihon-u.ac.jp

2) Nihon Univ., Chiba, Japan, imazato_masayuki@inl.ecs.cst.nihon-u.ac.jp

3) Nihon Univ., Chiba, Japan, kobayashi_ren@inl.ecs.cst.nihon-u.ac.jp

I. INTRODUCTION

We reported that isolated several tens of nano-meters FePt grains were fabricated by Rapid Thermal Annealing (RTA) for Pt / Fe double layered ultra-thin film deposited on thermally oxidized Si substrate[1]. It was unclear how the double layered Pt / Fe film turned to isolated magnetic grains during RTA process. In this report, we discuss about compositional dependency of morphological and magnetic properties of isolated FexPt100-x grains, and grain formation process during RTA by using the in-situ conductivity measurements.

II. EXPERIMENTAL METHODS

Pt / Fe double layered ultra-thin films were deposited on flat thermally oxidized Si substrate by DC magnetron sputtering in condition of a 0.18 Pa ArH (H_2: 3 vol. %) gas atmosphere. The base pressure was less than 4.0×10^{-5} Pa. The total deposited thickness of all double layered films was 1.88 nm. The composition ratio of deposited Fe_xPt_{100-x} was varied from x = 50 to 63.7. For fabrication of isolated FePt grains, the deposited continuous double layered films were annealed by RTA (heating rate was about 90 ℃/s) in the vacuum chamber (less than 3.5×10^{-3} Pa) with the 2 kW infrared ray lamp. At the target maximum temperature (T_m = 600 ℃), the shutter was closed to shut out the optical pass, and then N_2 gas flow was introduced to prevent the particle growth by quench with RCP (cooling rate was -60 ℃/s during 500 ℃ decrease). Morphology of isolated FePt grains was observed by a scanning electron microscope (SEM) and a transmission electron microscope (TEM). Crystalline structure of isolated FePt grains was analyzed by a x-ray diffraction (XRD). Characterization of magnetic properties was taken on Quantum Design MPMS3 SQUID magnetometer with VSM mode (Sensitivity: 5×10^{-8} emu).

III. COMPOSITIONAL DEPENDENCY OF ISOLATED Fe_xPt_{100-x} GRAINS

Fig. 1 shows an in-plane and out of plane hysteresis loops of the fabricated Fe_xPt_{100-x} grains (x =50 to 63.7) measured by a MPMS3. Fig. 2 shows compositional dependency of coercivity H_c derived from Fig. 1. In x = 50 and 55, rather isotropic and soft magnetic phase were appeared. In x = 57, 62 and 63.7, hard magnetic phase with large coercivity around 40 kOe was observed indicating the presence of large anisotropy, although x = 57 and 63.7 observed soft magnetic phase in low field region (bellow 10 kOe). These magnetic properties indicated perpendicular magnetic anisotropic properties with high H_c appeared by increasing Fe ratio x from 50 to 62. In x = 62, hard magnetic properties were obtained with high H_c. H_c increased by increasing x ratio from 50 to 62. In x = 62, value of H_c was maximum 42 kOe. However, in x = 63.7, H_c decreased to 37 kOe. Furthermore, in x = 62, M_r/M_s = 0.9 was the highest value in this composition range. These results meant the most amount of easy axis for perpendicular to film plane grains were fabricated. In this fabricated process, expected $L1_0$ FePt type hard magnetic phase was appeared in more Fe-rich composition rate than $Fe_{50}Pt_{50}$. From the compositional dependency of magnetic properties, it is suggested that the existence of 0.41 nm dead layer originated from first deposited Fe.

Arata TSUKAMOTO
E-mail: tsukamoto.arata@nihon-u.ac.jp
tel: +81-474-695455

IV. FORMATION PROCESS OF FePt GRAINS

For clarification of how the layered Pt/Cu/Fe film turned to isolated magnetic grains during RTA process, the in-situ conductivity measurement was performed. The target material was 1.88 nm thick of $Fe_{43}Cu_{14}Pt_{43}$. The film was turn to insulator form conductor around 9 s before elevating to maximum temperature of 572.8 ℃. From SEM observation, isolated grains were emerged. In case of RTA with maximum temperature of 486.8 ℃, it keeps conductive property with un-isolated morphology. It is clarified that the deposited continuous film turn to isolated particles within few second at threshold temperature during RTA.

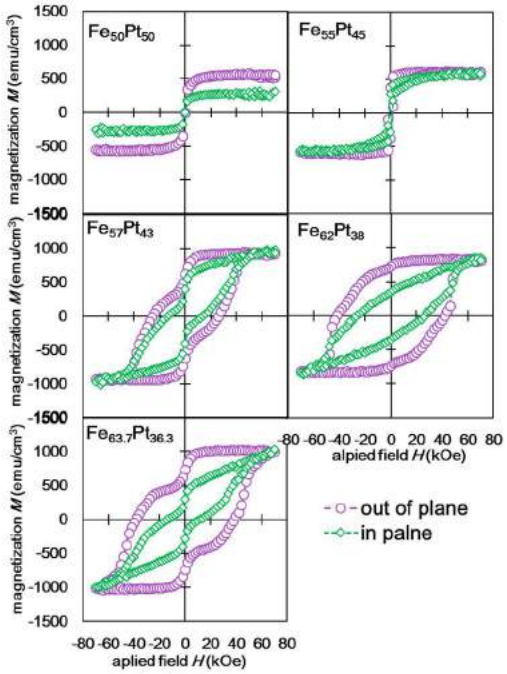

Fig. 1 Magnetic hysteresis loops of each samples.

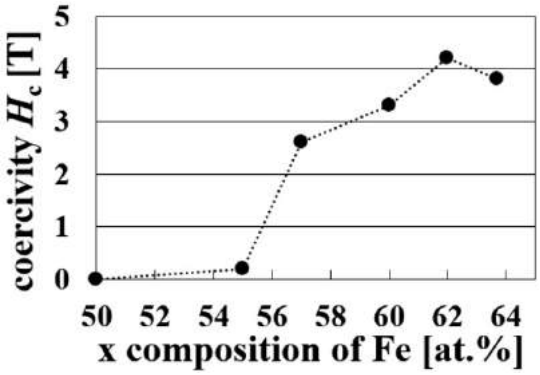

Fig. 2 The relation between controlled x ratio and Hc of isolated Fe_xPt_{100-x} grains in conditions of total deposited thickness = 1.88 nm and x = 50 to 63.7.

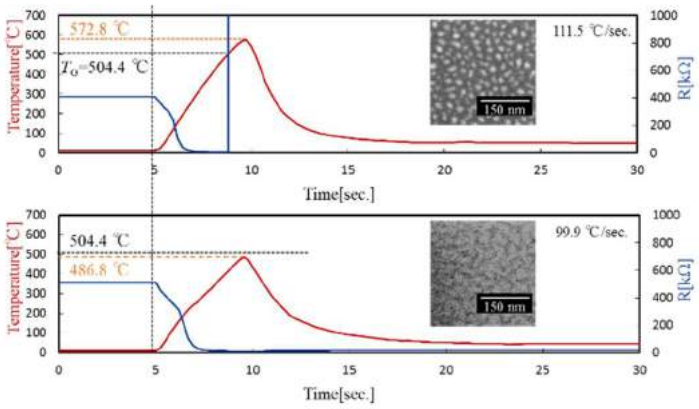

Fig. 3 In-situ conductivity measurements during RTA.

ACKNOWLEDGEMENT

This work is partially supported by Storage Research Consortium and MEXT-Supported Program for the Strategic Research Foundation at Private Universities, 2013-2017.

REFERENCES

1) A. Itoh, A. Tsukamoto, S. Okame, and K. Mizusawa, *Jpn. J.Magn. Soc*. 36, 62-65 (2012).

2D LDPC CODES AND JOINT DETECTION AND DECODING FOR TWO-DIMENSIONAL MAGNETIC RECORDING

Chaitanya Kumar MATCHA[1], Shounak ROY[1], Mohsen BAHRAMI[2],
Shayan Garani SRINIVASA[1] and Bane VASIC[2]
[1]Department of Electronics Systems Engineering, Indian Institute of Science, Bengaluru, 560012, India.
[2]Department of Electrical and Computer Engineering, University of Arizona, Tucson, 85721, USA.
Correspondence Email: shayan.gs@dese.iisc.ernet.in

I. INTRODUCTION

Two-dimensional magnetic recording (TDMR) is a promising technology for boosting areal densities using sophisticated signal processing algorithms within a systems framework. The read/write channel architectures have to effectively tackle the 2D inter-symbol interference (ISI), 2D synchronization errors, media and electronic noise sources as well as thermal asperities resulting in burst erasures. 1D low-density parity check (LDPC) codes are well studied to correct large 1D burst errors/erasures. However, such 1D LDPC codes are not suitable to correct 2D burst errors/erasures due to the 2D span of the errors. In this paper, we propose the construction of a true 2D LDPC code to effectively correct 2D burst erasures. We also propose a joint detection-decoding algorithm based on the generalized belief propagation (GBP) algorithm to simultaneously handle 2D ISI as well as correct bit/burst errors for TDMR channels. Our work is novel in two aspects: (a) We propose construction of true 2D LDPC code to correct large 2D burst erasures, (b) We develop a 2D joint signal detection-decoder engine that incorporates 2D ISI constraints and modulation code constrains along with LDPC decoding. The proposed 2D LDPC code gives burst erasure correction capability of greater than 22% than the 1D LDPC codes reported earlier. Further performance improvement can be achieved by code optimization. The proposed joint detection-decoding algorithm is observed to achieve a signal-to-noise ratio (SNR) gain of > 0.2 dB in bit error rate (BER) performance ($\sim 5\%$ increase in areal densities around the 1 Tb/in^2 regime with grain sizes of 10 nm) as compared to a decoupled detector-decoder system configuration. The efficacy of our proposed algorithm and system architecture is evaluated by assessing areal density (AD) gains via simulations for a TDMR configuration comprising of a 2D generalized partial response (GPR) over the Voronoi media model assuming perfect 2D synchronization.

II. RESULTS

Figure 1 shows the architecture of the proposed joint detection-decoding scheme in TDMR. In this architecture, a GBP based joint detection-decoding algorithm is used to equalize as well as decode the readback samples from a Voronoi based TDMR channel model. Figure 2 shows the region graph used by the joint detection-decoding algorithm. The algorithm minimizes the Kikuchi approximation of the Gibbs free-energy defined based on the region graph under the parity check constraints defined by the LDPC code. The regions in the region graph are defined based on the 2D ISI as well as the LDPC code constraints.

For burst erasure correction in TDMR, a defect detector [1] estimates the location of burst erasure using the output of 2D soft-output Viterbi algorithm (SOVA). LDPC code is used to correct the burst erasures as well as the random errors seen at the output of the 2D SOVA. The identified defect location is indicated to the LDPC decoder to effectively correct the burst erasure.

We simulate the TDMR channel using a Voronoi based media model with CTC = 10 nm, bit size = 25x25 nm achieving channel bit density of 1 Tb/in^2. Figure 3 shows the performance of the proposed 2D LDPC as against a traditional 1D quasi-cyclic LDPC code with the same code rate (0.87) and length of 32k corresponding to a sector of data. The proposed construction of 2D LDPC code could correct 42x42 bursts with similar performance as the 1D LDPC code with 38x38 bursts. Figure 4 shows that the proposed joint detection and decoding algorithm performs with > 0.2 dB gain in SNR corresponding to $\sim 5\%$ gain in areal density.

SHAYAN GARANI SRINIVASA*
Fax: +91-80-2293-2290
Tel: +91-80-2360-0810 (232)
Email: shayan.gs@dese.iisc.ernet.in

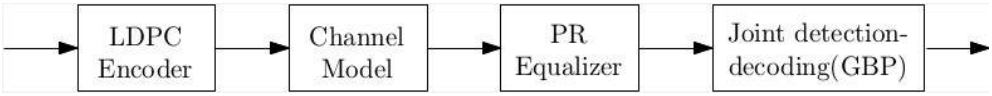

Fig. 1 The samples from the Voronoi based media model are partial response (PR equalized) before the samples are jointly detected and decoded by GBP algorithm.

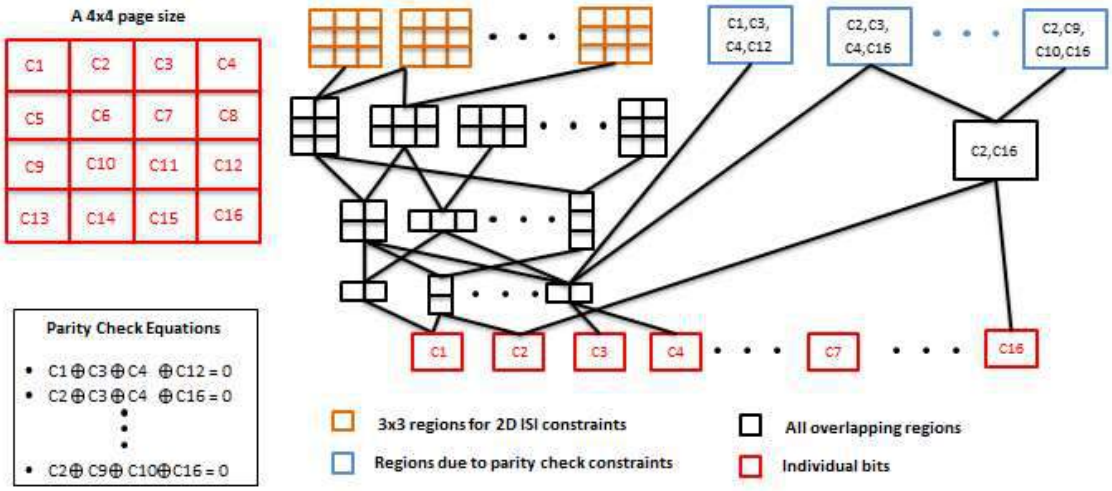

Fig. 2 An example of a region graph used by the GBP algorithm for joint-detection decoding is shown. The regions are chosen based on 2D ISI as well as LDPC code parity check constraints.

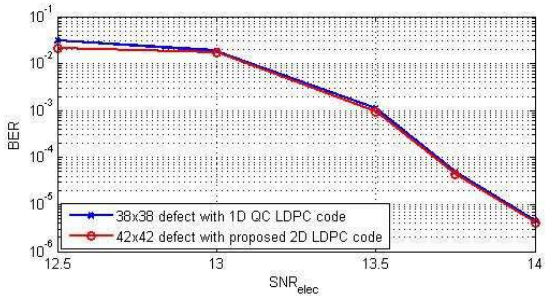

Fig. 3 The proposed 2D LDPC code is able to correct 42x42 burst erasures with the same performance as 1D LDPC codes correcting 38x38 burst erasures under identical channel conditions.

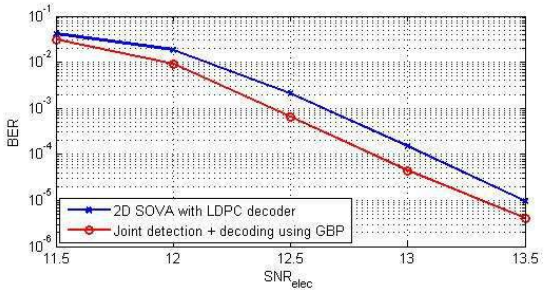

Fig. 4 The proposed joint detection and decoding scheme using GBP performs 0.2 dB better than the separate detection and decoding using 2D SOVA and belief propagation (BP) algorithm.

REFERENCES

1) C. K. Matcha, and S. G. Srinivasa, "Defect Detection and Burst Erasure Correction for TDMR," in *IEEE Trans. Magn.*, Nov. 2016.
2) M. Bahrami, *et. al*, "Investigation into Harmful Patterns over Multi-Track Shingled Magnetic Detection using the Voronoi Model," in *IEEE Trans. Magn.*, Jul. 2015.
3) C. K. Matcha, and S. G. Srinivasa, "Generalized Partial Response Equalization and Data-Dependent Noise Predictive Signal Detection over Media Models for TDMR," in *IEEE Trans. Magn.*, Oct. 2015.

ACKNOWLEDGEMENT

The work presented in this paper is funded by Indo-US Science and Technology Forum (grant no. JC-Data Storage Research/16-2014).

INFLUENCE OF PROTECTION LAYERS ON LOCAL HEATING IN HEAT ASSISTED MAGNETIC RECORDING

K. KIMURA, Y. HAYASHI, Y. ASHIZAWA, S. OHNUKI, and K. NAKAGAWA
Nihon University, Funabashi, Chiba, Japan

I. INTRODUCTION

Heat assisted magnetic recording (HAMR) is studied to realize high recording density over 4 Tbit/inch^2. A near-field transducer (NFT) is used to heat a local area by surface plasmon effect. We have studied structures of the NFT and a plasmonic waveguide (PWG) without protection layers, such as a lubricant layer and overcoat layers of diamond-like carbon, to keep temperature which is lower than 150 °C at the NFT tip, when a recording medium is heated up to 277 °C [1]. It is, however, not clear about the effect of the protection layers on the heating of the medium and the temperature rise of the NFT. Therefore, we analyzed energy convergence and temperature rise of the NFT with the protection layers by computational simulation.

II. SIMULATION MODEL

Calculations of electromagnetic wave and heat conduction are performed by a Finite-Difference Time-Domain (FDTD) method and an Alternating Direction Implicit (ADI) method. A model of a structure of a HAMR head for thermal calculation is shown in Fig. 1. A PWG is constructed by a Ta_2O_5 core, an Al_2O_3 clad and a gold sheet along the Ta_2O_5 core. A thickness of the gold sheet is 100 nm, and a distance between the Ta_2O_5 core and the gold sheet is 190 nm, as an efficient condition for delivering surface plasmon polaritons [2]. Diamond-like carbon (DLC) layers with 1 nm-thick are put on the NFT and a recording medium. A lubricant of 1 nm is placed on the DLC layer of the recording medium side. The light source is located in the Ta_2O_5 core and the incident light angle to the surface between the Ta_2O_5 core and Al_2O_3 clad is 60°. The recording medium is a granular structure of the FePt grains covered with SiO_2. Optical and thermal constants are shown in Table 1.

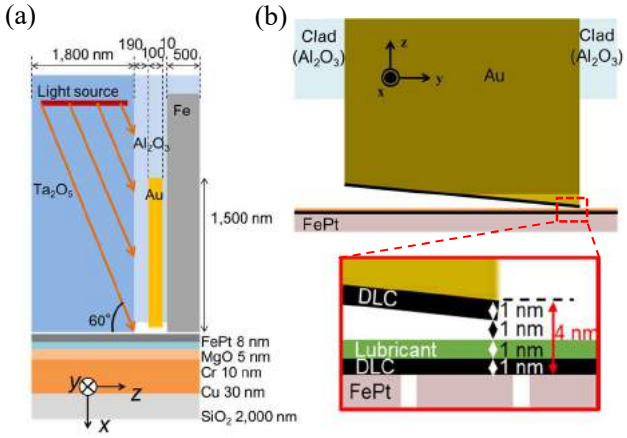

Fig. 1 The structure of HAMR head when covering a DLC and a lubricant for thermal calculation. Side view (a), NFT enlarged view (b).

Table 1 Optical and thermal constants

Material	Refractive index n	Extinction coefficient κ	Specific heat C [J/kg/K]	Thermal Conductivity K [W/m/K]	Density D [kg/m^3]
Fe	2.8	3.8	453	28	7.86×10^3
Au	0.174	4.86	453	28	1.928×10^4
Cu	0.242	4.85	440	400	9×10^3
FePt	3	4	200	100	15×10^3
MgO	1.73	0	500	4	4×10^3
Cr	4.11	4.35	360	100	7×10^3
Ta_2O_5	2.17	0	207	2	8.73×10^3
Al_2O_3	1.76	0	779	2	8.73×10^3
SiO_2	1.47	0	740	1.38	2.19×10^3
Head Overcoat	2.5	0.2	570	1.3	1.9×10^3
Lubricant	1	0	2.0×10^3	0.2	900
Medium Overcoat	2.3	0.2	570	1.3	1.9×10^3

III. CALCULATION RESULTS

Normalized power density distributions along to a cross truck direction with and without the protection layers are evaluated. The calculation model and observation line are shown in Fig. 2 (a). The power density distributions are observed in the DLC or vacuum layers on the surface of the FePt layer. In Fig. 2 (b), it is found that a full width at a half maximum (FWHM) of the normalized power density distribution without the protection layers is less than 10 nm, which is the required value to achieve 4 Tbit/inch^2 in density. Even if the case of with protection layers, FWHM is also the same value. The result shows that such protection layers do not affect the energy convergence from the NFT tip to the recording

Kousuke KIMURA
E-mail: csko17014@g.nihon-u.ac.jp
tel: 080-2027-3772

medium.

Temperature distributions in the FePt recording layer along to a cross truck direction and down truck direction with and without the protection layers are shown in Fig. 3. Temperature distributions are observed at 0.5 nm under the surface of the FePt layer. When the recording temperature is kept at 277 ºC by adjusting incident light power, the side lobes of temperature is suppressed by using the protection layers. The temperature rise of the NFT tip is also suppressed from 165 ºC to 103 ºC in this condition.

Two effects by using the protection layers were found. 1) the side lobes of temperature in the FePt recording layer were suppressed. 2) the temperature rise of the NFT tip can be lower than 150 °C.

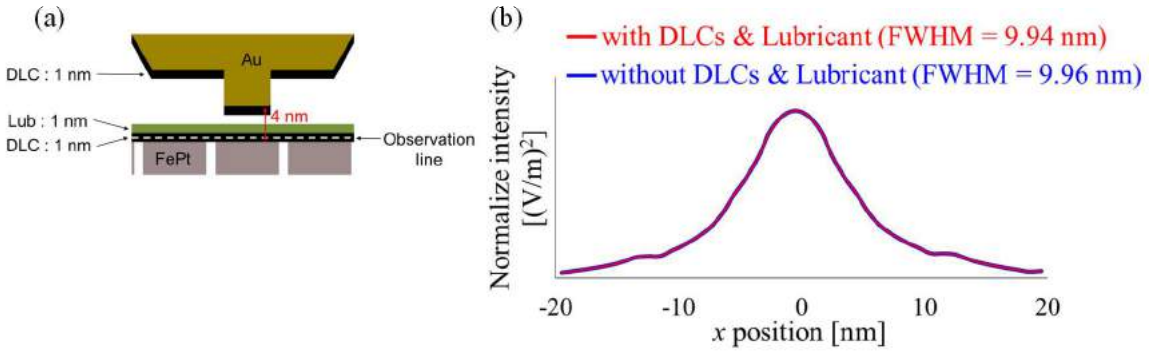

Fig. 2 Calculation model and observation line (a). Power density distributions in DLC or vacuum layer along to a cross truck direction with and without the protection layers (b).

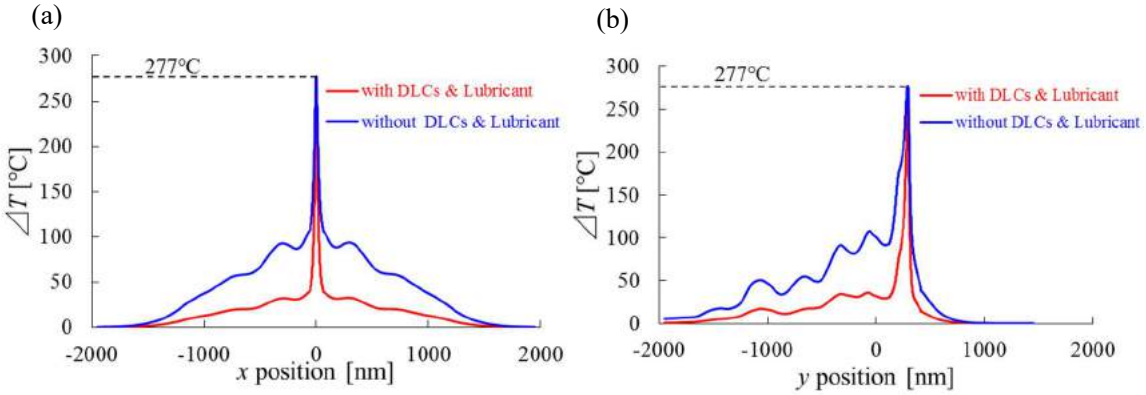

Fig. 3 Temperature distributions in the FePt recording medium along to a cross truck direction (a) and down truck direction (b) with and without the protection layers.

REFERENCES

1) Y. Hayashi, K. Tamura, Y. Ashizawa, S. Ohnuki, and K. Nakagawa, *Digest of TMRC 2016,* **I2**, 99 (2016).

2) K. Tamura, Y. Ashizawa, S. Ohnuki, and K. Nakagawa, *J. Magn. Soc. Jpn*., **38**, 131 (2014).

ACKNOWLEDGMENT

This work is supported by a Grant of Advanced Storage Research Consortium and a Grant of MEXT-Supported Program for the Strategic Research Foundation at Private Universities, 2013-2017.

CHARACTERIZATION OF MgO-BASED MAGNETIC TUNNEL JUNCTIONS' NONLINEAR FERROMAGNETIC RESONANCE MODES

Ekaterina AUERBACH[1], Norbert LEDER[1], Savas GIDER[2], Holger ARTHABER[1] and Dieter SUESS[1]

1) Vienna University of Technology, Vienna, Austria, ekaterina.auerbach@tuwien.ac.at, norbert.leder@tuwien.ac.at, holger.arthaber@tuwien.ac.at, dieter.suess@tuwien.ac.at

2) Western Digital Corporation, San Jose, USA

I. INTRODUCTION

In a simple MgO-based magnetic tunnel junction (MTJ), two ferromagnetic layers are separated by a thin, crystalline MgO barrier. The two ferromagnetic layers are known as the free layer (FL) and the pinned layer (PL). The tunneling of electrons through the MgO insulating layer results in electrical conductivity, which depends on the relative orientation between the magnetizations of the FL and PL. Thermal fluctuations of the FL and PL magnetizations cause magnetic noise, the fundamental limit of the MTJ's signal-to-noise ratio (SNR) [1]. Magnetic thermal noise is closely related to the ferromagnetic resonance (FMR) described by the Kittel equation, which connects the resonance frequency and applied field. Two commonly used techniques are thermal noise FMR (T-FMR) and spin-torque FMR (ST-FMR) [2]–[4]. Here we present an alternative FMR measurement technique, which compensates for some of the known techniques' drawbacks. Measured FMR spectra revealed not only the linear FL and PL modes but also the nonlinear ones.

II. MEASUREMENT TECHNIQUE

In Fig. 1(a), the signal generator and the spectrum analyzer are synchronized. The directional coupler is used to make the RF wave travel preferably towards the MTJ before being reflected in the direction of the instrument. The DC power supply provides the DC bias so that the MTJ is excited by a combination of AC and DC signals. The signal generator's frequency is swept from 1 to 10 GHz. At each frequency, the noise level difference (ΔNL) between the two states is computed: at zero and non-zero DC bias. Under non-zero DC bias, magnetization fluctuations of the FL and PL add to the noise floor of the carrier (Fig. 1(b)).

Similar to T-FMR and ST-FMR in the frequency domain, this measurement technique is susceptible to artifacts arising from heating. Compared to commonly used FMR techniques, the proposed measurement system has several advantages: 1) it does not suffer from the large background arising from mismatched interfaces, 2) its observation time is independent from the FL/PL magnetizations' relaxation time constants, and 3) the spectrum analyzer's resolution bandwidth (RBW) can be as low as 1 Hz, which significantly improves the system's noise performance.

III. RESULTS

The FMR spectra were obtained for a set of AC power levels (Fig. 2). Higher signal generator power levels revealed not only the linear FL and PL FMR modes but also mode splitting and sub-harmonics below the FL resonance frequency. The nonlinear FL and PL sub-harmonics are located at precisely 1/3 the frequency of the FL and PL. We suggest that these modes appear due to fractional synchronization, which may happen at $r < 1$, where r is the ratio between the driving frequency and the oscillation frequency [5]. For large AC power levels, the coupling between the oscillating magnetic layer and the source becomes nonlinear, resulting in a fractional synchronization regime. At higher AC power levels, both the nonlinear FL and PL sub-harmonics also exhibit splitting.

REFERENCES

EKATERINA AUERBACH
E-mail: ekaterina.auerbach@tuwien.ac.at
Tel: +43 664 4933808

1) N. Smith and P. Arnett, "White-noise magnetization fluctuations in magnetoresistive heads," *Appl. Phys. Lett.*, vol. 78, no. 10, pp. 1448–1450, (2001).
2) Y. Guan *et al.*, "Thermal-magnetic noise measurement of spin-torque effects on ferromagnetic resonance in MgO-based magnetic tunnel junctions," *Appl. Phys. Lett.*, vol. 95, (2009).
3) L. Xue *et al.*, "Network analyzer measurement of spin transfer torques in magnetic tunnel junctions," *Appl. Phys. Lett.*, vol. 101, (2012).
4) C. Wang *et al.*, "Time-resolved measurement of spin-transfer-driven ferromagnetic resonance and torque in magnetic tunnel junctions," *Nat. Phys.*, vol. 7, pp. 496–501, (2011).
5) S. Urazhdin *et al.*, "Fractional synchronization of spin-torque nano-oscillators," *Phys. Rev. Lett.*, vol. 105, (2010).

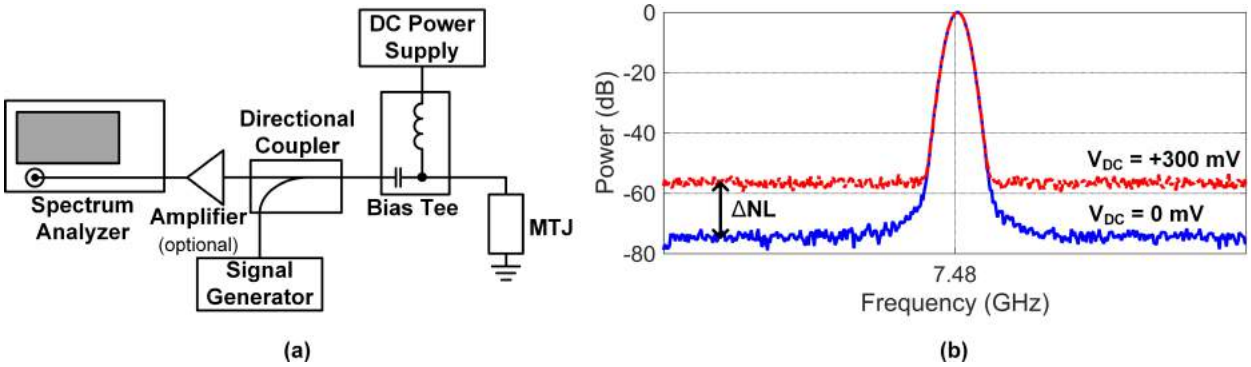

Fig. 1 (a) Proposed FMR measurement system. (b) Change in the noise floor with the bias voltage around the central frequency of the FL mode. Positive DC bias corresponds to the electron flow from the PL to FL.

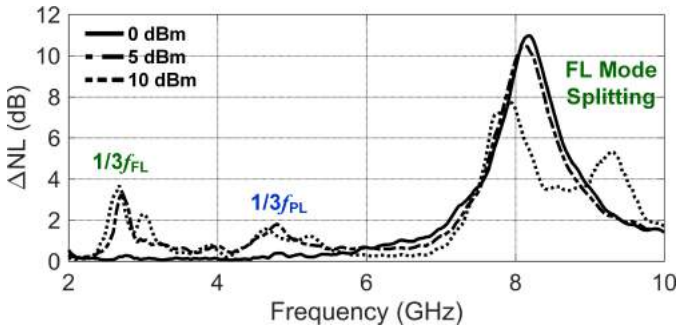

Fig. 2. FMR spectra showing nonlinear FL and PL sub-harmonics and mode splitting. The DC bias voltage is +300 mV while the AC powers are readings from the signal generator.

INTERLACED MAGNETIC RECORDING CHANNEL SIGNAL PROCESSING FOR MITIGATING INTER-TRACK INTERFERENCE

Euiseok HWANG
Gwangju Institute of Science and Technology (GIST), Gwangju, South Korea, euiseokh@gist.ac.kr

I. INTRODUCTION

Magnetic recording industry are intensely exploring technologies for continuing the enhancements of recording density in a cost-effective way such as two-dimensional magnetic recording (TDMR) without major modifications in the media or recording physics [1]. Likewise, recently proposed interlaced magnetic recording (IMR) shows potential areal density capability (ADC) gain by the write strategy change that recording tracks in the interlaced orders with controlled linear densities [2]. Consequently, the tracks are partitioned into two groups depending on the squeeze state, and the overall ADC can be improved based on the separate customization of the track and linear densities, particularly for the non-squeezed tracks with an aggressive linear density scaling. On the other hand, the squeezed tracks suffer from severe inter-track interference (ITI), and may limit the extra ADC gain by the poor off-track performance.

In this study, a novel ITI mitigating signal processing scheme is proposed for IMR channel, where severed ITI in the squeezed track is suppressed based on the effectively synchronized ITI estimation and subsequent filtering. Note that the block-wise ITI cancellation (ITIC) for magnetic recording discussed for shingled recording with negligible frequency offsets [3] cannot be applied for the asynchronously recorded IMR channel due to the intentional frequency offsets between neighboring tracks. In the proposed ITI mitigation scheme, effective synchronization can be addressed by the oversampling of the squeezed track with the baud-rate of side tracks, which dynamically adjusts the relative timing difference between asynchronously recorded tracks. Figure 1 shows a block schematic of the read channel signal processing for IMR with the proposed ITI mitigating scheme. As illustrated, tracks are recorded by the interlaced order, for example odd ones first with a linear density L_s and even ones later with an L_n, $L_n > L_s$, which forms squeezed and non-squeezed track groups, respectively. During read-back, the squeezed track signal is 1) over-sampled by a factor of $\gamma = L_n / L_s > 1$, denoted by $\mathbf{x}_{\gamma x,si}$, 2) processed for the ITI error signal estimation, $\mathbf{e}_{\text{iti},\gamma x,si}$, with the extracted ITI response and the saved track data of both sides, 3) filtered to subtract the ITI contribution in the over-sampled domain, and 4) re-sampled to its baud-rate, $\mathbf{x}_{1x,c,si}$, by the interpolated timing recovery (TR) [4].

II. RESULTS

The proposed ITI mitigating signal processing scheme is numerically evaluated with the micro-pixelated magnetic channel model [2] with the IMR of near 1 Tb/in^2 scenario. The widths of writer and reader are set to 60 and 45 nm, respectively and head electronics SNR (HESNR) is accounted up to 30 dB. The bit error rate (BER) performance is investigated by the partial response (PR) equalizer and Viterbi detector for the baud-rate samples with and without ITI mitigation. Figure 2 (a) shows the on-track BER of the squeezed track as a function of HESNR with the track density of 529.2 kTPI with the set of linear densities L_s = 2,080 and L_n = 2,600 kBPI, yielding γ = 1.25. The BER can be reduced by the proposed ITI mitigation for IMR, for example from $10^{-1.01}$ to $10^{-1.48}$ under 30 dB HESNR. In addition, the ITI suppression is also effective at the off-track locations, and Fig. 2 (b) shows the BER scanning results with read offsets along the cross-track direction. As illustrated, the bathtub shape curve can be deeper and wider by the proposed ITI mitigation, for example, the width at the target BER of $10^{-1.0}$ is broadened from 6.8 to 31.0 nm. For comparison, similar on-track performance can be achieved without the ITI mitigation at the lower density of 488.5 kTPI, L_s = 2,000, and L_n = 2,500 kBPI. As expected, the proposed ITI mitigation enhances the squeezed track BER performance significantly in the IMR channel, and can provide extra ADC push on top of the original IMR gain by enabling higher track density channel operation.

EUISEOK HWANG
E-mail: euiseokh@gist.ac.kr
tel: +82-62-7153223

REFERENCES

1) R. Wood, *et al*., "The feasibility of magnetic recording at 10 terabits per square inch on conventional media ," *IEEE Trans. Magn.,* 45(2) 917-923, (2009).
2) E. Hwang, *et al*., "Interlaced magnetic recording," *IEEE Trans. Magn.,* 53(4) 3101407, (2017).
3) E. F. Haratsch, *et al*., "Inter-track interference cancellation for shingled magnetic recording," *IEEE Trans. Magn.,* 47(10) 3698–3703, (2011).
4) Z. Wu, *et al*., "A MMSE interpolated timing recovery scheme for the magnetic recording channel," *IEEE Int. Conf. Commun.* 1997.

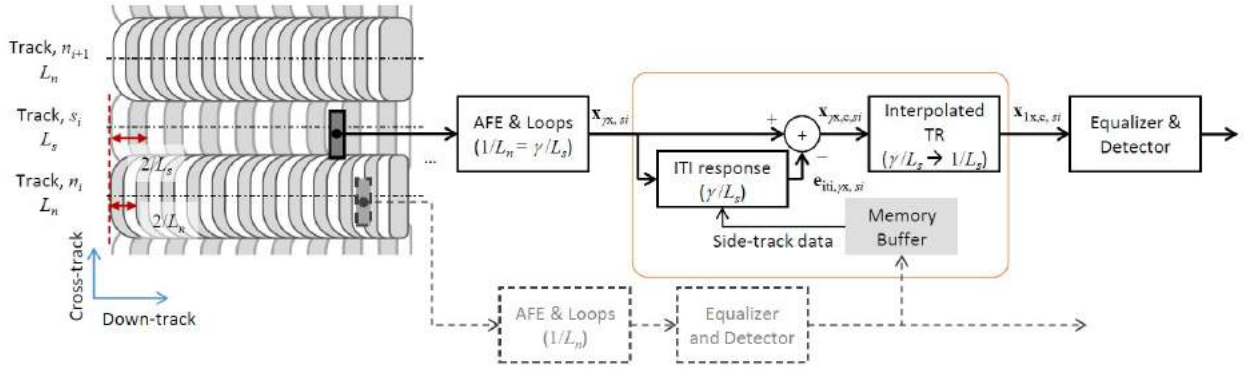

Fig. 1 Schematic of the read channel signal processing blocks of IMR with the proposed ITI mitigating scheme.

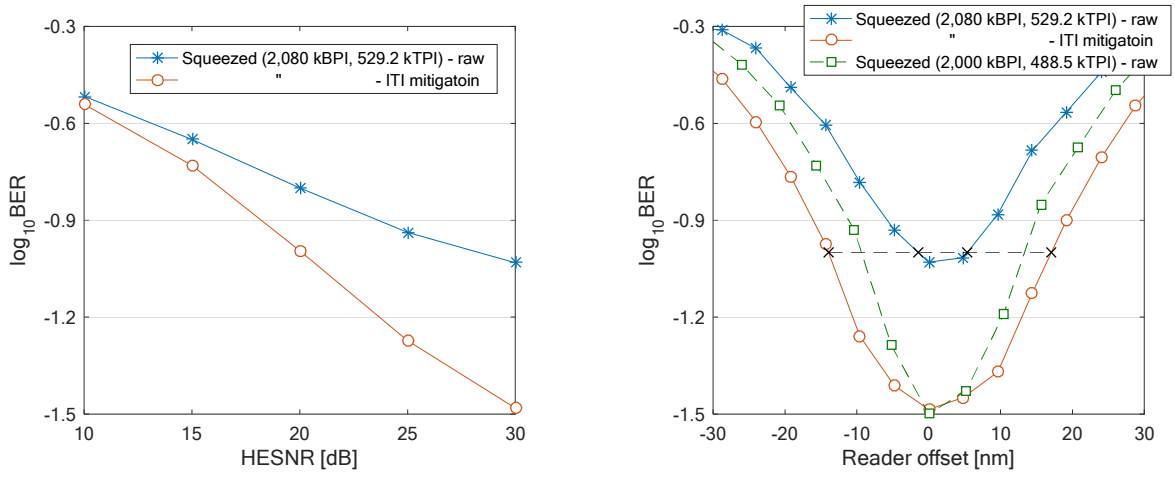

Fig. 2 BER performance of the IMR with the proposed ITI mitigating scheme (a) as a function of HESNR at on-track location with 529.2 kTPI, L_s = 2,080 and L_n = 2,600 kBPI, and (b) bathtub curves at HESNR=30dB with the previous condition, and with 488.5 kTPI, L_s = 2,000 and L_n = 2,500 kBPI for comparison.

REALIZATION OF HIGH QUALITY EPITAXIAL CURRENT-PERPENDICULAR-TO-PLANE GIANT MAGNETORESISTIVE PSEUDO SPIN-VALVES ON Si(001) WAFER USING NiAl BUFFER LAYER

Jiamin CHEN[1,2], J. LIU[2], Y. SAKURABA[2], H. SUKEGAWA[2], S. LI[2] and K. HONO[2,1]

[1]University of Tsukuba, Tsukuba, Japan
[2]National Institute for Materials Science, Tsukuba, Japan
E-mail address: chen.jiamin@nims.go.jp

I. INTRODUCTION

Spintronics is one of the research fields that have rapidly developed in these two decades. However, only a few applications reached to the practical level so far, i.e. there is still large gap between fundamental studies and practical applications in spintronics field. Although many previous studies on epitaxial current-perpendicular-to-plane giant magnetoresistive (CPP-GMR) devices reported excellent device performances, they are always regarded as fundamental studies because unpractical MgO single crystalline substrate is needed.[1] In this study, we report to use NiAl buffer layer as a template for the integration of epitaxial CPP-GMR devices on a Si(001) single crystalline substrate. We confirmed by a careful microstructure analysis that the epitaxial CPP-GMR devices with half-metallic $Co_2FeGa_{0.5}Ge_{0.5}$ (CFGG) Heusler electrode grown on the buffered Si(001) substrate have a very flat and sharp interface structures. Excellent magnetoresistive (MR) output that is comparable with the devices grown on an MgO(001) substrate were clearly observed in the device on Si substrate, demonstrating the possibility of epitaxial spintronic devices with NiAl template for practical applications.[2]

II. EXPERIMENT DETAIL

A fully epitaxial multi-layer stack of NiAl(50)/CoFe(0 or 10)/Ag(50)/CFGG(10)/Ag(5)/CFGG(10)/Ag(5)/Ru(8) (thickness in nm) was deposited onto Si(001) single-crystalline substrates using the ultrahigh vacuum magnetron sputtering system. Crystal structure, surface roughness, magneto-resistance property and microstructure were analysed by XRD, RHEED, AFM, direct current four-probe method and TEM, respectively.

III. EXPERIMENT RESULT

Figure 1 shows the XRD patterns accompanied with RHEED patterns for samples with single 50 nm thick NiAl layers deposited on a Si(001) substrate at different temperatures. At the deposition temperature of T_s=300°C, NiAl(011) and NiAl(022) peaks appear, indicating the NiAl layer grows with the (011) orientation in the out-of-plane direction, which is different from the (001) orientation of Si substrate. A very broad NiAl(011) peak shown in the two dimension XRD image suggests that the crystallinity is low at this deposition temperature. A RHEED pattern taken along the NiAl[100] azimuth gives a rings-centered pattern, which means a polycrystalline growth of the NiAl layer. When deposition temperature increases to T_s = 400°C, the NiAl(011) and NiAl(022) peaks disappear; instead, the NiAl(001) and NiAl(002) peaks appear. The appearance of NiAl(001) peak suggests that the NiAl has B2 ordered structure and its crystal orientation becomes (001) to the out-of-plane direction.

Figure 2 shows the stacking structure of multilayer for the whole CPP-GMR devices and the RHEED patterns for each layer. The sharp streaks in RHEED patterns for each layer demonstrate a nice epitaxial growth of CPP-GMR devices on a Si(001) single-crystalline substrate using NiAl as a buffer material. The epitaxial relationship of Si(001)[110]//NiAl(001)[110]//CoFe(001)[110]//Ag(001)[100]//CFGG(001)[110] can be confirmed for all the layers. The usage of NiAl buffer layer successfully overcomes the difficulty of growing high quality epitaxial ferromagnetic (FM) films on Si.

Figure 3 summarizes the MR outputs of resistance change-area product (ΔRA) for the epitaxial CPP-GMR devices grown on a Si(001) substrate (red stars) as a function of annealing temperature. High MR output (ΔRA of 8.56 mΩ· μm^2 and MR ratio of 27.8%) are achieved using the CFGG Heusler alloy as ferromagnetic layers on Si(001) substrate. It is important to point out that by inserting CoFe as a diffusion barrier, MR output is further enhanced to 9.54 mΩ· μm^2 and 37%, which presents comparable MR output with those grown on an MgO(001) substrate. This means we can replace the expansive impractical MgO

substrate with the Si substrate to achieve high performance epitaxial CPP-GMR devices for practical sensor applications, which is a great breakthrough. More importantly, by combining this epitaxial Si/NiAl/CoFe template with the wafer bonding technique,[3] various types of spintronic devices such as CPP-GMR, magnetic tunnel junctions, spin-field-effect transistors and lateral spin valves can be grown on a Si substrate and easily attached to other integrated circuits or magnetic shield layers, which is promising for next-generation spintronic applications based on epitaxial devices.

This work was supported in part by the ImPACT Program of Council for Science, Technology and Innovation, Japan.

IV. REFERENCE

1. Y. Du *et al.*, Appl. Phys. Lett. **103**, 202401 (2013).
2. J. Chen *et al.*, APL Mater. **4**, 056104 (2016).
3. H. Takagi *et al.*, Appl. Phys. Lett. **68**, 2222 (1996).

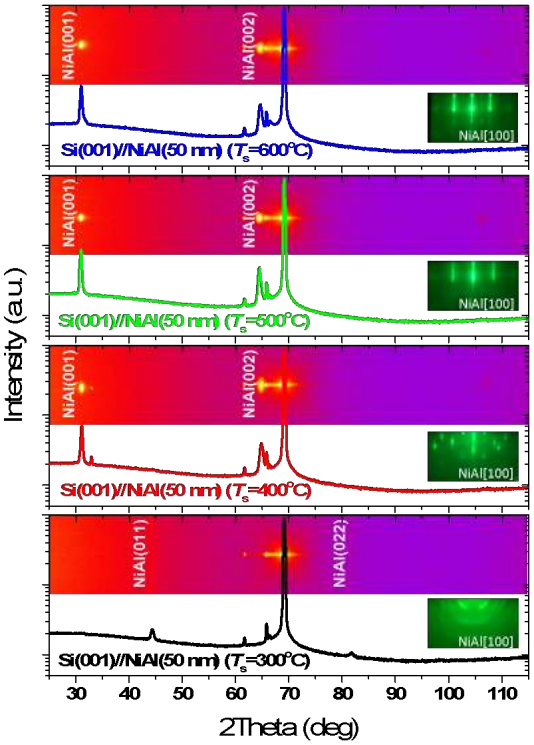

Fig.1 θ-2θ XRD profiles and corresponding two-dimensional diffraction images of 50 nm thick NiAl layer on Si(001) substrate with deposition temperature ranging from 300 to 600°C. Insets are RHEED patterns taken along <100> azimuth of each deposition temperature.

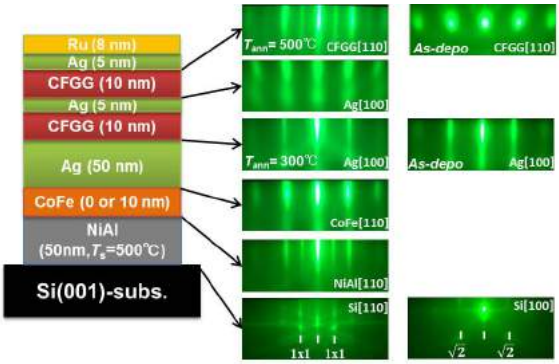

Fig.2 Structure illustration of whole CPP-GMR film stack and corresponding RHEED patterns for each layer.

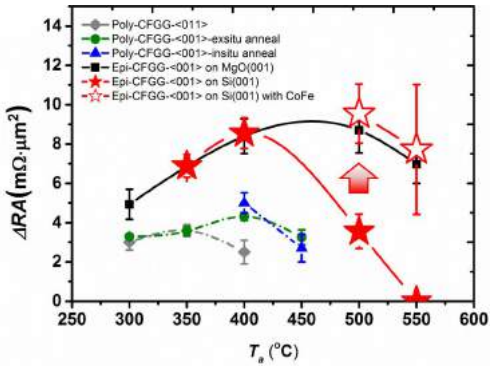

Fig.3 Annealing temperature dependence of ΔRA for various CPP-GMR devices.

LARGE NEGATIVE UNIAXIAL MAGNETIC ANISOTROPY OF COBALT FERRITE THIN FILMS

T. TAINOSHO, J. INOUE, S. SHARMIN, and H. YANAGIHARA
Univ. of Tsukuba, Tsukuba, Japan, s1630108@u.tsukuba.ac.jp

I. INTRODUCTION

Cobalt ferrite (CFO) is known as a magnetic material that possess large magneto-elastic coupling and therefore, uniaxial magnetic anisotropy can be introduced in a form of epitaxial films through magnetoelastic effect. Indeed, a CFO thin film on MgO(001) substrate showed extremely large uniaxial magnetic anisotropy energy K_u ($\simeq$ 1.4 MJ/m^3) [1]. In the phenomenological understanding of magnetoelastic effect, K_u is simply proportional to strain tensor. However, the linear relationship must be failed if the strain is large enough. In fact, from the view point of the recent electron theory [2], K_u seems to be saturated at highly distorted regime. At this moment, applicability of the phenomenological model regarding large strain is not clear for CFO. In this study, we investigated K_u of epitaxial CFO thin films with large distortion and compared it to the electron theory.

II. EXPERIMENT

CFO thin films (thickness :12.9 ~ 81.6 nm) were deposited on $MgAl_2O_4$(001) substrates by a reactive RF magnetron sputtering technique. The substrates were annealed at 773 K in a vacuum chamber. FeCo (3:1 atm ratio) was used as a sputtering target. Ar and O_2 mixed gas was flown as process gas at a rate of 30.0 sccm (~0.5 Pa) and 6.0 sccm (~0.1 Pa), respectively. The substrates were kept at 773 K and being rotated during the deposition. To change the amount of strain, several CFO thin films with different thickness (12.9 ~ 81.6 nm) were prepared. The surface structure of the films was characterized by reflection high-energy electron diffraction (RHEED). X-ray diffraction measurements were performed to examine both in-plane and out-of-plane lattice constants (a and c). MH-curves and magneto-torque curves were measured at 300 K.

III. RESULTS AND DISCUSSION

The RHEED pattern showed streaks typical for spinel structure suggesting an epitaxial growth of CFO. From Bragg positions of CFO(800) and (004) by XRD measurements, the in-plane and out-of-plane lattice constants were estimated to be 0.821 ~ 0.831 nm and 0.845 ~ 0.855 nm , respectively. In-plane MH-curves showed saturation magnetization comparable to that of a bulk. On the other hand, we could not saturate out-of-plane MH-curves due to its large anisotropy field. We measured torque curves to evaluate K_u, and saw-tooth-like curves (figure 1) were observed, indicating large magnetic anisotropy field exists. K_u was estimated to be -5.8 ~ -3.1 MJ/m^3 by Miyajima analysis. Figure 2 shows K_u vs χ ($\equiv c/a$ -1) plots. The linear relation between K_u and χ was confirmed despite the large strain. Assuming that the data plot passes through an origin, the magnetoelastic coefficient B_1 was estimated to be $0.131(\pm 0.019)$ GJ/m^3. This value is consistent to the bulk value (0.14 GJ/m^3) calculated from the elastic moduli C_{11} = 273 GPa, C_{12} =106 GPa, and magnetostiction constant λ_{100} = -590. We have succeeded in demonstrating that the phenomenological model of magnetoelastic theory for CFO is obviously valid for the strain of $\chi \simeq 0.04$, at least.

Takeshi Tainosho
E-mail: s1630108@u.tsukuba.ac.jp
tel: +81-29-853-5243

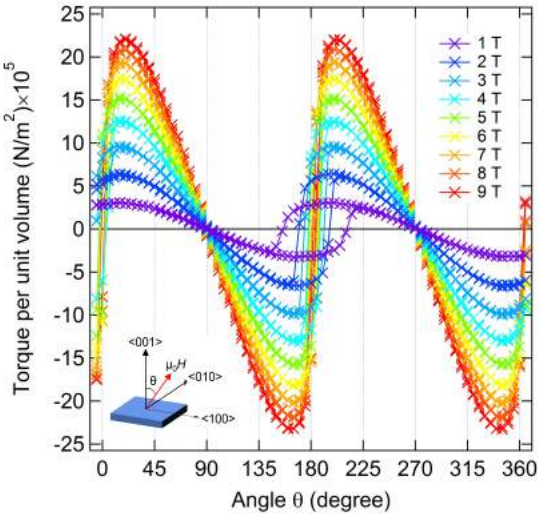

Fig.1 The torque curve of CFO (45 nm)/MAO. θ represents the angle between magnetic field vector and <001> direction of the film.

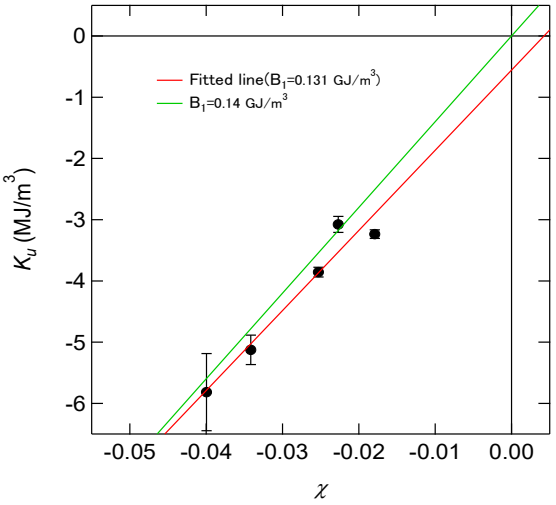

Fig.2 K_u vs χ plots. The fitting line is drawn by red one, and the green line indicates simple product $B_1\chi$ as B_1 = 0.14 GJ/m^3.

REFERENCES

1) T. Niizeki *et al*., "Extraordinarily large perpendicular magnetic anisotropy in epitaxially strained cobalt-ferrite CoxFe3-xO4(001) (x = 0.75, 1.0) thin films", Appl. Phys. Lett. 103 162407, (2013).

2) J. Inoue *et al*., "Electron theory of perpendicular magnetic anisotropy of Co-ferrite thin films", AIP advances 4 02711, (2014).

$L1_0$ ORDERED HIGH COERCIVITY FePt-C NANOGRANULAR FILMS WITH HIGH ASPECT RATIO FOR HEAT ASSISTED MAGNETIC RECORDING MEDIA

A. PERUMAL, J. WANG, H. SEPEHRI-AMIN, Y. K. TAKAHASHI and K. HONO
Research Center for Magnetic and Spintronic Materials, National Institute for Materials Science, 1-2-1 Sengen, Tsukuba 305-0047, Japan

INTRODUCTION

Heat assisted magnetic recording (HAMR) proposed as one of the alternative and new technologies to increase the areal density of beyond 2 Tbit/in^2 in hard disk drive (HDD) approaches its commercialization [1]. According to the standardization of Advanced Storage Technology Consortium (ASTC), this HAMR technology requires the recording medium consists of (i) densely dispersed ferromagnetic particles of high magnetocrystalline anisotropy (K_u) with uniform grain size between 4 and 6 nm and columnar type grains with aspect ratio, h/D (h is the height and D is average diameter of the grain) of at least 1.5 to obtain good signal to noise ratio, (ii) narrow size distribution between 10 and 15 % and reduced number of misoriented grains for obtaining controllable switching field distribution and (iii) high out-of-plane coercivity (H_C) of more than 3 T.

Among various materials available with high K_u, FePt based alloys are considered to be one of the promising materials. The realization of FePt-C based nanogranular films on single crystal MgO(001) substrates was first reported by Ko et al [2] and Perumal et al [3]. Subsequently, different research groups have attempted to fabricate FePt-C based nanogranular films on low cost substrates using different underlayers [4,5]. However, the development of FePt-C nanogranular films with high H_C and high aspect ratio remains challenge due to strong driving force for phase separation between FePt and C, which led to the formation of second layer of FePt-C with random orientation. To overcome the first problem, Zhang et al. added Ag into the FePt-C granular films to enhance the coercivity above 3 T [6] and demonstrated 550 Gbit/in^2 HAMR recording on the FePt-C granular films using a HAMR static tester [7]. On the other hand, the growth of FePt columnar grains was reported recently from industrial laboratories in FePt-X systems [8,9]. However, neither the information on the fabrication process of the columnar structure nor the type of X has been revealed. Varaprasad et al. reported an alternative way to achieve the columnar growth of FePt grain by using a compositionally graded sputtering method [10] with the stack structure of MgO(001)/ FePt-xC (2 nm)/ FePt-yC (2 nm)/ FePt-zC(2 nm)/ FePt-xC (2 nm)/ FePt-yC (2 nm) with x, y and z as 25, 30 and 35 vol.% of C, respectively. However, the achievable minimum grain size and highest aspect ratio was limited to 7.8 nm and 1.3, respectively. As to the reduction of the grain size and increase of aspect ratio, one needs to understand the detailed growth process of the columnar media structure from the nucleation and growth stage to the coarsening stage on heated substrates. Hence, we, in this study, report systematic investigations of layer-by-layer growth mode of FePt-C nanogranular films deposited as graded structure with different C volume fraction using magnetron sputtering technique to understand the growth mechanism of columnar FePt grains without the formation of second layer, reduced grain size of about 6.4 nm with narrow size distribution, high aspect ratio of about 2 and the resulting magnetic properties.

EXPERIMENTAL

FePt-C films were deposited by co-sputtering FePt and C targets onto single crystalline (001) oriented MgO substrate under 0.48 Pa Ar partial pressure. Although for industrial applications the FePt-C ferromagnetic layer must be grown on an appropriate seed layer through various buffer layers on glass disk substrates, in this study, we however used (001) MgO substrate as a model system. We have used stack structure for the deposition of the film with graded C vol. %. During film deposition, C target was continuously sputtered and the target power was controlled manually to vary C vol. % in different layers. For instance, the first film is made of 2 nm thick FePt-C(30.4 vol.%) only; while the second film consist of

Corresponding AUTHOR: Kazuhiro HONO
National Institute for Materials Science,
E-mail: Kazuhiro.hono@nims.go.jp

2 nm thick of each FePt-C (30.4 vol.%) and FePt-C (28.7 vol.%) layers and so on. The thickness of the each FePt-C layer with a particular C vol. % is fixed to be about 2 nm, e.g., two layer sequence gives a total thickness of 4 nm and 4 layer sequence provides 8 nm thick FePt-C film. Crystal structure and the degree of $L1_0$ order were analyzed using X-ray diffraction (XRD) with Cu-K_α radiation. Microstructures of the films were examined by in-plane and cross-sectional transmission electron microscopy (TEM) using FEI Tecnai 20. The room temperature magnetic properties were measured by superconducting quantum interference device vibrating sample magnetometer (SQUID-VSM, Quantum Design Inc.) with an applied magnetic field of up to ±7 T.

RESULTS

Fig. 1 shows the in-plane and cross-sectional TEM images of FePt-31vol.%C with the nominal thickness of 12 nm, which was deposited by the compositionally graded process. The in-plane TEM image shows a uniform microstructure with the average grain size of 6.4 nm and the cross sectional TEM image shows the aspect ratio of about 2. Note that the film thickness of 12 nm is double than the critical thickness of the single layer formation of 6 nm in the FePt-C system. The perpendicular H_C is 42 kOe with good squareness as required for recording media. In the in-plane magnetization curve, straight line and negligibly small hysteresis are evident. This indicates that the FePt grains are strongly [001] oriented in the perpendicular direction. The decreasing order of C concentration up to certain film thickness (6 nm in the present study) and the subsequent increase of C concentration provides excellent nanogranular films with good columnar growth of FePt grains without any second layer grains. With this study, we can selectively choose the total film thickness between 8 and 12 nm and then search for optimization methods to refine the grain size below 6 nm and the resulting magnetic properties by tuning the C vol. % in the films.

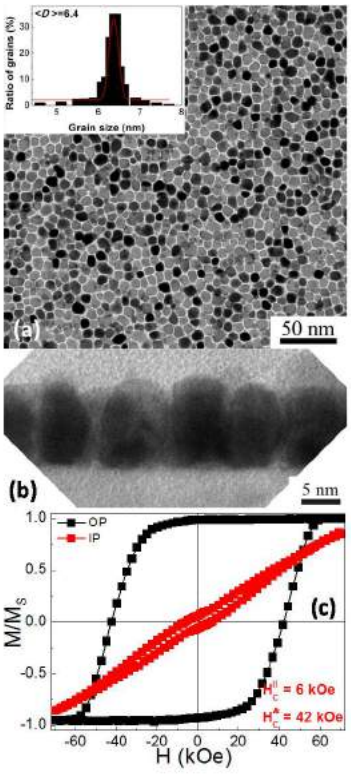

Fig. 1 In-plane and cross sectional TEM image of an optimized FePt-C film deposited by the compositionally graded process.

[1] D. Weller, G. Parker, O. Mosendz, E. Champion, B. C. Stipe, X. Wang, T. Klemmer, G. Ju, and A. Ajan, "A HAMR Media Technology Roadmap to an Areal Density of 4 Tbit/in2/in2", IEEE Trans. Magn. vol. 50, pp. 3100108, 2014.

[2] H. S. Ko, A. Perumal, and S.-C. Shin, "Fine control of L10 ordering and grain growth kinetics by C doping in FePt films", Appl. Phys. Lett. vol. 82, pp. 2311-2313, 2003.

[3] A. Perumal, H. S. Ko, and S.-C. Shin, "Magnetic properties of carbon-doped FePt nanogranular films", Appl. Phys. Lett. vol. 83, pp. 3326-3328-3331, 2003.

[4] J. S. Chen, Y. F. Ding, B. C. Lim, and E. J. Liu, "Nanogranular L10 FePt:C Composite Films for Perpendicular Recording", IEEE Trans. Magn. vol. 42, pp. 2363-2365, 2006.

[5] A. Perumal, Y. K. Takahashi, and K. Hono, "L10 FePt-C Nanogranular Perpendicular Anisotropy Films with Narrow Size Distribution", Appl. Phys. Exp. vol. 1, pp. 101301, 2008.

[6] L. Zhang, Y. K. Takahashi, A. Perumal, and K. Hono, "L10-ordered high coercivity (FePt)Ag–C granular thin films for perpendicular recording", J. Mag. Mag. Mater. vol. 322, pp. 2658-2664, 2010.

[7] L. Zhang, Y. K. Takahashi, K. Hono, B. C. Stipe, J. Y. Juang, and M. Grobis, "L10-ordered FePtAg-C granular thin film for thermally assisted magnetic recording media", J. Appl. Phys. vol. 109, pp. 07B703, 2011.

[8] R. Acharya, "Challenges and Recent Developments in heat assisted magnetic recording media" TMRC 2014, Berkley, August 11-13, 2014.

[9] O. Hellwig, "Challenges in Developing FePt L10 Granular Thin Film Media for Heat Assisted Magnetic Recording (HAMR)", Intermag 2015, AA-05, Beijing, May 11-15, 2015.

[10] B. S. D. Ch. S. Varaprasad, J. Wang, T. Shiroyama, Y.K. Takahashi, K. Hono, "Columnar Structure in FePt-C Granular Media for Heat Assisted Magnetic Recording", IEEE Trans. Magn. (2015).

BP-22

DESIGN OF A PCB-BASED VECTORIAL MAGNETIC FIELD SENSOR

Ping Hsun HSIEH[1], Shih-Jui CHEN[2,*],and Yean-Ren HWANG[3]

1) National Central University, Taoyuan City, Taiwan, 103383005@cc.ncu.edu.tw

2) National Central University, Taoyuan City, Taiwan, raychen@cc.ncu.edu.tw

3) National Central University, Taoyuan City, Taiwan, yhwang@cc.ncu.edu.tw

I. ABSTRACT

A PCB-based two-axis planar fluxgate magnetic field sensing system is presented. Through PCB fabrication procedure, the fluxgate sensor and lock-in amplifier circuit for signal detection were integrated together. The fluxgate sensor consisted of cross-shaped magnetic core, one excitation coil, and four sensing coils. The excitation and sensing coils were patterned in the opposite side of the circuit board with core pasted on it. The characteristic of the fluxgate sensor with respect to excitation signal was tested. Through the excitation signal optimizing, the fabricated two-axis fluxgate sensor showed nonlinearity below 5% in the range of 0-80 μT with 410 V/T sensitivity for the x-axis, and 436 V/T sensitivity for the y-axis, respectively. In addition, the sensing of vectorial magnetic field was demonstrated a great precision in both axes.

II. PRINCIPLE

The schematic diagram of the magnetic field sensor proposed is shown in figure 1. It consists of cross-shaped magnetic core, one excitation coil, and four sensing coils. With input AC signal in excitation coil, the alternate excitation magnetic field generated according to Ampere's circuital law causing the magnetic core saturated periodically. Due to the interaction with varying magnetic field, the induction voltage was emerged in sensing coil. Under the external magnetic field, the induction voltage of sensing coil was shifted. Through the difference of induction voltage, the sensing coils in the same axis were used to measure the external magnetic field.

III. CONCLUSION

In this paper, the integration of fluxgate sensor and lock-in amplifier circuit was successfully achieved by PCB technology. The fabricated magnetic sensor is shown in figure 2. By adjusting the parameter of the excitation signal, the performance of fluxgate magnetic field sensor had been optimized. Through the experiment result, the characteristic of the fluxgate sensor is shown in table I and figure 3. Furthermore, the component analysis of magnetic field is demonstrated in figure 4 shows a fine precision in both axes.

REFERENCES

1) O. Dezuari, Eric Belloy, Scott E. Gilbert, and Martin A. M. Gijs, "New hybrid technology for planar fluxgate sensor fabrication", *IEEE Transcations on Magnetics*, 35, 2111-2117, (1999).
2) Hae-Seok Park, Jun-Sik Hwang, Won-Youl Choi, Dong-Sik Shim, Kyoung-Won Na, and Sang-On Choi, "Development of micro-fluxgate sensors with electroplated magnetic cores for electronic compass", *Sensors and Actuators A: Physical*, 114, 224-229, (2004).
3) L. Perez, C. Aroca, P. Sanchez, E. Lopez, M.C. Sánchez, "Planar fluxgate sensor with an electrodeposited amorphous core", *Sensors and Actuators A: Physical*, 109, 208-211, (2004).

Shih-Jui Chen
E-mail: raychen@cc.ncu.edu.tw
tel: +886-3-4267300

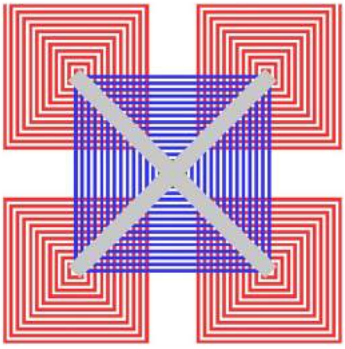

Fig. 1 Schematic of the fluxgate magnetic field sensor.

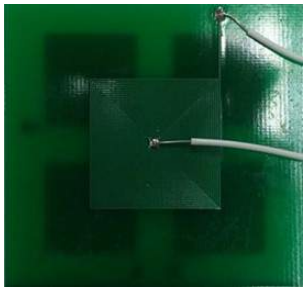

Fig. 2 Photograph of the fabricated magnetic field sensor.

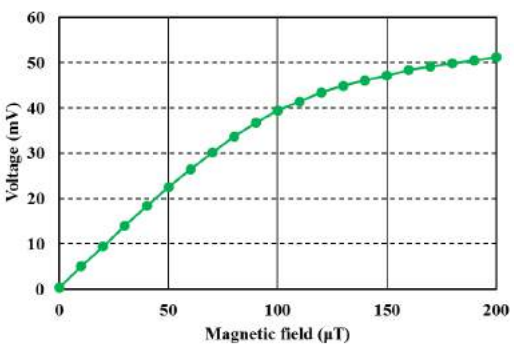

Fig. 3 Output voltage of fluxgate sensor in different magnetic field.

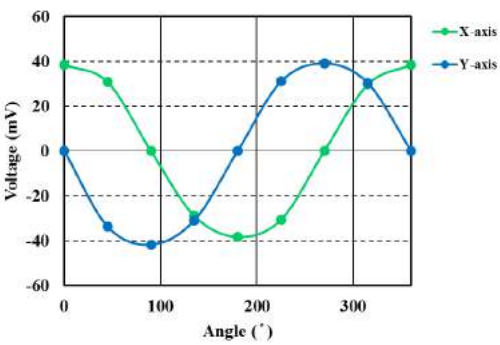

Fig. 4 The component analysis of magnetic field of 100 μT.

Table I Characteristic of the fluxgate sensor.

Excitation signal	50 kHz、0.75 A
Linear range	0-80 μT
X-axis sensitivity	410 V/T
Y-axis sensitivity	436 V/T

MICROMAGNETICS STUDY ON STRONGLY EXCITED SPINWAVES IN SUB-μm-WIDE NiFe STRIPS

G. OKANO[1] and Y. NOZAKI[1,2]

1) Keio Univ., Yokohama, Japan, {g.okano, nozaki.a2}@keio.jp

2) Center for Spintronics Research Network, Keio Univ., Yokohama, Japan, nozaki@phys.keio.ac.jp

I. INTRODUCTION

A fluctuation in local magnetic ordering propagates as spin-waves and corresponding bosonic quanta are called magnons. Magnons attract a strong attention in both fundamental physics and practical applications. Indeed, information transfer and data processing can be realized by utilizing magnons. A variety of alternative devices to traditional electric ones have been proposed; such as spinwave logic gates [1], spinwave interferometers [2], magnon transistors [3] and magnonic crystals [4]. Meanwhile, the excitation of a large amount of magnons leads to Bose-Einstein condensation (Magnon-BEC) [5]. In magnonic devices and magnon-BEC experiments, nonlinear interactions such as 3-magnon scattering play a significant role. Figure 1 shows the schematic 3-magnon scattering process where a k = 0 magnon is destroyed followed by a creation of two magnons having half the energy and opposite wave vectors. When the bottom of the magnon bands is lower than the half of the frequency f_0 of pumped field, 3-magnon scattering can occur. The band profile is, therefore, essential to identify the magnons. However, in narrow NiFe strips which is usually used for the spinwave devices, it is hard to obtain the band profile analytically. As a consequence, few studies on nonlinear magnon scattering processes in the confined metallic ferromagnets, such as NiFe strips, have been demonstrated, although many researches on bulk and solid films were conducted. The study on nonlinear scattering process in sub-μm scale ferromagnets are essential for realizing the nanoscale magnonic devices. In this study, we numerically investigated the magnetization dynamics and the consequent magnon interaction processes in sub-μm-wide NiFe strips. The numerical results are consistent with our previous experimental results.

II. MICROMAGNETICS SIMULATIONS – LINEAR REGIME

Micromagnetics simulations were demonstrated by using MuMax3 [6]. The numerical parameters used in the simulations are as follows; We used the magnetic parameters for NiFe; saturation magnetization M_s = 10 kG, exchange stiffness A_{ex} = 1.3×10^{-6} erg/cm^3, Gilbert damping constant α =0.01. The geometry of NiFe strip was 60 nm-thick and 5 μm-long with a periodic boundary condition along its length.

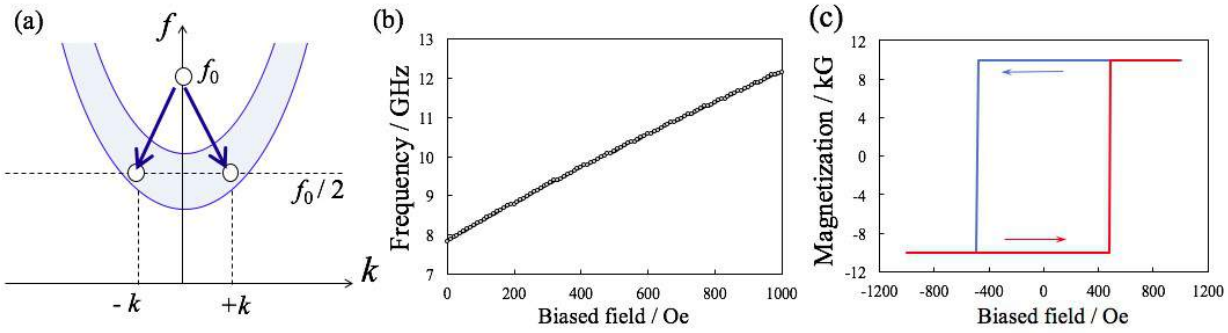

Fig. 1 (a) Schematic 3-magnon scattering process. (b) H_{ex} dependence of the resonant frequency in a linear regime. (c) Magnetization hysteresis of the NiFe strip.

The width of the NiFe strips were varied to discuss the dependence of the magnon scattering on the shape anisotropy. The numerical grid was a cube, 10 nm each side and a thermal fluctuation was not considered. Figure 1(b) shows H_{ex} dependence of the resonant frequency calculated for a 700 nm wide NiFe strip. Here, the resonant frequency was evaluated from the fast Fourier transformation of temporal variation of

GENKI OKANO
E-mail: g.okano@keio.jp
tel: +81-45-5661677

magnetization relaxation from a uniformly magnetized state at an angle of 1° from the longitudinal direction of the NiFe strip. The oscillation of magnetization during the relaxation is sufficiently small to simulate the linearly responding regime. Figure 1(c) shows a magnetic hysteresis loop of the NiFe strips. An external magnetic field was applied at an angle of 1° from the longitudinal direction of the NiFe strip. The rectangular shape of the magnetic hysteresis loop indicates a strong shape anisotropy of the 700 nm wide and 60 nm thick NiFe strip.

III. MICROMAGNETICS SIMULATIONS – NONLINEAR REGIME

The magnetization dynamics under the simultaneous applications of H_{dc} and microwave field with an amplitude of h_{ac} and a frequency of f_{ac}, were calculated for 10 ns. Here, a temporally averaged precession angle given by $\langle\theta_{cone}\rangle = \mathrm{Cos}^{-1}\langle M_x\rangle$ is used to evaluate the magnetization dynamics quantitatively, where $\langle M_x\rangle$ is a M_x value time-averaged from 9.5 to 10 ns. The averaging period of 500 ps is long enough to evaluate the stationary magnetization dynamics because f_{ac} is in the range from 5 to 15 GHz whose period is shorter than 200 ps. Figures 2(a)-2(c) show the color plots of $\langle\theta_{cone}\rangle$ in the parameter space of H_{dc} and f_{ac} calculated for (a) h_{ac}=10 Oe, (b) 50 Oe and (c) 100 Oe, respectively. It is clear that a subsidiary peak of $\langle\theta_{cone}\rangle$ appears along the dashed line in Fig. 2(c). The subsidiary resonance is attributable to the 3-magnon scattering. The detail of the numerical result will be presented at the conference.

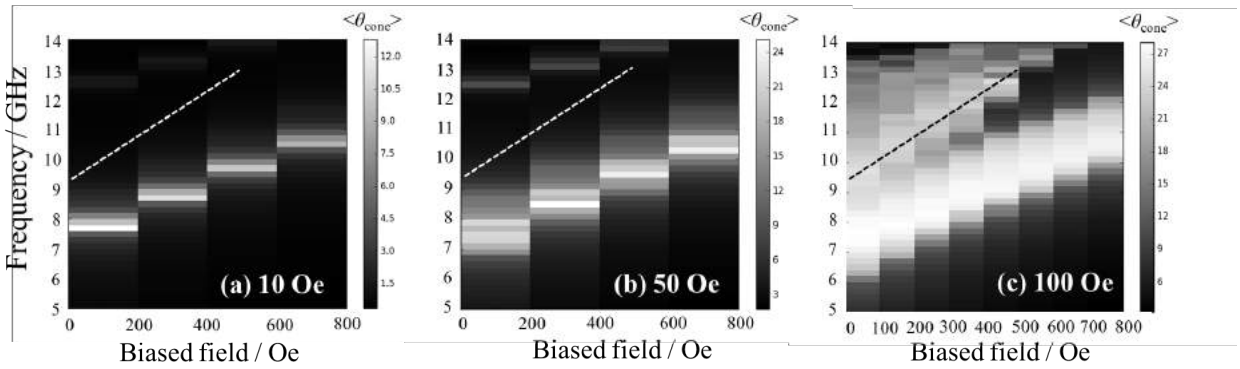

Fig. 2 Color plots of $\langle\theta_{cone}\rangle$ calculated for h_{ac} with an amplitude of (a) 10, (b) 50, and (c) 100 Oe.

REFERENCES

1) T. Schneider, A. A. Serga, B. Leven, B. Hillebrands, R. L. Stamps and M. P. Kostylev, "Realization of spin-wave logic gates", *Appl. Phys. Lett.* **92**, 022505 (2008).
2) K. S. Lee and S. K. Kim, "Conceptual design of spin wave logic gates based on a Mach-Zehnder-type spin wave interferometer for universal logic functions", *J. Appl. Phys*, **104**, 053909 (2008).
3) A. V. Chumak, A. A. Serga and B. Hillebrands, "Magnon transistor for all-magnon data processing", *Nat. Comms.,* **5**, 4700 (2014).
4) V. Cherepanov, I. Kolokolov and V. L'vov, "Spectra, thermodynamics, interaction and relaxation of magnons in a complex magnet", *Phys. Rep.,* **229**, 81-144 (1993).
5) S. O. Democritov, V. E. Demitov, O. Dzyapko, G. A. Melkov, A. A. Serga, B. Hillebrands and A. N. Slavin, "Bose-Einstein condensation of quasi-equilibrium magnons at room temperature under pumping", *Nature,* **443**, (2006).
6) A. Vansteenkiste, J. Leliaert, M. Dvornik, M. Helsen, F. Garcia-Sanchez and B. V. Waeyenberge, "The design and verification of MuMax3", AIP Advances, **4**, 107133, (2014).

IMPACT OF DAMPING CONSTANT IN HEAT-ASSISTED MAGNETIC RECORDING

Tadashi KOBAYASHI[1], Yoshinobu NAKATANI[2], Kohei ENOMOTO[1] and Yuji FUJIWARA[1]
1) Mie Univ., Tsu, Japan, kobayasi@phen.mie-u.ac.jp
2) Univ. of Electro-Communications, Chofu, Japan, nakatani@cs.uec.ac.jp

I. INTRODUCTION

We have already proposed a new model calculation [1, 2] for heat-assisted magnetic recording using the grain magnetization reversal probability and the attempt period, whose inverse is the attempt frequency f_0. f_0 is a function of the damping constant α [3], and α is also a function of temperature [4, 5]. Therefore, although knowledge of α at the writing temperature is necessary, it is unknown.

In this study, we calculate the bit error rate for α = 0.1 and 0.01 using our new model calculation, and discuss the results for various thermal gradients and linear velocities.

II. RESULTS

The new model calculation can obtain the bit error rate as a function of the writing field H_w. The bit error rates in this study are useful only in a comparison. Figure 1 shows the dependence of the minimum bit error rate (bER) on the thermal gradient for α = 0.1 and 0.01 within $H_w \leq$ 10 kOe where the linear velocity v = 10 m/s. When α = 0.1, the bER can be reduced as the thermal gradient increases since erasure-after-write can be suppressed. On the other hand, when α = 0.01, the bER becomes rather worse as the thermal gradient increases. Since the attempt period is long and the attempt number during writing is small for α = 0.01, the chance for writing decreases. The medium becomes cool before writing as the thermal gradient increases, and write-error increases. The coercivity becomes very high before writing, and a higher writing field $H_w >$ 10 kOe becomes necessary. We can consider writing slowly by reducing the linear velocity to reduce write-error since the writing chance increases. As expected, the bER can be reduced as the linear velocity decreases as shown in Fig. 2. The damping constant at the writing temperature is a very important parameter.

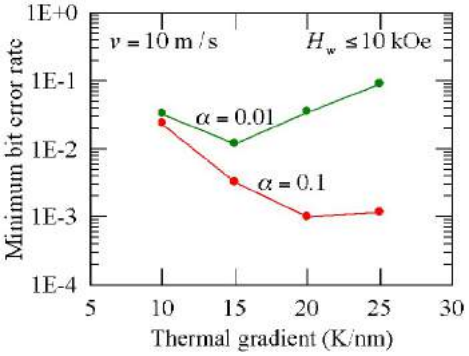

Fig. 1 Dependence of minimum bit error rate on thermal gradient for α = 0.1 and 0.01.

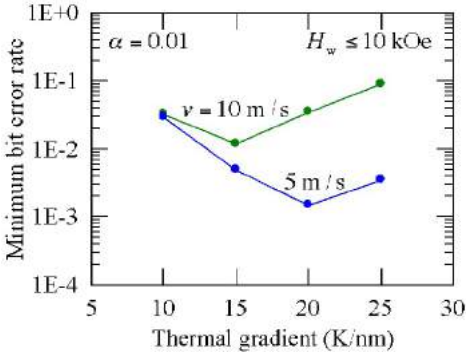

Fig. 2 Dependence of minimum bit error rate on thermal gradient for v = 5 and 10 m/s.

We acknowledge the support of the Advanced Storage Research Consortium (ASRC), Japan.

REFERENCES

1) T. Kobayashi, F. Inukai, K. Enomoto and Y. Fujiwara, *J. Magn. Soc. Jpn*., 41(1) 1-9, (2017).
2) T. Kobayashi, Y. Nakatani, F. Inukai, K. Enomoto and Y. Fujiwara, *J. Magn. Soc. Jpn*., 41(3) 52-57, (2017).
3) Y. Nakatani, Y. Uesaka, N. Hayashi and H. Fukushima, *J. Magn. Magn. Mat*., 168 347-351, (1997).
4) T. Kobayashi, H. Hayashi, Y. Fujiwara and S. Shiomi, *IEEE. Trans. Magn*., 41(10) 2848-2850, (2005).
5) C. D. Stanciu *et al*., *Phys. Rev. B*, 73 220402(R), (2006).

Tadashi Kobayashi
E-mail: kobayasi@phen.mie-u.ac.jp
Tel: +81-59-231-9731

BP-25

DESIGN OF A LOW-FREQUENCY ELECTROMAGNETIC ENERGY HARVESTER BY USING INDUCED MAGNETIC FORCE

Yao-Yun FENG[1], Shu-Yu LIU[2], and Shih-Jui CHEN[3,*]

1) National Central University, Taoyuan City, Taiwan, 103383004@cc.ncu.edu.tw

2) National Central University, Taoyuan City, Taiwan, 101323013@cc.ncu.edu.tw

3) National Central University, Taoyuan City, Taiwan, raychen@cc.ncu.edu.tw

I. ABSTRACT

An electromagnetic energy harvester using magnetic force to improve the insufficient bandwidth and the non-matching resonant frequency with the environmental vibration is proposed [1][2]. For the fabrication, we used MEMS process to produce a cantilever structure with a proof mass. Then, conductive coils and magnetic nickel film were added on the cantilever beam. The magnetic force between the nickel epoxy and a magnet was used to adjust the resonant frequency. The characteristics of the energy harvester with respect to magnetic force were tested, including resonant frequency, bandwidth, and voltage. When the distance between the energy harvester and the magnet was set from 10 to 2 mm, the resonant frequency was dropped from 197 to 185 Hz, and the induced voltage was increased from 1 to 5.3 mV. In addition, adjusting the overlapping position of the magnet and the energy harvester will increase the bandwidth of the generator. The fabricated devices are shown in figure 1 and figure 2.

II. PROCESS

The fabrication process of the energy harvester is shown in figure 3. First, a silicon cantilever device (include mass) was fabricated by microelectromechanical systems (MEMS) process [3]. Then, the coil and the magnetic nickel film were deposited on the cantilever by using dispensing process. During the fabrication, the materials were controlled with appropriate speed and pressure to make the structure.

III. CONCLUSION

In this research, the coil and magnetic nickel film were successfully fabricated on the cantilever device, and magnetic force was used to improve the insufficient bandwidth and the non-matching resonant frequency. Distance between the energy harvester and the magnet of the experiment result is shown in table I. The energy harvester induction voltage increased and resonant frequency decreased when the energy harvester was put closer to the NdFeB magnet. In table II, by adjusting the overlapping position of the magnet and the energy harvester, the resonant frequency and the bandwidth showed apparent difference.

REFERENCES

1) C.B. Williams, C. Shearwood, M.A. Harradine, and P.H. Mellor, "Development of an electromagnetic micro-generator", *Circuits, Devices and Systems, IEEE Proceedings*, 148(6), 337-342, (2001).

2) V.R. Challa, M.G. Prasad, Y. Shi, and F.T Fisher, "A vibration energy harvesting device with bidirectional resonance frequency tenability", *Smart Mater. Struct.*, 17, 015035, (2008).

3) Q. Zhang, L. Liu, and Z. Li , "A new approach to convex comer compensation for anisotropic etching of (100) Si in KOH", *Sensors and Actuators A*, 56, 251-254, (1996).

Shih-Jui Chen
E-mail: raychen@cc.ncu.edu.tw
tel: +886-3-4267300

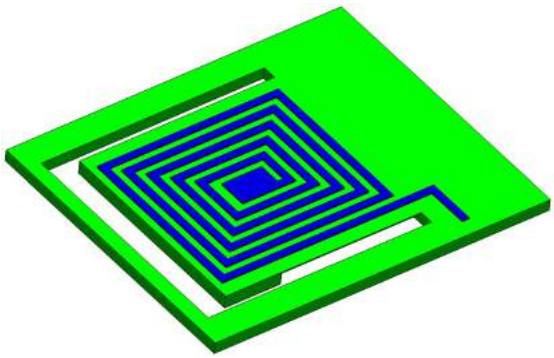

Fig. 1 Schematic of the energy harvester.

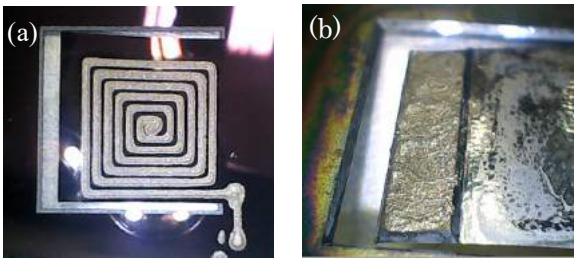

Fig. 2 Photo of the energy harvester device: (a) coil (b) magnetic nickel film.

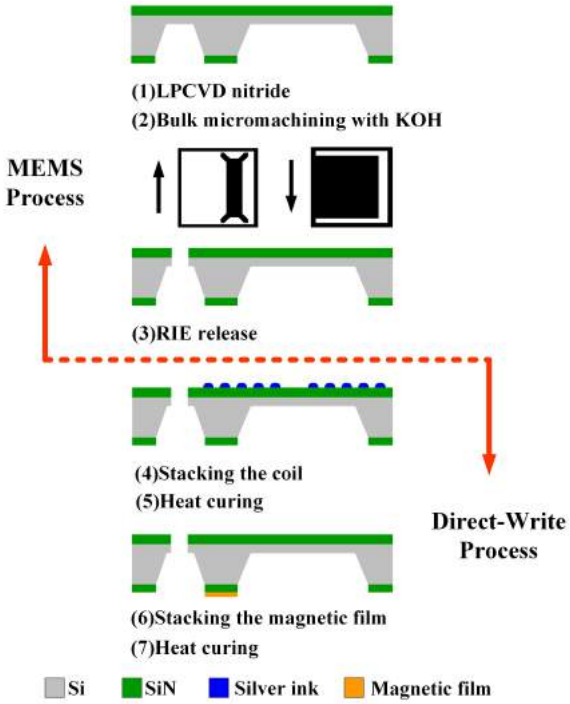

Fig. 3 The fabrication process of the device.

Table I System performance with respect to various vertical distances.

Displacement	Frequency	Voltage	Bandwidth
10 mm	197 Hz	48 mV	8.27 Hz
5 mm	188 Hz	102 mV	4.95 Hz
2 mm	185 Hz	264 mV	4.3 Hz

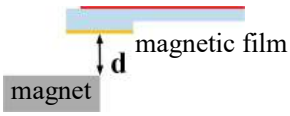

Table II System performance with respect to various overlapping lengths.

Type	Frequency	Voltage	Bandwidth
no magnetic film	195 Hz	198 mV	5.21 Hz
(a)	155 Hz	128 mV	24.94 Hz
(b)	185 Hz	264 mV	4.22 Hz

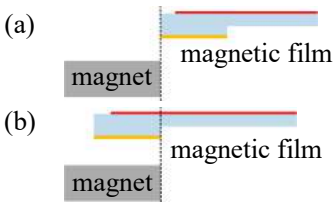

WRITER SYSTEM OPTIMIZATION USING TAU-MODEL

Masayuki TAKAGISHI[1], Tomokazu OKUBO[2] and Kenichiro YAMADA[3]
1) Toshiba Research Consulting Corporation
2) Toshiba Corporation, Storage products design & production div. common core engineering dept. PCB&LSI engineering group
3) Toshiba Corporation, Corporate R&D center, Spintronic Devices Lab.

Ⅰ. INTRODUCTION

In order to increase the areal density of Hard Disk Drive, high jump-up by HAMR, MAMR, or TDMR is required, but the current system optimizations such as head shape optimizations or write-current wave form optimizations are also required. Though LLG (Landau–Lifshitz–Gilbert equation) simulator is preferable for these optimizations, computation resource still tends to be huge to calculate SNR, fringe properties or BER (Bit Error Rate). In this paper, our newly developed FEM (Finite Element Method)-model called tau-model is proposed, which model can calculate time-dependent write field from write heads several ten times faster than LLG and can trace the LLG behavior.

Ⅱ. MODELING METHOD

Basic equations of tau-model are shown as follows.

$$rot(\nu_0 \cdot rot\vec{A}) - \nu_0 \cdot rot\vec{M} - \vec{J} = 0 \quad (1)$$

$$\vec{M} + \tau \cdot \frac{d\vec{M}}{dt} = \chi \cdot \vec{H} \quad (2)$$

(A: vector potential, M: magnetization, J: write current, ν: magnetic resistivity, χ: magnetic susceptibility)

The equation (1) is Maxwell equation and (2) provides the magnetizaion with phase delay. The damping parameter “tau” in this equation is derived from the magnetic transmission line model[1][2]. Tau model calculates these equations in coalition with FEM technique. Figure 1 shows magnetization time delay of write head’s main poles by using LLG and the tau-model. The horizontal axis of this figure shows the distance from ABS. The legend indicates yoke length of the write heads. Time delay calculated by tau-model is in good agreement with the result of LLG. This dependency was same for different writer models with several different yoke shapes. Every models were used by the same tau-value=0.6nsec. This fact means that this model can well trace LLG model results without changing the tau-value for minor changes of head shapes.

Ⅲ. CALCULATION RESULTS

Figure 2 shows time delay of yoke magnetization depending on coil shapes by the tau-model. The time delay of a toroidal coil shape is faster than a pan-cake shape’s by around 10%. It is well known that the toroidal coil has fast responses but the reason is generally supposed to be its lower electrical impedance. As this model does not include the impedance effect, the good performance of the toroidal coil causes only from the relative position relationship between the yoke and the coil. This result suggests the possibility for more optimization of the coil shape or the position. Tau-model can easily evaluate such dynamic performances of the writer.

Figure 3 shows BER depending on the write current wave forms using the tau-model. Each point of BER in this figure uses 34000 random bit pattern. The tau-model can be so fast as to make it possible to do

Masayuki Takagishi
E-mail: masayuki.takagishi@toshiba.co.jp
tel: +81-44-549-2391

such large scale calculation.

. REFERENCES

1) Erich P. Valstyn, "An Extended, Dynamic Transmission-Line Model for Thin-Film Heads", *IEEE Trans. Magn.,* 29(6) 3870-3872, (1993)
2) M. Takagishi, "The Effect of Yoke length on Nonlinear Transition Shift in Inductive/MR composite Heads", *IEEE Trans. Magn.,* 33(5) 2821-2823, (1997)

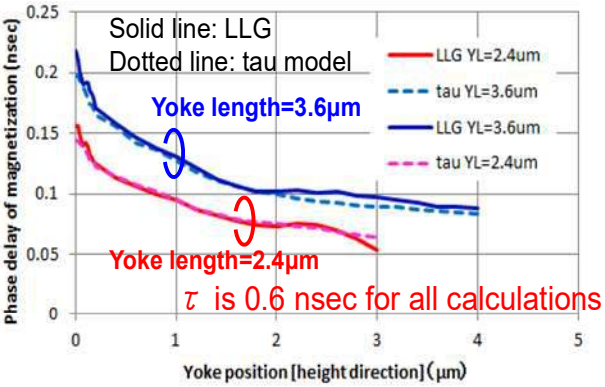

Fig. 1 Time delay of yoke magnetization comparison between tau-model and LLG

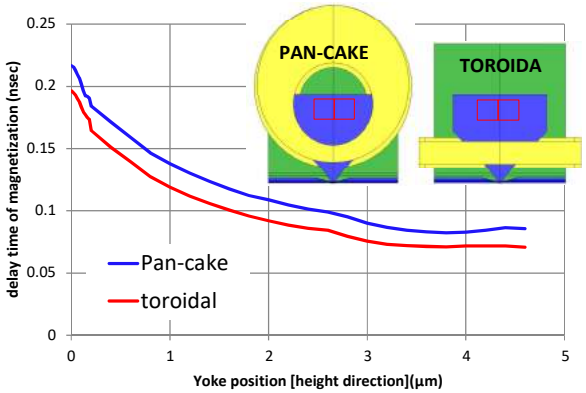

Fig. 2 Time delay of yoke magnetization depending on the coil shape.

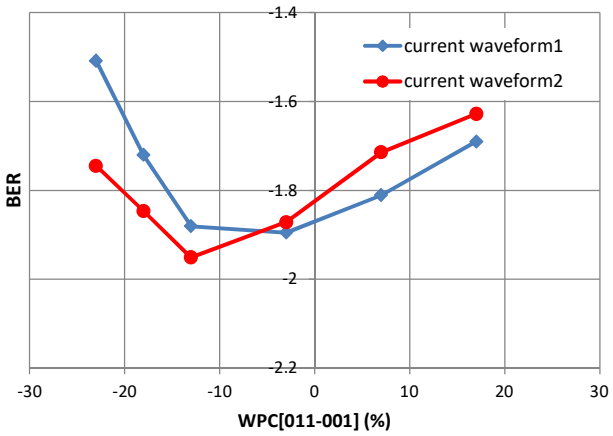

Fig. 3 BER depending on the write current wave form using tau-model
36000 random bits are used for each point.

LOW STACKING FAULTS CoPtRu ALLOY AS A BUFFER LAYER MATERIAL FOR PERPENDICULAR MAGNETIC RECORDING MEDIA

Yu SUZUKI [1], Ken INOUE[2], Shintaro HINATA[3] and Shin SAITO[4],

1) Furuya Metal Co., Ltd., ShimodateDaiichi Kogyodanchi, 1915, Morisoejima, Chikusei-shi, Ibaraki 308-0861, Japan, y_suzuki@furuyametals.co.jp
2) Tohoku University, Sendai, Miyagi, 980-8579 JAPAN, k_inoue@ecei.tohoku.ac.jp
3) Tohoku University, Sendai, Miyagi, 980-8579 JAPAN, s_hinata@ecei.tohoku.ac.jp
4) Tohoku University, Sendai, Miyagi, 980-8579 JAPAN, ssaito@ecei.tohoku.ac.jp

I. INTRODUCTION

Uniaxial crystal symmetry of Co-based ferromagnetic crystal grains is important for various magnetic devices such as magnetic recording media. It has been pointed out that the uniaxial magnetocrystalline anisotropy energy (K_u) of the Co -based alloy film has remarkably decreased when stacking faults (SFs) are introduced into the Co alloy grains [1]. However, only few papers reported about quantitative evaluation of degree of SFs in the Co alloy experimentally [2, 3]. We have found and established quantitative evaluation method for the structure with SFs in the *c*-plane oriented hexagonal phase (hereafter abbreviated as pseudo hcp) by a laboratory-scale X-ray diffractometer (XRD) [4-8]. When this evaluation method is applied to Co-Pt-Cr sputtered film formed on Ru underlayer at room temperature, it revealed that hexagonal stacking is stabilized at limited composition region with (Cr + Pt) concentration of 15-30 at% [9]. In this report, the degree of SFs was quantitatively evaluated for the Co-Pt-Ru pseudo hexagonal film in which Cr was replaced with Ru for the purpose of stabilizing the hexagonal stacking of Co-Pt alloys.

II. RESULTS AND DISCUSSION

Figure 1 shows the in-plane XRD profile for (a) $Co_{100-x}Pt_x$ and (b) $Co_{100-x}Ru_x$ alloy films with various *x*. It should be noted that *c*-plane orientation of all samples was confirmed by an out-of-plane XRD profile. For (a), diffraction from the hexagonal (10.0) plane is very weak for the film with $x = 0$ at.% (pure Co), and the intensity of the diffraction from (10.0) plane gradually increases as *x* increases until $x = 30$ at.%, and it decreases with increasing *x* from 30 to 100 (pure Pt) at.%. Increase of diffraction intensity from (10.0) plane in $x = 0$ to 30 at.% indicates that reduction of SFs in the hcp Co-Pt alloy due to increase of valence electron number [7]. Decrease of the diffraction from (10.0) plane suggests that excessive addition of Pt atom leads to collapse of the hcp atomic stacking. On the other hand, for (b), the diffraction from (10.0) plane increases with increasing *x* from 0 to 100 (pure Ru) at.%. This result shows that addition of Ru atoms stabilizes the hcp atomic stacking of the Co-Ru alloy.

Fig.2 shows the dependence of a corrected intensity ratio on the additional element concentration for the Co-Pt-Ru alloy film. The corrected intensity ratio is a value obtained by correcting the diffraction intensity ratio of the (10.0) plane and the (11.0) plane of the pseudo-hexagonal film with the atomic scattering factor, the Lorentz polarization factor, and the irradiation area [7]. Value of the corrected intensity ratio becomes 0 for the perfect face-center-cubic stacking, and becomes 0.25 for the perfect hcp stacking. Composition range where the corrected intensity ratio is 0.20 or more largely expanded from the Ru side, and thus Ru addition tends to stabilize the hcp stacking of the Co-Pt based alloys compared with Cr addition [9]. In the presentation, magnetic properties of Co-Pt-Ru alloy films, structure and magnetic properties of the Co-Pt-Ru-oxide granular film are also reported.

Yu SUZUKI
tel: +81-296-25-3434
y_suzuki@furuyametals.co.jp

REFERENCES

1) e. g. A. Ishikawa *et al., IEEE. Trans. Magn.*, **32**, 5 (1996).

2) Y. Takahashi *et al., J. Appl. Phys.,* **91**, 8022 (2002).

3) T. Kubo *et al., J. Appl. Phys.,* **99**, 08G911 (2006).

4,5) S. Saito, *et al., Digest of Ann. Conf. Magn. Soc. Jpn.*, 13pE-1 (2007) 12pA-13 (2008).

6) M. Takahashi *et al., J. Magn. Magn. Mat.*, **320**, 2868 (2008).

7) S. Saito, *et al, J. Phys. D.*, **42**, 145007 (2009).

8) S. Hinata, *et al, J. Appl. Phys.,* **105***,* 07B718 (2009).

9) S. Saito, et al., Digest of Ann. Conf. Magn. Soc. Jpn., 12aB-6 (2009).

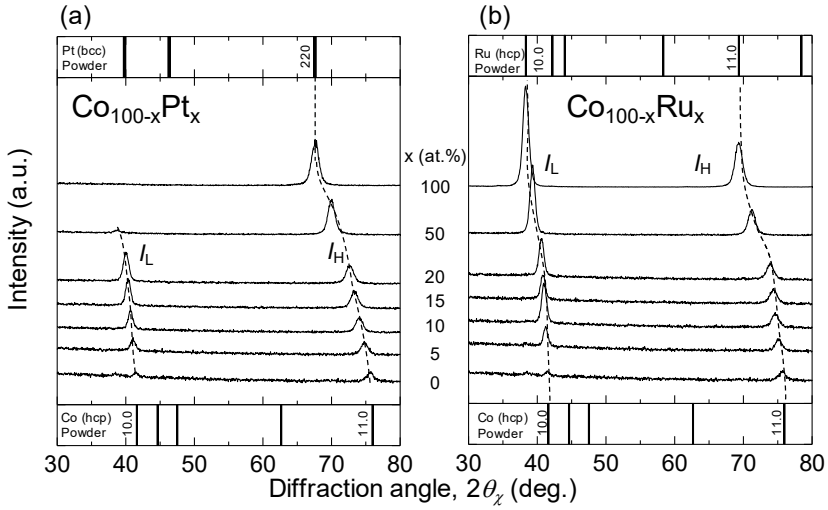

Fig. 1 In-plane XRD profiles for (a) $Co_{100-x}Pt_x$ and (b) $Co_{100-x}Ru_x$ films.

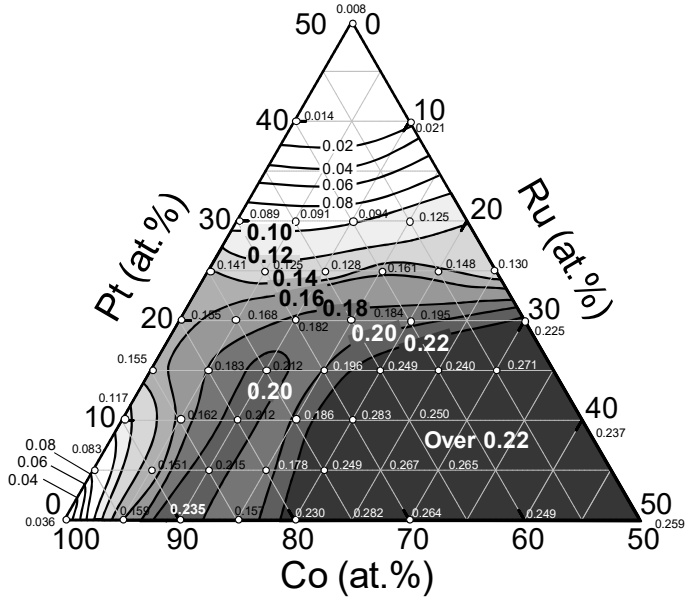

Fig. 2 Composition dependence of corrected integrated intensity ratio for *c*-plane oriented Co-Pt-Ru films.

SIMULTANEOUS ACQUISITION OF MAGNETIC DOMAIN STRUCTURE AND LOCAL MAGNETIZATION CHARACTERISTICS DURING FIELD SWEEPING

Yusuke ODAGIRI[1], Eiji YANAGISAWA[1], Sakae MEGURO[1], Shin SAITO[2]

1) Neoark Corporation, Tokyo, Japan, odagiri@neoark.co.jp

2) Tohoku University, Sendai, Japan, ssaito@ecei.tohoku.ac.jp

I. INTRODUCTION

Studies and developments of spintronics devices such as STT-MRAM are continuously expanding. Investigation of relationship between magnetic domain structure and local magnetization characteristics is essential because magnetic behaviors of local magnetization characteristics significantly influence device's performance. Magneto-optical Kerr effect (MOKE) based microscope is a well-known apparatus to study magnetization behaviors. In most MOKE microscopes, magnetic domain images are obtained by using imaging camera within its field of view at once. Furthermore, magnetization curves can be calculated from brightness in values of few pixels from observed images [1]. However, obtaining low noise magnetization curves by this method contains considerable difficulties due to the limitation of optical detection performance of the imaging camera. In this study, we report a successful development of a high contrast magnetic domain microscope equipped with low noise magnetization curves measurement system by using focused LASER.

II. RESULTS

Fig.1 shows a schematic of the optics for magnetic domain observation. Köhler illumination was used in optical system for magnetic domain observation, and a light beam was designed to focus to objective lens' back focus. Fig.2 shows a schematic of additional optical system for measuring magnetization curves. The LASER, wavelength 650nm, was adopted as a light source, and its beam was focused to a surface of a magnetic sample. The equipment was integrated with two types of optical systems in one package. For low noise magnetization curves measurement, superimposing an RF signal of 500 MHz on driving current of the LASER was carried out aiming for both speckle noise reduction due to decreasing of coherency [2] and Magneto Optical (MO) signal modulation. A lock-in technique was applied to demodulate the low noise MO signal. A compact balanced detector with Gran-Thompson prism (GTP) was developed as a light receiving device. "p wave" and "s wave" of incident LASER were separated by GTP and were converted from optical signal to electric signal. Measurement sensitivity was much improved by a processing of difference between both signals. The differentiated signal was input to a lock-in amplifier. A lock-in technique was applied to demodulate low noise MO signal. Output signal from lock-in amplifier is inputted to AD converter of computer. Bit resolution of AD converter for computer is higher than bit resolution of general industrial camera. It is one of advantage for magnetization curves measurement with the LASER.

Fig. 3 shows a typical comparison between magnetization curves obtained by brightness of pixels in a domain image and modulated LASER for a thin film. Less noise was observed in the magnetization curves measured by LASER compared with that by brightness. Figs. 4 show (a) magnetic domain image under zero magnetic field and (b)-(c) local magnetization curves in μm area for a NiFe patterned thin film. The pattern showed multi-domain state mainly caused by shape anisotropy. According to the local magnetization curves, different wall-motion and rotational magnetization processes are clearly observed due to low noise MO signal.

In conclusion, low noise magnetization curves combined with changes in domain structure revealed detailed information of magnetization in μm area.

Yusuke ODAGIRI
E-mail: odagiri@neoark.co.jp
tel: +81-42-627-7211

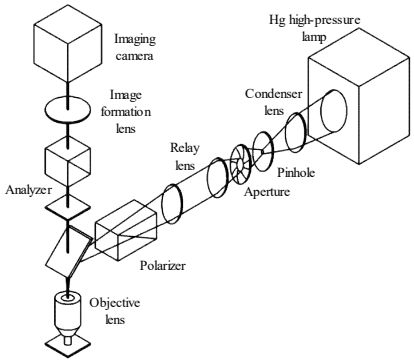

Fig. 1 Schematic of the domain observation microscope.

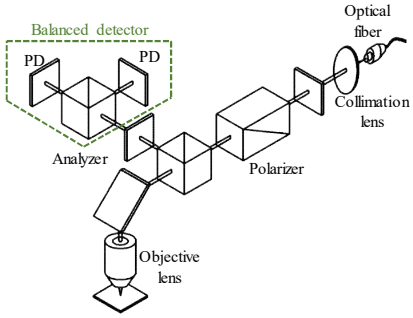

Fig. 2 Schematic of the additional optics for measuring magnetization curves.

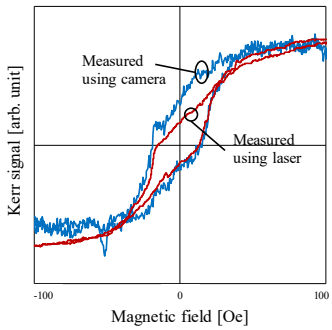

Fig. 3 Comparison of magnetization curves.

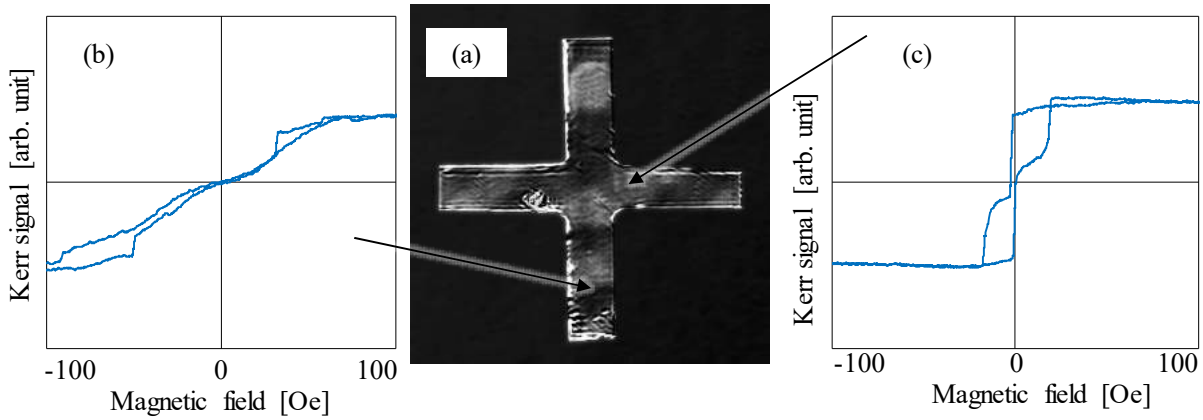

Fig. 4 Magnetic domain image and magnetization curves of the NiFe patterned thin film.

REFERENCES

1) S. Meguro, K. Akahane, S. Saito, and M. Takahashi, "Detection of magnetization process at μm-sized area obtained from hysteresis domain movie by longitudinal Kerr Microscope", Ann. Conf. Magn. Soc. Jpn., 22pB-5 (2005).
2) K. Akahane, T. Kimura, and Y. Otani, "Development of High Sensitive Micro-Kerr Magnetometer", Magn. Soc. Jpn., 28, No.S1, 122-127 (2004).

AMORPHOUS Cr-Ti LAYER FOR A HIGHLY (002) TEXTURED BCC Cr BASED ALLOY SEED LAYER FOR FePt-C HEAT-ASSISTED MAGNETIC RECORDING MEDIA

Akihiro SHIMIZU[1], Seong-Jae JEON[2], Shintaro HINATA[3] and Shin SAITO[4]

1) Tohoku University, Sendai, Miyagi, 980-8579 JAPAN s.akihiro@ecei.tohoku.ac.jp
2) Tohoku University, Sendai, Miyagi, 980-8579 JAPAN, jsjigst@ecei.tohoku.ac.jp
3) Tohoku University, Sendai, Miyagi, 980-8579 JAPAN, s_hinata@ecei.tohoku.ac.jp
4) Tohoku University, Sendai, Miyagi, 980-8579 JAPAN, ssaito@ecei.tohoku.ac.jp

I. INTRODUCTION

Heat-assisted magnetic recording (HAMR) media based on $L1_0$ FePt granular film is considered to extend the maximum areal density over 4 Tb/in^2 owing to the high magnetocrystalline anisotropy of $L1_0$ ordered phase for FePt ($K_u \sim 7\times10^7$ erg/cm^3) [1–3]. In order to realize the $L1_0$ ordered FePt granular film as a high recording density medium, it is necessary to enhance signal-to-noise ratio (SNR). Contribution to the SNR can result from variation in the angular distribution of *c* -axis orientation of $L1_0$ grains. Since the *c* -axis orientation, which corresponds to the easy magnetized axis for the $L1_0$ ordered FePt, can be adjusted by hetero-epitaxial growth from (002) textured crystalline seed layer (SL), the angular distribution of the *c* -axis is mainly attributed to that of SL. Recently, we reported the concept to suppress the angular distribution of the (002) orientation of SL [4]. The origin of the angular distribution of the crystal orientation can be described by considering the formation of crystalline facets during the solidification of liquid phase of sputtered atoms under the different wettability of SL on an amorphous-texture inducing layer (*a*-TIL). Low wettability condition induces the ball-shaped liquid phase of the sputtered atoms, whereas high wettability condition tends to spread the liquid phase over surface of *a*-TIL. During the solidification, the liquid phase changes to the crystalline facet in order to form the crystallographic texture. In the case of the low wettability, the crystalline facets have much more chance to form the crystalline plane with various angles from normal to the film plane. Consequently, the crystallographic texture can be slanted from normal to the film plane. In the case of the high wettability, the most surface of the crystalline facets is parallel to the normal to the plane, which induces the development of the crystallographic texture without a tilt of the crystal orientation. Providing that the texture is determined by the solidification, fabrication of the large grain SL is important. Based on the concept, a designed stacking structure is illustrated in Fig. 1. We found that the materials combination between bcc-Cr alloy SL and $Cr_{50}Ti_{50}$ *a*-TIL promoted the lateral grain growth for bcc-Cr alloy SL. However, crystallization of the $Cr_{50}Ti_{50}$ *a*-TIL suppressed the development of the lateral grain growth. In order to increase the grain size of bcc-Cr alloy SL, investigation on the degree of amorphous and thermal stability of amorphous is inevitable. In this research, quantitative study on the amorphous Cr-Ti TILs was carried out for (002) texture formation of bcc-Cr alloy SL.

II. RESULTS AND DISCUSSION

Figure 2 shows in-plane XRD patterns of (a) as-deposited and (b) post-annealed up to a temperature of 600 ºC for $Cr_{100-x}Ti_x$(20 nm) TILs on NiTa(2 nm)/glass substrate with various Ti content. In the case of (a) as-deposited state, two diffractions at Bragg angles of $2\theta_\chi$ = 44 º and 64 º were observed in x = 0 (pure bcc-Cr) TIL. These diffractions, which are identified as (110) and (220) diffractions of bcc-Cr powder, gradually shifted to lower angles with the increase of x = 0 to 20 at%. The result indicates that the atomic substitution from Cr to Ti induces the increase of the lattice volume while sustaining the crystalline structure. However, change of the diffraction width from the narrow to broad signal was observed with the further increase of x from 20 to 30 at%, and then the broad signal was confirmed regardless of the increase of x up to 75 at%. This result suggests that the amount of the constructive interference of X-rays decreases due to the randomly located atoms (i.e. amorphous phase). Again, two diffractions at Bragg angles of $2\theta_\chi$ = 35 º and 63 º were obtained in x = 100 (pure hcp-Ti) TIL. In the case of (b) post-annealed TILs, one can see that additional diffractions exist at $2\theta_\chi$ = 40 ~ 44º and 64º in x = 30, 70, and 75 at% as compared

Akihiro SHIMIZU
tel: +81-296-25-3438
s.akihiro@ecei.tohoku.ac.jp

with the as-deposited TILs. The result suggests that these films are crystallized. Only the films with x from 40 to 60 at% maintained the amorphous phase against the heat treatment.

Figure 3 shows the angular distribution of (002) crystal orientation of bcc-SL derived from full width at half maximum (FWHM) plotted against T_{sub} and x. Measured range for (002) sheet texture (gray region) is limited by both $T_{sub} \geq 300$°C and $30 < x$ (at%) < 75. Note that this composition range corresponds to the amorphous formation region for $Cr_{100-x}Ti_x$ TILs. In addition, magnitude of FWHM along the same x decreased with increasing T_{sub} (solid circle ●) and then, decreased with further increasing T_{sub} (open circle ○) within x of 50 to 70 at%.

At the presentation, relation between Ti content and grain diameter of the CrMn seed layer, and magnetic properties of FePt-C will be discussed.

REFERENCES

1) M. H. Kryder, E. C. Gage, T. W. McDaniel, W. A. Challener, R. E. Rottmayer, G. Ju, Y.-T. Hsia, and M. F. Erden, *Proc. IEEE*, **96**, 1810 (2008).
2) A. Q. Wu, Y. Kubota, T. Klemmer, T. Rausch, C. Peng, Y. Peng, D. Karns, X. Zhu, Y. Ding, E. K. C. Chang, Y. Zhao, H. Zhou, K. Gao, J.-U. Thiele, M. Seigler, G. Ju, and E. Gage, *IEEE Trans. Magn.*, **49**, 779 (2013).
3) X. Wang, K. Gao, H. Zhou, A. Itagi, M. Seigler, and E. Gage, *IEEE Trans. Magn.*, **49**, 686 (2013).
4) Seong-Jae Jeon, Shintaro Hinata, Shin Saito, and Migaku Takahashi, *J. Appl. Phys.*, **117**, 17A924 (2015).

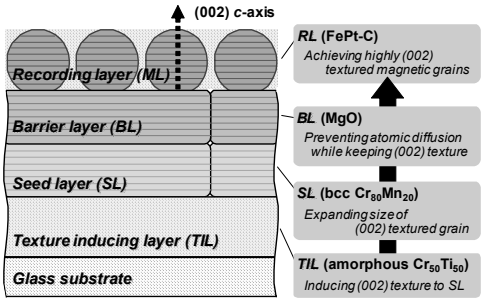

Fig. 1 Schematic representation to suppress angular distribution of (002) c-axis orientation for FePt-C granular film

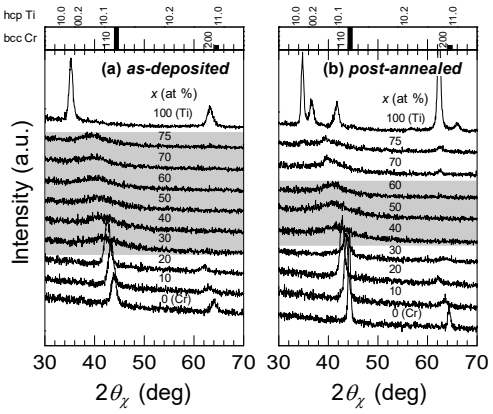

Fig. 2 In-plane XRD patterns of (a) as-deposited and (b) post-annealed $Cr_{100-x}Ti_x$ (20 nm) TILs on NiTa (2 nm)/glass substrate with various Ti compositions, x.

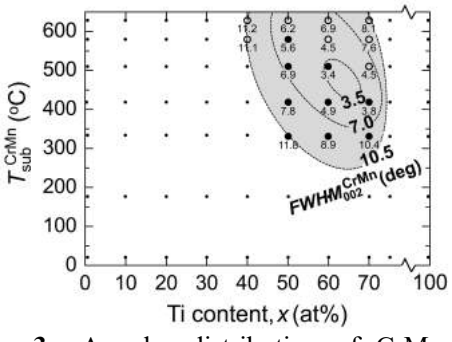

Fig. 3 Angular distribution of CrMn (002) crystal orientation (FWHM) varied with substrate temperature (T_{sub}) and Ti composition, x.

BP-30

TIME-DEPENDENT MAGNETIC SWITCHING AT PICOSECOND TIME SCALE

Jingyue MIAO[1], Dan WEI[2] and Chuan LIU[3]

1) Tsinghua Univ., Beijing, China, miujy15@mails.tsinghua.edu.cn

2) Tsinghua Univ., Beijing, China, weidan@mail.tsinghua.edu.cn

3) Peking Univ., Beijing, China, liuchuan@pku.edu.cn

I. INTRODUCTION

Recently, the thermodynamic equilibrium and nonequilibrium behavior of ferromagnetic materials have been studied extensively due to the applications in laser-induced magnetization switching in heat-assisted magnetic recording (HAMR) and all-optical switching (AOS) in the picosecond regime.

The micromagnetics simulation using Landau-Lifshitz-Bloch (LLB) equations can take the thermal activation into account by introducing a stochastic thermal fluctuation term; however, the energy minimum cannot be achieved and the length scale of thermal activation is limited to nanoscale [1], [2]. The new hybrid Monte Carlo (HMC) micromagnetics by Wei et.al [3] is a self-consistent method for the thermally dynamic magnetic studies. It can accurately describe the distribution of magnetization at temperature T by solving Hamilton equations, using Hybrid Monte Carlo algorithm to find a configuration of magnetizations $\{M_i\}$ obeying the Boltzmann-like distribution $e^{-F[\{\vec{M}_i\}]/kT}$. In hybrid Monte Carlo algorithm, the iteration of the Hamilton canonical equations follows a fictitious time τ, which is broken up into consecutive trajectories. The total iteration time is given by $\tau = N_{tra}\, N_{\text{step}}\, \delta\tau$, where N_{tra} is the number of trajectories, and N_{step} and $\delta\tau$ are the number of steps in one trajectory and the duration time of each step, respectively. And if we compare the simulation results with the experiments, we can obtain the relationship between τ and the real time t.

II. RESUTLS AND DISCUSSIONS

We have studied the time-dependent coercivity in a time scale 10^{-5} to 10^{-8} s [4]. In this work, we would like to further analyze the time-dependent switching at a shorter time-scale.

A granular film with Voronoi polycrystalline structure is simulated. The film area is 24nm×24nm×3nm (with in-plane periodic boundary conditions) and divided into a regular mesh of 1nm×1nm×1nm micromagnetic cells. At 0K, in crystalline grains, the saturation M_s is 700 emu/cc, the exchange constant A^*_1 is 0.5×10^{-6} erg/cm and the anisotropy energy K is 4.2×10^7erg/cm^3; in the grain boundary, M'_s is 70 emu/cc, A^*_2 is 0.1×10^{-7} erg/cm and K' is 2.94×10^7erg/cm^3.

In a constant-field model, a constant magnetic field is applied in the opposite direction of initial magnetization M. In Fig.1, the simulated time-dependent coercivity reasonably agrees with Sharrock's law in a time scale 10^{-8}s<t<10^{-5}s with 10 to 10^4 HMC trajectories. So that in this case a trajectory ($\tau=10^{-3}$) in the HMC algorithm is roughly equal to 1 ns in the real time scale.

The fictitious time τ is broken up into consecutive trajectories, given by $\tau = N_{tra}\, N_{\text{step}}\, \delta\tau$. So that the length of a trajectory varies with the parameter N_{step} and $\delta\tau$. We use two sets of parameters of N_{step} and $\delta\tau$, Set A and Set B, to simulate the magnetization switching in a same constant-field model. As can be seen in fig.2, the results show that the magnetization decay and switching follows the similar process in two different time scales. Notably, simulations with parameters of Set B have derived the conclusion that a trajectory is close to 1 ns. As a result, in the simulations with parameters of Set A, a trajectory can be inferred to be close to 1 ps from comparison. Thus we can investigate the thermodynamic magnetization switching in the picosecond regime if we put emphasis on the first hundreds or thousands of trajectories. Therefore, the HMC

Jingyue MIAO
E-mail: miujy15@mails.tsinghua.edu.cn
tel: +86 1305132620

micromagnetics can be used to study the laser-induced magnetization switching in HAMR and AOS with a reasonable approximation to the temperature profile in the process of heating and recovery as well as the accurate microstructure of the recording medium included.

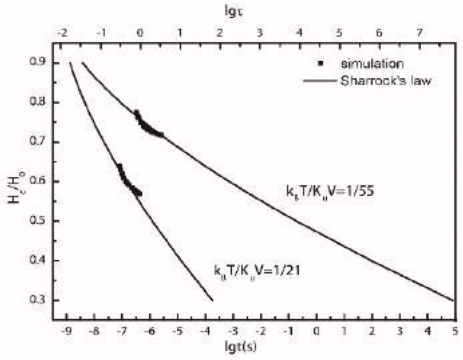

FIG. 1 Comparison of the time-dependent coercivity derived by simulation and the Sharrock's law.

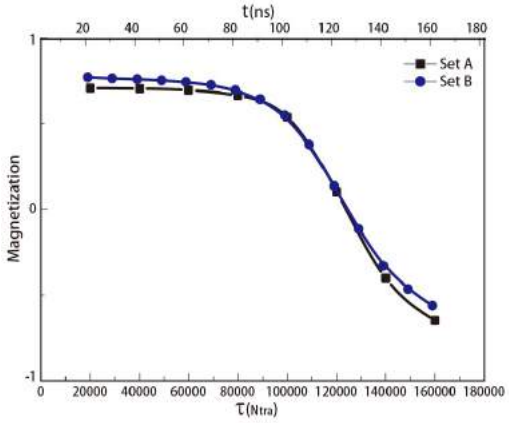

FIG. 2 Magnetization switching in two time scales. The upper horizontal axis is in a real time scale corresponding to the number of trajectories N_{tra} in model with parameters of Set B, and the under horizontal axis is in the time scale of the N_{tra} in model with parameters of Set A.

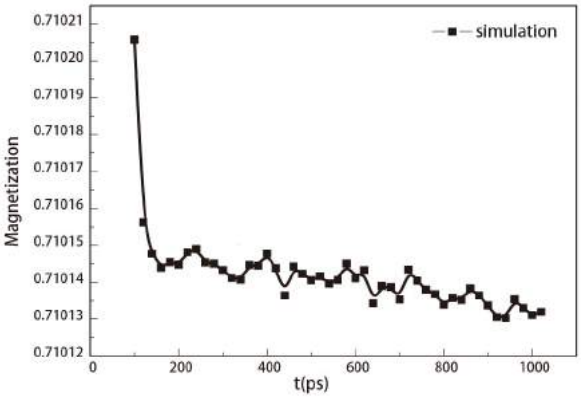

FIG. 3 Magnetization decay in the picosecond regime. The horizontal axis is in the real time scale corresponding to the N_{tra} in model with parameters of Set A.

REFERENCES

1) W. Brown. "Thermal fluctuation of fine ferromagnetic particles," *IEEE Transactions on Magnetics,* 1979, pp. 1196-1208

2) R. Skomski, P. Kumar, G. C. Hadjipanayis and D. J. Sellmyer. "Finite-temperature micromagnetism," *IEEE Transactions on Magnetics,* 2013, pp. 3229-3232.

3) D. Wei, J. Song and C. Liu. "Micromagnetics at Finite Temperature," *IEEE Transactions on Magnetics, 2016, pp. 1-8.*

4) Miao J Y, Wei D, Liu C. Micromagnetic studies of time-dependent coercivity [C]//Magnetics Conference (INTERMAG), 2017 IEEE. IEEE, 2017

A HEAT TRANSFER STUDY IN THE HEAD DISK INTERFACE WITH APPLICATION TO HAMR ABS DESIGN

Haoyu WU[1], Prof. David B. BOGY[2]

1) University of California, Berkeley, California, 94720, USA, wuhaoyu@berkeley.edu
2) University of California, Berkeley, California, 94720, USA, dbogy@berkeley.edu

I. INTRODUCTION

In the hard disk drive (HDD) industry, heat-assisted magnetic recording (HAMR) is being pursued and is expected to help increase the areal density to $\sim 10\mathrm{Tb/in^2}$ in HDDs to fulfill future worldwide data storage demands. In HAMR, the magnetic media is heated locally ($\sim 50 \times 50\mathrm{nm^2}$) and momentarily ($\sim 1\mathrm{ns}$) close to its Curie temperature ($\sim 450°\mathrm{C}$) by a laser energy source that is focused by a near field transducer (NFT). Since the required temperature of the NFT is much lower than the media's Curie temperature, the heat can flow back from the media to the NFT, thereby heating the NFT. Therefore, understanding the heat transfer in the head disk interface (HDI) in the area of the NFT is important.

The embedded contact sensor (ECS) and the thermal fly-height control (TFC) technologies have been developed by the industry over the last several years. The ECS is a temperature sensitive resistor embedded on the slider surface of the head near the read/write transducers, so it can detect head-disk contact. The TFC heater is a metallic resistor embedded in the slider's body somewhat above the read/write transducer. When power is supplied to the heater, it generates heat, which increases the local temperature and causes a local protrusion, thereby adjusting the fly-height. Both the ECS and the TFC heater can be used for the study of the heat transfer in the HDI.

In this paper, we report on a series of experiments and simulations for the heat transfer in the HDI. We show that the design of the air bearing surface (ABS) can significantly affect the pressure distribution in the read/write transducer area, and thereby affect the convective heat transfer coefficient. This can provide insights into the ABS design that can reduce the back heating from the disk to the NFT.

II. EXPERIMENTS

In the experiments, perpendicular magnetic recording (PMR) heads and disks were used. There are two setups. In the first setup, the head flies on the disk rotating at 5400 RPM, which is called the “fly” setup. In the second setup, there is no disk near the head, which is called the “non-fly” setup. In both setups, we increase the power of the TFC heater and monitor the resistance change of both the ECS and the TFC heater. The TFC power is increased until touch-down is reached in the fly setup or to $30\mathrm{mW}$ in the non-fly setup.

Since both the ECS and the TFC heaters are metallic resistors, their resistances increase as their temperatures increase. The relationship is approximately linear in the range of interest, expressed as

$$\Delta T = \frac{1}{\alpha R_0}\Delta R, \quad (1)$$

where ΔR is resistance change, α is the temperature coefficient of resistivity, ΔT is the temperature increase and R_0 is the resistance at the room temperature. We can then compare the temperature change of the same element in the different scenarios by comparing the resistance change.

The results of the experiments are shown in Fig. 1. Fig. 1(a) shows the resistance increase of the ECS and the TFC heater in both the fly and non-fly setups. While all four curves appear to be almost linear, it is not the case for the ECS in the fly setup. The temperature increase is greater in the non-fly setup than in the fly setup for both elements.

The reason for the different temperature increase rates is the different heat transfer coefficients at the slider's air bearing surface (ABS) in the fly and non-fly setups. In the non-fly setup, the convection on the ABS is free air convection; in the fly setup, it is usually modeled in terms of the air bearing cooling, and the convection coefficient is much larger than that of the free air convection. Therefore, the cooling on the ABS is much larger in the fly setup, thereby mitigating the temperature increases of both the ECS and the TFC heaters.

It is also noted that the only non-linear curve in Fig. 1(a) is the ECS resistance increase in the fly setup.

David Bogy
E-mail: dbogy@berkeley.edu

All other curves are linear. This is because in the non-fly setup, the boundary condition does not change with the TFC power. Therefore, the temperature field is linear with the sole heating source, the TFC power. However, in the fly setup, the convection coefficient increases as the TFC power increases and the head-disk gap decreases, providing more cooling to the ECS, causing the reduction of its rate of temperature increase. But the TFC heater is barely affected since it is buried inside the slider's body.

Since the resistance increase rate in the fly condition is directly affected by the cooling on the ABS, we can quantitatively compare the resistance increase rates for the different setups. Here we define a temperature change ratio (ξ) as the ratio of the resistance increase in the non-fly setup to that in fly setup at a certain TFC power,

$$\xi = \frac{\Delta R_{non-f}}{\Delta R_{fly}}\Big|_{P_{TFC}}. \quad (2)$$

The ratios ξ for the ECS and the TFC heater are shown in Fig. 1(b) as a function of TFC power. It is seen that ξ_{TFC} remains constant at ~ 4, for the complete power range, but ξ_{ECS} increases from ~ 2 to ~ 5 and it crosses ξ_{TFC} at $P_{TFC} \sim 18$mW.

The ECS is located at the surface of the slider, which is more sensitive to the change of the heat transfer coefficient across the HDI (h_{HDI}), while the TFC heater is buried in the slider's body, which is less sensitive. Therefore, intuitively, we expect when the slider switches from the non-fly status to the fly status, there should be more cooling on the ECS than the TFC heater, i.e., $\xi_{ECS} > \xi_{TFC}$. However, from Fig. 1(b), we see that $\xi_{ECS} < \xi_{TFC}$ at low P_{TFC}, which is opposite to our intuition.

III. SIMULATIONS

To understand better the experimental results, we carried out a series of simulations using the CMLAir software. The slider surface used in the simulations was similar to that in the experiments. Two cases were simulated with P_{TFC} at 0 and 65mW, called Case 1 and 2. The convective heat transfer coefficient (h_{HDI}) based on the air bearing cooling model in CMLAir for the two cases are shown in Fig. 2. Fig. 2(a) shows the results for Case 1 and Fig. 2(b) shows the results for Case 2. It is noted that plots of pressure would look similar to those in Fig. 2. The red arrows in Figs. 2 indicate the location of the ECS. It is noted that the dimension of the ECS is $\sim 1\mu$m, which is much smaller than the TFC heater, which has the dimension of $\sim 20\mu$m. As a direct result, the air convection that is far ($\sim 10\mu$m) away from the ECS has little effect on the heat transfer of the ECS, while such a distance is still within the range of the TFC. From Fig 2(a), we can see that the ECS is located in a "valley" of the h_{HDI} distribution. Therefore, the cooling around the ECS is actually relatively low, causing $\xi_{ECS} < \xi_{TFC}$ at low P_{TFC}. However, as P_{TFC} increases, the protrusion causes the h_{HDI} to increase at the ECS location, and the "valley" disappears finally, as shown in Fig 2(b), causing $\xi_{ECS} > \xi_{TFC}$ at high P_{TFC}.

This observation may provide insights into designing a HAMR ABS to control the back heating from the disk to the NFT. We see that the ABS design directly influences the pressure distribution and the heat transfer coefficient distribution. Therefore, it may be possible to design the ABS such that the air bearing pressure at the location of the NFT is lower, which will potentially lower the back heating from the media.

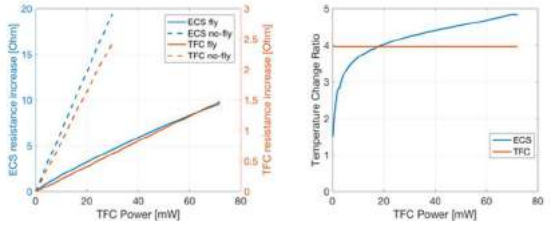

Figure 1 The experimental results.

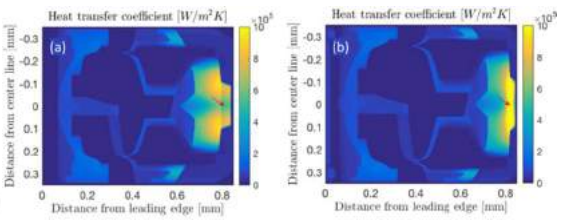

Figure 2 The simulation results.

MAGNETIC SKYRMION LOGIC GATES

Xichao ZHANG[1, 2], Motohiko EZAWA[3], and Yan ZHOU[1]

1) Chinese Univ. of Hong Kong, Shenzhen, China, zhangxichao@co.cuhk.edu.cn, zhouyan@cuhk.edu.cn

2) Nanjing Univ., Nanjing, China

3) Univ. of Tokyo, Tokyo, Japan, ezawa@ap.t.u-tokyo.ac.jp

I. INTRODUCTION

Magnetic skyrmions, which are topological particle-like excitations in ferromagnets, have attracted a lot of attention recently. Skyrmionics is an attempt to use magnetic skyrmions as information carriers in next generation spintronic devices. Proposals of manipulations and operations of skyrmions are highly desired. It has been demonstrated that a skyrmion can be generated by converting a domain-wall pair at a narrow-wide junction [1]. In this work, we show that the conversion, duplication and merging of isolated skyrmions with different chirality and topology are possible all in one system. We also demonstrate the conversion of a skyrmion into another form of a skyrmion, i.e., a bimeron. We design spin logic gates such as the AND and OR gates based on manipulations of skyrmions. These results provide important guidelines for utilizing the topology of nanoscale spin textures as information carriers in novel magnetic sensors and spin logic devices.

II. RESULTS

We investigated the skyrmion conversion between different magnetic materials. The results are shown in Fig. 1. Fig. 1a shows the reversible conversion between a domain-wall pair and a skyrmion, which has been report in ref. 1. For Fig. 1b, we have assumed the sign of the DMI is positive in the left input region, while it is negative in the right output region. The helicity is determined by the DMI. The helicity of skyrmion in the left region is 0 while 1 for the skyrmion in the right region. Fig. 1c shows the skyrmion conversion when the magnetization between the left and right side with the same DMI. The stable skyrmion in the left region is a skyrmion while an anti-skyrmion in the right region. And the helicity is also reversed. Fig. 1d shows that skyrmion conversions when both the sign of the DMI and the direction of the magnetization are opposite between the left and right region. The skyrmion with the helicity of 0 is converted into an anti-skyrmion with the helicity of 0.

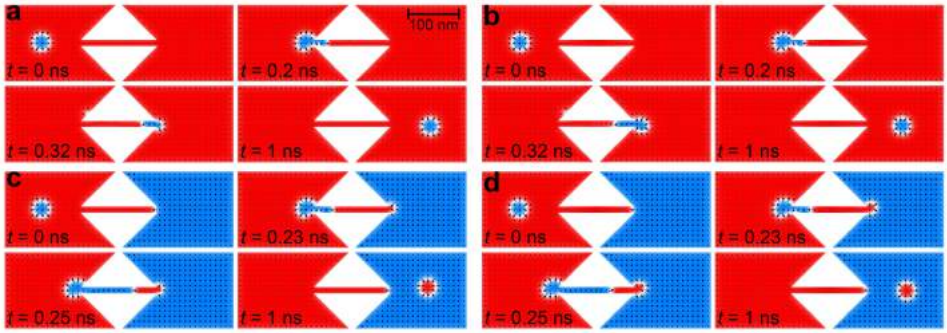

Fig. 1 Conversions between skyrmions and anti-skyrmions. a) Conversion between a skyrmion and a skyrmion with identical out-going helicity. b) Conversion between a skyrmion and a skyrmion with opposite in-going helicity. c) Conversion between a skyrmion and an anti-skyrmion with opposite in-going helicity. d) Conversion between a skyrmion and an anti-skyrmion with identical out-going helicity.

The conversion between a skyrmion and a bimeron has been demonstrated in this work. For the skyrmions in the materials with perpendicular magnetic anisotropy (PMA), the tail must be up or down direction. In the easy-plane sample, the tail must be in-plane. Then, in the right output region, a skyrmion is converted into a bimeron, which is a pair of merons. A bimeron (anti-bimeron) has a skyrmion number of 1 (-1) and is another form of a skyrmion which exists in easy-plane sample.

Yan ZHOU
E-mail: zhouyan@cuhk.edu.cn
tel: +86-755-84273832

Based on the reversible conversion between skyrmions and domain-wall pairs, we design the logical OR and AND operations, as shown in Fig. 2. In the skyrmion-based logic gates, binary 0 corresponds to the absence of a skyrmion and binary 1 corresponds to the present of a skyrmion. The OR (0+0=0, 0+1=1, 1+0=1, and 1+1=1) and AND (0+0=0, 0+1=0, 1+0=0, and 1+1=1) gates can be realized by using skyrmions in the designed devices. For the process of 0+0=0, there is no output when there is no input.

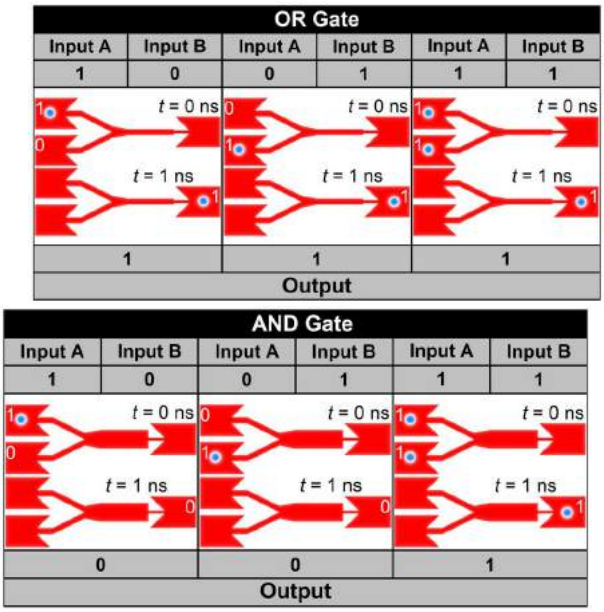

Fig. 2 Skyrmion-based logical OR and AND operation.

REFERENCES

1) Y. Zhou and M. Ezawa, “A reversible conversion between a skyrmion and a domain-wall pair in junction geometry”, *Nat. Commun.* 5, 4652, (2014).

MAGNETIC SKYRMIONIUM: A NEW BUILDING BLOCK FOR RACETRACK MEMORY

Xichao ZHANG[1, 2], Jing XIA[1], Yan ZHOU[1],
Daowei WANG[3], Xiaoxi LIU[4], Weisheng ZHAO[5], and Motohiko EZAWA[6]
1) Chinese Univ. of Hong Kong, Shenzhen, China, zhangxichao@co.cuhk.edu.cn, jingxia0817@gmail.com, zhouyan@cuhk.edu.cn
2) Nanjing Univ., Nanjing, China
3) Central South Univ., Changsha, China, dwwang@nudt.edu.cn
4) Shinshu Univ., Nagano, Japan, liu@cs.shinshu-u.ac.jp
5) Beihang Univ., Beijing, China, weisheng_zhao@163.com
6) Univ. of Tokyo, Tokyo, Japan, ezawa@ap.t.u-tokyo.ac.jp

I. INTRODUCTION

Magnetic skyrmionium is a non-topological soliton with a doughnut-like spin texture [1, 2], which can be phenomenologically viewed as a coalition of a skyrmion and an anti-skyrmion, as shown in Fig. 1. It has been theoretically suggested that the skyrmionium can be created and remain stable in magnetic nanodisks with the Dzyaloshinskii-Moriya interaction (DMI). In this work, we systematically study the generation, manipulation and motion of a skyrmionium in nanostructures with a magnetic field or a spin current. We demonstrate the degeneration of a skyrmionium with $Q = 0$ into a skyrmion with $Q = +1$ or $Q = -1$ triggered by a magnetic field pulse. We show the transformation of a skyrmionium with $Q = 0$ into two skyrmions with $Q = +1$. In addition, we investigate the motion dynamics of a skyrmionium as well as a bilayer-skyrmionium compared to that of a skyrmion. The velocity of a skyrmionium driven by vertical current can be faster than that of a skyrmion at a reasonable driving current density. The results have technological implications in the emerging field of skyrmionics.

II. RESULTS

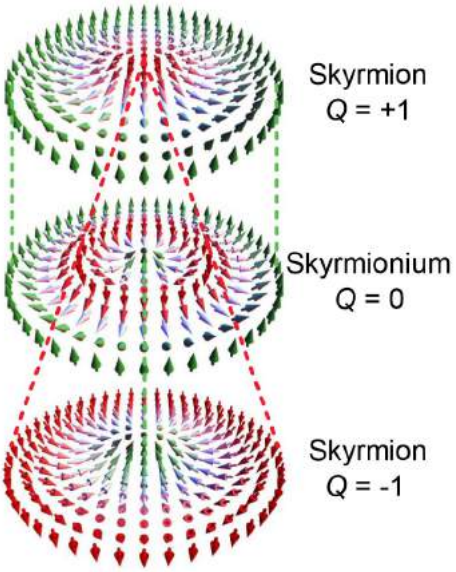

Fig. 1 Illustration of a magnetic skyrmionium.

First we compare the energy level of the skyrmionium with possible states, that is, the ferromagnetic (FM) state, the skyrmion, and the 3π rotation state, in a magnetic nanodisk with the DMI. The radius of the nanodisk is fixed. By giving the FM state, skyrmion, skyrmionium, and 3π state as the initial magnetization configuration of the nanodisk separately, we calculate the total micromagnetic energy E_{total} of the relaxed nanodisk as a function of the DMI constant D. For our parameter set, the FM state is the most stable state when $D < 3.8$ mJ m^{-2}, while skyrmion and skyrmionium become more stable than the FM state when $D > 3.8$ mJ m^{-2}. When $D > 4$ mJ m^{-2}, the 3π state also become more stable than the FM state. Larger D favors higher magnetization rotation in the nanodisk, especially when the nanodisk radius is larger than the anisotropy-free period $L_0 = 4\pi A/D$, and A is the Heisenberg exchange constant. For the parameter set in this work, we have $L_0 = 47$ nm at $D = 4$ mJ m^{-2}; thus it is reasonable to obtain a stable skyrmionium in the nanodisk with $r = 1.6\ L_0$. A stable skyrmionium in the nanodisk can be obtained by applying a spin-polarized current locally with the current-perpendicular-to-plane (CPP) geometry in this work.

We also investigate the spin-polarized current-driven motion of a skyrmionium. For the CPP geometry, a spin-polarized current is injected into the nanotrack from the bottom. For the CIP geometry, a spin-polarized current is injected into the nanotrack from the left end. For contrast and comparison

Motohiko EZAWA
E-mail: ezawa@ap.t.u-tokyo.ac.jp

Yan ZHOU
E-mail: zhouyan@cuhk.edu.cn
tel: +86-755-84273832

purposes, we simulate the spin-polarized current-driven motion of skyrmion in the same device. The results are shown in Fig. 2. For the case of CIP geometry, the skyrmionium and skyrmion attain the same current-velocity (j-v) relation for the given range of driving current density. Indeed, both v_{skium} and v_{sk} at a given j increase with the strength of nonadiabatic spin-transfer torque (STT) β. By contrast, for the case of CPP geometry, v_{skium} is clearly higher than v_{sk} when $j > 2$ MA cm^{-2}. And the velocity difference between v_{skium} and v_{sk} increases with increasing j. When the driving current with the CPP geometry $j > 15$ MA cm^{-2}, the moving skyrmionium will be destroyed caused by the skyrmion Hall effect. Similarly, when the driving current density with the CPP geometry $j > 17$ MA cm^{-2}, the moving skyrmion will be destroyed at the upper edge of the nanotrack. Because the distortion and destruction of the skyrmionium in the high-speed operation are detrimental to practical applications, we therefore construct the bilayer skyrmionium in a nanotrack consisting of two antiferromagnetically exchange-coupled FM layers, similarly to the bilayer skyrmion reported in Ref. [3]. The steady velocity of the bilayer-skyrmionium $v_{\text{bi-skium}}$ as a function of current density j is also shown in Fig. 2. The bilayer skyrmionium has the same j-v relation as the skyrmionium for the case of CIP geometry. However, for the case of CPP geometry, $v_{\text{bi-skium}}$ is basically a half of v_{skium} at a certain j. The reason is that for the CPP geometry the current is only injected into the bottom FM layer, but drives both skyrmioniums in the bottom and the top FM layers.

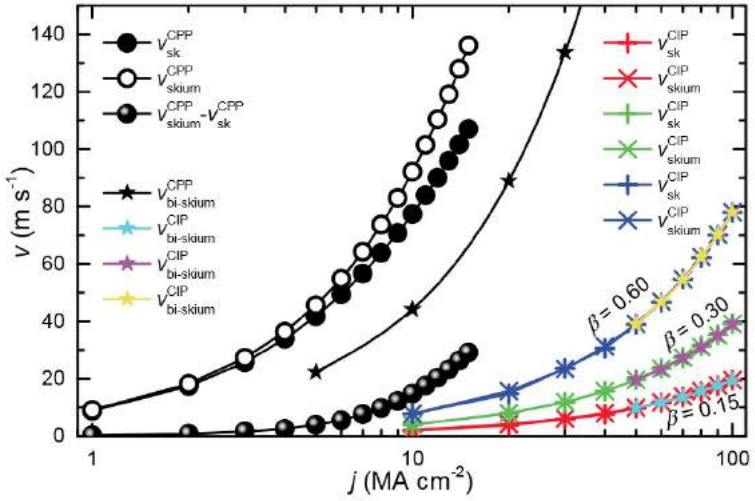

Fig. 2 Velocity for the skyrmion v_{sk}, skyrmionium v_{skium}, and bilayer skyrmionium $v_{\text{bi-skium}}$ driven by the spin-polarized current with the CPP or CIP geometry as a function of the driving current density j in the nanotrack.

REFERENCES

1) A. Bogdanov and A. Hubert, “The stability of vortex-like structures in uniaxial ferromagnets”, *J. Magn. Magn. Mater*. 195, 182-192 (1999).

2) X. Zhang, J. Xia, Y. Zhou, D. Wang, X. Liu, W. Zhao, and M. Ezawa, “Control and manipulation of a magnetic skyrmionium in nanostructures”, *Phys. Rev. B* 94, 94420 (2016).

3) X. Zhang, Y. Zhou, and M. Ezawa, “Magnetic bilayer-skyrmions without skyrmion Hall effect”, *Nat. Commu*n. 7, 10293 (2016).

STRUCTURAL, MAGNETIC AND MAGNETO-TRANSPORT PROPERTIES OF EQUIATOMIC CoFeMnSi EPITAXIAL THIN FILMS

L. BAINSLA,[1] R. YILGIN,[1] J. OKABAYASHI,[2] A. ONO,[1] K. SUZUKI,[1] S. MIZUKAMI[1]
1) WPI-Advanced Institute for Materials Research, Tohoku University, Sendai, Japan
2) Research Center for Spectrochemistry, The University of Tokyo, Tokyo, Japan

I. INTRODUCTION

Half-metallic ferromagnetic (HMF) materials have fully spin polarized band structures and therefore suitable for spintronic applications [1]. Among the large families of HMF materials, Co-based Heusler alloys attracted a lot of attention due to their theoretically predicted half-metallic nature and experimentally observed high spin polarization with high Curie temperatures [1-6]. Equiatomic quaternary Heusler alloys (EQHAs), with Y-type crystal structure are relatively new class of materials and explored very little [7,8]. Depending on the occupation of different lattice sites, there are three types of structural configurations are possible for a Y-type structure [8]. In addition, EQHAs (such as ABCD, where A, B and C are the transition-metal elements and D is a main group element) are prone to possess a various type of chemical disorder. When there is mixing of A and B (A=B), the material becomes Heusler-type $L2_1$ alloy with the composition of A_2CD. Therefore, when A=B in an EQHAs, it is referred as a $L2_1$ ordered system. Another type of possible disorder is C-D disorder, and termed as B2 ordered system. The third type of possible disorder is A2 (bcc) disorder, where all the atoms are randomly distributed. Properties of these materials greatly depend on the chemical ordering in the system. CoFeMnSi (CFMS) is one of the EQHAs, which has been predicted as a spin gapless semiconductor [9,10] and the spin-polarization was relatively high, evaluated by the Point-Contact Andreev Reflection in bulk form [10]. However, there are no reports available on magnetic tunnel junctions (MTJs) with CFMS thin film electrode. In this study, we investigate the structural and magnetic properties of CFMS epitaxial thin films with tunnel magnetoresistance (TMR) for MTJs.

II. EXPERIMENTAL DETAILS

30 nm thick CFMS films were grown on single crystalline (001) MgO substrate buffered by 40 nm thick Cr layer using the UHV magnetron sputtering system with a base pressure of less than 2×10^{-7} Pa. Samples with CFMS post-annealed (T_a) at 300, 400, 500 and 600ºC were prepared. The composition of the deposited CFMS films was confirmed to be $Co_{25}Fe_{24}Mn_{24}Si_{26}$ (at. %) using the inductively coupled plasma (ICP) analysis, which is almost ideal stoichiometric composition for EQHAs.

III. RESULTS AND DISCUSSION

The in-plane XRD patterns show CFMS (200) and (400) peaks for samples with $T_a \geq 400$ºC as shown in Fig. 1(a), which indicates that the films are grown with high degree of crystal orientation with respect to MgO (001). Crystallinity of the thin films improves with increase in the T_a. The respective $L2_1$ and $B2$ order parameters for CFMS could be obtained by using the extended Webster model [11]. The respective $B2$ and $L2_1$ orders are estimated using the long-range order parameters $S_{B2}^2 = (I_{002}/I_{004})/(I_{002}^R/I_{004}^R)$ and $(S_{L21}(3-S_{B2})/2)^2 = (I_{111}/I_{220})/(I_{111}^R/I_{220}^R)$, respectively, where I_{hkl} and I_{hkl}^R are the experimental X-ray diffraction intensity for (hkl) plane and reference intensity calculated for a fully ordered system, respectively. The estimated order parameters are shown in Fig. 1(b). ϕ scan for (111) and (220) plane was performed by tilting the sample [χ = 54.7º for (111) plane and χ = 45º for (220) plane], which shows a fourfold symmetry for samples with $T_a \geq 400$ºC and thus confirms epitaxial growth of CFMS thin films. In order to get the intensity of CFMS (111) and (220) diffraction peaks, 2θ-θ scan was performed with χ=54.7º and χ=45º. These data indicate that the CFMS films contain the $B2$ and $L2_1$ long range orders that change with the T_a. Because of almost similar scattering factors for Co and Fe, it is virtually impossible to distinguish between Y-type and $L2_1$ ordering

LAKHAN BAINSLA
E-mail: lakhan@tohoku.ac.jp
tel: +81-22-217-6004

using the Cu-K_α radiation.

All the films show in-plane magnetic anisotropy. Saturation magnetization (M_S) value increases with increase in T_a and it attains a value of 590 emu/cm^3 for sample with T_a = 600ºC. The obtained M_S value is less than the experimental observed M_S (690 emu/cm^3) value for bulk CFMS case [10]. These magentization data are in accord with x-ray magnetic circular dichroism measurements (XMCD). Coersive field (H_C) value also changes with T_a, and attains H_C = 10 Oe for T_a = 600ºC sample. Thus, samples with $T_a \geq$ 500ºC exhibit a soft ferromagnetic behavior similar to other Heusler alloys [2-4,6], therefore they have a high potential for magnetic sensor applications. We emphasize that the samples with high crystallinity represent high M_S and low H_C values.

Tunneling magneto-resistance effect measurements were performed on the MTJs with optimized growth conditions. The stacking structure of MgO(001) substrate/Cr(40 nm)/CFMS(30 nm)/Mg(0.4 nm)/MgO(1.6 nm)/CoFe(5 nm)/IrMn(10 nm)/Ta(3 nm)/Ru(5 nm) was used for TMR studies. In order to improve the crystallinity of MgO barrier and to obtain exchange bias, MTJs were annealed after the microfabrication in presence of in-plane magnetic field (5 kOe) at different temperatures. TMR was observed with respect to the ex-situ annealing. Preliminary measurements on the MTJs show maximum TMR ratio of 70% for the ex-situ annealing of 450ºC.

This work was partially supported by the ImPACT program and Grant-in-Aide for Scientific Research (No. 16K14244).

REFERENCES

[1] C. Felser, G.H. Fecher, B. Balke, Angew. Chem. Int. Ed. 46, 668 (2007).
[2] K. Inomata, N. Ikeda, N. Tezuka, R. Goto, S. Sugimoto, M. Wojcik, E. Jedryka, Sci. Technol. Adv. Mater 9, 014101 (2008).
[3] L. Bainsla, K.G. Suresh, A.K. Nigam, M. Manivel Raja, B.S.D.ChS. Varaprasad, Y.K. Takahashi, K. Hono, J. Appl. Phys. 116, 203902 (2014).
[4] H.-X. Liu, Y. Honda, T. Taira, K.-I. Matsuda,M. Arita, T. Uemura, M. Yamamoto, Appl. Phys. Lett. 101, 132418 (2012)
[5] M. Oogane and S. Mizukami, Phil. Trans. R. Soc. A. 369, 3037 (2011).
[6] Y. Sakuraba and K. Takanashi, Heusler Alloys. (Eds., Caludia Felser & Atsufumi Hirohata, Springer Series in Materials Science Vol. 222), Chap. 16 (2015) pp. 389-400.
[7] L. Bainsla, K. G. Suresh, Applied Physics Reviews 3, 031101 (2016).
[8] X. Dai, G. Liu, G.H. Fecher, C. Felser, Y. Li, H. Liu, J. Appl. Phys. 105, 07E901 (2009).
[9] V. Alijani, J. Winterlik, G. H. Fecher, S. S. Naghavi, C. Felser, Phys. Rev. B 83, 184428 (2011).
[10] L. Bainsla, A. I. Mallick, M. Manivel Raja, A. K. Nigam, B.S.D.Ch.S. Varaprasad, Y. K. Takahashi, Aftab Alam, K. G. Suresh, K. Hono, Phys. Rev. B 91, 104408 (2015).
[11] Y. Takamura, R. Nakane, S. Sugahara, J. Appl. Phys. 105, 07B109 (2009).

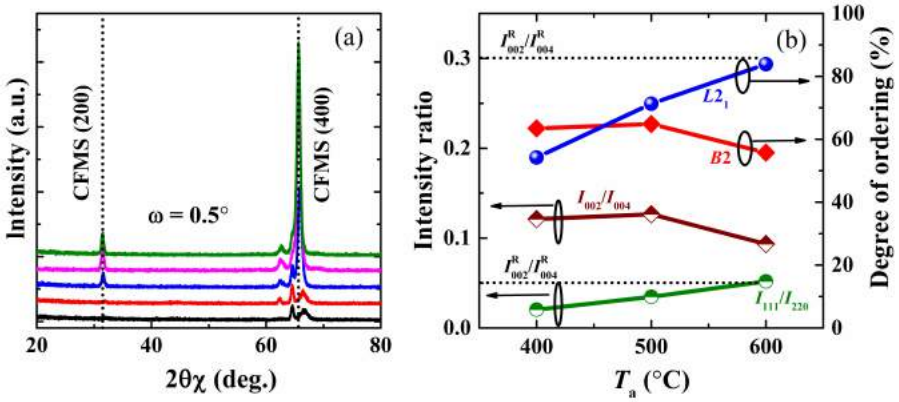

Fig. 1. (a) In-plane XRD measurements. (b) Experimental (I_{111}/I_{220} and I_{002}/I_{004}) and calculated intensity ratios (I^R_{111}/I^R_{220} and I^R_{002}/I^R_{004}) with respect to T_a are plotted on the left-hand scale, while percentages of ordering parameters are plotted on the right-hand scale.

PERPENDICULAR MAGNETIC TUNNEL JUNCTIONS USING ULTRATHIN MnGa ELECTRODES

Kazuya SUZUKI, Reza RANJBAR, Shigemi MIZUKAMI
WPI Advanced Institute for Materials Research, Tohoku University, Sendai 980-8577,Japan
E-mail: kazuya.suzuki.d8@tohoku.ac.jp

Ordered Mn-Ga alloy films have a large perpendicular magnetic anisotropy, small saturation magnetization and small damping constant, thus it is potentially attractive for spin-transfer-torque (STT) applications such as STT-MRAM and STT-oscillator/diode devices with sub-THz range.[1] However, the fabrication process high quality ultrathin films with thickness below several nm have been not established yet.[2-5] Recently, we have succeeded a highly-ordered ultra-thin MnGa films using paramagnetic B2 CoGa buffer layer. It showed the well perpendicular magnetic anisotropy with well magnetic squareness ratio even the thickness of 1 nm.[6,7] In this presentation, we will report the structural and magnetic properties of the ultrathin L10-MnGa film grown on the paramagnetic B2-CoGa buffer layer, and demonstrate perpendicular magnetic tunnel junctions using the ultrathin MnGa films.

The device stacking structure of (001) single crystalline MgO substrate / Cr(40) /CoGa(30)/MnGa(t_{MnGa} 1-5) /MgO(2) /CoFeB(1) / Ta(3) / Ru(5) (thickness is in nm) were prepared by an ultra-high vacuum sputtering system. All the layers were deposited at room temperature (RT) and the heating treatments were performed only for the MgO substrate, Cr, and CoGa layer at 700, 700, and 500℃, respectively. The films were patterned into the micron-sized MTJs by a conventional ultraviolet photo-lithography and Ar ion milling.

Figure 1 shows the out-of-plane polar Kerr loops for these films without CoFeB/Ta/Ru layers. The loops with squareness close to unity are observed even at t_{MnGa}= 1 nm. The HAADF-STEM image of CoGa/MnGa/MgO layers is shown in Fig.2. The atomically flat interfaces and well-ordered crystalline structure of the MnGa layer was observed. In addition, it was clarified that the ultrathin MnGa layer has an in-plane lattice constant close to that of the CoGa layer owing to the epitaxial strain. XMCD measurement confirmed no diffusion of Co atoms into MnGa layer. Moreover, the first-principles calculations showed that the strained MnGa has a fully spin-polarized band structure along the c-axis, indicating that the huge TMR will be obtained.

Figure 3 shows annealing temperature (T_a) dependence of the room temperature TMR ratios for the p-MTJs with different MnGa thickness. The TMR ratios increase with increasing T_a, then those turn to decrease at T_a of about 250-300℃. The maximum TMR ratios at room temperature are 5-7% at T_a of 250℃. This annealing temperature dependences may originate from the diffusion of Mn or Ga atoms into the MgO or CoGa layer. Figure 4. Shows measurement temperature dependence of the p-MTJs with different MnGa thickness. Here, MTJs were annealed at 250℃. All the p-MTJs show the increase in the TMR ratio with decreasing the measurement temperature, which is similar to that reported in the p-MTJs with 30-nm-thick MnGa grown on Cr buffer layer in previous report.[8] The maximum TMR ratios are almost independent of the MnGa thickness except for the p-MTJ with t_{MnGa}= 1 nm. However, the first principles calculations suggest that spin-polarized band structure is sensitive for epitaxial strain along the c-axis.[7] This independent TMR may originate from the surface structure of MnGa and/or composition effect.[9,10]

ACKNOWLEDGMENTS

We would like to thank Prof. T. Miyazaki for fruitful discussion.The authors thank Y. Kondo for technical assistance. This work is in part supported by ImPACT program “Achieving ultimate Green IT Devices with long usage times without charging”, Grant-in-Aid for Scientific Research (No. 16K14244), and Asahi glass foundations.

Kazuya Suzuki
E-mail: kazuya.suzuki.d8@tohoku.ac.jp

REFERENCES

1) S. Mizukami *et al.*, Phys. Rev. Lett. **106**, 117201 (2011).
2) F. Wu *et al.*, IEEE Trans. Magn. **46**, 1863 (2010).
3) A. Kohler *et al.*, Appl. Phys. Lett. **103**, 162406(2013).
4) M. Li, X. Jiang, *et al.*, Appl. Phys. Lett. **103**, 032410 (2013).
5) Y. H. Zheng *et al.*, J. Appl. Phys. **115**, 043902 (2014).
6) K.Z. Suzuki *et al.*, Jpn. J. Appl. Phys. (RC) **55**, 010305 (2016).
7) K.Z. Suzuki *et al.* Sci. Rep. **6**, 30249 (2016).
8) Q. L. Ma *et. al.*, IEEE Trans. Mag. **48**, 2808 (2012)
9) Y.Miura *et.al.* IEEE Trans. Mag, **50**,1400504 (2014)
10) J. Jeong, *et al.* Nat. Commun. **7**, 10276 (2016)

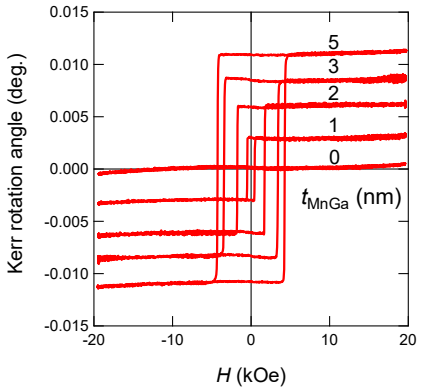

Fig. 1 Out-of-plane hysteresis curves measured by polar-MOKE

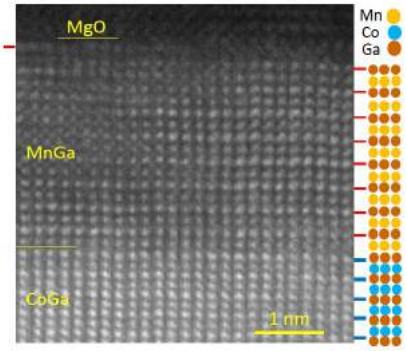

Fig.2 The HAADF-STEM image of the CoGa/MnGa/MgO layers.

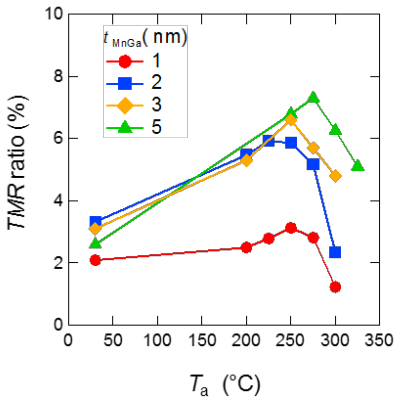

Fig.3 The TMR ratios measured at R.T. as a function of the T_a for p-MTJs with t_{MnGa}=1-5 nm.

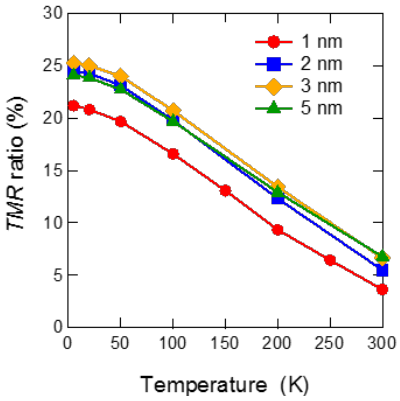

Fig. 4 The TMR ratios as a function of measurement temperature for p-MTJ with t_{MnGa}=1-5 nm.. All the MTJs were annealed at 250℃

INVESTIGATION OF MAGENTOTRANSPORT PROPERTIES OF HEUSLER-ALLOY-BASED MAGNETIC TUNNEL JUNCTIONS WITH A $Cu(In_{0.8}Ga_{0.2})Se_2$ SEMICONDUCTOR BARRIER WITH A LOW RESISTANCE-AREA PRODUCT

K. MUKAIYAMA[1], S. KASAI[1, 2], Y. K. TAKAHASHI[1], P-H. CHENG[1, 3], IKHTIAR[1], K. MASUDA[1], Y. MIURA[1, 4], S. MITANI[1, 3], and K. HONO[1, 3]

1) National Institute for Materials and Science, Tsukuba, Japan
2) RIKEN, Wako, Japan
3) University of Tsukuba, Tsukuba, Japan
4) 2Kyoto Institute of Technology, Kyoto, Japan

The magnetoresistance (MR) effect is indispensable phenomenon for future device applications such as read head sensors of HDDs over 2 Tbit/in^2. In order to realize highly sensitive read head sensors, a large MR ratio at a low resistance-area product (*RA*) of ~ 0.1 Ω·μm^2 is required [1]. This requirement is a great challenge for conventional MR devices such as the magnetic tunnel junctions (MTJs) with MgO barriers and the current perpendicular to plane giant magnetoresistance devices with Heusler-alloy ferromagnetic electrodes devices, although many attempts have been made to obtain an adequate *RA* value of 0.1 Ω·μm^2, for example, the optimization of deposition conditions of ultrathin MgO barriers [2] and the investigation of new metallic spacers [3, 4]. Another interesting approach is to utilize semiconducting barriers, because their smaller band gaps may lead to an adequate *RA* without degrading MR ratios. In this study, we demonstrate a large MR ratio and a high output voltage at *RA* ~ 0.1 Ω·μm^2 by using the MTJs with a $Cu(In_{0.8}Ga_{0.2})Se_2$ (hereafter, CIGS) compound semiconductor barrier, having a good lattice matching with the Heusler alloys such as $Co_2Fe(Ga_{0.5}Ge_{0.5})$ (hereafter, CFGG).

A film consisting of Ru(8)/Ag(5)/CFGG(10)/CIGS(2)/CFGG(10)/Ag(100)/Cr(10) (unit :nm) was deposited on a MgO (001) substrate by magnetron sputtering. After ex-situ annealing at 300°C, Films were patterned into rectangular or elliptical pillars by electron beam lithography and Ar ion milling. The size of pillars was varied between 200 × 150 nm^2 and 800 × 300 nm^2. Transport properties were measured by the dc-4-probe method at room temperature.

Figure 1 shows the HAADF-STEM image taken from a CFGG/CIGS/CFGG tri-layer part. A well defined layered and crystalized structure with sharp interfaces is clearly observed. The CFGG and CIGS layers have the epitaxial relationship with $(001)[110]_{CFGG}$ // $(001)[110]_{CIGS}$. The CIGS layer is found to have the chalcopyrite structure, which is the low temperature phase. Moreover, the bottom and top CFGG layers were $L2_1$ and $B2$ structures, respectively. Figure 2 shows the bias voltage (V_{bias}) dependence of the (a) MR ratio and (b) output voltage ΔV (= MR ratio × V_{bias}) at 300 K. As shown in the inset of figure 2 (a), a large MR ratio of 47 % is observed at V_{bias} ~ 0 mV with a desired *RA* value of 0.14 Ωμm^2. First-principles calculation results have shown this is due to the Δ_1 electrons' coherent tunneling [5]. The MR ratio does not decrease significantly with increasing V_{bias}, resulting in a large ΔV of 24 mV at V_{bias} = 60 mV. These results suggest that CIGS is a promising barrier for read head sensors of HDDs over 2 Tbit/in^2.

This work was supported by the ImPACT program.

1) M. Takagishi *et al.*, "Magnetoresistance Ratio and Resistance Area Design of CPP-MR Film for 2–5 Tb/in^2 Read Sensors", *IEEE Trans. Magn.*, **46**, 2086 (2010).
2) H. Maehara *et al.*, "Tunnel Magnetoresistance above 170% and Resistance–Area Product of 1 Ω (μm)^2 Attained by In situ Annealing of Ultra-Thin MgO Tunnel Barrier", *Appl. Phys. Express* **4**, 033002 (2011).
3) T. Nakatani *et al.*, "High signal output in current-perpendicular-to-the-plane giant magnetoresistance sensors using In–Zn–O-based spacer layers", *Appl. Phys. Express* **8**, 093003 (2015).
4) H. Narisawa *et al.*, "Current perpendicular to film plane type giant magnetoresistance effect using a Ag–Mg spacer and $Co_2Fe_{0.4}Mn_{0.6}Si$ Heusler alloy electrodes", *Appl. Phys. Express* **8**, 063008 (2015)
5) K. Masuda *et al.*, "First-principles study on magnetic tunneling junctions with semiconducting $CuInSe_2$ and $CuGaSe_2$ barriers", *Jpn. J. Appl. Phys.* **56**, 020306 (2017)
6) S. Kasai et al., "Large magnetoresistance in Heusler-alloy-based epitaxial magnetic junctions

K. Mukaiyama
MUKAIYAMA.Koki@nims.go.jp

with semiconducting $Cu(In_{0.8}Ga_{0.2})Se_2$ spacer", *Appl. Phys. Lett.*, **109**, 032409 (2016)
7) K. Mukaiyama *et al.*, "High output voltage of magnetic tunnel junctions with a $Cu(In_{0.8}Ga_{0.2})Se_2$ semiconducting barrier with a low resistance–area product", *Appl. Phys. Express* **10**, 013008 (2017)

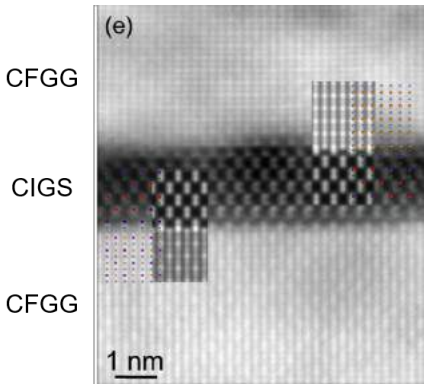

Figure1 HAADF-STEM images of CFGG/CIGS/CFGG films

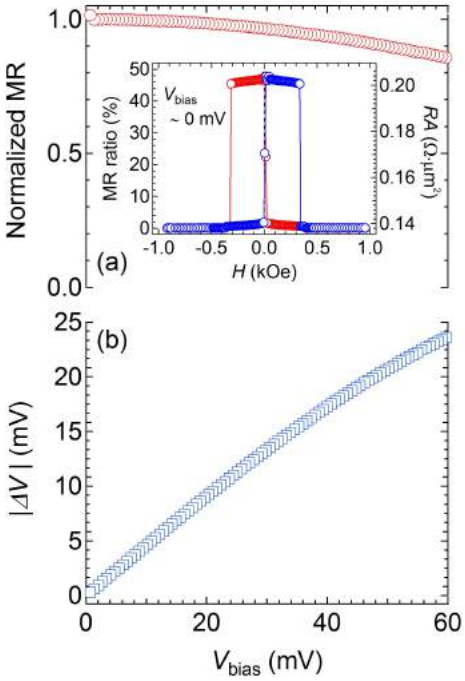

Figure 2 Bias voltage dependence of (a) normalized MR and (b) output voltage at 300 K.

CONTROL OF EPITAXIAL STRAIN AND MAGNETIC ANISOTROPY IN COBALT-FERRITE THIN FILMS BY VARIOUS BUFFER LAYERS

H. ONODA[1], Y. HISAMATSU[2], J. INOUE[1], H. SUKEGAWA[2], S. SHARMIN[1] and H. YANAGIHARA[1]

(1. Division of Applied Physics, University of Tsukuba, 2. NIMS)

onodahrs@gmail.com

I. Introduction

Large PMA can be introduced via the magnetoelastic effects in a uniaxial distortion by a substrate-induced epitaxial strain[2], for example. In fact, cobalt-ferrite (CFO) thin films grown on MgO(001) substrate suffering 0.6% in-plane tensile strain, results in introducing a large perpendicular magnetic anisotropy (PMA) K_u^{eff} of 14.7 Merg/cm^3 [1]. Likewise, CFO films grown on Mg_2AlO_4(001) substrate suffering 3.6 % in-plane compressive strain, exhibits as large as negative K_u of – 60 Merg/cm^3. In addition, even though such a large lattice strain, those induced PMA of CFO(001) epitaxial films can be quantitatively explained within a framework of magneto-elastic theory[3]. In other words, the induced magnetic anisotropy can be quantitatively explained by the phenomenological magneto-elastic effect in this lattice distortion range, at least. Therefore, even larger PMA by inducing 3~4 % tensile strain can be expected. In this study, we report various buffer layers to introduce the larger lattice constant than MgO(001) and the magnetic anisotropy, especially induced K_u of CFO(001).

II. Experimental

We selected Mg_2SnO_4 (MSO) as buffer layers and grew it by using a reactive rf-magnetron co-sputtering of Mg and Sn metal targets. The reactive gas was pure oxygen. We grew CFO films by using a reactive rf-magnetron sputtering of a CoFe alloy target. We evaluated surface and crystal structure for the CFO films by a reflection high energy electron diffraction (RHEED) and X-ray diffraction techniques. Magnetization and magnetic anisotropy constants were measured by using a SQUID magnetometer and a magnetic torque measurement.

III. Results

RHHED images of both MSO and CFO films show the streak patterns, suggesting a single crystal and sufficiently flat surfaces. Figure 1 shows in-plane and out-of-plane MH-loops of 10-nm-thick CFO film on an 80-nm-thick MSO buffer layer. The value of the saturation magnetization was 460 emu/cm^3, which is larger than 425 emu/cm^3 for bulk CFO. Surprisingly, in-plane magnetization was not saturated at all even when 70 kOe was applied. Apparently, a strong PMA presents in the film. From a magnetic torque measurement, the intrinsic K_u^{eff} was estimated to be over 20 Merg/cm^3.

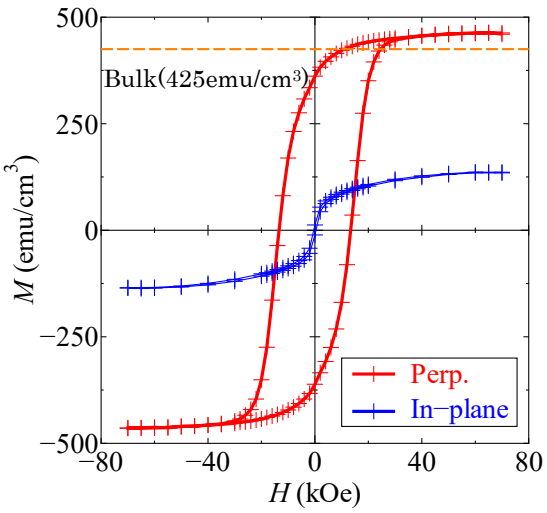

Figure 1: MH loops of the thin film (CFO thickness: 10 nm)

REFERENCES

1) T. Niizeki, *et al*., *Appl. Phys. Lett*., **103**, 162407 (2013).
2) J. Inoue, *et al*., *IEEE Trans. Mag*., **49**, 3269 (2013).
3) Tainosho, *et al*., The 39th The Magnatics Society of Japan 08pB-14

Hiroshige Onoda
E-mail: onodahrs@gmail.com
tel: +81-29-853-5243

FIRST-PRINCIPLES STUDY FOR MAGNETIC TUNNELING JUNCTIONS WITH SEMICONDUCTOR BARRIERS $CuInSe_2$ AND $CuGaSe_2$

Keisuke MASUDA[1] and Yoshio MIURA[1,2,3,4]

1) National Institute for Materials Science (NIMS), Tsukuba, Japan, MASUDA.Keisuke@nims.go.jp

2) Kyoto Institute of Technology, Kyoto, Japan, MIURA.Yoshio@nims.go.jp

3) Center for Materials Research by Information Integration, National Institute for Materials Science (NIMS), 1-2-1 Sengen, Tsukuba 305-0047, Japan

4) Center for Spintronics Research Network (CSRN), Graduate School of Engineering Science, Osaka University, Machikaneyama 1-3, Toyonaka, Osaka 560-8531, Japan

Magnetic tunneling junctions (MTJs), in which an insulating barrier layer is sandwiched between ferromagnetic electrodes, have attracted much attention due to their potential applications to high performance spintronic devices, such as ultrahigh-density hard disk drives (HDD) and Gbit-class non-volatile magnetic random access memories (MRAM). To realize such applications, MTJs are required to have low resistance-area products (*RA*) in addition to high magnetoresistance ratios (MR ratios). Up to the present, elaborate deposition techniques for making ultrathin MgO barriers have been established in order to decrease *RA* of MgO-based MTJs with high MR ratios [1]. However, MR ratios tend to decrease when the barrier thicknesses are reduced. Moreover, such ultrathin barriers lead to poor controllability of the MTJs. On the other hand, the use of Heusler alloys increased the MR ratios of current-perpendicular-to-plane giant magnetoresistance (CPP-GMR) devices with quite low *RA*. Although the current highest MR ratio is 80 % at room temperature [2], more improvement is needed to achieve high performance in the above-mentioned devices. Another possible way to obtain high MR ratios and low *RA* is using semiconductors as barrier layers instead of band insulators. Recently, Kasai *et al*. demonstrated that the MTJs with semiconductor barriers $CuIn_{1-x}Ga_xSe_2$ (CIGS) have high MR ratios (40 % at room temperature and 100 % at low temperature) and low *RA* (0.3-3 $\Omega\mu m^2$). We can expect high controllability and high breakdown voltage in these systems due to the sufficient thickness of CIGS (~2 nm).

In order to understand high MR ratios and low *RA* in the CIGS-based MTJs, we theoretically investigated transport properties of MTJs with semiconductor barriers, $CuInSe_2$ (CIS) and $CuGaSe_2$ (CGS), which are two terminal compounds of CIGS. For simplicity, bcc Fe is adopted as ferromagnetic electrodes in both the MTJs. On the basis of the density-functional method implemented in the Vienna *ab-initio* simulation program (VASP) [4,5], we first optimized the atomic structures of the supercells, Fe(3)/CIS(17)/Fe(3) and Fe(3)/CGS(17)/Fe(3), where each number represents the number of layers of each compound. Using the optimized supercells, we calculated transmittances of the CIS- and CGS-based MTJs by means of the quantum code ESPRESSO [6] for both cases of parallel and antiparallel magnetization of Fe electrodes. Since our system has a two-dimensional periodicity in the *xy* plane, the transmittances can be classified by an in-plane wave vector $\mathbf{k}_{//}=(k_x,k_y)$. Finally, the MR ratios and *RA* were evaluated from the calculated transmittances. In the present work, we took into account the on-site Coulomb interaction *U* in the Cu 3*d* states of both the CIS and CGS barriers to study the band-gap dependence of MR ratio and *RA* systematically.

Figure 1(a) shows the $\mathbf{k}_{//}$ dependence of the majority-spin transmittance in the CIS-based MTJ with U=5 eV and with parallel magnetization of Fe electrodes. We see that the transmittance has a large value around $\mathbf{k}_{//}=(0,0)$, which is a clear evidence of the coherent tunneling of wave functions [7]. By analyzing the complex band structures of the CIS-based MTJ, it was found that the Δ_1 wave functions give the dominant contributions to the total transmittance. Although not shown here, we also found that the coherent tunneling of the Δ_1 wave functions occurs in the CGS-based MTJs [8]. Figure 1(b) shows the MR ratios and *RA* values of the CIS- and CGS-based MTJs. We also show those of the MgO-based MTJs for comparison. We see that the CGS-based MTJs have larger MR ratios (~300 %) than the CIS-based MTJs. Note here that a larger Coulomb interaction *U* gives a larger band gap of the semiconductor. In addition,

Keisuke MASUDA
Masuda.Keisuke@nims.go.jp

CGS has a larger band gap than CIS for the same *U*. Thus, we can conclude that the MTJ with a larger band gap of the semiconductor gives a higher MR ratio. The *RA* values of the CIS- and CGS-based MTJs are nearly six orders of magnitude smaller than those of the MgO-based MTJs with similar barrier thicknesses. If the thickness of the MgO barrier is sdecreased from 3 to 1 nm, the *RA* is still larger than those of the CIS- and CGS-based MTJs. These results on the *RA* values and MR ratios are in good agreement with experimental ones on the CIGS-based MTJs [3].

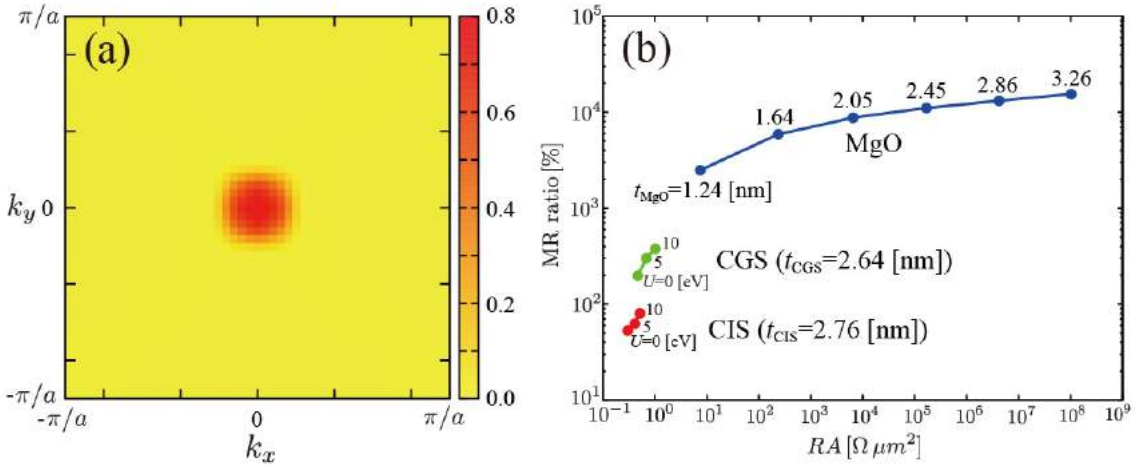

Fig. 1. (a) The $\mathbf{k}_{//}$ dependence of the majority-spin transmittance in the CIS-based MTJ with U=5 eV and with parallel magnetization of Fe electrodes. (b) The MR ratios and RA values of the CIS-, CGS-, and MgO-based MTJs. The barrier thickness (t_{CIS}, t_{CGS}, or t_{MgO}) is defined as the distance between two Fe layers closest to the barrier.

REFERENCES

1) H. Maehara *et al*., Appl. Phys. Express **4**, 033002 (2011).
2) J. W. Jung *et al*., Appl. Phys. Lett. **108**, 102408 (2016).
3) S. Kasai *et al*., Appl. Phys. Lett. **109**, 032409 (2016).
4) G. Kresse and J. Furthmüller, Phys. Rev. B **54**, 11169 (1996).
5) G. Kresse and D. Joubert, Phys. Rev. B **59**, 1758 (1999).
6) S. Baroni, A. Dal Corso, S. de Gironcoli, and P. Giannozzi, Quantum ESPRESSO package. For more information, see http://www.pwscf.org.
7) W. H. Butler, X.-G. Zhang, T. C. Schulthess, and J. M. MacLaren, Phys. Rev. B **63**, 054416 (2001).
8) K. Masuda and Y. Miura, Jpn. J. Appl. Phys. **56**, 020306 (2017).

LARGE REDUCTION OF FABRICATION TEMPERATURE FOR FULLY EPITAXIAL Fe/GaO_x/Fe MAGNETIC TUNNEL JUNCTIONS

H. SAITO[1], N. SAI KRISHNA[1], N. MATSUO[1,2], N. DOKO[1,2], and S. YUASA[1]

1) National Institute of Advanced Industrial Science and Technology, Spintronics Research Center Umezono 1-1-1, Central 2, Tsukuba, Ibaraki 305-8568, Japan

2) On leave from Chiba Institute of Technology, 2-17-1 Tsudanuma, Narashino, Chiba 275-0016, Japan

I. INTRODUCTION

Semiconducting materials have recently attracted considerable attention to the tunnel barrier of MTJs because they provide unique properties and functions to the MTJ such as very low resistance-area product [1] and tunability of a tunneling current by electric fields [2]. Very recently, we have reported a high MR ratio up to 92% in fully epitaxial Fe(001)/GaO_x(001)/Fe(001) MTJs [3], where the GaO_x is one of the emerging semiconductors for practical applications. Although GaO_x is amorphous in the as-grown state, a single-crystalline GaO_x with a $MgAl_2O_4$–type spinel structure was successfully formed by an *in situ* annealing of the as-grown GaO_x layer. However, the formation temperature of the single-crystalline GaO_x is too high (~500ºC) to apply to practical applications. In this study, we developed a novel fabrication process that can largely reduce the formation temperature of the fully epitaxial MTJ from 500°C to 250°C.

II. SAMPLE PREPARATIONS

MTJ films were prepared by molecular beam epitaxy. The structure of the MTJ was Au (10 nm) cap / Co (5 nm) pinned layer / Fe (5 nm) upper electrode / GaO_x (2 nm) tunnel barrier / MgO (1 nm) seed layer / Fe (30 nm) bottom electrode / MgO (10 nm) buffer layer on MgO(001) substrates. The GaO_x barrier layer was deposited at 80°C under an O_2 pressure of 1×10^{-6} Torr. Then, an *in situ* annealing at the temperature T_{GaO}, where T_{GaO} ranges from 250°C to 500°C, was carried out under an O_2 pressure of 1×10^{-7} Torr. The Fe upper electrode was grown and annealed at T_{Fe} = 250°C under the high vacuum below 1×10^{-9} Torr. The T_{GaO} and T_{Fe} of the present MTJs are listed in Table I.

III. RESULTS

Figures 1 (a)-(l) show reflection high-energy electron diffraction (RHEED) images of the GaO_x barrier layers (upper panels), the Fe upper electrode in the as-grown state (middle panels) and after an *in situ* annealing at T_{Fe} = 250°C (bottom panels) of the MTJs, respectively. For the GaO_x layers, no clear diffraction patterns were observed in the RHEED images for the as-grown state (Fig. 1a) and after the annealing at T_{GaO} = 250°C (Fig. 1b). With increasing T_{GaO}, streaky patterns started to appear at around T_{GaO} = 350°C (Fig. 1c), and finally sharp streaky patterns could be observed at T_{GaO} = 500°C (Fig. 1d). These indicate that the GaO_x barrier layers are amorphous for the samples A and B, mixture of amorphous and crystalline for the sample C and single-crystalline for the sample D, respectively.

Table I. Sample name, *in situ* annealing temperatures of GaO_x barrier (T_{GaO}) and Fe upper electrode (T_{Fe}) for the MTJ samples.

Sample name	T_{GaO} (°C)	T_{Fe} (°C)
A	w/o	250
B	250	250
C	350	250
D	500	250

The Fe upper electrodes of the samples A and B exhibited broad ring RHEED patterns in the as-grown state (Figs. 1e and 1f), suggesting polycrystalline Fe. In contrast, RHEED images of the samples C and D showed spotty patterns (Figs. 1g and 1h, respectively), implying single-crystalline Fe electrodes. It should be remarked that the broad ring patterns observed in the samples A and B changed to streak ones after an *in situ* annealing at T_{Fe} = 250°C as displayed in Figs. 1(i) and 1(j), respectively. Consequently, the Fe upper electrodes for all the samples revealed similar sharp streak

HIDEKAZU SAITO
E-mail: h-saitoh@aist.go.jp
tel: +81-29-8615457

patterns after the *in situ* annealing at T_{Fe} = 250°C. This strongly suggests that a single-crystalline Fe upper electrode can be formed even on the as-grown GaO_x barrier layer without a high temperature annealing up to 500°C.

From the RHEED observations, we can expect the existence of coherent spin-polarized tunneling, and thereby a high MR ratio beyond the Julliere's model even for the samples A and B. Figure 2(a) shows a typical MR curve of sample A. The MR ratio up to 102% was observed at RT, which is close to the reported value in the fully epitaxial MTJ (92%) [3] As plotted in Fig. 2(b), the MR ratio hardly depends on the T_{GaO}, suggesting that there is no remarkable difference in the magneto-transport properties among the MTJ samples.

IV. CONCLUSIONS

We investigated structural and magneto-transport properties of Fe/GaO_x(MgO)/Fe MTJs grown by different *in situ* annealing conditions for amorphous GaO_x tunnel barrier. Fabrication of fully epitaxial MTJ was possible even without the *in situ* annealing of the GaO_x barrier, resulting in a large reduction on the formation temperature of the fully epitaxial structure from 500°C to 250°C.

ACKNOWLEDGMENTS

This work was supported by the ImPACT Program of the Council for Science, Technology and Innovation (Cabinet Office, Government of Japan) and Grant-in-Aid for Scientific Research on Innovative Area, "Nano Spin Conversion Science" (Grant No. 26103003).

REFERENCES

[1] S. Kasai, Y. K. Takahashi, P. -H. Cheng, Ikhtiar, T. Ohkubo, K. Kondou, Y. Otani, S. Mitani, and K. Hono, *Appl. Phys. Lett.* **109**, 032409 (2016).

[2] T. Kanaki, H. Asahara, S. Ohya, and M. Tanaka, *Appl. Phys. Lett.* **107**, 242401 (2015).

[3] N. Matsuo, N. Doko, T. Takada, H. Saito, and S. Yuasa, *Phys. Rev. Applied* **6**, 034011 (2016).

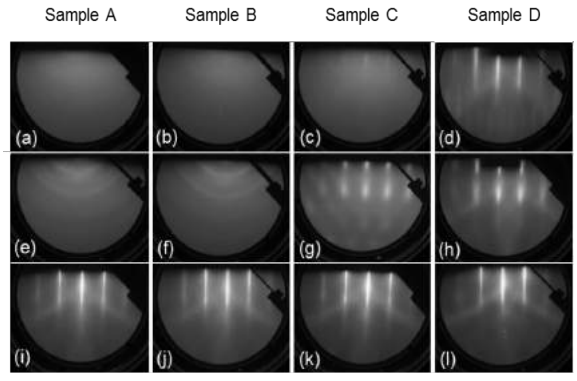

Figs. 1 RHEED images of the (a) GaO_x barrier layer in the as-grown state, (b)-(d) same layer after *in situ* annealing at T_{GaO}, (e)-(h) Fe upper electrode in the as-grown state, and (i)-(l) same layer after an *in situ* annealing at T_{Fe}, respectively.

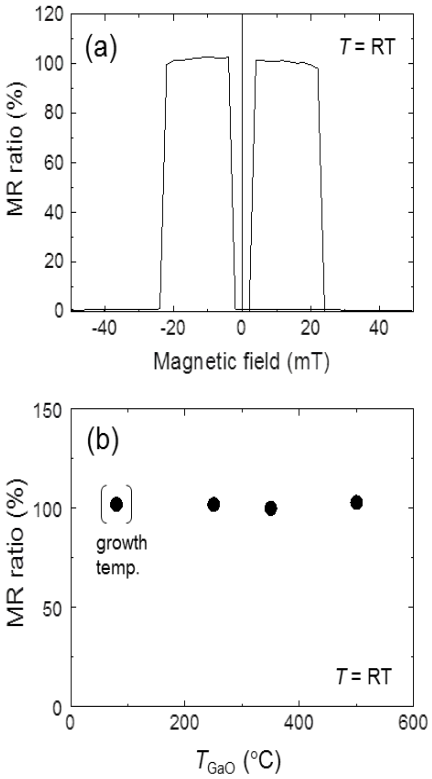

Figs. 2 (a) Typical MR curve of sample A and (b) MR ratio as a function of T_{GaO} at RT, respectively.

DP-09

THEORY OF MICROWAVE ASSISTED MAGNETIZATION REVERSAL

Tomohiro TANIGUCHI
Spintronics Research Center, National Institute of Advanced Industrial Science and Technology (AIST),
central 2, 1-1-1, Umezono, Tsukuba 305-8568, Japan,
tomohiro-taniguchi@aist.go.jp

I. Background

Microwave assisted magnetization reversal (MAMR) is a method to switch the magnetization direction in nanostructured ferromagnet by applying a direct magnetic field smaller than the anisotropy field of the ferromagnet. The microwave having the frequency close to ferromagnetic resonance (FMR) frequency efficiently excites a large amplitude oscillation of the magnetization around the easy axis, and assists the magnetization switching by a small direct field [1]. A quantitative analysis on a relation between the switching field and microwave frequency has been made by using the Landau-Lifshitz-Gilbert (LLG) equation in a rotating frame [2]. In the rotating frame, the microwave field is converted to a direct field pointing in the switched direction, where the magnitude of this additional field is proportional to the microwave frequency. This additional field in the rotating frame has been considered as an origin of the reduction of the switching field [3]. It should be, however, pointed out that this theoretical view is insufficient to understand the physical mechanisms of MAMR because of the following reason. The numerical simulation of MAMR has clarified that the switching field decreases with increasing the microwave frequency, which is consistent with the physical picture in the previous work. However, when the microwave frequency becomes larger than a certain threshold value, the switching field significantly increases, and the assist effect by the microwave field disappears. The discontinuous change of this switching field with respect to the microwave frequency cannot be explained by the physical mechanism discussed in the previous works, where, since the additional field is proportional to the microwave frequency, the switching field is expected to be decreased monotonically with increasing the microwave frequency. A micromagnetic simulation clarifies that an excitation of spin wave is a possible reason on the discontinuous change of the switching field [4]. It should be, however, mentioned that the jump of the switching field appears even when a macrospin model is used [4].

II. Results in this work

In this work, we present a theory of MAMR based on the macrospin model [5]. We notice that the microwave field in the rotating frame provides not only the direct field but also a torque pointing in the direction of the damping torque. The magnitude of this damping-like torque is also proportional to the microwave frequency. With increasing the microwave frequency, this damping-like torque prevents the switching, resulting in the discontinuous increase of the switching field. Applying the averaging method of the LLG equation on a slowly varying variable, we derived equations determining the switching fields in both low and high frequency regions separated by the threshold frequency [5]. A good agreement between our theory and macrospin simulation guarantees the validity of our study. The result provides a comprehensive picture of MAMR in the macrospin limit.

We also derived the simplified analytical expression of the threshold (critical) frequency in Ref. [6]. In this work, the spin torque switching assisted by microwave was investigated. As pointed out in Ref. [5], the damping-like torque appeared in the rotating frame of MAMR is mathematically similar to the spin torque. This analogy enables us to apply the theory of spin transfer torque switching to the analysis of MAMR. In Ref. [6], we derived the analytical theory of the spin torque switching with microwaves. We notice that the mathematical method developed in Ref. [6] can also be applied to reduce the equations determining the switching field in MAMR. Then, the analytical expression of the critical frequency in MAMR could be

Tomohiro Taniguchi
E-mail: tomohiro-taniguchi@aist.go.jp
tel: +81-29-861-2794

obtained as [6]

$$f = \frac{\gamma}{2\pi} H_K \frac{\left(H_{ac}/H_K\right)^{2/3}}{\sqrt{1-\left(H_{ac}/H_K\right)^{2/3}}}\left[2-\frac{5}{3}\left(H_{ac}/H_K\right)^{2/3}\right], \quad (1)$$

where γ is the gyromagnetic ratio, whereas H_K and H_{ac} are the anisotropy field and the magnitude of the microwave field, respectively (see Eq. (D14) in Ref. [6]). We note that the main work in Ref. [6] is the spin torque switching with microwave, and the derived formula of the critical frequency in MAMR in Ref. [6] is mathematically identical to the equations in Ref. [5], and should be regarded as a simplified equation; that is, Eq. (1) is mathematically identical to Eq. (10) in Ref. [5]. We emphasize that the theory determining the critical frequency of MAMR was originally derived in Ref. [5].

We note that a theoretical analysis similar to our work [5] was independently done by Suto *et al*. simultaneously [7].

This work is supported by the Japan Society and Technology Agency (JST) strategic innovation promotion program "Development of new technologies for 3D magnetic recording architecture". The author is also supported by JSPS KAKENHI Grant-in-Aid for Young Scientists (B) 16K17486.

REFERENCES

1) J. G. Zhu, X. Zhu, and Y. Tang, "Microwave Assisted Magnetic Recording", *IEEE Trans. Magn.,* 44 125-131, (2008).
2) G. Bertotti, A. Magni, I D. Mayergoyz, and C. Serpico, "Bifurcation analysis of Landau–Lifshitz–Gilbert dynamics under circularly polarized field", *J. Appl. Phys.* 89, 6710, (2001).
3) S. Okamoto, M. Igarashi, N. Kikuchi, and O. Kitakami, "Microwave assisted switching mechanism and its stable switching limit", *J. Appl. Phys.* 107, 123914 (2010).
4). S. Okamoto, N. Kikuchi, M. Furuta, O. Kitakami, and T. Shimatsu, "Switching Behaviors and its Dynamics of a Co/Pt Nanodot Under the Assistance of rf Fields", *Phys. Rev. Lett.* 109, 237209 (2012).
5) T. Taniguchi, "Magnetization reversal condition for a nanomagnet within a rotating magnetic field", *Phys. Rev. B* 90, 024424 (2014).
6) T. Taniguchi, D. Saida, Y. Nakatani, and H. Kubota, "Magnetization switching by current and microwaves", *Phys. Rev. B* 93, 014430 (2016).
7) H. Suto, K. Kudo, T. Nagasawa, T. Kanao, K. Mizushima, R. Sato, S. Okamoto, N. Kikuchi, and O. Kitakami, "Theoretical study of thermally activated magnetization switching under microwave assistance: Switching paths and barrier height", *Phys. Rev. B* 91, 094401 (2015).

DP-10

VOLTAGE-CONTROL SPINTRONICS MEMORY (VoCSM) FABRICATED BY TWO-STEP SELF-ALIGNED (TSSA) PROCESS

Y. OHSAWA, H. YODA, S. SHIROTORI, H. SUGIYAMA, M. SHIMIZU, B. ALTANSARGAI, N. SHIMOMURA, Y. SAITO, T. INOKUCHI, Y. KATO, K. KOI, S. OIKAWA, M. ISHIKAWA, Y. KAMIGUCHI, K. IKEGAMI, A. TIWARI, and A. KUROBE

Toshiba Corporation, Kawasaki, Japan, yuichi.osawa@toshiba.co.jp

I. Concept of VoCSM and TSSA process

The voltage-control spintronics memory (VoCSM) whose writing principle using spin Hall effect (SHE) under voltage-controlled magnetic anisotropy (VCMA) effect and device structure of multi-MTJs lining up on the same SHE electrode is designed for high density, low energy consumption, and high robustness against read-disturbance. The first conceptual demonstration was performed successively [1]. The two-step self-aligned (TSSA) process of VoCSM is designed for low write current (*i.e.* low energy consumption) and mass production by means of coincidence in widths of SHE electrode and magnetic tunnel junctions (MTJs) each other.

II. Experimental

The TSSA process is shown in Fig. 1. A mask pattern in a stripe configuration is formed on the MTJ stack located on the SHE electrode film (a). The MTJ stack is patterned into multi-stripes configuration on the SHE electrode film to form parallel aligned MTJ multi-wires by means of Ar-ion-beam etching (b). Both the multi-wires and remaining SHE electrode film are then etched using stripe masks orthogonal to the multi-wires (c)-(d). Finally, voltage-controlled magnetic anisotropy (VCMA) electrodes which apply assist voltage for write or no-write control of each storage layer are formed on the MTJs, respectively (e). A cross-sectional transmission electron microscope (XTEM) image of one of the MTJs on the SHE electrode is shown in (f). Since the edges of MTJ and SHE electrode coincides each other by means of TSSA process, the write current flows in the SHE electrode would interacts to the storage layer effectively. Conformation of writing is performed by tunnel magnetoresistance (TMR) readout between the VCMA and SHE electrodes.

MTJs with in-plane anisotropy whose easy axis aligns orthogonal to direction of write current are used for write tests. The mainly used MTJ stack and SHE electrode films are Ta (5nm)/ IrMn (8nm)/ CoFe (1.8nm)/ Ru (0.9nm)/ CoFeB (1.8nm)/ MgO (1.7nm)/ CoFeB (1.2nm)[storage layer] / Ta (10nm) [SHE electrode] from top. The films were sputter-deposited on a thermally-oxidized Si wafer. The TMR ratio and resistance-area product (RA) of the films are around 150% and 1kΩ μ m^2, respectively.

III. Results and discussion

Figure 2 shows I_c for a writing pulse width of 20 ns as a function of the MTJ area without any voltage assist. The inset shows configuration of the MTJ/SHE element schematically. The short axis widths of the storage layer were changed from 35 nm to 55 nm and the long axis widths were changed from 145 nm to 345 nm which were the same width as the SHE electrode widths. We find intrinsic scalability in MTJ size dependence of a critical write current (I_c) which is defined as current with a 50% writing probability. The I_c decreases monotonically as the MTJ size decreases. About 200μA of I_c at 20nsec for a MTJ size of 7600 nm^2 whose value was comparable to that for STT-writing with the similar dimension was obtained. Furthermore, I_c

Yuichi OHSAWA
E-mail: yuichi.osawa@toshiba.co.jp
tel: +81-44-5492130

decreased about 50μA at a -0.8V-VCMA electrode voltage due to the VCMA effect. The linear correlation between MTJ area and I_c predicts much smaller I_c would be obtained by means of reduction in size of MTJs, *i.e.* decrease in cross section of SHE electrode (width x thickness), and moreover increase in VCMA effect would also decrease in I_c as well.

IV. Conclusion

The I_c of about 200μA was obtained at 20nsec writing pulse width whose value is comparable to that for matured STT-MRAM with the similar dimension. It is concluded that by applying both the SHE and the VCMA effect, the VoCSM using TSSA process has a potential of high write-efficiency and strong candidate for spintronic memories.

Acknowledgement

This work was partly supported by the ImPACT Program of the Council for Science, Technology and Innovation (Cabinet Office, Government of Japan). We acknowledge Prof. M.Sahashi for guidance of this research.

REFERENCES

1) H. Yoda et al., "Voltage-Control Spintronics Memory (VoCSM) Having Potentials of Ultra-Low Energy-Consumption and High-Density", IEDM16-679

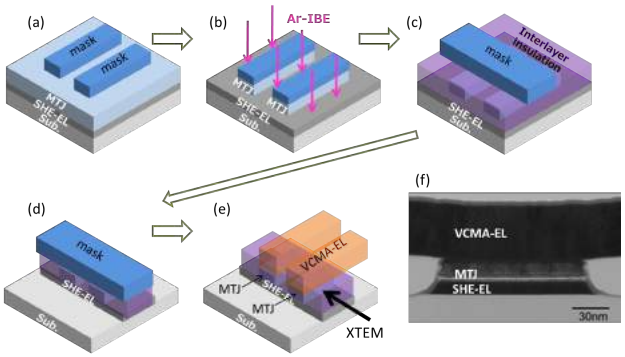

Fig. 1. Illustration of TSSA process. XTEM image (f) was observed from the direction indicated by the arrow in (e)

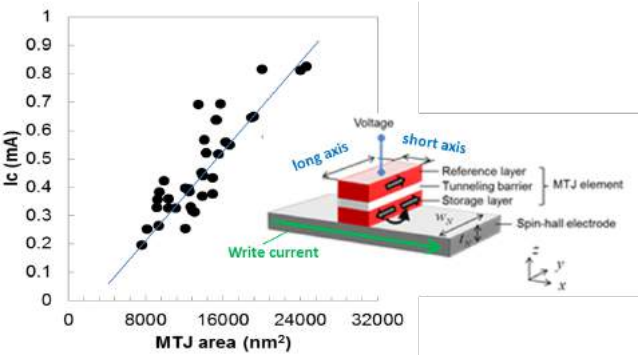

Fig. 2. I_c as a function of MTJ area. The line is a guide for the eyes. The inset shows configuration of the MTJ/SHE element. Easy axis in the storage layer aligns along the long axis.

ESTIMATION ON CURRENT-DRIVEN DOMAIN WALL MOTION IN MAGNETIC NANOWIRE BY USE OF MAGNETIC FIELD ASSIST

Mayumi KAWANA, Mitsunobu OKUDA, Yasuyoshi MIYAMOTO and Norihiko ISHII
Science & Technology Research Laboratories, NHK (Japan Broadcasting Corporation),
Tokyo, JAPAN, kawana.m-fe@nhk.or.jp

I. INTRODUCTION

A current-driven domain wall motion in magnetic nanowire with perpendicular anisotropy has been utilized in MRAM[1]. We also believe it can contribute to realize ultra-high-speed storage[2], however, larger current density is required to realize fast speed driving of domain walls. While magnetic field is simply applied normal direction to the nanowire, adjacent domain walls move opposite direction each other, *i.e.* a domain is forced to expand or compress improperly. In this study, in order to achieve reduction of required current and increase of domain wall velocity, we estimated the current-driven domain wall velocity dependence of direction and strength of applied magnetic field using a Landau–Lifshitz–Gilbert(LLG) equation with spin transfer torque term. The magnetic domain velocity was increased by use of adequate local magnetic field modulation. Our analyses indicate that in-plane component of the applied field is important for fast domain wall driving.

II. RESULTS AND DISCUSSIONS

The structure that we have used in our simulations is shown in Fig. 1. The dimensions of target nanowire are 1500 nm length, 60 nm width, and 20 nm thickness, respectively. Magnetic properties were set as follows: the saturation magnetization of 0.25 T, the uniaxial anisotropy H_k of 7.06 x 10^5 A/m, the exchange stiffness of 1.2 x 10^{-11} J/m, and the Gilbert damping constant of 0.02. The simulation cell size is 4 x 4 x 4 nm^3. We calculated the current-driven domain wall motion using a LLG equation with spin transfer torque term. In order to apply current induced spin transfer torque, current in the negative x-direction was applied. The applied current pulse is 6.4 x 10^{-6} A/cm^2 with 0.8 ns width. The white region in the figure is the magnetization toward the upward direction, while the black region indicates the magnetization toward the downward direction. To increase the domain wall velocity, pairs of permanent micromagnets were attached on top and bottom of the target nanowire for inducing local magnetic field modulation. Here, one of the calculation condition for applied field modulation is shown in Fig. 2. Figure 2 (a), (b), and (c) show x, y, and z component of the applied magnetic field modulation, by use of micromagnets with saturation magnetic flux density of 1T. In this conditions, magnetic field modulation with only in-plane components are applied to nanowire. Figure 3 shows the relationship between the moving distance of magnetic domain wall and elapsed time. By applying magnetic field modulation with in-plane component under allocated condition as shown in Fig.2, the velocity of domain wall could be improved approximately 2 times faster than that without magnetic field at the same driving current. Local magnetic field modulations seem to be effective for controlling the behavior of current-driven domain wall motion.

REFERENCES

1) S. Fukami, et al. “Low-current perpendicular domain wall motion cell for scalable high-speed

Mayumi KAWANA
Science & Technology Research Laboratories,
NHK (Japan Broadcasting Corporation),
E-mail: kawana.m-fe@nhk.or.jp
Tel/Fax: +81-3-5494-3234
1-10-11 Kinuta, Setagaya, Tokyo 157-8510

MRAM," *2009 symposium on VLSI technology. Digest Tech*. 24, pp.230-231 (2009)
2) M. Okuda, et al. "Operation of [Co/Pd] Nanowire Sequential Memory Utilizing Bit-Shift of Current-Driven Magnetic Domains Recorded and Reproduced by Magnetic Head," *IEEE Trans. Magn.,* Vol. 52, No. 7, 3401204, pp.3401204.1-3401204.4 (2016)

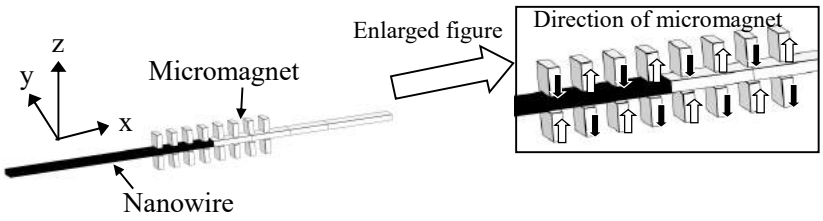

Fig. 1 Simulation model of nanowire and micromagnet.

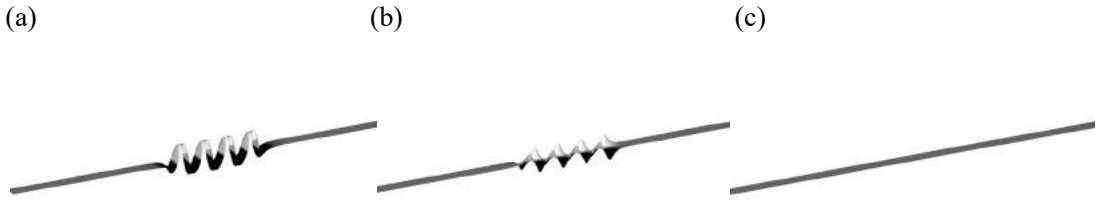

Fig. 2 (a)x, (b)y and (c)z components of the magnetic field modulation applied to the nanowire.

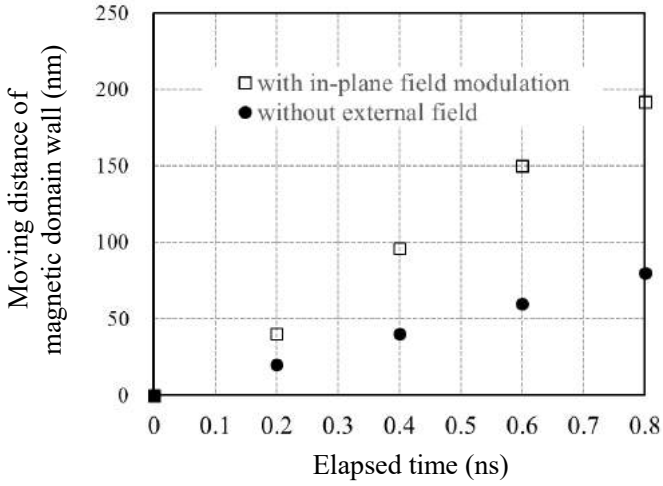

Fig. 3 Relationship between moving distance of magnetic domain wall and the elapsed time.

TRANSIENT TIME OF SELF-SYNCHRONIZED SPIN TORQUE OSCILLATOR

S. TSUNEGI[1], E. GRIMALDI[2], R. LEBRUN[2], H. KUBOTA[1], K. YAKUSHIJI[1], J. GROLLIER[2], A. FUKUSHIMA[1], S. YUASA[1] and V. CROS[2]

1) AIST, Tsukuba, Japan, tsunegi.sb@aist.go.jp

2) CNRS/Thales, Palaiseau, France

I. INTRODUCTION

Spin torque oscillators (STOs) with large non-linear characteristics have been studied in detail in the last decade, with the expectation of developing new microwave spintronic devices for next generation[1]. Earlier studies revealed that the large non-linearity enables to achieve synchronization among STOs, where the STO phase is synchronized with those of other STOs or with the external rf signals.[2,3] Recently, we succeeded in demonstrating self-synchronization of STO by using a delayed feedback circuit. In this case, both stationary point and stability are strongly dependent on the phase difference between the STO and the feedback current.[4] Such synchronizing phenomena are important for developing high frequency devices as well as for some applications such as reservoir computing which uses a system of nonlinear transient states as its basis [5]. In the reservoir or neural computing, transient time is a factor that cannot be overlooked. The time usually is investigated through analysis of amplitude noise in the single STO [6], but little is known for synchronized STO. In this work, we focused our attention on investigating the transient time τ of the self-synchronized STO.

II. EXPERIMENTS

The STO used was vortex based STO. The stack of the STO consists of buffer/PtMn(15nm)/CoFe(2.5 nm)/Ru(0.9 nm)/CoFeB(2 nm)/MgO(1.1 nm)/FeB(4 nm)/MgO(1.1 nm)/Ta(5 nm)/Ru(5 nm). The self-synchronization was carried out in the delayed feedback circuit, where the emitted rf current from STO was reflected at the close end and re-injected into STO. The phase difference $\Delta\phi$ can be controlled by changing the feedback time of the re-injected current. The transient time was evaluated by analyzing the auto-correlation function of the amplitude noise.

III. RESULT AND DISCUSSION

Figure 1 shows the dependence of transient time on the phase difference between the STO and feedback current. Interestingly, the transient time oscillates periodically with the phase difference. Similar behavior is observed for stationary point (not shown). The transient time behavior is explained by the Thiele model where rf spin transfer torque is taken into account.[4] Such transient time modulation will be a key issue in rf spintronics applications such as neuro-inspired STO based devices.

REFERENCES

[1] N. Locatelli, et. al., Nat. Mater 13, 11 (2014).
[2] F.B. Mancoff, et. al., Nature 437, 393 (2005)
[3] W. H. Rippard, et. al., Phys. Rev. Lett. 95, 067203 (2005)
[4] S. Tsunegi, et. al., Sci. Rep. 6, 26849 (2016)
[5] J. Torrejon, et. al., APS march meeting 2016, R11.00003
[6] L. Bianchini, et. al., Appl. Phys. Lett. 97, 032502 (2010)

Sumito Tsunegi
E-mail: Tsunegi.sb@aist.go.jp
tel: +81-29-861-5381

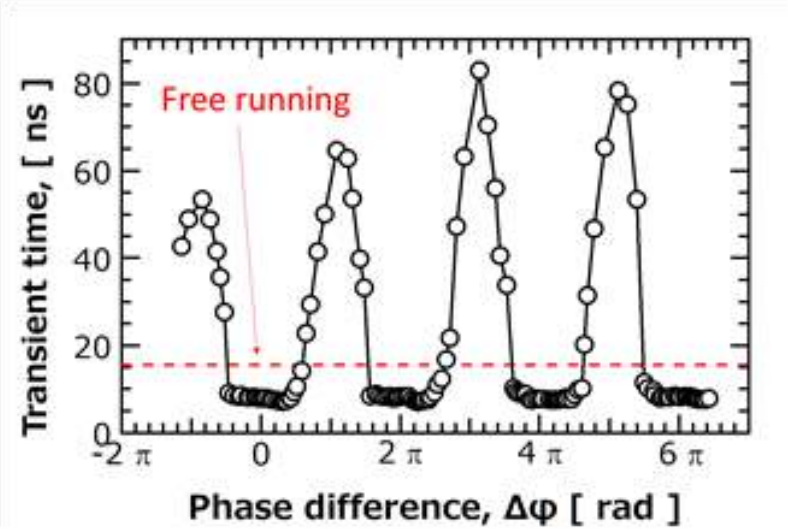

Fig. 1 The dependence of transient time on the phase difference. The red line indicates that of the free run STO.

PHYSICAL ORIGIN AND THEORETICAL LIMIT OF THE PHASE STABILITY OF A SPIN TORQUE OSCILLATOR STABILIZED BY PHASE LOCKED LOOP

S. TAMARU[1], H. KUBOTA[1], K. YAKUSHIJI[1], A. FUKUSHIMA[1] and S. YUASA[1]
1) National Institute of Advanced Industrial Science and Technology, Spintronics Research Center, Tsukuba, Ibaraki, 305-8568, Japan,
*shingo.tamaru@aist.go.jp

I. INTRODUCTION

The spin torque oscillator (STO) has been attracting significant interest as the next generation microwave signal source in radio frequency (RF) integrated circuits since its advent, due to its many attractive features such as ultra-small dimension, low power consumption and compatibility with semiconductor processes. To date, however, there has been no practical microwave system that actually uses an STO. One of the most serious problems hampering the adoption of STOs in real electronic systems is its poor phase stability, in other words, large phase noise. Currently, the typical phase noise levels of free running STOs are several orders of magnitude larger than those of conventional transistor based microwave oscillators. Hence, it is of paramount importance to stabilize an STO such that its signal quality meet industry specifications for the target application. For this purpose, we recently developed a phase locked loop (PL) circuit to actively stabilize an STO, and demonstrated successful phase locked oscillation characterized by an extremely sharp spectral peak [1]. Although this is a major step toward the productization of STOs, the spectrum measurement result still showed significantly larger residual phase noises than state-of-the-art semiconductor PLL chips, indicating that further performance improvement is crucial.

In this work, we performed a thorough characterization of the residual phase error of an STO stabilized by a PLL circuit, and also calculated the residual phase error using the standard linear system theory, aiming at establishing a methodology to quantitatively characterize the phase stability of the STO under free running, and clarifying the underlying physical mechanism and theoretical limit of the residual phase error of the STO stabilized by a PLL circuit.

II. EXPERIMENTAL AND ANALYSIS RESULTS

Fig. 1 shows the block diagram of the PLL circuit for stabilizing a STO built in this work. This basically follows the standard integer type PLL configuration, but with some customizations to control a STO, which has drastically different behaviors from conventional oscillators in terms of some parameters such as the bias voltage range and phase stability. The STO is nominally biased by a voltage V_{DC} to generate a microwave signal near 6.48 GHz. The generated microwave goes through the RF path of a bias-tee, amplified and downcounted by N, and eventually sent to one input of the phase frequency detector (PFD). The other input of the PFD is fed a very stable reference clock with a frequency f_r. The phase difference between these two signals is converted into a voltage signal V_E, which is filtered by a loop filter (LF) block and added to V_{DC} and fed back to the STO to dynamically tune the frequency such that the phase difference at the PDC is always minimized. Fig. 2 shows the phase error spectral density (PESD) of the STO under free running in red, phase locked to f_r = 135 MHz in purple, 270 MHz in blue and 405 MHz in green, respectively. The integration of the PESD, in other words, the area under the PESD curve, corresponds to the variance of the phase error, which is equivalent to the variance of the timing jitter. A black broken line superimposed on top of each curve is the theoretical calculation result for each oscillation condition. These results all showed excellent agreement between the experimentally observed and theoretically calculated PESD, which strongly supports the validity of the theory used in these calculations. This means that now we can assess the influence of each circuit parameter in the PLL circuit on the final performance of the STO stabilized by the PLL. The theory suggests the following. First, there

Shingo TAMARU
E-mail: shingo.tamaru@aist.go.jp
tel: +81-29-861-3007

may be some room for further reduction of the variance of the timing jitter by roughly another one order of magnitude by tightly integrating all the blocks and element in the circuit to speed up the PLL circuit response. Second, it is crucial to reduce the FESD of the free running performance of the STO in order to further reduce the residual phase error of the STO stabilized by the PLL.

In the poster, we will present the detail of these analyses such as characterization methodology, data processing algorithm and theory for calculating the PESD of the STO, as well as future direction of the STO research and development for better signal quality.

REFERENCES

1) S. Tamaru, et. al., “Extremely coherent microwave emission from spin torque oscillator stabilized by phase locked loop.", Sci. Rep., 5 18134, (2015).
2) S. Tamaru, et. al., “Physical origin and theoretical limit of the phase stability of a spin torque oscillator stabilized by phase locked loop.", submitted to Phys. Rev. Applied (2017).

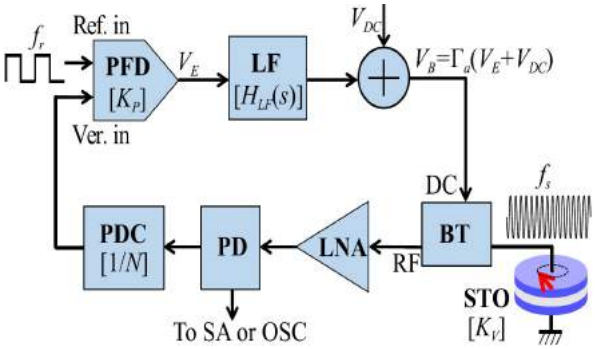

Fig. 1, Block diagram of the PLL circuit stabilizing a STO. Each functional block is labeled as, PFD: Phase Frequency Detector (proportionality constant for phase difference to voltage conversion denoted as K_P); LF: Loop Filter (transfer function denoted as $H_{LF}(s)$); STO: Spin Torque Oscillator (agility constant denoted as K_V); BT: Bias-Tee; LNA: Low Noise Amplifier; PD: Power Divider; PDC: Programmable Down Counter (divider ratio denoted as N); SA: Spectrum analyzer; and OSC: Oscilloscope. The two inputs of the PFD are abbreviated as, Ref. in: Reference frequency input; Var. in: Variable frequency input.

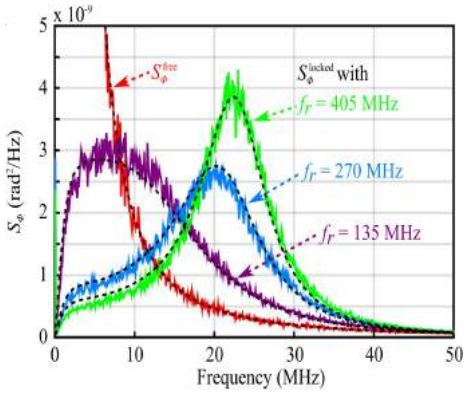

Fig. 2, PESD of the STO output signal. The four lines drawn with red, purple, blue and green represent the PESD when the STO is free running, phase locked to three different reference frequencies of f_r = 135 MHz, 270 MHz and 405 MHz, respectively. The broken line superimposed on each line is the theoretically calculated PESD.

PERPENDICULAR MAGNETIC ANISOTROPY OF AN Fe/MgO INTERFACE INDUCED BYW BUFFER AND Tb CAP LAYERS

Yuki IIDA[1], Jun OKABAYASHI[2] and Seiji MITANI[3]

1) Graduate School of Pure and Applied Sciences, University of Tsukuba, Tsukuba 305-8577, Japan, IIDA.Yuki@nims.go.jp

2) Research Center for Spectrochemistry, The University of Tokyo, Tokyo 113-0033, Japan, jun@chem.s.u-tokyo.ac.jp

3) National Institute for Materials Science, Tsukuba 305-0047, Japan, mitani.seiji@nims.go.jp

I. INTRODUCTION

Interface perpendicular magnetic anisotropy (PMA) of ferromagnetic metal/oxide layered structures is an important topic in perpendicularly magnetized magnetic tunnel junctions (MTJs), which are employed as a main element of magnetoresistive random access memory (MRAM) devices that can realize both low power consumption and high density integration in computing systems. The PMA energy density is a crucial physical quantity that determines thermal stability of magnetization states of the MTJs. Considering the volume of the ferromagnetic layer for spin transfer torque MRAMs with a perpendicular easy axis, PMA energy density of 1 MJ/m^3 is required to hold the data for 10 years.

CoFeB/MgO is the most popular layered structure in obtaining interface PMA of ferromagnetic metal/oxide systems. A perpendicularly magnetized CoFeB/MgO-based MTJ was developed by using a sputter-deposition technique suitable for commercial productions, and it exhibits a PMA energy density of 0.21 MJ/m^3 in the CoFeB layer [1]. On the other hand, ab initio calculations predict that the PMA energy in Fe/MgO interfaces is larger than that in Co/MgO interfaces [2]. This large PMA is often discussed based on the hybridization between Fe $3d_z^2$ and O $2p_z$ states [2,3]. In a corresponding experiment, PMA energy density of 1.4 MJ/m^3 was achieved in a molecular beam epitaxy (MBE)-grown Fe/MgO bilayer [4], suggesting that pure Fe based interfaces are preferable to obtain large PMA characteristics. However, Fe/MgO based perpendicular MTJs have never been fabricated by sputter-deposition processes, since boron presumably plays a key role to form a CoFeB/MgO interface with significant interface PMA.

In this work, by using specific buffer and cap layers, we tried to fabricate sputter-deposited Fe/MgO layered structures with perpendicular magnetization.

II. EXPERIMENT

Multi-layer stacks of W-buffer(3nm)/Fe(0.85-2nm)/MgO(2nm)/Tb-cap(2nm) were deposited on thermally oxidized Si substrates using an rf sputtering method (Figure 1). After completing all the depositions, in-situ annealing treatment was performed at 550˚C for 1 hour. Magnetic properties were measured using a vibrating sample magnetometer (VSM) for in-plane and perpendicular-to-plane directions. PMA energy densities were determined from the area surrounded by the two M-H curves. To evaluate the element-specific spin and orbital magnetic moments, x-ray absorption spectroscopy (XAS) and x-ray magnetic circular dichroism (XMCD) measurements were performed for Fe $L_{2,3}$-edge and Tb $M_{4,5}$-edge.

III. RESULTS

By choosing an optimized Fe layer thickness, we succeeded in the growth of the samples with PMA energy as much as that of CoFeB/MgO [1]. Figure 2 shows magnetization curves of W/Fe(0.9nm)/MgO/Tb, from which the PMA energy density (K_{eff}) is evaluated to be 0.22 MJ/m^3. Figure 3 shows Fe layer thickness dependence of K_{eff}. The saturation magnetization in our samles is much lower than that in Fe/MgO interfaces fabricated by an MBE technique [3]. A 0.63 nm thick Fe dead-layer was found to be

Yuki Iida
E-mail: IIDA.Yuki@nims.go.jp

formed, which can cause the low value of saturation magnetization.

The role of W buffer and Tb cap layers were considered from a structural point of view. When a 3 nm W layer is deposited on the Si/SiO_2 substrate at room temperature, it forms an amorphous structure [5]. Therefore, Fe is also grown as an amorphous structure, even though the Fe layer does not contain boron. When it is annealed, Fe layer can be crystallized from the interface with MgO. When Tb is not inserted, the easy magnetization axis aligns along the in-plane direction, and the saturation magnetization decreases. The Analysis of XMCD deduces the anisotropic orbital magnetic moments in Fe, while no XMCD signals are observed in Tb, suggesting that Tb does not directly contribute to the PMA in Fe/MgO interface. Therefore, the role of Tb layer can be regarded as absorbing the excess oxygen in Fe/MgO interfaces.

This study was partly supported by JSPS KAKENHI Grant Nos. 16H06332 and 15H03562.

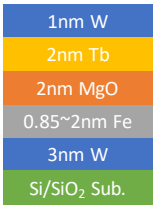

Fig. 1. Schematic of sample structures of W(3nm)/Fe(0.85-2nm)/MgO(2

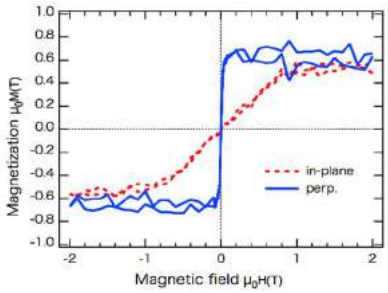

Fig. 2. Magnetization curves of a W/Fe(0.9nm) /MgO/Tb layered structure in the in-plane and perpendicular-to-plane directions

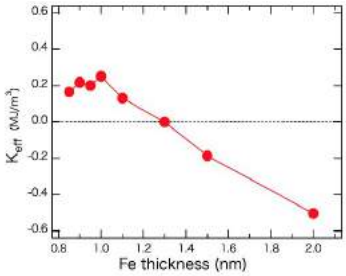

Fig. 3. Fe layer thickness dependence of PMA energy density K_{eff}.

REFERENCES

1) S. Ikeda, K. Miura, H. Yamamoto, K. Mizunuma, H. D. Gan, M. Endo, S. Kanai, J. Hayakawa, F. Matsukura, and H. Ohno, Nature Mater. **9**, 721 (2010).
2) H. X. Yang, M. Chshiev, B. Dieny, J. H. Lee, A. Manchon, and K. H. Shin, Phys. Rev. B **84**, 054401 (2011).
3) J. W. Koo, S. Mitani, T. T. Sasaki, H. Sukegawa, Z. C. Wen, T. Ohkubo, T.Niizeki, K. Inomata, and K. Hono, Appl. Phys. Lett. **103**, 192401 (2013).
4) J. Okabayashi, J. W. Koo, H. Sukegawa, S. Mitani, Y. Takagi, and T. Yokoyama, Appl. Phys. Lett. **105**, 122408 (2014).
5) Jun Liu, Tadakatsu Ohkubo, Seiji Mitani, Kazuhiro Hono, and Masamitsu Hayashi, Appl. Phys. Lett. **107**, 232408 (2015).

MICROWAVE-ASSISTED MAGNETIZATION SWITCHING FOR A 2-μm Co/Pt DOT

R. HIRAMATSU[1], H. KUBOTA, S. TSUNEGI, S. TAMARU, A. SUGIHARA, K. YAKUSHIJI, A. FUKUSHIMA, and S. YUASA

1) AIST, Tsukuba, Ibaraki, r-hiramatsu@aist.go.jp

I. INTRODUCTION

Microwave-assisted magnetization switching (MAS), which greatly reduces the switching field of recording bits with the help of an rf magnetic field h_{rf}, is promising technique to increase recording density in a hard-disk drive. So far, studies based on the simulation have revealed that a circularly-polarized h_{rf} had an advantage over a linearly-polarized h_{rf} in terms of MAS efficiency [1,2]. In experiments, Suto et al. recently reported MAS for a circularly-polarized h_{rf} [3]. For the actual device application the comparison of MAS for a linearly- and circularly-polarized h_{rf} is imperative, but it is not well evaluated. We aimed to evaluate MAS efficiency for both linearly- and circularly-polarized h_{rf}. In this study, we fabricated Co/Pt dot samples with perpendicular magnetic anisotropy and studied MAS properties through the anomalous Hall effect.

II. EXPERIMENTS

A stacking structure of the sample is as follows; sub./Ta 3.0/Ru 6.0/Pt 2.0/$[$Co 0.24/Pt 0.16$]_3$/Co 1.7/$[$Pt 0.16/Co 0.24$]_3$/Pt 0.3/Ru 2.0 (thickness are in nm). The effective magnetic anisotropy field of the film was tuned by inserting a thin Co film in-between the Co/Pt multilayer part to be 4.0 kOe. The Co/Pt single dot with 2-μm in diameter was fabricated by using electron beam lithography and Ar-ion etching. The Ta/Ru underlayer was fabricated to form a Hall cross bar. After covering SiO_2, Ti 5 nm/Au 200 nm was deposited to make an rf line. Figure 1 shows an optical microscope image of the sample with the measurement circuit. Magnetization direction of the dot is detected by a Hall voltage through the anomalous Hall effect [4].

III. RESULT AND DISCUSSION

Typical experimental result is shown in Fig. 2. For this sample, as a first step, linearly-polarized h_{rf} was applied with the rf power of 8 dBm, which corresponds h_{rf} of 25 Oe (estimated from the electromagnet calculation). After magnetization direction of the dot was set to the negative direction, the magnetic field was swept toward the positive direction. When the rf frequency (f_{rf}) was set to be between 3 GHz and 7 GHz, the switching field (H_{sw}) was reduced with the minimum to be 440 Oe at 6 GHz, while there was no change in H_{sw} for f_{rf} <3 GHz and f_{rf} >6 GHz. H_{sw} as a function of f_{rf} are plotted in Fig. 3. It shows that the H_{sw} monotonically reduces with increasing f_{rf} up to a critical frequency (6 GHz). Then, H_{sw} vs. f_{rf} was investigated under various rf power (Fig. 3). The result indicates that H_{sw} is lowered when the high rf power is applied, which would be beneficial to the effective switching. However, this behavior is quite different from a previous report [5]. Although the reason of the discrepancy has been unclear, our result can be explained by the domain-wall motion which occurs at relatively low field because the dot size is enough large to induce it.

REFERENCES

1) J. G. Zhu, and Y. Wang, "Microwave Assisted Magnetic Recording Utilizing Perpendicular Spin Torque Oscillator With Switchable Perpendicular Electrodes", *IEEE Trans. Magn.,* 46(3) 751-757, (2010).
2) S. Okamoto, M. Igarashi, N. Kikuchi, and O. Kitakami, “Microwave assisted switching mechanism and its stable switching limit”, *J. Appl. Phys.* 107 123914, (2010).
3) H. Suto, T. Kanao, T. Nagasawa, K. Kudo, K. Mizushima, and R. Sato, “Magnetization Switching of a Perpendicular Magnetic Nanodot in a Rotating Microwave Magnetic Field”, *The 64th JSAP Spring Meeting* 14p-P10-1-98 (2017).
4) S. Okamoto, N. Kikuchi, J. Li, O. Kitakami, T. Shimatsu, and H. Aoi, “Frequency and Time Dependent

RYO HIRAMATSU
E-mail: r-hiramatsu@aist.go.jp
tel: +03-29-861-2075

Microwave Assisted Switching Behaviors of Co/Pt Nanodots", *Appl. Phys. Express* 5 043001, (0212).
5) S. Okamoto, N. Kikuchi, M. Furuta, O. Kitakami, and T. Shimatsu, "Switching Behaviors its Dynamics of a Co/Pt Nanodot Under the Assistance of rf Fields", *Phys. Rev. Lett.* 109 237209, (2012).

ACKNOWLEDGEMENT

The present work is supported by the Japan Science and Technology Agency strategic innovation promotion program "Development of new technologies for 3d magnetic recording architecture."

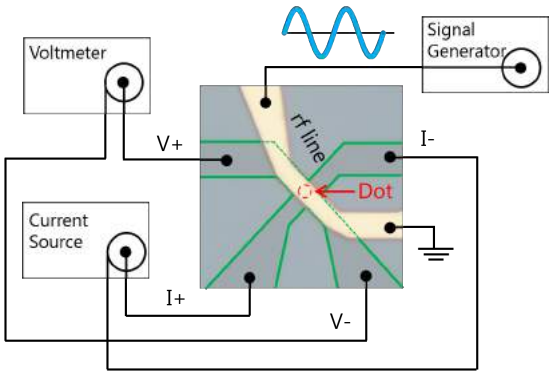

Figure 1 Optical microscope image and the measurement circuit.

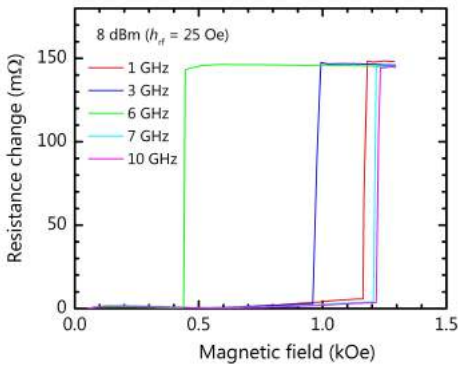

Figure 2 Example of the MAS experiment. RF power of 8 dBm (h_{rf} = 25 Oe) is injected in the rf line. Hall resistance is calculated by dividing the Hall voltage by injected current. The vertical axis shows Hall resistance change from Hall resistance at 0 Oe.

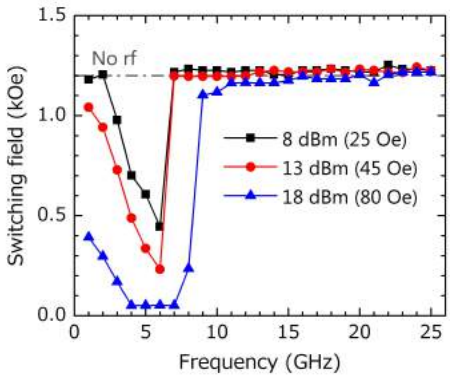

Figure 3 Switching field as a function of rf frequency under various rf power.

MULTI-BIT STT-MEMORY CELL WITH DOUBLE MAGNETIC FREE LAYER

Akio FUKUSHIMA, Tomohiro TANIGUCHI, Kay YAKUSHIJI, Hitoshi KUBOTA and Shinji YUASA

National Institute of Advance Industrial Science and Technology, Spintronics Research Center, Tsukuba, Ibaraki 305-8568, Japan

I. INTRODUCTION

Increase of the capacity of data storage is one of the curial demands. For that demand, we proposed the multi-bit memory cell using the freedom of magnetic configurations in a synthetic antiferromagnetic (SAF) layer [1]. Four different states can be stored in one magnetic tunnel junction (MTJ) using combination of the magnetization direction of the magnetic free layer and the head-to-head or the tail-to-tail configuration in the SAF layer. In the previous study [1], we demonstrated that four different states can be realized using a perpendicularly magnetized MTJ (p-MTJ) by an external magnetic field. However, the bit operation for data writing and reading by the external magnetic field is not practical. The bit operation by an electric current is much desirable for memory applications.

For that issue, we developed the multi-bit STT memory (MBSM) cell; the p-MTJ with double magnetic free layer, in which the second magnetic free layer is inserted between the MgO barrier and the SAF layer. Because the current control of magnetic configuration in the strong SAF layer [2] is impossible, we put in the second magnetic free layer with almost decoupled from the SAF layer by the non-magnetic metallic layer.

II. EXPERIMENTS

Figure 1 shows the schematic structure of the MBSM cell. The film structure is (from bottom to top) SiO_2 sub./ Buffer layer/ CoPt-Ru-CoPt (SAF reference layer)/ CoB-W (intermediate layer)/ CoFeB (the second magnetic free layer)/ MgO-barrier/ FeB (the first magnetic free layer)/ MgO-capping layer/ Capping layer. The second magnetic free layer and the SAF reference layer were almost decoupled by the non-magnetic CoW-B metallic layer. By means of an e-beam based microfabrication, the film was formed into around 60 nm diameter MTJ. The MTJs show MR ratio of about 110% and the resistance area product (RA) of 3.1 $\Omega \cdot \mu m^2$. Because of the low RA values, this multi-bit STT memory cell can be switched at lower switching voltage of less than 200 mV.

III. RESULTS AND DISCUSSIONS

Figures 2 shows a typical voltage-current (VI) and voltage-resistance (RV) curve of the MBSM cell at zero magnetic field. The MBSM cell indicates a unique feature that the resistance changes two times sequentially in the both current direction. The definition of positive current direction is that electrons flow from the SAF layer to the free layers. In the voltage sweep from 200 mV to −200 mV, the cell is initialized to the low resistance state at 200 mV, then the first switching from the low to the high occurs at −100 mV, the second switching from the high to the low at −120 mV. For the opposite sweep from −200 mV to 200 mV, the cell is initialized at the low resistance state at −200mV, then the two switching events occur two times sequentially at 90 mV and 140 mV in a similar way.

When the positive current flows through the MBSM cell with the initialized magnetization direction of the first and the second layer denoting (down, down), firstly the second free layer switches [to (down, up)], then the first free layer switches [to (up, up)]. On the contrary, when the negative current flows through the cell with the initialized magnetization direction of (up, up), firstly the first layer may switch [to (down, up)], and the second layer switches [to (down, down)].

Akio FUKUSHIMA
E-mail: akio.fukushima@aist.go.jp
tel: +81-29-861-5572

Still there remains the question whether the (up, down) configuration could be realized by STT switching, this multi-bit memory cell has three different states controllable by the current which can be worth for high density memory cell.

REFERENCES

1) A. Fukushima, K. Yakushiji, M. Konoto, H. Kubota, H. Imamura, S. Yuasa, "Multi-bits memory cell using degenerated magnetic states in a synthetic antiferromagnetic reference layer," *J. Mag. Mag. Mater.* **400**, 370 (2016).
2) K. Yakushiji, H. Kubota, A. Fukushima, and S. Yuasa, "Perpendicular Magnetic Tunnel Junctions with a Strong Antiferromagnetic Interlayer Exchange Coupling at First Oscillation Peak," *Appl. Phys. Express* **8**, 083003 (2015).

ACKNOWLEDGEMENT

This work was supported by the ImPACT Program of the Council for Science, Technology, and Innovation.

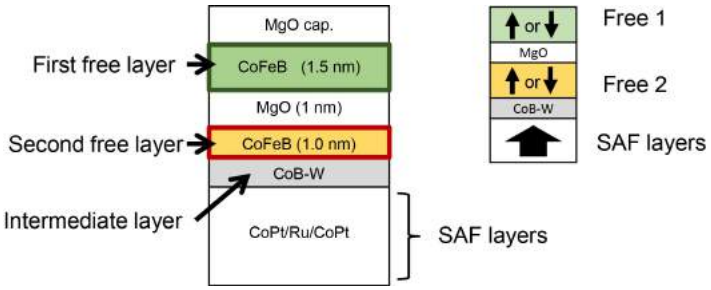

Fig. 1 Schematic structure of the multi-bit STT memory cell; the p-MTJ with double magnetic free layer.

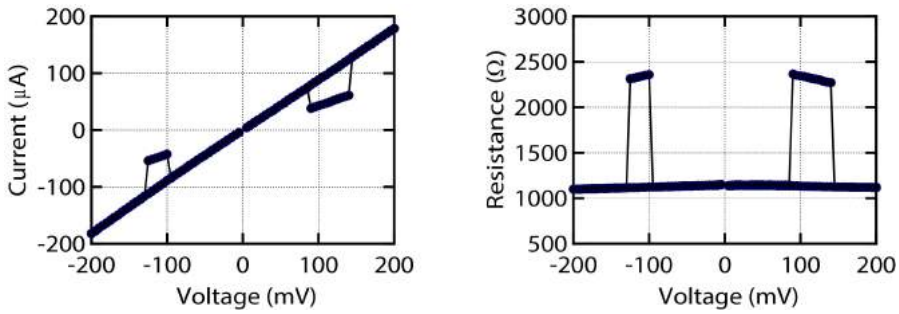

Fig. 2 VI curve (left) and VR curve (right) at zero magnetic field of the multi-bit STT memory cell.

A 6.75F^2/BIT VOLTAGE-CONTROL SPINTRONICS MEMORY ARRAY BY TWO MEMORY LAYERS STACKING AND BURIED-WORDLINE CELL TRANSISTORS

Satoshi TAKAYA, Kazutaka IKEGAMI, Shinobu FUJITA, Naoharu SHIMOMURA, and Hiroaki YODA

Corporate R&D Center, Toshiba Corporation, Kawasaki, Japan

satoshi1.takaya@toshiba.co.jp

I. INTRODUCTION

Voltage-Control Spintronics Memory (VoCSM) [1] is proposed as high density and low power nonvolatile memory to replace Dynamic Random Access Memory (DRAM). However, VoCSM cell contains 8 magnetic tunnel junctions (MTJs) and 9 access transistors in 1 string unit which stores 8 bits (Fig. 1). To reduce cell area, we should improve layout of cell unit. In high density 6 F^2/bit DRAM cell layout, the buried word lines and the slanted angle of active area patterns are mostly used [2]. When we adapt these high density DRAM cell techniques to the cell layout, high density VoCSM can be realized.

II. VOLTAGE-CONTROL SPINTRONICS MEMORY

The VoCSM string contains 8 MTJs and 9 access transistors. Each source node of the access transistors is connected to bitlines (BLs), and gate node of the access transistors is connected to wordline (WL). The SO layer is the bottom electrode of MTJs and connected to the selection transistor and source line (SL). To realize high density VoCSM, we should layout these elements in the small area.

III. HIGH DENSITY CELL LAYOUT

The 6 F^2 DRAM layout that contains 1 access transistor and via to storage node. The layout can be realized by using the buried word lines and the slanted angle of active area patterns. When we connect the vias to the storage node to the top electrodes of the MTJ, high density cell layout can be realized. However, there is no space to layout MTJ string and connection vias to top electrode of MTJ in same layer, we share the space to next column and stack 2 memory layers (Fig. 2). The first layer contains the access transistors of 2 strings of the VoCSM cell. The second layer contains the vias to both of the VoCSM strings and one of the VoCSM string. The third layer is the connection space to SL. The fourth layer contains the other VoCSM string. Then the 8-bit VoCSM string can be layouted above 9 access transistors which total area is 54 F^2, and the cell area is 6.75 F^2/bit.

IV. CONCLUSIONS

The 6.75 F^2/bit class VoCSM cell layout is proposed. We adapt the high density memory cell techniques and 2 memory layers stacking to the layout.

ACKNOWLEDGEMENTS

The authors would like to thank K. Abe for her technical contributions. This work was funded by ImPACT Program of Council for Science, Technology and Innovation (Cabinet Office, Government of Japan).

Satoshi Takaya
E-mail: satoshi1.takaya@toshiba.co.jp
tel: +81-44-549-2212

REFERENCES

1) H. Yoda, N. Shimomura, Y. Ohsawa, S. Shirotori, Y. Kato, T. Inokuchi, Y. Kamiguchi, B. Altansargai, Y. Saito, K. Koi, H. Sugiyama, S. Oikawa, M. Shimizu, M. Ishikawa, K. Ikegami, and A. Kurobe, " Voltage-Control Spintronics Memory (VoCSM) Having Potentials of Ultra-Low Energy-Consumption and High-Density," 2016 IEEE International Electron Devices Meeting (IEDM), pp. 27.6.1-27.6.4, 2016.

2) T. Schloesser, F. Jakubowski, J. v. Kluge, A. Graham, S. Slesazeck, M. Popp, P. Baars, K. Muemmler, P. Moll, K. Wilson, A. Buerke, D. Koehler, J. Radecker, E. Erben, U. Zimmermann, T. Vorrath, B. Fischer, G. Aichmayr, R. Agaiby, W. Pamler, T. Schuster, W. Bergner, and W. Mueller, "6F^2 Buried Wordline DRAM Cell for 40nm and Beyond," 2008 IEEE International Electron Devices Meeting (IEDM), pp. 809-812, 2008.

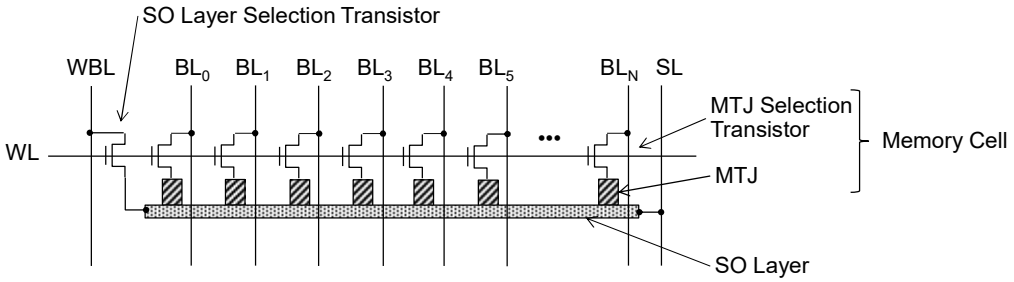

Fig. 1 A schematic drawing of the VoCSM.

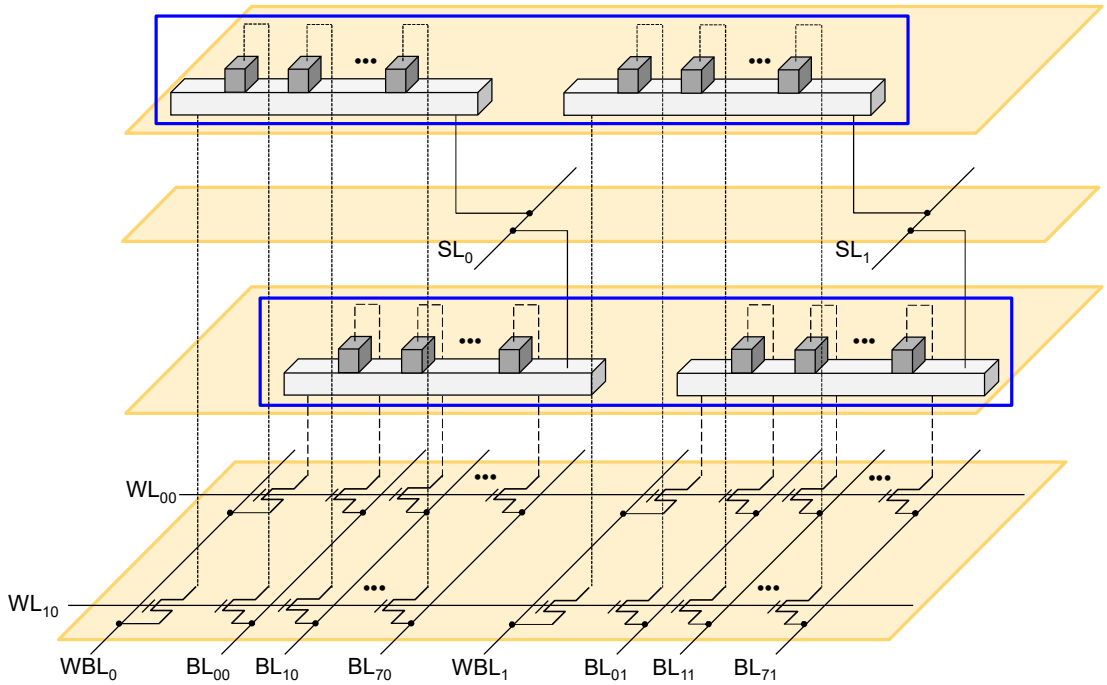

Fig. 2 Connection of access transistors and VoCSM cells.

SIGNIFICANT INFLUENCE OF DC CURRENT ON SPIN TORQUE FERROMAGNETIC RESONANCE

S. HIRAYAMA [1, 2], S. KASAI [2] and S. MITANI [1, 2]

1) Graduate School of Pure and Applied Sciences, University of Tsukuba, Tsukuba 305-8577, Japan

2) National Institute for Materials Science, Tsukuba 305-0047, Japan,

hirayama.shigeyuki@nims.go.jp, kasai.shinya@nims.go.jp, mitani.seiji@nims.go.jp

I. Introduction

Spin Hall effect is a key phenomenon to manipulate magnetization via spin angular momentum transfer from a heavy metal into an adjacent ferromagnetic metal. The efficiency of spin current generation from electric current flowing in a heavy metal, so called spin Hall angle, has been demonstrated for several heavy metals such as Pt, Ta, W [1, 2]. In spin torque ferromagnetic resonance (ST-FMR) excited by the spin Hall effect in such a ferromagnetic metal/heavy metal bilayers, a voltage output can be obtained as follows:

$$V = {k}/{\Delta}[SF_S(H_{res}) + AF_A(H_{res})], \quad (1)$$

where k, Δ, S, A, F_S, F_A and H_{res} are the coefficient related to resistance, the half width at half maximum of the resonant peak, the coefficient of symmetric part of voltage signal, the coefficient of asymmetric part of voltage signal and the Lorentzian and anti-Lorentzian functions of the resonant field H_{res}, respectively. If the damping torque can be compensated with the spin torque due to spin Hall effect, it is possible to develop a microwave oscillation. So far, many studies have been performed to fully understand the spin dynamics in ST-FMR [3, 4]. However, there are still many issues under debate, being related with underlying physics. In this study, we found unexpected behavior of the Lorentzian part of ST-FMR caused by adding a dc current to the excitation rf current.

II. Experimental

We prepared a NiFe (5 nm)/Pt (8 nm) bilayer on a sapphire substrate by using rf-sputtering and fabricated it into rectangular devices of 6 μm in length and 1 μm in width. ST-FMR measurements were performed with the combination of a signal generator and a lock-in amplifier. The frequency was fixed at 12 GHz, and an external magnetic field was applied (swept from 0 to 2.8 kOe). Dc currents up to 4.15×10^{11} A/m^2 were applied in Pt, in addition to the rf current through a bias-tee.

III. Results and discussion

Fig. 1(a) shows dc current dependence of the output voltage of ST-FMR at $\theta = 10^{\circ}$, which can be separated into symmetric and asymmetric Lorentzian components, as shown in Figs. 1(b) and 1(c), respectively. Here, θ corresponds to the angle between the applied magnetic field and the current direction. The shape of resonant signal significantly changes as the magnitude of dc current increase, which would be an unexpected behavior in the current understanding of ST-FMR. In Figs. 1(b) and 1(c), it turns out that it is due to the contribution of the symmetric part of the signal, which corresponds to the effect of the spin Hall spin transfer toque in Pt. As dc current is varied from $+4.15\times10^{11}$ A/m^2 to -4.15×10^{11} A/m^2, the symmetric part of ST-FMR in Fig.1(b) shows a decrease of the signal amplitude at the resonant field and then a sign change occurs. This in contrast to the behavior that the asymmetric part does not show any significant dependence to dc current, as shown in Fig. 1(c). Interestingly, these dependences can cause the change in the evaluated spin Hall angle η of Pt, as shown in Fig. 2, although spin Hall angle that is a physical quantity specific to the material should be constant.

Figs. 3(a) and (b) show *kS and kA* of the symmetric and asymmetric parts, respectively, as a function of *θ,* □□□□□□□□□□□□□. We firstly checked the dc current dependence of *kS* and *kA* at each angle (not shown here) and these data were fitted with $kS = k_0 + k_1 I_{dc} + k_2 I^2_{dc}$ and $kA = k_0 + k_1 I_{dc} + k_2 I^2_{dc}$, respectively.

S. Hirayama
E-mail: hirayama.shigeyuki@nims.go.jp
tel: +81-29-859-2137

k_0 and k_2 of both of kS and kA can be fitted by $\sin 2\theta \cos\theta$, which can be attributed to the anisotropy magnetoresistance (AMR) because the voltage signals appear based on the AMR of the device. On the other hand, k_1, especially of kS, can be fitted by $\sin 2\theta$, which can not be explained by the conventional understanding of ST-FMR. This unconventional behavior of k_1 may make us take it into account that out-of-plane magnetization dynamics occurs via unknown torques beyond the model described in Eq. (1). Another possibility is that the observation can simply be explained by the inverse spin Hall effect.

REFERENCES

1) L. Liu *et al*., Phys. Rev. Lett. **106**, 036601 (2011).
2) L. Liu *et al*., Science **336**. 555-558 (2102).
3) W. Zhang *et al*., Nature Physics **11**, 496-502 (2015).
4) K. Kondou *et al*., Appl. Phys. Express **9**, 023002 (2016).

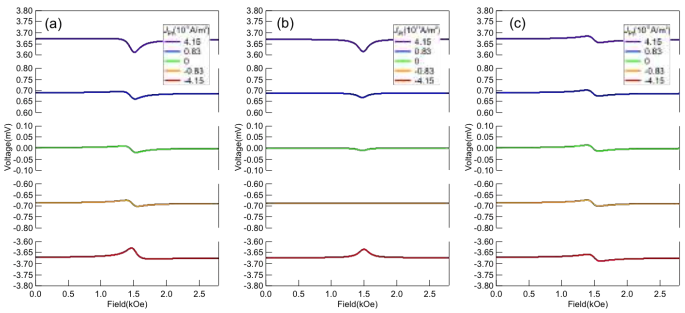

Fig. 1. ST-FMR spectra of a NiFe (5 nm)/Pt (8 nm) bilayer at θ = 10˚; (a) fitted curves, (b) symmetric component and (c) asymmetric component.

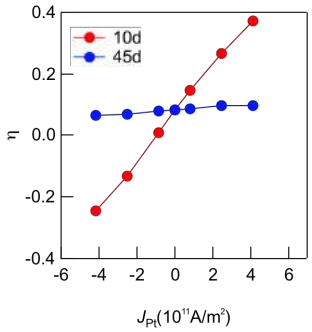

Fig. 2. Spin Hall angles evaluated for Pt at θ = 10˚ and 45˚.

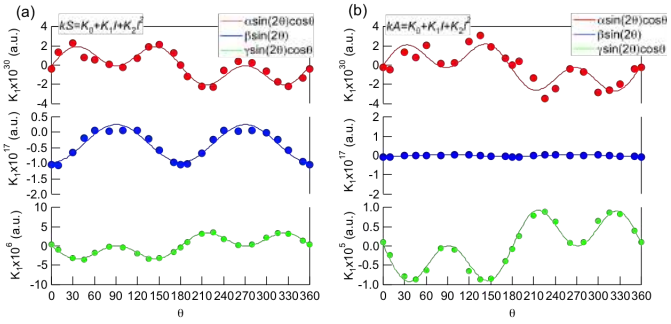

Fig. 3. (a) kS and (b) kA as a function of θ.

MAGNETIZATION SWITCHING OF A DOT COMPOSED OF DOUBLE AFC LAYERS UNDER THE ASSISTANCE OF RF FIELDS

Yuming LU[1], Satoshi OKAMOTO[1,2], Nobuaki KIKUCHI[1,2], Osamu KITAKAMI[1,2], and Takehito SHIMATSU[2,3,4]

1) IMRAM Tohoku University, Sendai, Japan, ymlu@swu.edu.cn, okamoto@tagen.tohoku.ac.jp

2) CSRN, Tohoku University, Japan, 3) FRIS, Tohoku University, Japan

4) RIEC, Tohoku University, Japan

I. INTRODUCTION

Microwave-assisted magnetization recording (MAMR) has been expected as one of the next generation ultra-high density magnetic recording technologies [1]. By introducing MAMR technology, rf frequency becomes a writing parameter as well as a magnetic field. This allows us to realize multilevel recording by using a layered recording media with different resonance frequency. By tuning the frequency and magnetic field, the magnetization of each layer can be selectively switched. Very recently, this selective magnetization switching using a dot of two magnetic layers has been successfully demonstrated [2]. In terms of practical use, interlayer and/or interdot dipolar interactions have to be suppressed as small as possible because the dipolar interaction modifies the resonance frequency of each layer depending on the surrounding magnetization state. As a solution for this problem, antiferromagnetically coupled recording media has been expected [3-5]. In this study, we have studied the microwave-assisted switching behavior of a dot composed of double AFC layers.

II. EXPERIMENTALS

The dot of double AFC layers with the diameter of 400 nm is fabricated from a film of MgO sub./Ta(1)/Pt(25)/AFC^1/Pt (10)/AFC^2/Pt(10) by using electron beam lithography and Ar ion etching. The numbers in brackets are the layer thickness in nanometers. The AFC layer is composed of hard and soft Co/Pt multilayers (MLs) coupled with a thin Ru interlayer. By turning the Co layer thickness, the hard Co/Pt ML of AFC^1 exhibits somewhat larger switching field than that of AFC^2. The Pt underlayer is patterned into a cross shaped electrode for anomalous Hall effect (AHE) measurements. An Au stripline is fabricated just above the dot after covering the dot with an insulating layer. A microwave signal from a signal generator is fed into the Au stripline, and then the linearly polarized rf field of 470 Oe is generated.

III. RESULTS AND DISCUSSION

Fig. 1 shows the AHE curve of the dot in the absence of rf field. Starting from the negative saturation, the magnetization directions of soft-Co/Pt MLs in AFC^1 and AFC^2 gradually change in the field range from −4 to −2 kOe, and then antiferromagnetic magnetization states in AFC layers are obtained. With increasing the magnetic field furthermore, clear steps can be observed at around 4 kOe and 5.5 kOe. These steps correspond to the switching fields H_{sw1} and H_{sw2} of the hard-Co/Pt MLs in AFC^1 and AFC^2, respectively. Here, the step heights of these switching are quite different, and the remanence AHE signal is not zero, due to the electrical shunt effect. Under the assistance of rf fields, the values of H_{sw1} and H_{sw2} significantly decrease as shown in Fig. 2. Fig. 2 is the contour plot of the AHE signal as functions of magnetic field and rf frequency f_{rf}. The values of H_{sw1} and H_{sw2} linearly decrease with increasing the rf frequency f_{rf} until the certain critical frequencies over which the microwave-assistance effect disappears. These behaviors are identical to that observed in a single layer dot [1]. The critical frequencies for AFC^1 and AFC^2 are about 14 and 12 GHz, respectively. Except for the frequency range of 12 ~ 14 GHz, H_{sw2} is always smaller than H_{sw1}, indicating that the switching sequence of AFC^1 and AFC^2 does not change. On the other hand, for the

Yuming Lu and Satoshi Okamoto
E-mail: okamoto@tagen.tohoku.ac.jp
tel: +81-22-2175359

frequency range of 12 ~ 14 GHz, H_{sw1} and H_{sw2} become the same. The representative AHE curves correspond to the vertical dotted lines in Fig. 2 are also shown. Obviously, the AHE curve for the frequency range of 12 ~ 14 GHz exhibits a single step. Thus, we have not succeeded to change the switching sequence of AFC[1] and AFC[2] using this film structure of double AFC layers. We will further explore to realize the selective switching using a double AFC dot.

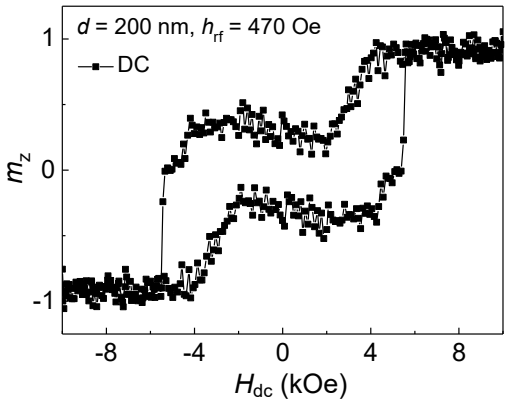

Fig. 1 AHE curve of dot composed of double AFC layers.

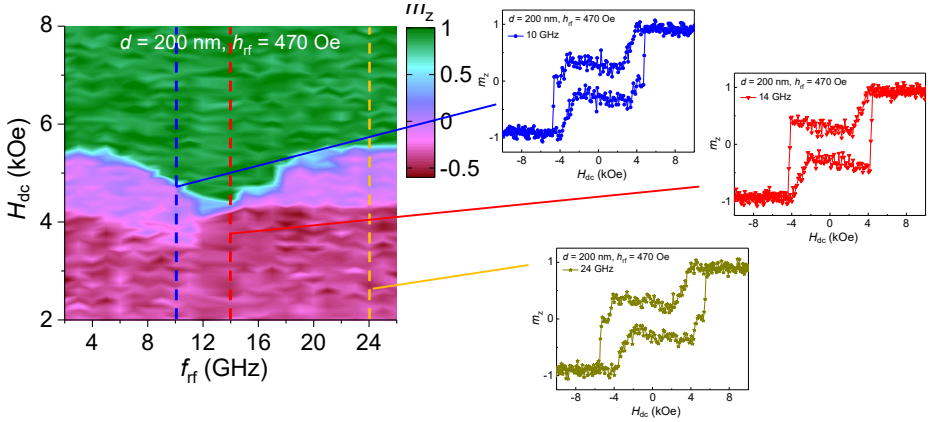

Fig. 2 Contour plot of AHE signal as functions of magnetic field H_{dc} and rf frequency f_{rf}. Representative AHE curves corresponding to the vertical dotted lines are also presented.

REFERENCES

[1] S. Okamoto et al., J. Phys. D **48**, 353001 (2015).
[2] H. Suto et al., Phys. Rev. Appl. **5**, 014003 (2016).
[3] Y. Nakayama et al., IEEE Trans. Magn. **52**, 3201203 (2016).
[4] T. Yang et al., J. Appl. Phys. **114**, 213901 (2013).
[5] H. Suto et al., Nanotechnology **25**, 24550 (2014).

EXPERIMENTAL STUDY ON MICROWAVE-ASSISTED MAGNETIZATION SWITCHING: EFFECT OF MICROWAVE-FIELD POLARIZATION AND SUBNANOSECOND SWITCHING

H. Suto, T. Kanao, T. Nagasawa, K. Mizushima, and R. Sato
Corporate Research & Development Center, Toshiba Corporation, Kawasaki, Japan.
hirofumi.suto@toshiba.co.jp

I. BACKGROUND

Applying a microwave magnetic field to a magnet induces ferromagnetic resonance (FMR) excitation, which can decrease the switching field [1-4]. This switching scheme is called microwave-assisted magnetization switching (MAS) and attracts attention as a writing method in next-generation magnetic recordings such as microwave-assisted magnetic recording (MAMR) and three-dimensional (3D) magnetic recording. In MAMR, a microwave field induces excitation of media magnetization, which enables writing to a high-anisotropy media material required for high-density recording [2,3]. In 3D recording, multiple recording layers are stacked to increase the recording density. By designing each recording layer to have a different FMR frequency and by controlling the microwave-field frequency, magnetization excitation can be induced selectively in a target recording layer, which enables layer-selective writing by MAS [3,4]. When designing recording devices that utilize MAS, we must consider the frequency of the microwave field because FMR is a resonance phenomenon, and previous experimental studies have revealed the dependence of MAS on the microwave-field frequency [3]. In addition to the frequency, the polarization of the microwave field, e.g. linear polarization (LP) where the field direction alternates in one direction and circular polarization (CP) where it rotates, must be considered. This is because FMR is a precessional motion of the magnetization and is most efficiently induced by a CP microwave field that rotates in the same rotation direction as the magnetization precession. However, it has not yet been experimentally studied how the polarization affects MAS behavior. Other than these microwave-field properties, the timescale of MAS is practically crucial because it determines the writing rate. During MAS, magnetization excitation gradually grows until it reaches the amplitude required for switching; therefore a microwave field must be applied for a certain period of time. However, this timescale of MAS has not yet been studied, either. In this study, we report MAS of a nanomagnet with perpendicular magnetic anisotropy focusing on the microwave-field polarization and the timescale of MAS.

II. EXPERIMENTAL

Figure 1 shows the sample structure and the measurement setup. Switching of a perpendicularly magnetized nanomagnet with a 50 nm diameter is studied by applying a z-direction dc magnetic field and a microwave field. The microwave field is generated by introducing microwave signals to two CPWs that cross at a right angle above the nanomagnet. The microwave-field polarization is controlled by the phase delay between the two signals. When no microwave field is applied, the switching z-direction magnetic field (H_{sw}) of the nanomagnet is 7.1 kOe.

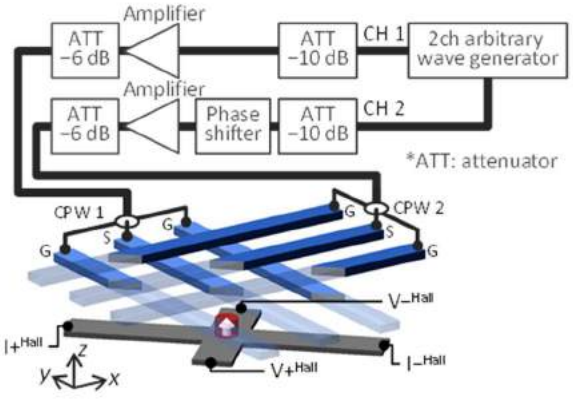

FIG. 1. Sample structure and experimental setup.

III. RESULTS AND DISCUSSION

Figure 2 (a) shows the dependence of the switching field on the delay phase between the microwave signals introduced to the two CPWs. When the delay phase is around 90°, the CPWs generate a circularly

Hirofumi SUTO

hirofumi.suto@toshiba.co.jp

polarized microwave field rotating clockwise in the *x*-*y* plane. This microwave field reduces the switching field only when the nanomagnet reverses from the down to up direction because the rotation directions of the microwave field and the magnetization precession coincide. At around 270°, the microwave field changes the rotation direction and MAS occurs only when the nanomagnet reverses in the opposite way.

Next, we fix the phase delay to 90° to examine MAS in a CP microwave field. Figure 2(b) shows the dependence of the switching field on the microwave-field frequency. H_{sw} decreases almost linearly with increasing the frequency and suddenly increases after the minimum, which is typical of MAS. In comparison with MAS in an LP microwave field, a CP microwave field induces the same MAS effect with half the microwave-field amplitude (data not shown). This result is consistent with the fact that an LP microwave field is the sum of two CP microwave fields that respectively rotate clockwise and counterclockwise and have half the field amplitude.

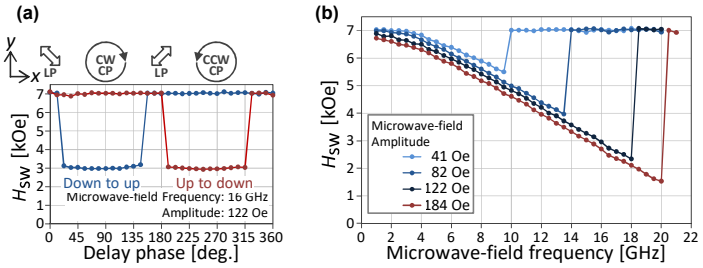

FIG. 2. (a) H_{sw} versus delay phase of the signal in CPW 1 with respect to that in CPW 2. Schematics above the plot depict the polarization of the generated microwave field. (b) H_{sw} versus microwave-field frequency in CP microwave fields.

Figure 3 shows the dependence of H_{sw} on the microwave-field duration. For 10 GHz to 18 GHz, H_{sw} is almost the same when the duration is equal to or larger than 0.5 ns showing that the FMR excitation saturates within this time scale. When the duration is smaller than 0.5 ns, H_{sw} increases gradually because the FMR excitation is still developing on this time scale. However, a large MAS effect still occurs for this short microwave field. When the duration is 0.1 ns (0.2 ns for 16 GHz), H_{sw} increases steeply and almost no MAS effect appears. For 20 GHz, which corresponds to the minimum H_{sw}, it takes 0.5 ns for the FMR excitation to become sufficient for MAS, which is slightly longer than other frequencies.

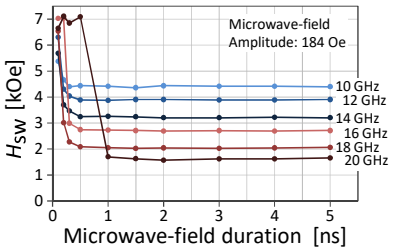

FIG. 3. H_{sw} versus microwave-field duration in CP microwave fields.

It was shown that MAS occurs when the rotation direction of the CP microwave field matches with that of the FMR precession of the nanomagnet. This result indicates that the microwave field polarization must be considered when MAS-based recording devices are designed. A large MAS effect from 7.1 kOe to 1.5 kOe was demonstrated showing that MAS is an effective method to write to a high-anisotropy media material. MAS was induced by a microwave field with a duration of 0.3 ns showing that a high writing rate can be achieved.

REFERENCES

[1] C. Thirion, W. Wernsdorfer, and D. Mailly, Nature Mater. **2**, 524 (2003).

[2] J.-G. Zhu, X. Zhu, and Y. Tang, IEEE Trans. Magn. **44**, 125 (2008).

[3] S. Okamoto, N. Kikuchi, M. Furuta, O. Kitakami, and T. Shimatsu, J. Phys. D: Appl. Phys. **48**, 353001 (2015).

[4] H. Suto, T. Nagasawa, K. Kudo, T. Kanao, K. Mizushima, and R. Sato, Phys. Rev. Appl. **5**, 014003 (2016).

This work is supported by Strategic Promotion of Innovative Research and Development from Japan Science and Technology Agency, JST.

EFFICIENCY OF SPIN TRANSFER TORQUE SWITCHING IN A PERPENDICULARLY MAGNETIZED FREE LAYER WITH THE FIRST- AND SECOND-ORDER UNIAXIAL MAGNETIC ANISOTROPIES

R. MATSUMOTO[1], H. ARAI[2], S. YUASA[3] and H. IMAMURA[4]

1) AIST, Spintronics Research Center, Tsukuba, Japan, rie-matsumoto@aist.go.jp

2) AIST, Spintronics Research Center, Tsukuba, Japan and PRESTO, JST, Kawaguchi, Japan, arai-h@aist.go.jp

3) AIST, Spintronics Research Center, Tsukuba, Japan, yuasa-s@aist.go.jp

4) AIST, Spintronics Research Center, Tsukuba, Japan, h-imamura@aist.go.jp

I. INTRODUCTION

Second-order perpendicular magnetic anisotropy (K_{u2}) has been attracting a great deal of attention because faster spin-transfer-torque (STT) switching with higher STT-switching efficiency (κ) is theoretically expected [2] in the case of a conically magnetized free layer (c-FL) [3] compared with the case of a conventional perpendicularly magnetized free layer (p-FL) without K_{u2}. Here, κ is defined as $\kappa \equiv \Delta_0/I_{sw}$ where Δ_0 is the thermal stability factor and I_{sw} is switching current. In c-FL, the angle (θ) of a magnetization ($\boldsymbol{m}$) is tilted from z-direction (see Fig. 1(a)) due to the energetic competition between the first- and second-order magnetic anisotropies ($K_{u1,eff}$ and K_{u2}). κ of c-FL ($\kappa^{(c)}$) can be about 1.3 times larger than that of the conventional p-FL ($\kappa^{(p0)}$). In this study [4], we theoretically expect the further enhancement of κ in p-FL with finite K_{u2}.

II. MODEL

The system we consider is illustrated in Fig. 1(a). The magnetic energy density (g_L) and the effective potential (Φ) of the free layer is given by

$$g_L = K_{u1,eff} \sin^2 \theta + K_{u2} \sin^4 \theta, \quad (1)$$

$$\Phi = g_L + M_s (a_J/\alpha) \cos \theta. \quad (2)$$

Here, $K_{u1,eff}$ and K_{u2} are the first- and second-order magnetic anisotropy constants. In $K_{u1,eff}$, demagnetization energy is subtracted. M_s and α are the saturation magnetization and the Gilbert damping constant of the free layer. (a_J/α) represents the effective field by STT and a_J is defined as $a_J = hIP/(4\pi eM_sV)$. h is the Planck constant, P is the spin polarization, I is the applied current, e (> 0) is the elementary charge, and V is the volume of the free layer.

The equilibrium direction of $\boldsymbol{m}$ is determined by minimizing $g_L(\theta)$. The phase diagram of the equilibrium direction is shown in Fig. 1(b). We assume $K_{u1,eff} \geq 0$ and the perpendicular state is stable or metastable.

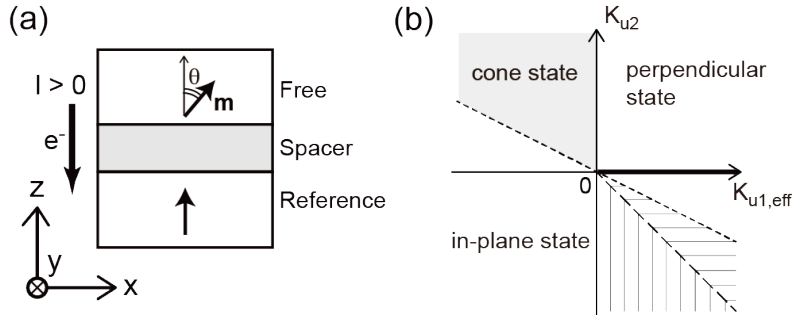

Fig. 1 (a) Schematic illustration of the system we considered. Positive I is defined as electrons (e-) flowing from the free layer to the reference layer. (b) Phase diagram of equilibrium direction of $\boldsymbol{m}$. The conventional perpendicular state with $K_{u2} = 0$ is

Rie MATSUMOTO
E-mail: rie-matsumoto@aist.go.jp
tel: +81-29-861-2751

indicated by the thick solid line. Metastable regions are hatched.

III. RESULTS AND DISCUSSIONS

κ of the free layer can be calculated by analyzing Δ_0 from Eq. (1) and I_{sw} from Eq. (2). By normalizing Δ_0 with I_{sw}, the dependence of κ on $K_{u1,eff}$ and K_{u2} is obtained as

$$\kappa/\kappa^{(p0)} = (3\cdot 6^{1/2}/2)\, r_K^{1/2}\,(1+ r_K)/(1 + 2\, r_K)^{3/2} \qquad \text{for } r_K > 1/4, \tag{3}$$

$$\kappa/\kappa^{(p0)} = 1 + r_K \qquad \text{for } -1/2 \le r_K \le 1/4, \tag{4}$$

$$\kappa/\kappa^{(p0)} = -1/(4r_K) \qquad \text{for } r_K < -1/2. \tag{5}$$

Here, κ is normalized by $\kappa^{(p0)}$, and r_K represents the ratio of K_{u2} to $K_{u1,eff}$, that is $r_K = K_{u2}/K_{u1,eff}$. In Fig. 2, the normalized switching efficiency ($\kappa/\kappa^{(p0)}$) of the p-FL given in Eqs. (3) - (5) is plotted as a function of r_K. It should be noted that $\kappa/\kappa^{(p0)}$ is larger than unity for a positive r_K and takes a maximum value of $2^{1/2}$ at r_K =1.

IV. CONCLUSIONS

The analytical expression of the STT-switching efficiency is derived for the perpendicularly magnetized free layer with the second-order uniaxial magnetic anisotropy. The switching efficiency is maximized at $K_{u1,eff} = K_{u2}$. $\kappa/\kappa^{(p0)}$ in the p-FL with the positive K_{u2} can be larger than those in the p-FL without K_{u2} and in the c-FL.

IV. ACKNOWLEDGMENTS

This work was partially supported by JSPS KAKENHI Grant Number JP16K17509.

REFERENCES

1) R. Matsumoto et al., "Spin-transfer-torque switching in a spin-valve nanopillar with a conically magnetized free layer", *Appl. Phys. Express.,* 8 063007, (2015).
2) D. Apalkov and W. H. Butler, U.S. Patent No. 8,780,665 (15 July 2014).
3) R. Matsumoto et al., "Theoretical analysis of thermally activated spin-transfer-torque switching in a conically magnetized nanomagnet", *Phys. Rev. B*, 92 140409 (2015).
4) R. Matsumoto et al., "Efficiency of Spin-Transfer-Torque Switching and Thermal-Stability Factor in a Spin-Valve Nanopillar with First- and Second-Order Uniaxial Magnetic Anisotropies", *Phys. Rev. Applied,* 7 044005, (2017).

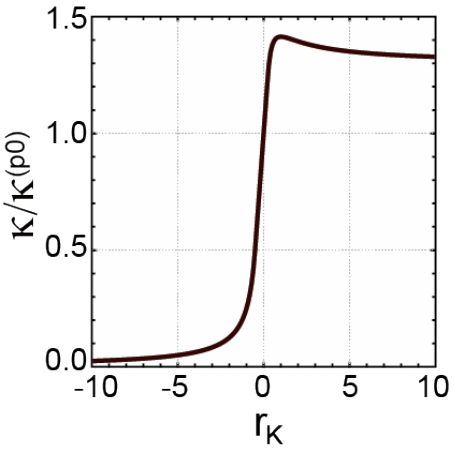

Fig. 2 r_K dependence of the normalized switching efficiency ($\kappa/\kappa^{(p0)}$).

THE Fe/Cr INTERCHANGE INDUCES SIGN CHANGE IN VOLTAGE-CONTROL MAGNETIC ANISOTROPY

Indra PARDEDE,[1] Tomosato KANAGAWA,[1] Nurul IKHSAN,[1] Masao OBATA,[1, 2] Tatsuki ODA,[1, 2]

[1]Graduate School of Natural Science and Technology, Kanazawa University, Kakuma-machi, Kanazawa, 920- 1192, Japan
[2]Institute of Science and Engineering, Kanazawa University, Kakuma-machi, Kanazawa, 920-1192, Japan

A new perspective in utilizing additional degrees of freedom of electron, i.e spin by using the electric field (EF) get increasing attention in research activity in the recent year. Manipulation of the spin using EF effect is a promising technology on a magnetic device due to low power consumption, non-volatility, high-speed reading/writing and good compatibility with the conventional semiconductor industry technology [1]. In case of magnetic data storage, this field shows a great potential application, especially taking into account the recent initiative in internet of things, big data, artificial intelligence, and cloud computing. There are a lot of experimental works and theoretical investigations on the modulation and switching of magnetism in order to understand the mechanism and the demand for better performance. Several physical mechanisms have been proposed such as the modulation of spin-orbit interaction by charge accumulation and depletion [2,3,4], Rashba effect [5,6] voltage redox reaction [7] and electromigration [8]. Nevertheless, there are still many challenges in understanding the physics behind this phenomena and introduce several material systems including tuning strategies such as sign in EF effect. In the case of dynamic switching, the accurate magnetic switching can occur when the direction of total magnetic anisotropy changes from perpendicular to in-plane direction or vice versa purely by EF.

In this work, we systematically investigated EF effect in Fe/MgO interface systems with Cr underlayers by introducing the interchange of Cr and Fe layers. Our model using slab system, vacuum (0.79 nm)/Cr (6ML)/Fe (1ML)/Cr (1ML)/Fe (3ML)/MgO (5ML)/vacuum (0.79 nm) and vacuum (0.79 nm)/Cr (5ML)/Fe (1ML)/Cr (1ML)/Fe (1ML)/Cr (1ML)/Fe (2ML)/MgO (5ML)/vacuum (0.79 nm). We carried out first principles electronic structure calculations [9,10] which employ fully relativistic and scalar relativistic ultrasoft pseudopotentials and plane wave basis by using the generalized gradient approximation (GGA) for the exchange-correlation energy. The magnetic anisotropy energy (MAE) was calculated from the total energy difference between in-plane magnetization ([100] direction) and out-of-plane magnetization ([001] direction), MAE = E[100] – E[001]. In order to impose the EF, we have applied the scheme of effective screening method (ESM) developed by Otani and Sugino [11]. Some tiny number of electrons is subtracted from or added to the system for induction of the EF. The strength of EF (E) is estimated from the slope of electrostatic potential at the front of ESM.

We found an opposite sign in the modification of MAE (γ) as EF dependence, as shown in Fig. 1. Interestingly, the change of γ sign can be achieved only by increase thickness of [Fe/Cr] interchanges. This result shows that underlayer structure is very sensitive to Fe layers at the interface since EF may screen only at the interface. We attribute this a unique behavior of electronic structures in the interface resonance state of Fe/MgO. Beside concerning hybridization between the orbitals of Fe $d(3z^2\text{-}r^2)$ and O $p(z)$ which keeps the $d(3z^2\text{-}r^2)$ away from the Fermi level, Fe-Cr hybridization in the formation of antiferromagnetic (AFM) ground state may play a crucial role in electronic structure. Furthermore, a large change in the number of electron filling for 3d orbital spin states may correspond to the sensitivity modulation of MAE when applied EF. The EF modulation in the electronic structure around the Fermi level can be related with MAE by the using second order perturbative formula [12].

Opposite sign in the modification of MAE also found experimentally by Shiota *et al* in CoFeB/MgO with different underlayer, Ta or Ru respectively [13]. They confirmed such phenomenon by both the static magnetoresistance and voltage-induced ferromagnetic resonance measurement. Discussion for the reason of observed opposite sign is related to a different spin-orbit coupling in the underlayer, a difference in crystallinity, etc. but the origin is still an open question. Regarding this issue, a comprehensive study may be needed in order to clarify and propose some possible origin against underlayer effect. Additionally, the

Indra Pardede
pardede@cphys.s.kanazawa-u.ac.jp

MAE variation on band-filling may contribute to a fundamental understanding in the physics of EF effect, particularly, the orbital occupancy in the 3d orbitals.

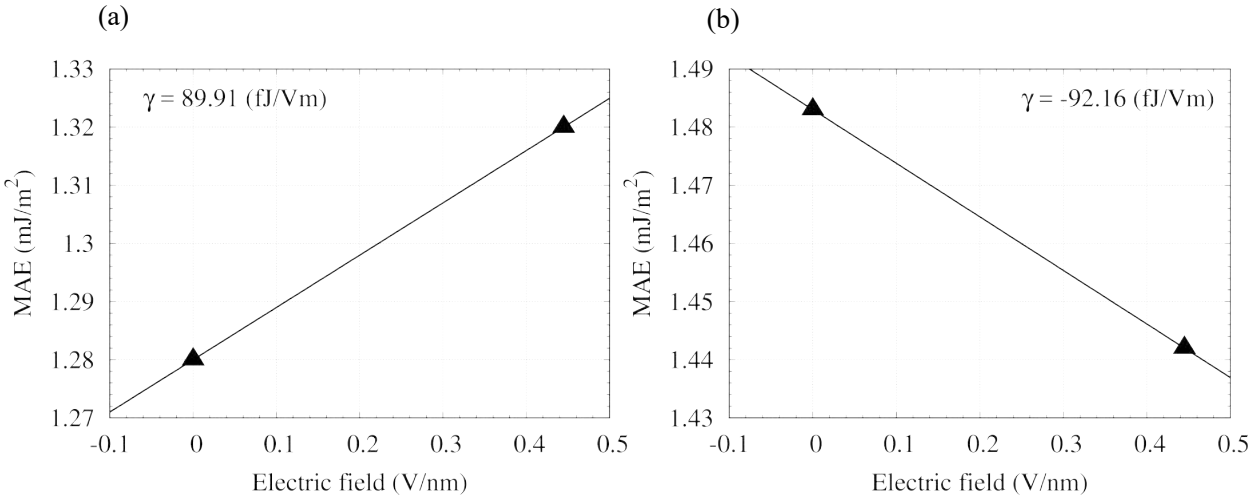

Fig. 1 EF variation of MAE in system (a). Cr (6ML)/Fe (1ML)/Cr (1ML)/Fe (3ML)/MgO (5ML) and (b) Cr (5ML)/Fe (1ML)/Cr (1ML)/Fe (1ML)/Cr (1ML)/Fe (2ML)/MgO (5ML).

This work was supported by ImPACT Program of Council for Science, Technology and Innovation (Cabinet Office, Japan Government) and by the Kanazawa University SAKIGAKE Project.

REFERENCES

[1] C. Song, B. Cui, F. Li, X. Zhou and F. Pan, Progress in Material Science. 87, 10.1016, (2017)

[2] C.-G. Duan, J. P. Velev, R. F. Sabirianov, Z. Zhu, J. Chu, S. S. Jaswal, and E. Y. Tsymbal, Phys. Rev. Lett. 101,137201 (2008).

[3] K. Nakamura, R. Shimabukuro, Y. Fujiwara, T. Akiyama, T. Ito, and A. J. Freeman, Phys. Rev. Lett. 102, 187201 (2009).

[4] M. Tsujikawa and T. Oda, Phys. Rev. Lett. 102, 247203 (2009).

[5] L. Xu and S. Zhang, J. Appl. Phys. 111, 07C501 (2012).

[6] S. E. Barnes, J. Ieda, and S. Maekawa, Sci. Rep. 4, 4105 (2013).

[7] U. Bauer, L. Yao, A. J. Tan, P. Agrawal, S. Emori, H. L. Tuller, S. van Dijken, and G. S. D. Beach, Nat. Mater. 14, 174 (2015).

[8] A. Rajanikanth, T. Hauet, F. Montaigne, S. Mangin, and S. Andrieu, Appl. Phys. Lett. 103, 062402 (2013)

[9] T. Oda, A. Pasquarello, and R. Car, Phys. Rev. Lett. 80, 3622, (1998).

[10] T. Oda and A. Hosokawa, Phys. Rev. B 72, 224428 (2005).

[11] M. Otani and O. Sugino, Phys. Rev. B 73 115407, (2006)

[12] D. S. Wang, R. Wu, and A. J. Freeman, Phys. Rev. B 47, 14932 (1993).

[13] Y. Shiota, F. Bonell, S. Miwa, N. Mizuochi, T. Shinjo, and Y. Suzuki, Appl. Phys. Lett. 103, 082410 (2013).

DP-23

THEORETICAL PREDICTION ON THICKNESS TUNABLE MAGNETIC ANISOTROPY ENERGY AND ELECTRIC FIELD EFFECT ON Cr-BUFFERED Fe/MgO INTERFACE

Nurul IKHSAN[1], Tomosato KANAGAWA[1], Indra PARDEDE[1], Masao OBATA[1,2] and Tatsuki ODA[1,2]

1) Graduate School of Natural Science and Technology, Kanazawa University, Kakuma, Kanazawa, 920-1192, Japan, ikhsan@cphys.s.kanazawa-u.ac.jp

2) Institute of Science and Engineering, Kanazawa University, Kakuma, Kanazawa, 920-1192, Japan

I. INTRODUCTION

Thin film containing Fe/MgO interface has unique magnetic characteristic, such as perpendicular magnetic anisotropy (PMA) and voltage controlled magnetic anisotropy (VCMA). By combining this novel properties, we try to create disruptive memory technologies with high density and low power consumption. Proposed technology seems to be mature, but there is still room for improvement. The current value of PMA in this interface is still below 1 mJ/m^2 [1]. This value needs to be improved to prevent the memory deterioration due to disturbance of external field.

II. METHOD AND SYSTEM

In search for superior features, systematic approach on the thickness variation of ferromagnet layer in Cr-buffered Fe/MgO interface has been performed by the current state-of-the-art of density functional theory (DFT). Generalized gradient approximation with high density of k-mesh, equipped with spin-orbit interaction [2], is employed to estimates the total energy difference of perpendicular and in-plane magnetizations. In addition to such energy of DFT, the magnetic dipole interaction energy (MDI) correction was carried out to estimate the total magnetic anisotropy energy (MAE).

III. RESULTS

Figure 1 shows the theoretical prediction in thinner layer compared to the experimental ones. Two calculation result of MAE are presented, the first MAE contribution comes only from spin-orbit interaction (SOI), the latter from SOI and MDI. As decreasing the thickness of ferromagnet layer, the PMA increases. In the other side, electric field effect (EFE) is decreasing until the sign finally reaches to negative one. Theoretical prediction at ultrathin configuration (2 monolayers) shows improvement of PMA and the negative of sign of EFE. This change may be related to the large change in electronic structure.

Basic mechanism of PMA based on second order perturbation theory is used to explain the positive contribution to MAE. Different way of electron filling mechanism of the iron at the interface in 2 ML configuration may relate to the change of its sign. The large peak of electron density of states just above the Fermi level may relate to the formation of interface resonant state (IRS). Non-rigid band filling mechanism of such IRS is observed at ultrathin configuration starting from 2 to 5 MLs. But the detail mechanism of this abrupt change in MAE and EFE may be attributed to electron filling of the local 3d orbitals on the interface Fe.

III. DISCUSSIONS

It has been predicted previously that the buffer modification (from Pd to Pt) in the 2-dimensional ferromagnet interface could provide change of EFE [3]. But currently we discuss that the ferromagnet thickness modification in this theoretically perfect Fe/MgO interface could lead to the similar physical properties, without the need of heavy metals [4] in the thin film stacking. This negative sign of EFE is interested for device application, because its consume less energy to modify the magnetization of each

Nurul Ikhsan
E-mail: ikhsan@cphys.s.kanazawa-u.ac.jp

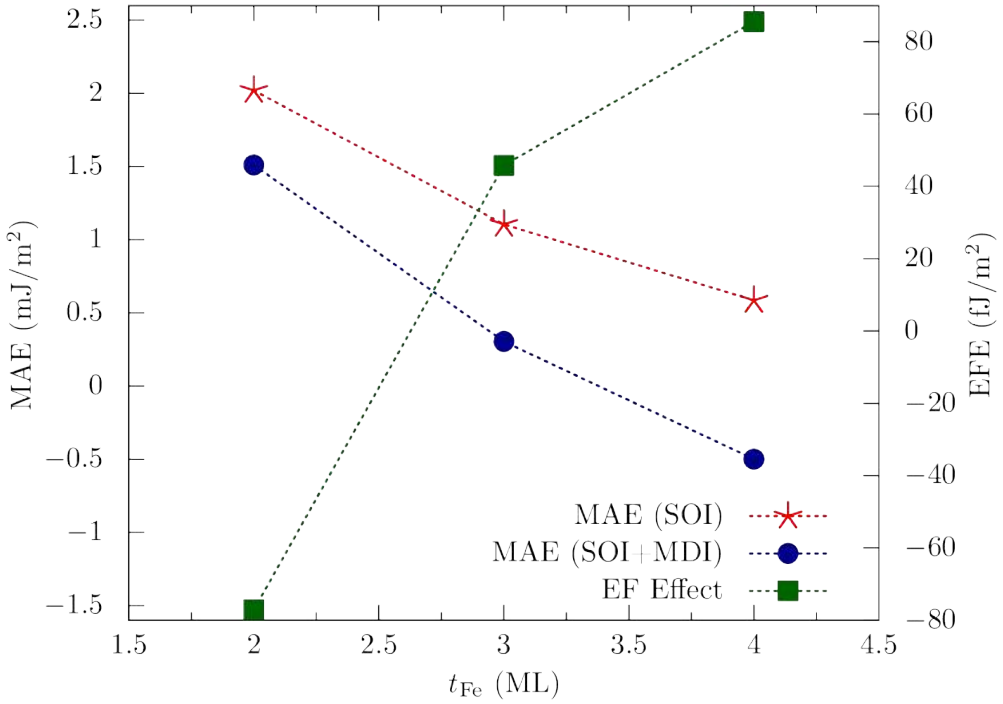

Figure 1. Theoretical prediction on magnetic anisotropy energy and electric field effect in ultra-thin ferromagnet configuration

magnetic tunnel junction (MTJ) cell. Also supported with larger PMA, theoretically this thin film configuration has huge potential for the high density and low power memory cell device. Continues development toward accurate prediction on searching for superior characteristic in this interface are still performed.

This work was supported by ImPACT Program of Council for Science, Technology and Innovation (Cabinet Office, Japan Government) and by the Kanazawa University SAKIGAKE Project.

REFERENCES

1) T. Nozaki et al. (2016). Phys. Rev. Appl. **5**, 044006 (2016).
2) T. Oda and A. Hosokawa (2005), Phys. Revw. B **72**, 224428 (2011).
3) S. Haraguchi et al., J. Phys. D: Appl. Phys. **44**, 064005 (2011).
4) D. Yoshikawa et al., Appl. Phys. Exp., **7**, 113005 (2014).

HUGE ELECTRIC-FIELD-INDUCED MAGNETIC ANISOTROPY OF THE 5*d* TRANSITION-METAL MONOLAYERS ON Fe(001) AND Co(0001)

M. TSUJIKAWA[1,2], M. SHIRAI[1,2]
1) RIEC, Tohoku Univ., Sendai, Japan
2) CSRN, Tohoku Univ., Sendai, Japan

I. INTRODUCTION

The voltage-torque magnetoresistive random access memory is the ultra-low energy consumption non-volatile memory based on voltage-controlled magnetic anisotropy (VCMA). The variation of the magnetic anisotropy energy (MAE) upon the electric field was reported to be 30-40 fJ/Vm for the MgO/Fe/Au and MgO/CoFeB/Ta films [1, 2]. Recently, large VCMA effect (290 fJ/Vm) was reported for the MgO/Fe/Cr film [3]. However VCMA effect larger than 1000 fJ/Vm is required for realizing voltage-induced magnetization switching in MTJ below 30nm. The purpose of this work is to design the magnetic film exhibiting huge VCMA. We theoretically investigated the electric-field modulation of MAE for Fe(001) and Co(0001) films covered by the 5*d* transition-metal monolayer (ML).

II. METHOD

We have carried out first-principles electronic structure calculations with employing the projector augmented-wave with plane wave basis set by using the Vienna ab initio simulation package [4]. We estimated MAE and its electric-field modulation for TM(1ML)/bcc-Fe(4ML)/Cu(001)(5ML) and TM(1ML)/hcp-Co(4ML)/Cu(111)(5ML) films (TM = Hf, Ta, W, Re, Os, Ir, Pt, Au). The MAE was estimated by using the magnetic force theorem. To discuss the origin of the MAE and its electric-field modulation, we also evaluated the contribution of the MAE from the second-order perturbation of the spin-orbit coupling [5].

III. RESULT

Figures 1(a) and (b) show the MAE and its electric-field modulation, respectively, for the TM/Fe/Cu and TM/Co/Cu films. The modulation lager than 100 fJ/Vm was obtained for the Ta/Fe, W/Fe, Ir/Fe, Hf/Co and Ir/Co films. In particular, the Ir/Fe film has the largest value, 263 fJ/Vm, which is about 8 times larger than that for the Fe surface (-32 fJ/Vm). The Ir/Fe, Os/Fe and Ir/Co films have huge perpendicular magnetic anisotropy (PMA) energy greater than 10 mJ/m^2 and thus films are promising for the voltage-controlled MRAM application. We also evaluated the electric-filed modulation of MAE for the MgO/TM/Fe films. Huge electric- field modulation is obtained for the MgO/Os/Fe (176 fJ/Vm) and MgO/Ir/Fe (-298 fJ/Vm) films.

IV. DISCUSSION

We discuss the origin of huge PMA and its electric-field modulation of the Ir/Fe film. Figures 2(a) and (b) show the contribution arising from the second-order perturbation of spin-orbit coupling to the MAE and its electric-field modulation, respectively, for the Ir and Fe atoms in the Ir/Fe film. We found that the PMA and tis electric-field modulation are predominantly originated from the Ir layer. The contribution from the Fe layers is smaller by several orders of magnitude compared to that from the Ir layer. As shown in Fig. 2(a), the spin-flip term between occupied majority-spin and unoccupied minority-spin states ($E_{\uparrow\downarrow}$) mainly contributes to the PMA of the Ir layer. We cannot ignore the spin-flip term for the 5d-transition-metal atoms, since both the majority- and minority-spin states exist near the

Masahito Tsujikawa
E-mail: t-masa@riec.tohoku.ac.jp
tel: +08-022-217-5077

Fermi level due to the small exchange splitting. Especially, the matrix element $\langle d_{yz,\uparrow}|\hat{\ell}_x|d_{3z^2-r^2,\downarrow}\rangle$ of the Ir atom plays an important role in the huge PMA, since the density of states projected on the minority-spin d_{yz} and the majority-spin $d_{3z^2-r^2}$ orbital exhibits prominent peak structure below and above the Fermi level, respectively. On the other hand, spin-conservation term between occupied and unoccupied majority-spin states ($E_{\uparrow\uparrow}$) and the spin-flip term between occupied minority- and unoccupied majority-spin states ($E_{\downarrow\uparrow}$) contribute to the electric-field modulation of MAE (see. Fig. 2(b)).

V. SUMMARY

We investigated the MAE and its electric-field modulation of the Fe and Co films covered by the 5*d* transition-metal ML. The huge MAE and its electric-field effect are expected for the Of/Fe, Ir/Fe, Ir/Co films. The enhancement of MAE and electric-field modulation can be attributed to strong spin-orbit coupling as well as large induce spin moment of 5*d* transition-metals.

ACKNOWLEDGEMENT

This work was funded by ImPACT Program of Council for Science, Technology and Innovation (Cabinet Office, Government of Japan).

REFERENCES

1) T. Nozaki *et al.*, *Appl. Phys. Lett.* 96, 022506 (2010).
2) M. Endo *et al.*, *Appl. Phys. Lett.* 96, 202503 (2010).
3) T. Nozaki *et al.*, *J. Phys. Rev. Appl.* 5, 044006 (2016).
4) G. Kresse and J. Furthmuller, Vienna Ab-initio Simulation Package University of Wien, 2001
5) Y. Miura *et al.*, J. Phys.: Condens. Matter 25, 106005 (2013).

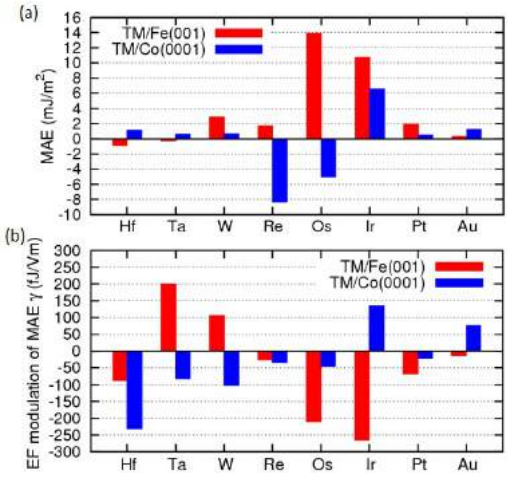

Fig. 1 Magnetic anisotropy energy (MAE) (a) and its electric field modulation γ (b) for the 5*d*-TM/Fe(001) and 5*d*-TM/Co(0001) surface.

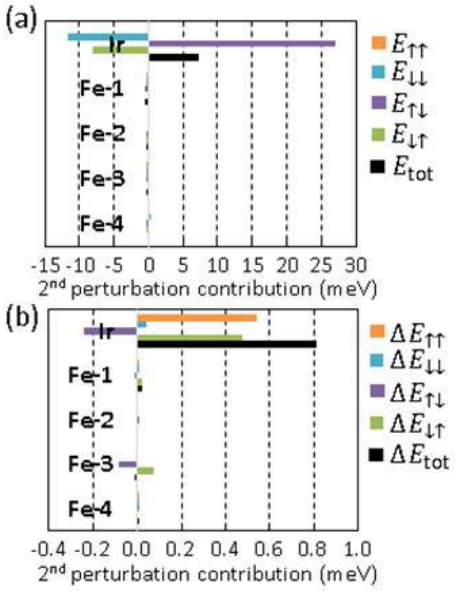

Fig. 2 The contribution arising from the second-order perturbation of spin-orbit coupling to the MAE (a) and its variation ΔE at the electric field of -0.5 GV/m (b) for the Ir/Fe film.

WRITE ERROR RATE OF VOLTAGE-DRIVEN MAGNETIZATION SWITCHING IN PERPENDICULARLY-MAGNETIZED MAGNETIC TUNNEL JUNCTIONS

Tatsuya YAMAMOTO[1], Yoichi SHIOTA[1], Takayuki NOZAKI[1], Shingo TAMARU[1], Kay YAKUSHIJI[1], Hitoshi KUBOTA[1], Akio FUKUSHIMA[1], Shinji YUASA[1], and Yoshishige SUZUKI[1,2],

1) National Institute of Advanced Industrial Science and Technology, Spintronics Research Center, Tsukuba, Ibaraki 305-8568, Japan

2) Graduate School of Engineering Science, Osaka University, Toyonaka, Osaka 560-8531, Japan

I. INTRODUCTION

Voltage-controlled magnetic anisotropy (VCMA) in ferromagnetic metal thin films [1] has attracted much attention from both physical and practical points of view, and that has provided a playground for designing a variety of experiments and devices. In particular, the demonstration of magnetization switching in magnetic tunnel junctions (MTJs) by applying sub-nanosecond voltage pulses [2] has opened a new way of developing ultralow-energy-consumption magnetic random access memories (MRAMs), the so-called voltage-torque MRAMs. In the voltage-torque MRAMs, the information is stored in magnetic "free" layers and the writing process is proceeded using precessional dynamics of magnetization induced by VCMA effect. As the amplitude of the voltage required to switch the magnetization is determined by the balance between the VCMA effect and the uniaxial magnetic anisotropy constant (K_u) of free layer, it is very important to realize a large VCMA effect as well as a large K_u in order to minimize the energy consumption while securing an enough thermal stability.

In addition to a large VCMA effect and a large K_u, there is a growing need for improving the writing error rate (WER). In contrast to spin-transfer-torque MRAMs in which the switching direction is determined by the polarity of dc current, the magnetization switching in voltage-torque MRAMs is currently only possible for one voltage polarity, and the WER is sensitive to the duration time of voltage pulse (τ_{pulse}). Recently, we evaluated WER in perpendicularly-magnetized MTJs (p-MTJs) consisting of an MgO/$Fe_{80}B_{20}$/W stacking structure [3]. The WER of the p-MTJs indeed showed a strong dependence on τ_{pulse}, and a minimum WER of $\sim 4 \times 10^{-3}$ was achieved at τ_{pulse} corresponding to half the period of magnetization precession. This WER is, however, not sufficient for most of the practical use.

According to the simulation based on a macrospin model in Ref [3], the WER can further be reduced by improving the thermal stability factor and the VCMA effect in the free layer. In this study, we perform a systematic investigation using Ta/$(Co_xFe_{100-x})_{80}B_{20}$/MgO stacking structures. By varying the Co-Fe composition ratio in $(Co_xFe_{100-x})_{80}B_{20}$, we study the dependence of alloy composition and annealing temperature on magnetic properties and VCMA effect in order to gain guidelines to improve the WER. We also study an influence of the change in pulse shape, such as differences in rise and fall time, on the WER.

II. EXPERIMENTAL PROCEDURES

Figure 1 schematically illustrates the p-MTJ along with the measurement circuit used for the evaluation of WER. The p-MTJ consists of a Ta (5 nm)/$(Co_xFe_{100-x})_{80}B_{20}$ (1.1 or 1.2 nm)/MgO (1.4 nm) free layer and a 1.4-nm-thick $(Co_{10}Fe_{90})_{80}B_{20}$ reference layer whose magnetization direction is fixed by a [Co/Pt]-based perpendicularly-magnetized synthetic antiferromagnetic layer. Thin films were prepared on a chemical-mechanical-polished Si substrate with bottom electrode using a sputtering system (Canon ANELVA EC7800) at room temperature. The Fe-Co composition ratio was controlled by co-sputtering an $Fe_{80}B_{20}$ and a $Co_{80}B_{20}$ alloy targets. After an ex-situ annealing, the prepared films were microfabricated into the device structure by combining electron-beam lithography, photolithography, and Ar-ion etching. In order to evaluate WER, the p-MTJ was connected to a pulse generator via a microwave probe and voltage

Tatsuya YAMAMOTO
E-mail: yamamoto-t@aist.go.jp
tel: +81-29-861-3432

pulses were applied through the rf port of bias tee, whereas the resistance change associated with the magnetization switching was monitored by an oscilloscope. All the measurements were performed at room temperature.

III. EXPERIMENTAL RESULTS

As expected from the Slater-Pauling behavior, $(Co_{31}Fe_{69})_{80}B_{20}$ films showed the largest saturation magnetization among the prepared films. Moreover, the largest PMA and the VCMA effect were obtained for $(Co_{31}Fe_{69})_{80}B_{20}$. Owing to the large PMA and thereby the improved thermal stability, at an optimum condition, the p-MTJ with Ta/$(Co_{31}Fe_{69})_{80}B_{20}$ (1.1 nm)/MgO exhibited a minimum WER of 2×10^{-5}, which is two orders of magnitude lower than that obtained for those using MgO/$Fe_{80}B_{20}$/W [3].

Then, we will discuss the influence of the change in pulse shape on WER. Figure 2 displays the minimum WER obtained with changing the slope of voltage pulse, where hollow (filled) symbols correspond to the dependence of WER on the rise (fall) time, $\tau_{rise\ (fall)}$. It can be seen that WER almost monotonically increases with τ_{rise}. However, interestingly, a slight increase of τ_{fall} exhibits clear improvement in WER under optimal condition. For τ_{fall} = 0.156 ns the WER became about half the value of that for τ_{fall} = 0 ns. This experimental result would be useful to design the device assembly.

REFERENCES

1) T. Maruyama et al., "Large voltage-induced magnetic anisotropy change in a few atomic layers of iron", *Nat. Nanotech*., **4**, 158 (2009).
2) Y. Shiota et al., "Induction of coherent magnetization switching in a few atomic layers of FeCo using voltage pulses", *Nat. Mater*., **11**, 39 (2012).
3) Y. Shiota et al., "Evaluation of write error rate for voltage-driven dynamic magnetization switching in magnetic tunnel junctions with perpendicular magnetization", *Appl. Phys. Express*, **9**, 013001 (2016).

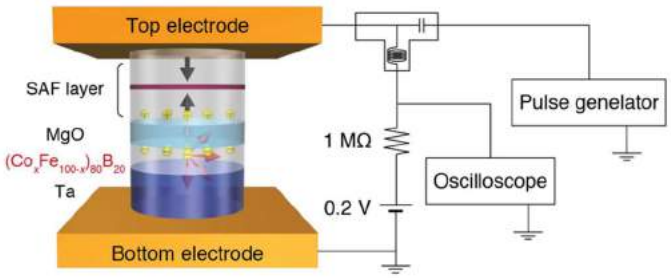

Fig. 1: Schematic illustration of the device structure along with the measurement circuit used for the evaluation of WER.

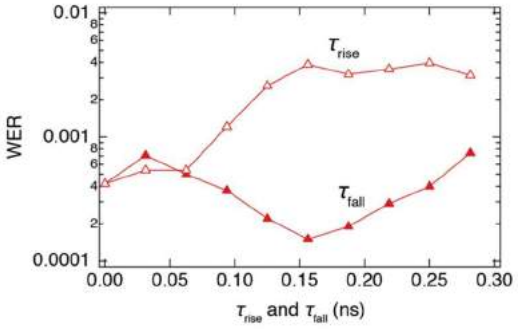

Fig. 2: WER as a function of τ_{rise} and τ_{fall}. Hollow and filled symbols correspond to the dependence of WER on τ_{rise} and τ_{fall}, respectively.

HIGH MAGNETIC STABILITY IN p-SAF TYPE PERPENDICULAR MAGNETIC TUNNEL JUNCTIONS FOR SPIN-TRANSFER-TORQUE MAGNETIC RANDOM ACCESS MEMORY BY UTILIZING Ir SPACER LAYER

A. SUGIHARA, K. YAKUSHIJI, A. FUKUSHIMA, H. KUBOTA, and S. YUASA
National Institute of Advanced Industrial Science and Technology, Tsukuba, Japan, a.sugihara@aist.go.jp

I. INTRODUCTION

A perpendicularly magnetized magnetic tunnel junction (p-MTJ) is a promising candidate as a memory cell of spin-transfer-torque switching magnetic random access memory (STT-MRAM). To yield steady read and write operation of the STT-MRAM's memory cells, perpendicularly magnetized synthetic antiferromagnetic (p-SAF) structure in the reference layer should have sufficient stability of antiferromagnetic (AF) exchange coupling which depends on the spacer layer material. So far, mainly Ru has been employed as the spacer layer material because of its high potential for strong AF exchange coupling [1, 2]. In this study, we studied AF coupling in p-SAF structure with Ir and Rh spacer layer as another candidate and also evaluated STT-switching properties in the p-MTJs [3].

II. EXPERIMENTS

Stacking structure of the p-SAF-structured films is Si-O substrate / Ta(50) / Ru(60) / Pt(20) / $[Pt(1.6)/Co(2.4)/]_{n=6}$/ Spacer(t) / $[Pt(1.6)/Co(2.4)]_{n=6}$ / Pt(20) / capping layer (thicknesses are in Å), where n is repetition number. AF exchange coupling energy (J_{ex}) for each film was estimated from M-H curves. The p-MTJ films based on the p-SAF structure with Ir spacer layer were microfabricated into nano-pillars (18 - 60 nm in diameter(ϕ)) to evaluate the STT-switching properties.

III. RESULTS AND DISCUSSIONS

Figure 1 shows M-H curves for Ir, Ru, and Rh spacer layer whose thickness (t) is 4.5, 4.3 and 19 Å. The t value is selected to show best J_{ex} value for each material. The J_{ex} value was estimated from the formula of $J_{ex} = M_s \cdot t_{FM} \cdot H_{ex}$, where M_s and t_{FM} are saturation magnetization and thickness of the [Pt/Co] layer and H_{ex} is AF exchange coupling field which is found as a shift of hysteresis in the M-H curve as shown in Fig.1. The largest H_{ex} value for Ir in Fig.1 (12 kOe) indicates that Ir shows maximum J_{ex} value in this work. On the other hand, no large H_{ex} was found for Rh spacer layer.

Figure 2 shows the J_{ex} for various spacers as the function of t and the magnified image for the range of t = 3 - 7.5 Å in the inset. The maximum J_{ex} values were 2.6 erg/cm^2, which is over 20% higher than that for the Ru [2]. Moreover, the first peak for the Ir is broader than that for the Ru, suggesting that Ir has very high potential for manufacturability of STT-MRAM because it tolerates the thickness variation of the spacer layer.

Figure 3 and Fig.4 show a minor loop of an R-H curve and switching properties for the 25 nmϕ nano-pillar with 4.8 Å-thick Ir spacer layer. The H_{ex} exceeding 8 kOe and the high TMR of 133% at low RA-product of 5.2 $\Omega\mu m^2$ are achieved. Moreover, switching efficiency was estimated to be about 2, which is rather higher than that for Ru spacer layer. These results indicate that the p-SAF with Ir spacer layer is superior to that with Ru spacer layer and more suitable for STT-MRAM.

ATSUSHI SUGIHARA
E-mail: a.sugihara@aist.go.jp
tel: +81-29-861-4621

REFERENCES

1) S. S. P. Parkin, "Systematic Variation of the Strength and Oscillation Period of Indirect Magnetic Exchange Coupling through the 3d, 4d, and 5d Transition Metals", *Phys. Rev. Lett.* **67**, 3598 (1991).
2) K. Yakushiji, H. Kubota, A. Fukushima, and S. Yuasa, "Perpendicular Magnetic Tunnel Junctions with a Strong Antiferromagnetic Interlayer Exchange Coupling at First Oscillation Peak", *Appl. Phys. Express* **8**, 083003 (2015).
3) K. Yakushiji et al., "Very Strong Antiferromagnetic Interlayer Exchange Coupling with Iridium Spacer Layer for Perpendicular Magnetic Tunnel Junctions", *Appl. Phys. Lett.,* **110**, 092406 (2017).

ACKNOWLEDGEMENT

This work was supported by the ImPACT Program of the Council for Science, Technology, and Innovation.

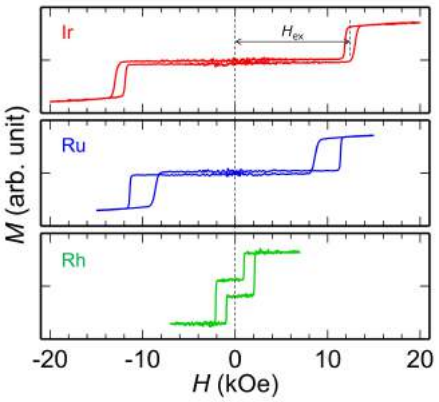

Fig.1 Magnetization curves for p-SAF structures with the Ir, Ru, and Rh spacer layers. Spacer layer thickness (t) of the each layer is t = 4.5, 4.3 and 19 Å, respectively.

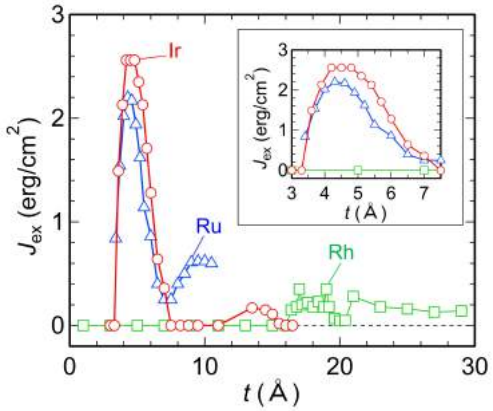

Fig.2 Antiferromagnetic exchange coupling energy (J_{ex}) for functions of t. The inset shows magnified image for the range of t = 3 – 7.5 Å.

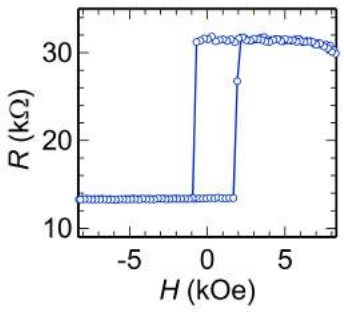

Fig.3 Minor loop of an *R-H* curve for the 25 nmϕ nano-pillar with the Ir-spacered p-SAF reference layer.

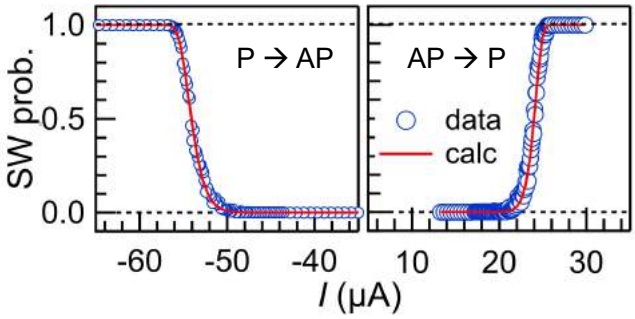

Fig.4 STT-switching properties for the nanopillar with Ir spacer layer whose size is 25 nmϕ.

SPECIFIC NONLINEARITY OF VOLTAGE CONTROLLED MAGNETIC ANISOTROPY IN Fe/MgO LAYERED STRUCTURES

Qingyi XIANG[1], Zhenchao WEN[2], Hiroaki SUKEGAWA[3], Shinya KASAI[3], Takeshi SEKI[4], Takahide KUBOTA[4], Koki TAKANASHI[4] and Seiji MITANI[1]

1) Graduate School of Pure and Applied Sciences, University of Tsukuba & National Institute for Materials Science (NIMS), Tsukuba 305-0047, Japan

2) Center for Spintronics Research Network (CSRN), Tohoku University, Sendai 980-8577, Japan

3) NIMS, Tsukuba 305-0047, Japan

4) Institute for Materials Research & CSRN, Tohoku University, Sendai 980-8577, Japan

XIANG.Qingyi@nims.go.jp

I. INTRODUCTION

Voltage-controlled magnetic anisotropy (VCMA) in a ferromagnetic metal layer attracts a lot of interest in recent years. This technology can help to realize low-power manipulation of spin, which is a key technique for next generation magnetization random access memories (MRAMs). It used to be considered impractical since the insulator barrier layer in a typical magnetic tunnel junction (MTJ) makes the electric field penetrate only into the metal in a limited range, namely, only near the interface. However, recently it has been achieved to realize VCMA effect in an ultrathin Fe layer based all-solid-stat devices [1]. This led to an approach to develop voltage controlled MRAM, via direct manipulation by voltage or assistance to spin-transfer toque. More recently, a large VCMA effect over 200 fJ/Vm has been demonstrated in Fe/MgO structures [2].

The magnitude of perpendicular magnetic anisotropy (PMA) is also a key factor to provide a high memory density and better thermal stability. It was predicted a large PMA can be realized in Fe/MgO structure, and a large PMA around 1.4 MJ/m^3 was reported in a previous work [3]. The mechanisms of PMA and VCMA are somehow different, but both strongly depend on the metal/oxide interface conditions. Considering the Fe/MgO case, hybridization between Fe-3d and O-2p orbitals appears to play a key factor to realize large PMA, meanwhile the spin-dependent screening may also affect the electronic occupancy of 3d orbitals.

In this work, we investigated PMA and VCMA with different annealing conditions, to explore how these two effects interplay with each other. The PMA in this work is roughly 1 MJ/m^3 and the VCMA is as large as 266 fJ/Vm, i.e., both are comparable to the previous works.

II. EXPERIMENT METHOD

A fully epitaxial stack of MgO (5 nm)/Cr (30 nm)/Fe (0.7 nm)/MgO (2.2 nm)/Fe (2 nm)/Ru (15 nm) was deposited on a MgO (100) substrate by molecular beam epitaxy. The substrate was annealed at 800°C for cleaning, followed by depositing a 5-nm-thick MgO at 450°C as a seed layer. The Cr buffer layer was deposited at 150°C, and then a 800°C annealing process was performed to get a flat surface. The ultrathin Fe was grown at the 150°C and post-annealed at 250°C to increase the surface flatness. Then the barrier MgO layer was deposited at 150°C. After the deposition of MgO layer, further annealing was performed at different temperatures of 325°C, 350°C, 375°C, and 400°C to obtain interface PMA at the Fe/MgO with different interface conditions. Subsequently, the in-plane-magnetized reference Fe layer was deposited at 150°C without annealing. Finally, a Ru layer was sputter-deposited at room temperature for capping. The samples were fabricated into $5 \times 10\mu m$ ellipses by photo-lithography, ion-beam milling and lift-off process. The tunnel magnetoresistance (TMR) ratio was measured using physical property measurement system (PPMS) under an in-plane external field at RT and low temperatures.

III. RESULT AND DISCUSSION

Fig. 1(a) shows a TMR curve for the Fe/MgO MTJ with a 90˚ magnetization configuration. When applying an external field, the magnetization of the top Fe is saturated immediately, and then the resistance

Qingyi Xiang
E-mail: XIANG.Qingyi@nims.go.jp
tel: +81-08091735207

of the junction changes as a function of the relative angel of magnetizations of the bottom Fe and top Fe. Thus, we can write the in-plane magnetization component of the bottom Fe as follows:

$$\frac{M_{in-plane}}{M_s} = \cos\theta = \frac{R_{90}-R(\theta)}{R(\theta)}\frac{R_p}{R_{90}-R_p} \quad (1)$$

Then we can analyze how the perpendicular anisotropy changes depending on the annealing temperatures and different bias voltages. As shown in Fig.1 (b), the different annealing temperatures caused different PMA energy densities. The sample annealed at 350°C has the largest PMA energy density.

Fig. 2 shows the PMA energy density ($K_{eff}t_{Fe}$) as a function of an applied electric field. Large VCMA behavior was obtained, and it took a maximum of 266 fJ/Vm for the post-annealing at 350˚C. More interestingly, despite the difference in annealing temperature, all the VCMA curves show similar non-linear behavior in which there exists a local minimum around 100 mV/nm. Furthermore, it was confirmed that the local minimum around 100 mV/nm appears, being independent of measurement temperature, while the PMA energy densities clearly increase with decreasing temperature (not shown). The local minimum appears to be the VCMA behavior specific to Fe/MgO, which can be experimental evidence for the electronic origin of VCMA phenomena.

REFERENCES

1) Maruyama T, et al., "Large voltage-induced magnetic anisotropy change in a few atomic layers of iron", *Nat. Nanotechnol.* **4** 158 (2009)
2) Nozaki T, et al., "Large Voltage-Induced Changes in the Perpendicular Magnetic Anisotropy of an MgO-Based Tunnel Junction with an Ultrathin Fe Layer", *Phys. Rev. Appl.* **5** 044006 (2016)
3) Koo J W, et al., "Large perpendicular magnetic anisotropy at Fe/MgO interface" *Appl. Phys. Lett.* **103** 192401 (2013)

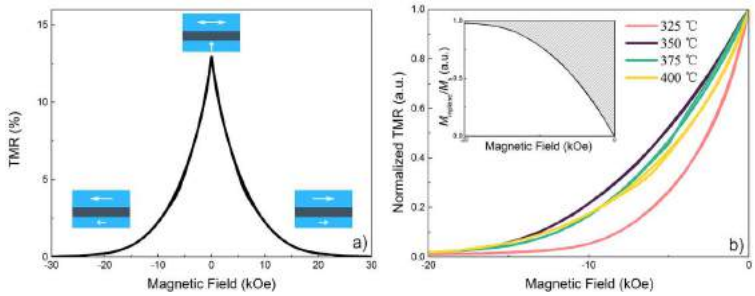

Fig. 1 (a) Typical full TMR curve for a sample annealed at 400°C, (b) normalized TMR curves for different annealing temperatures. The inset is the in-plane component of magnetization where the shadow area represents the PMA energy density.

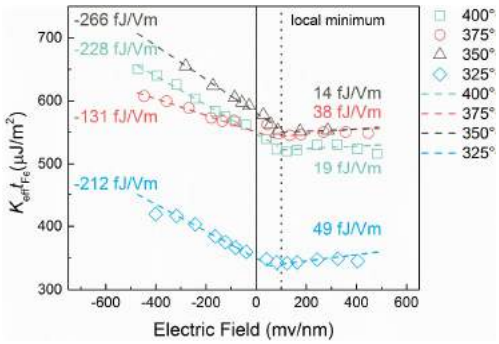

Fig.2 VCMA curves under different annealing temperatures, the dashed line is the linear fitting. A local minimum around 100 mV/nm can be clearly found for different annealing temperatures.

CRITICAL FREQUENCY OF MICROWAVE ASSISTED MAGNETIZATION SWITCHING

H. ARAI[1], and H. IMAMURA[2]

1) AIST, Spintronics R. C., Tsukuba, Japan, and PRESTO, JST, Kawaguchi, Japan, arai-h@aist.go.jp

2) AIST, Spintronics R. C., Tsukuba, Japan, h-imamura@aist.go.jp

I. INTRODUCTION

The microwave-assisted switching (MAS) of magnetization is a promising method for reducing the switching field of ultrahigh-density magnetic recording media [1]. The most important feature of MAS is that the switching field decreases with increasing frequency f of the radio frequency (rf) field H_{rf}, and it takes a minimum value at a certain critical frequency f_c. Although past studies based on the macrospin model in a rotating frame revealed the physics behind f_c, an analytical expression for f_c has not been obtained; i.e., f_c was obtained only by numerical calculation. In this paper, we theoretically analyzed MAS in a perpendicularly magnetized circular disk and derived an analytical expression for f_c by analyzing the presence of a quasi- periodic mode by calculating the energy change over one precession period in the rotating frame [2].

II. MODEL AND THEORY

Schematic illustration of the system we studied is shown in Fig. 1(a). We assumed a perpendicularly magnetized circular disk. A static magnetic field $\boldsymbol{H}_{dc}$ is applied in the negative z-direction. A circularly polarized rf field $\boldsymbol{H}_{rf}(t)$ is also applied in the x-y plane, where the amplitude is H_{rf} and the angular frequency is ω. We adopt a rotating frame where X- and Y- axes rotate around the z-axis, which keeps the X-axis follows the rf field as shown in Fig. 1(b). The dimensionless Landau-Lifshitz-Girbert (LLG) equation in the rotating frame is given by,

$$d\boldsymbol{m}/d\tau = -\mathrm{m}\times\boldsymbol{h}_{\mathrm{eff}}^{\mathrm{rot}} - \alpha\,\boldsymbol{m}\times(\boldsymbol{m}\times\boldsymbol{h}_{\mathrm{eff}}^{\mathrm{rot}}) - \alpha\omega_{\mathrm{d}}\,\boldsymbol{m}\times(\boldsymbol{m}\times\boldsymbol{e}_{z}), \quad (1)$$

where $\boldsymbol{h}_{\mathrm{eff}}^{\mathrm{rot}} = [\, H_{\mathrm{rf}}\boldsymbol{e}_{X} + (-H_{\mathrm{dc}}+H_{\mathrm{k}}^{\mathrm{eff}}m_{z})\,\boldsymbol{e}_{z}\,]/M_{\mathrm{s}}$, $\omega_{\mathrm{d}} = \omega/\gamma M_{\mathrm{s}}$, $\tau = \gamma M_{\mathrm{s}}t$, and $\boldsymbol{e}_{i}$ is the unit vector along i-axis. We assume $\alpha \ll 1$. The effective anisotropy field is defined as, $H_{\mathrm{k}}^{\mathrm{eff}} = 2K_{\mathrm{u}}/(\mu_0 M_{\mathrm{s}})-M_{\mathrm{s}}$, where K_{u} is the uniaxial anisotropy constant, μ_0 is the magnetic permeability of vacuum, M_{s} is the saturation magnetization.

The fixed points of Eq. (1) are obtained by setting $d\boldsymbol{m}/d\tau = 0$. They are called periodic (P) modes, because the fixed points in the rotating frame represent the state rotating with ω in the laboratory frame [3]. The stability of the P mode is analyzed by a linearized equation of motion for a small deviation of $\delta\boldsymbol{m}$ from the fixed point, $d\delta\boldsymbol{m}/d\tau = A\delta\boldsymbol{m}$, where A is the matrix. In the simple analysis, f_c is obtained $\det A = \mathrm{Tr}A$ and is larger than that obtained by numerical simulations [4].

The discrepancy is solved by considering quasiperiodic (Q) modes, which represent limit cycles in the rotating frame [3]. The magnetization switching is the transition from the initial P mode to the final P mode. If an attractive Q mode exists between them, the switching is interrupted. Such Q mode appears in the lower frequency than f_c given by the simple analysis [5]. The presence of the Q mode is analyzed by calculating the change over one precession period at the saddle point of the magnetic energy density, $d\varepsilon/d\tau = w_{\mathrm{dis}} + w_{\mathrm{rf}}$, where w_{dis} represents the work of dissipation and w_{rf} represents the work of the rf field. By integrating over one precession period, one obtain the energy loss (gain) due to dissipation (rf field). The value of f_c is obtained by solving the equation where energy loss and energy gain are balanced,

$$f_{\mathrm{c}} = \gamma H_{\mathrm{k}}^{\mathrm{eff}} F^{2/3}\{6-5F^{2/3}\} / (6\pi\{1-F^{2/3}\}^{1/2}) \quad (2)$$

in SI unit. Here F is $H_{\mathrm{rf}}/H_{\mathrm{k}}^{\mathrm{eff}}$. For a small rf field satisfying $H_{\mathrm{rf}} \ll H_{\mathrm{k}}^{\mathrm{eff}}$, the critical frequency is approximated as $f_{\mathrm{c}} \sim \gamma/\pi\{H_{\mathrm{k}}^{\mathrm{eff}}H_{\mathrm{rf}}^{2}\}^{2/3}$.

Hiroko Arai
E-mail: arai-h@aist.go.jp
tel: +81-29-862-6639

III. RESULTS

Figure 1(c) shows switching field as a function of rf frequency numerically obtained from magnetization dynamics solved by LLG equation. We set initial state as $m_z = 1$. Applying H_{dc} and $H_{rf}(t)$ at $t = 0$, magnetization dynamics is calculated for 100 ns. Then if $m_z < 0$, we clarified the magnetization is switched. The dots in Fig. 1(c) indicate that the magnetization is switched. Material parameters are assumed as $M_s = 1.0$ MA/m, $K_u = 0.85$ MJ/m^3, and $\alpha = 0.01$. The value of f_c is found at 4.6 GHz for $H_{rf} = 0.4$ kOe (31.8 kA/m). Figure 1(d) shows H_{rf} dependence of f_c. The dots indicate the numerical results, and dashed line indicates the analytical result calculated by Eq. (2). Our analytical expression agrees well with the numerical results.

IV. SUMMARY

We analyzed the presence of a quasiperiodic mode for magnetization dynamics in the rotating frame, and obtained the analytical expression for the critical frequency in magnetization switching assisted by rf field. The value of f_c is expressed as a function of H_{rf} and H_k^{eff}. The validity of the analytical formula is confirmed by comparing with the numerical simulations.

REFERENCES

1) J. G. Zhu, X. Zhu and Y. Tang, "Microwave Assisted Magnetic Recording," IEEE Trans. Magn., 44(1), 125-131, (2008).
2) H. Arai and H. Imamura, "Analytical expression for critical frequency of microwave assisted magnetization switching", Jpn. J. Appl. Phys., 55, 028002, (2016).
3) G. Bertotti, I. D. Mayergoyz, and C. Serpico, "*Nonlinear Magnetization Dynamics in Nanosystems*", Chap. 7, Elsevier, 2009.
4) S. Okamoto, N. Kikuchi, M. Furuta, O. Kitakami, and T. Shimatsu, "Microwave assisted magnetic recording technologies and related physics", J. Phys. D, 48 (35), 353001, (2015).
5) H. Suto, K. Kudo, T. Nagasawa, T. Kanao, K. Mizushima, R. Sato, S. Okamoto, N. Kikuchi, and O. Kitakami, "Theoretical study of thermally activated magnetization switching under microwave assistance: Switching paths and barrier heigh", Phys. Rev. B, 91, 094401, (2015).
6)
7)

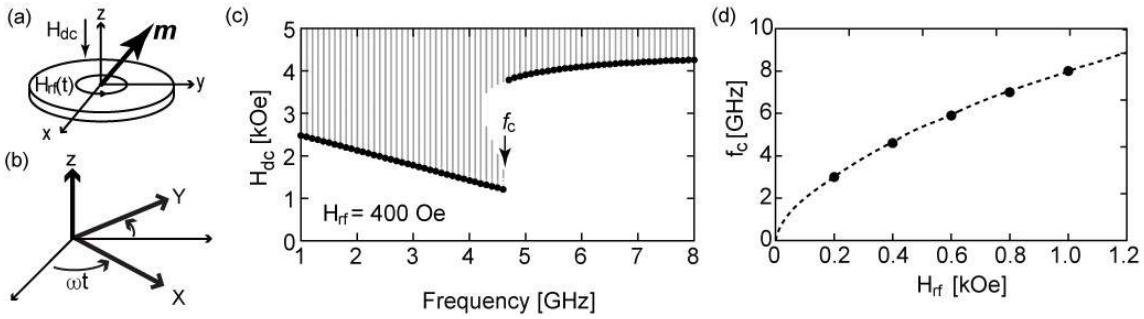

Fig. 1 (a) Schematic illustration of the circular disk and laboratory frame. (b) Definition of the rotating frame. (c) Numerically obtained switching condition. In the colored area, ***m*** is switched. Critical frequency (f_c) is indicated by the arrow. (d) H_{rf} dependence of f_c. Circles represent numerically obtained f_c. Dashed line represents f_c given by Eq. (2).

THEORETICAL STUDY OF SPIN WAVE EXCITATION IN PERPENDICULARLY MAGNETIZED SINGLE LAYER

Toshiki YAMAJI[1] and Hiroshi IMAMURA[2]

1) AIST, Spintronics RC, Tsukuba, Japan, toshiki-yamaji@aist.go.jp

2) AIST, Spintronics RC, Tsukuba, Japan, h-imamura@aist.go.jp

I. INTRODUCTION

Microwave assisted switching (MAS) of magnetization has attracted much attention as a novel switching technique to reduce the switching field of ultra-high-density magnetic recording media [1]. The reduction of the switching field of MAS of a nano-magnet is well understood by analyzing the dynamics of a macrospin-model in a rotating frame synchronized with the applied radio frequency (rf) field. In the rotating frame, the rf field acts as a static field parallel to the rotating axis and reduces the switching field. For MAS, however a certain critical frequency, f_c exits [1-2]. A switching field, h_{sw} monotonically decreases with increase of rf frequency, f and it takes a minimum value h_{min} at f_c. Once f exceeds f_c the h_{sw} shows sudden increase and takes almost the same value as that without rf field. Thus in principle the h_{sw} can't be reduced below the h_{min} on MAS.

Recently S. Okamoto et al. has reported that a significant reduction of the h_{sw} is realized in a single Co/Pt nanodot with perpendicular magnetic anisotropy by applying a large rf field but one much smaller than the effective anisotropy field [2]. The large amplitude nonuniform magnetization motion, that is, spin wave (SW) was exited in the Co/Pt nanodot with the large diameter whereas that was not observed in the Co/Pt nanodot with the small diameter. The h_{sw} of the Co/Py with the small diameter was conventionally analyzed by the macrospin model. It was found that the f_c increase due to the excitation of the large amplitude SW and the reduction of the h_{sw} is consequently much more significant than the theoretical prediction based on the single macrospin model.

So far we have studied the MAS behavior and its dynamics of a perpendicularly magnetized single layer by a Landau-Lifshitz-Gilbert (LLG) numerical simulation and theoretical analysis. It was revealed from the LLG numerical simulation that the large amplitude SW is exited above a certain critical layer thickness, $d_{c(SW)}$ and that the f_c increases due to the excitation of the large amplitude SW above a certain critical layer thickness $d_{c(f)}$. It was furthermore found that the $d_{c(SW)}$ is not equal to $d_{c(f)}$ ($d_{c(SW)} < d_{c(f)}$). In this study the analytical estimation of the $d_{c(SW)}$ a was established from the analysis of **P**-modes and SW instabilities on LLG phase diagram.

II. P-MODE AND SPIN WAVE INSTABILITY

By setting $d\theta/dt = d\varphi/dt = 0$ in a normalized LLG equation expressed by the zenith and azimuth angles, θ and φ, one obtains the equations (1) and (2) for the fixed points, i.e., **P**-modes of the magnetization dynamics in the rotating frame:

$$\nu_0 = \frac{h_{az} - \omega}{\cos\theta_0} + \kappa_{eff}, \tag{1}$$

$$\nu_0^2 = \frac{h_{a\perp}^2}{\sin^2\theta_0} - \alpha^2\omega^2, \tag{2}$$

where $\nu_0 = \alpha\omega\cot\varphi_0$. α and ω are the damping constant and the angular frequency of the rf field. h_{az} and $h_{a\perp}$ are the static magnetic field, H_{dc} and the circularly polarized rf field, H_{rf} normalized by the saturation magnetization, M_s, respectively. θ_0 and φ_0 are the angles identifying the **P**-modes. The effective anisotropy field, κ_{eff}:

$$\kappa_{eff} = \kappa + N_\perp - N_z \tag{3}$$

Hiroshi IMAMURA
E-mail: h-imamura@aist.go.jp
tel: +81-29-862-6713
fax: +81-29-861-3422

where the normalized anisotropy field $\kappa = 2K_1 / \mu_0 M_s^2$. K_1 is the physical anisotropy constant, μ_0 is the magnetic permeability of vacuum. $N_\perp$ and N_z are the demagnetization factors. The demagnetization factors satisfy the relation: $N_z + 2N_\perp = 1$.

The SW instability matrix A_q is as follows,

$$A_q = \frac{1}{1+\alpha^2}\begin{pmatrix} 1 & -\alpha \\ \alpha & 1 \end{pmatrix}\begin{pmatrix} -\alpha\omega\cos\theta_0 & -\nu_q \\ \nu_q - \kappa_q \sin^2\theta_0 & -\alpha\omega\cos\theta_0 \end{pmatrix} \quad (4)$$

where $\nu_q = \nu_0 - N_\perp + q^2 + (1/2)\sin^2\theta_q$, $\kappa_q = \kappa$ -1 + (3/2) $\sin^2\theta_q$. q is the wavevector constant. θ_q is the angle between the direction of the wavevector and the static magnetization, therefore $\sin\theta_q$ is zero for the current perpendicularly magnetized layer model.

When the stable **P**-mode with $\cos\theta_0 \sim 1$ vanishes as h_{az} increases, the fixed point moves to another **P**-mode with $\cos\theta_0 \sim 0.87$. If this **P**-mode is located in the inside of the red line satisfying $\det A_q \leqq 0$, the large amplitude SW is expected to be exited. The $d_{c(SW)}$ can be therefore analytically estimated from the condition, $\det A_q = 0$ after substitution of h_{az}, ν_0 and θ_0 satisfying that the line for the Eq. (1) is tangent to one for the Eq. (2) into Eq. (4).

II. LLG SIMULATION AND ANALYTICAL RESULT

Figure 1 shows a schematic illustration of an effective spin model of the single layer used for the LLG numerical simulation where the perpendicularly magnetized each cells with 1 nm thickness are coupled with each other by the exchange stiffness coupling, A_{ex}. H_{dc} is applied along the z-direction and H_{rf} is applied in the xy-plane. As seen in Figure 2, the analytical result for the $d_{c(SW)}$ is good agreement with the result of the LLG simulation. The estimation of the $d_{c(SW)}$ established in this study is expected to be important feature for improving the ultra-high density of the magnetic recording.

ACKNOWLEDGMENT

This work was supported by JSPS KAKENHI Grant-in-Aid for Young Scientists (B) 17K18412.

REFERENCES

1) J. G. Zhu, X.Zhu, and Y.Tang, *IEEE Trans. Magn*., **44**, 125 (2008).
2) S. Okamoto, N. Kikuchi, M. Furuta, O. Kitakami, and T. Shimatsu, *J. Phys. D: Appl. Phys.*, **48**, 353001 (2015)
3) G. Bertotti, I. D. Mayergoyz, C. Serpico, *J. Appl. Phys.*, **91**, 8656 (2002).

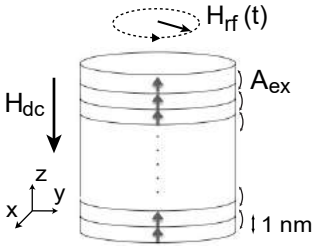

Fig. 1 Effective spin model of perpendicularly magnetized single layer.

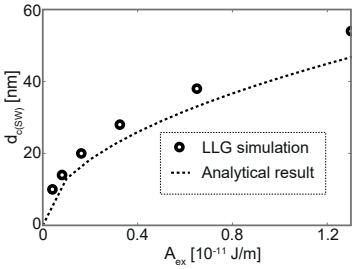

Fig. 2 Results of LLG simulation and SW instability analysis for $d_{c(SW)}$.

NOTE

NOTE

Empty